Polarized Ultracold Neutrons: their transport in diamond guides and potential to search for physics beyond the standard model

Mark F. Makela

Dissertation submitted to the faculty of the Virginia Polytechnic Institute and State University in partial fulfillment of the requirements for the degree of

Doctor of Philosophy
In
Physics

R. Bruce Vogelaar, Chair
John Ficenec
Randy Heflin
Mark Pitt
Tatsu Takeuchi
Chia Tze

January 24, 2005
Blacksburg, Virginia

Keywords: Polarized Ultracold Neutrons, Polarized Neutron Guides, Pulsed Laser Deposition, Diamond-Like Carbon, Neutron Beta Decay, Standard Model Tests

Polarized Ultracold Neutrons: their transport in diamond guides and potential to search for physics beyond the standard model

Mark F. Makela

ABSTRACT

Experiments with polarized "ultracold neutrons" (UCN) offer a new way to measure the decay correlations of neutron beta decay; these correlations can be used to test the completeness of the Standard Model and predict physics beyond it. Ultracold neutrons are very low energy neutrons that can be trapped inside of material and magnetic bottles. The decay correlations in combination with the neutron and muon lifetimes experimentally find the first element (V_{ud}) of the Cabibbo-Kobayashi-Maskawa (CKM) quark mixing matrix. The CKM matrix is a unitary transform between the mass and weak eigenstates of the d, s and b quarks; if the matrix is not unitary this would imply that the Standard Model is not complete. Currently the first row of the CKM matrix is over 2 sigma from unitarity and V_{ud} is the largest component of the row.

The UCNA experiment looks at the correlation between the polarization of the neutron and the momentum of the electron resulting from the beta decay of the neutron (the A-correlation). The keys to making a high precision measurement of A-correlation are a near 100% polarization of the neutrons that decay, low–backscatter electron detectors, and small, well characterized backgrounds. UCN can be 100% polarized by passing them through a seven Telsa magnetic field. The key to the UCNA experiment is keeping them polarized until they decay or are lost.

This dissertation covers the development of guides that are minimally depolarizing and efficient transporters of UCN and their use in the UCNA experiment. The entire guide development process is covered from conception to manufacturing and testing. This

process includes development of a pulsed laser deposition, diamond-like carbon coating system and materials studies of the resulting coatings. After the initial studies of the guide coating, meter–long sections of guide are tested with UCN to determine their depolarization and transport properties.

The guide technology developed in this dissertation has been used in the entire UCNA experiment. Also, this technology is currently the state of the art for polarized and non-polarized UCN guide systems and it is being implemented in several new UCN experiments.

Table of Contents

List of Figures

List of Tables

Grants

This work was funded primarily by the National Science Foundation though grants 0099448 and 0401526.

Acknowledgment

First of all I would like to acknowledge my advisor Dr. R. Bruce Vogelaar for accepting me as a graduate student and helping me to become a contributing researcher in the field of ultracold neutron physics. I would also like to thank the rest of my committee (Dr. John Ficenec, Dr. Randy Heflin, Dr. Mark Pitt, Dr. Tatsu Takeuchi, Dr. Chia Tze and Dr. Richard Zallen) for their time, guidance and help during my graduate career at Virginia Tech. In addition, I would like to thank Dr. Albert Young of North Carolina State University for his guidance and encouragement on this project.

This project would not have been possible without the help of the Virginia Tech Material Science and Engineering Department, in particular Dr. Carlos Suchicital and Dr. Robert Hendricks.

Special thanks to Steve MacCartney and Frank Cromer of Virginia Tech for help analyzing my samples, and teaching me how to run their instruments.

Graduate students Henning Back, Martin Dress, and Brian Dickerson provide help and support whenever it was needed, thanks. Thanks also to Robert Pattie for taking time away from his undergraduate class load to help on the depolarization experiments and other parts of the project.

Tom Bowles, Chris Morris, Bill Teasdale, Andy Saunders and Axel Pichlmaier (now at PSI) of Los Alamos National Lab, thanks for making the UCNA depolarization experiments possible.

Thank you, Chris Thomas for all the help during my time at VT. It would be much harder without you there helping the graduate students, and not as much fun.

Finally, I would like to thank my family (Diane, AJ and Troy) for helping me through this long process.

Dedication

This dissertation is dedicated to a few people that make my life a great one. First of all it is dedicated to my wife Diane and our children Andrew and Troy. Diane and Andrew have supported me through the whole process, while Troy has just joined us for the end. It is also dedicated to my parents and brother who have watched over, helped and supported me for so long. Finally, it is dedicated to the Vaughans who have accepted me and supported me in this endeavor.

1 Introduction

Experiments with polarized ultracold neutrons (UCN) offer a new way to measure the decay correlations of neutron beta decay; these correlations can be used to test the completeness of the Standard Model and predict physics beyond it. Ultracold neutrons are very low energy neutrons that can be trapped inside of material and magnetic bottles. The decay correlations in combination with the neutron and muon lifetimes experimentally find the first element (V_{ud}) of the Cabibbo-Kobayashi-Maskawa (CKM) quark mixing matrix. The CKM matrix is a unitary transform between the mass and weak eigenstates of the d, s and b quarks; if the matrix is not unitary this would imply that the Standard Model is not complete. Currently the first row of the CKM matrix is over 2 sigma from unitarity and V_{ud} is the largest component of the row[1, 2].

Precision measurements of V_{ud} are obtained from two different types of experiments: the decay correlation between the electron and the polarized neutron (A–correlation, "A", A_0 – the subscript zero implies that the value has been corrected for known effects like recoil) in neutron beta decay and the super-allowed $0^+ \rightarrow 0^+$ nuclear beta decays. The super-allowed $0^+ \rightarrow 0^+$ decays currently give the most accurate values of V_{ud}, but theoretical errors dominate the uncertainly.[1, 2, 3] Neutron beta decay has less theoretical uncertainty but the experimental errors are great and the various experiments do not agree with each other. The goal of the UCNA experiment (an experiment to measure the A–correlation using UCN) is to lower the experimental error in V_{ud} obtained from neutron beta decay so that it is comparable to that from super-allowed $0^+ \rightarrow 0^+$ decays.

The UCNA experiment will be the first measurement of the A–correlation of polarized neutron beta decay using UCN; the previous precision measurements were made with cold neutron beams at reactors. The UCNA experiment will be a complete departure from previous cold neutron experiments with different, and lower backgrounds and corrections to be applied in the extraction of the A–correlation. The two main advantages of the UCNA experiment are 100% polarization of the neutrons and a pulsed beam

induced prompt background. The neutron source is a pulsed spallation target, rather than a reactor, so the backgrounds are time dependent and very different than previous reactor based cold neutron beam experiments. The 100% polarization of the neutrons is achieved by passing the UCN through a seven Tesla magnetic field; one spin-state is blocked by the interaction of the neutron's magnetic moment with the field, while the other is accelerated through it. In order to have high polarization in the experiment the UCN must maintain polarization until they decay or leave the decay region.

The UCN travel a couple of meters and bounce off the guide walls many times between the polarizer and the decay region; each of these wall interactions can potentially depolarize the UCN. This thesis details the development and testing of special diamond-like carbon (DLC) coated guides for transporting polarized UCN in the UCNA experiment. The result of this work sets a new standard in neutron guides for both polarized and unpolarized UCN.

With the approaching data taking cycle of the UCNA experiment, a new high precision value of the A–correlation in neutron beta decay will add to the data on the unitarity of the CKM matrix.

1.1 Polarized Neutron Decay and the Unitarity of the Cabibbo-Kobayashi-Maskawa Quark Mixing Matrix

Neutron beta decay, in conjunction with the muon lifetime, can be used to find V_{ud} the largest element of the first row of the CKM matrix. The weak charged coupling constant found from neutron beta decay is used with the Fermi coupling constant extracted from muon decay to calculate V_{ud}. Since neutron beta decay is a mixture of vector and axial currents the value of the weak charged coupling constant is derived using two decay relations: a decay correlation and the neutron lifetime. The unitarity of the first row of the CKM matrix can be tested by combining the squares of V_{ud}, V_{us} and V_{ub}; V_{us} and V_{ub} are obtained from accelerator–based experiments.

There are several decay correlations that can be observed in neutron beta decay, but only the correlation between the spin of the parent neutron and the resulting electron (A-correlation) is found with sufficient precision to make a useful extraction of V_{ud}. Improvements in the measurement of the A–correlation and/or the neutron lifetime can both lead to an improved value for V_{ud} and a better check on CKM unitarity.

1.1.1 Correlation Coefficients of Neutron Beta Decay

The correlation coefficients of neutron beta decay are defined in the differential decay probability for oriented nuclei derived by J. D. Jackson et al.[4] The c-coefficient is not present in neutron decay since the second term is zero.

$$W\left(\langle J\rangle \mid E_e,\Omega_e,\Omega_{\bar{\nu}}\right)dE_e d\Omega_e d\Omega_{\bar{\nu}} = \frac{1}{(2\pi)^5} p_e E_e (E_0 - E_e)^2 dE_e d\Omega_e d\Omega_{\bar{\nu}} \xi$$
$$\times\left[1 + a\frac{\vec{p}_e\cdot\vec{p}_{\bar{\nu}}}{E_e E_{\bar{\nu}}} + b\frac{m_e}{E_e} + c\left(\frac{1}{3}\frac{\vec{p}_e\cdot\vec{p}_{\bar{\nu}}}{E_e E_{\bar{\nu}}} - \frac{\left(\vec{p}_e\cdot\vec{j}\right)\left(\vec{p}_{\bar{\nu}}\cdot\vec{j}\right)}{E_e E_{\bar{\nu}}}\right)\left(\frac{J(J+1) - 3\left\langle\left(\vec{J}\cdot\vec{j}\right)^2\right\rangle}{J(2J-1)}\right) + \frac{\langle\vec{J}\rangle}{J}\cdot\left(A\frac{\vec{p}_e}{E_e} + B\frac{\vec{p}_{\bar{\nu}}}{E_{\bar{\nu}}} + D\frac{\vec{p}_e\times\vec{p}_{\bar{\nu}}}{E_e E_{\bar{\nu}}}\right)\right]$$

$m_e \equiv$ electron mass

$E_e \equiv$ electron energy

$E_0 \equiv$ electron endpoint energy

$\vec{p}_{\bar{\nu}} \equiv$ antineutrino momentum

$\vec{p}_e \equiv$ electron momentum

$J \equiv$ nuclear spin of the original nucleus

$\vec{J} \equiv$ expectation value of the vector angular momentum of the original nucleus

$\vec{j} \equiv$ unit vector in the direction of $\vec{J}$

$a, c, A, B, D \equiv$ correlation coefficients

$b \equiv$ Feirz interference term

$c = \hbar = 1$

In the article by Jackson et al. the correlation coefficients are expressed in terms of the coupling constants proposed by Lee and Yang[5]. The constants (C_S, C_V, C_A, C_T) are (scalar, vector, axial vector, tensor) coupling constants and the (unprimed, primed) constants are (parity conserving, parity non-conserving) terms. If time reversal invariance is violated, the coupling constants are complex and the correlation coefficients would be expressed in terms of the 8 complex coupling constants as follows.

$$\xi = \left(|C_S|^2 + |C_V|^2 + |C'_S|^2 + |C'_V|^2\right) + 3\left(|C_T|^2 + |C_A|^2 + |C'_T|^2 + |C'_A|^2\right)$$
$$a\xi = \left(-|C_S|^2 + |C_V|^2 - |C'_S|^2 + |C'_V|^2\right) + \left(|C_T|^2 - |C_A|^2 + |C'_T|^2 - |C'_A|^2\right)$$
$$b\xi = \pm \mathrm{Re}\left[\left(\left(C_S C_V^*\right) + \left(C'_S\, C'^*_V\right)\right) + 3\left(\left(C_T C_A^*\right) + \left(C'_T\, C'^*_A\right)\right)\right]$$
$$A\xi = 2\,\mathrm{Re}\left[\pm 2\left(\left(C_T C'^*_T\right) - \left(C_A C'^*_A\right)\right) + \left(\left(C_S C'^*_T\right) + \left(C'_S\, C_T^*\right) - \left(C_V C'^*_A\right) - \left(C'_V\, C_A^*\right)\right)\right]$$
$$B\xi = 2\,\mathrm{Re}\left[2\left(\frac{m_e}{E}\left(\left(C_T C'^*_A\right) + \left(C'_T\, C_A^*\right)\right) \pm \left(C_T C'^*_T\right) + \left(C_A C'^*_A\right)\right)\right]$$
$$- \mathrm{Re}\left[\left(\left(\left(C_S C'^*_T\right) + \left(C'_S\, C_T^*\right) + \left(C_V C'^*_A\right) + \left(C'_V\, C_A^*\right)\right) \pm \frac{m_e}{E}\left(\left(C_S C'^*_A\right) + \left(C'_S\, C_A^*\right) + \left(C_V C'^*_T\right) + \left(C'_V\, C_T^*\right)\right)\right)\right]$$
$$D\xi = 2\,\mathrm{Im}\left[\left(\left(C_S C_T^*\right) - \left(C_V C_A^*\right) + \left(C'_S\, C'^*_T\right) - \left(C'_V\, C_A^*\right)\right)\right]$$

This sea of coupling constants was reduced to C_V and C_A by the early 1960's. First, since the Feirz interference term was small or nonexistent the coupling has to be predominately C_S and C_T or C_V and C_A.[6, 7] Second, the work by Burgy et al. and Clark et al. showed that the D coefficient was very small, this implied that the coupling constants were dominantly real.[8, 9] Burgy et al. also showed that the weak interaction was dominantly V-A by measuring the values of the A and B-correlations.[8] With the resulting relations $C_S = C_T = 0$, $C_V = C'_V$ and $C_A = C'_A$ and setting $\lambda = C_A / C_V$ the correlation coefficients are generally expressed as:

$$a_0 = \frac{1-|\lambda|^2}{1+3|\lambda|^2}\ ,\ \mathrm{b}=0,\ A_0 = -2\frac{|\lambda|^2 + \mathrm{Re}(\lambda)}{1+3|\lambda|^2},\ B_0 = 2\frac{|\lambda|^2 - \mathrm{Re}(\lambda)}{1+3|\lambda|^2} \text{ and } D_0 = 2\frac{\mathrm{Im}(\lambda)}{1+3|\lambda|^2}.$$

1.1.2 From the Correlation Coefficients to V_{ud}

In the standard model the Lagrangian for beta decay is $L_{\mathrm{int}} = \frac{1}{2}\frac{G_V}{\sqrt{2}}\left(V_\mu + A_\mu\right)\left(v^\mu - a^\mu\right)$

where $V_\mu = i\overline{\Psi}_p\left[f_1(k^2)\gamma_\mu + \frac{f_2(k^2)}{2m_p}\sigma_{\mu\nu}k^\nu + if_3(k^2)k_\mu\right]\Psi_n$ and

$A_\mu = i\overline{\Psi}_p\left[g_1(k^2)\gamma_\mu\gamma_5 + \frac{g_2(k^2)}{2m_p}\sigma_{\mu\nu}k^\nu\gamma_5 + ig_3(k^2)k_\mu\gamma_5\right]\Psi_n$ in the first term are vector and axial hadronic currents and $k_\mu = (p_\mu - p'_\mu)$ is the momentum transfer from the hadrons to the leptons and the final term represents the leptonic currents.[10, 11, 12] In the

zero momentum transfer limit, $\left.\begin{array}{l} f_1(k^2) = g_V \\ f_2(k^2) = g_M \\ f_3(k^2) = g_S \\ g_1(k^2) = g_A \\ g_2(k^2) = g_T \\ g_3(k^2) = g_P \end{array}\right\} k^2 \to 0$ the form factors are known as vector, weak magnetism, induced scaler, axial vector, induced tensor, and induced pseudoscalar. The Lagrangian is generally written as:

$$L_{\text{int}} = \frac{1}{2}\frac{G_V}{\sqrt{2}}\overline{\Psi}_p\left(\gamma_\mu\left(g_V + g_A\gamma_5\right) + \frac{\mu_p - \mu_n}{2m_p}\sigma_{\mu\nu}k^\nu\right)\Psi_n\overline{\Psi}_{e^-}\gamma^\mu\left(1-\gamma_5\right)\Psi_{\bar{\nu}},$$

where the weak magnetism term is written as the difference in the neutron and proton magnetic moments.

V_{ud} can be extracted from beta decay via the following relations:

$$G_V = V_{ud}\, g_V(k^2 \to 0) G_F$$
$$G_A = V_{ud}\, g_A(k^2 \to 0) G_F \text{ ,}$$

where the weak charged coupling constants G_V and G_A replace C_V and C_A in the Lee and Yang notation.[5, 10]

The value of G_V is obtained by solving the neutron lifetime equation,

$$\tau = \frac{2\pi^3\hbar^7}{f^r m_e^5 c^4}\frac{1}{G_V^2(1+3\lambda^2)} = 885.7 \pm .8\,\text{sec.}^{10}$$

with the value of lambda obtained from a correlation coefficient measurement. G_F is obtained from the muon lifetime equation,

$$\frac{1}{\tau_\mu} = \frac{G_{F\mu}^2 m_\mu^5}{192\pi^3}\left(1+\Delta q\right)$$

$$G_{F\mu}\Big/(\hbar c)^3 = 1.16637(1)\times 10^{-5}\, GeV^{-2} \quad .^{13, 14}$$

Δq represents higher order QED corrections

The final relation needed to calculate V_{ud} is that the value of $g_V(k^2 \rightarrow 0)$ is one. The error in G_F from muon decay is around 0.0008% so the error in V_{ud} is dominated by the error in the correlation coefficient and neutron lifetime.

The most accurate formula for calculating V_{ud} including current values for the inner and outer radiative corrections, is

$$|V_{ud}|^2 = \frac{4908 \pm 4\,\text{seconds}}{\tau_n\left(1+3\lambda^2\right)} = \frac{4908 \pm 4\,\text{seconds}}{885.7 \pm .8\ \text{seconds}\left(1+3(-1.2695 \pm .0029)^2\right)}, \qquad \text{Equation 1}$$

$$|V_{ud}|^2 = .9497 \pm .0038$$

using current PDG values for lambda and the neutron lifetime.[1,2] Currently the errors in the numerator are dominated by theoretical error, while the errors in the denominator are dominantly experimental.[1,3]

1.1.3 V_{ud} and Cabibbo-Kobayashi-Maskawa Mixing Matrix Unitarity

In the Standard Model the CKM quark mixing matrix is a very well defined unitary matrix; testing its unitarity with elements found experimentally tests the completeness of the standard model. It is the matrix that rotates the mass eigenstates of the quarks into their weak eigenstates. In the representation below the unprimed quarks (b,s,d) are in their mass eigenstates and the primed quarks (d',s',b') are weak eigenstates.

$$\begin{pmatrix} d' \\ s' \\ b' \end{pmatrix} = \begin{pmatrix} V_{ud} V_{us} V_{ub} \\ V_{cd} V_{cs} V_{cb} \\ V_{td} V_{ts} V_{tb} \end{pmatrix} \cdot \begin{pmatrix} d \\ s \\ b \end{pmatrix}$$

The elements (V_{ud}, V_{us}, $V_{ub,\ldots}$) of the matrix are found from weak interaction experiments with various baryons and mesons; in particular the first element V_{ud} is deduced from neutron decay, V_{us} from Kaon decays, and V_{ub} from B meson decays.[3]

Since the CKM matrix is a unitary transform between eigenstates it must satisfy the relation

$$\begin{pmatrix} V_{ud} V_{us} V_{ub} \\ V_{cd} V_{cs} V_{cb} \\ V_{td} V_{ts} V_{tb} \end{pmatrix} \begin{pmatrix} V_{ud} V_{us} V_{ub} \\ V_{cd} V_{cs} V_{cb} \\ V_{td} V_{ts} V_{tb} \end{pmatrix}^{h.c.} = \begin{pmatrix} 100 \\ 010 \\ 001 \end{pmatrix}.$$

h.c. → *Hermitian Conjugate*

Experiments can test the completeness of the Standard Model by checking the validity of this relation; neutron beta decay can be used in combination with other experiments to verify the first row unitarity relation $|V_{ud}|^2 + |V_{us}|^2 + |V_{ub}|^2 = 1$. Using values from the Particle Data Group (PDG)[3] (V_{us}=.2200(.0026) and V_{ub}=3.67(.47)x10^{-3}), this relation yields $|V_{ud}| = \sqrt{1 - |V_{us}|^2 - |V_{ub}|^2} = .9755 \pm .0006$. The PDG value is ($V_{ud}$=.9738±.0005), this value is derived from super-allowed $0^+ \rightarrow 0^+$ nuclear beta decays (V_{ud}=.9740±.0005) in combination with muon decay and neutron beta decay (V_{ud}=.9725±.0013).[3] These values of V_{ud} differ by about three standard deviations, but new values of V_{us} and V_{ub} give values of V_{ud} that are close to the PDG average experimental value. It should also be noted that using the 2004 PDG values for A_0, the neutron lifetime and equation 1 the value of V_{ud} is 0.9745±.0023 which is very close to the $0^+ \rightarrow 0^+$ value.

New experimental values for V_{us} and V_{ub} in conjunction with new calculations of the radiative corrections show the first row to be near unity.[2] The E865 collaboration at Brookhaven National Laboratory and the KTeV collaboration at Fermilab both extract new values of V_{us} that when analyzed similarly are 0.2288±.0033 and 0.2252±.0024 respectively.[2] The BaBar collaboration has extracted a new value of V_{ub} = (4.62±.62)x10^{-3}, but this is not very significant in the unitarity sum.[2] Using the average of these new V_{us} values, the BaBar V_{ub} and the V_{ud} from super-allowed $0^+ \rightarrow 0^+$ decays the first row sum is $|V_{ud}|^2 + |V_{us}|^2 + |V_{ub}|^2 = .9997 \pm .0014$, which is in agreement with unitarity compared to the PDG value 0.9969±.0015 which is two sigma off. These new values need to be tested further with the new experiments that are – and will be – running

in the near future, but the case for unitarity is increasing if the neutron decay results are ignored.

With the addition of the PERKEO 2 results, the value of V_{ud} extracted from neutron beta decay (.9725±.0013) is below that needed for unitarity by two sigma (using PDG values) and less than one sigma using the new values of V_{us} and V_{ub}. The spread in extracted values for V_{ud} from demanding CKM unitarity, super-allowed $0^+ \rightarrow 0^+$ decays, and neutron decay experiments can be seen in Figure 1.1. The neutron data has the highest error and spread.

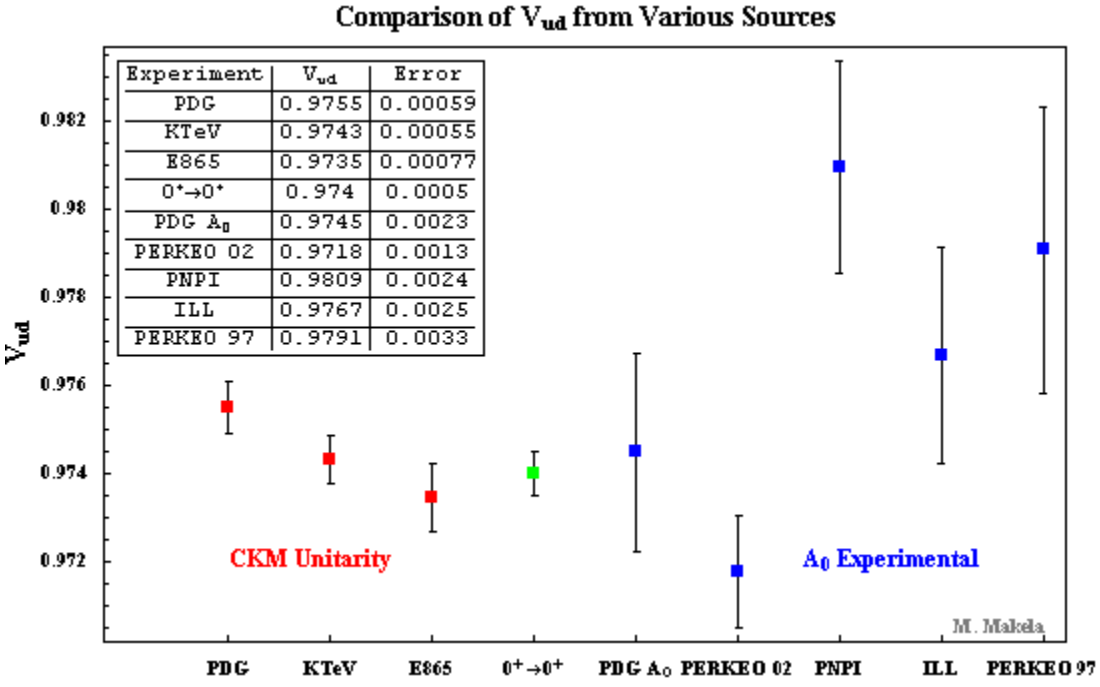

Figure 1-1 Comparison of V_{ud} extracted from various sources: The red values are from using V_{us} and V_{ub} to calculate V_{ud} assuming unitarity of the first row. The green value is the PDG value for V_{ud} from super-allowed $0^+ \rightarrow 0^+$ nuclear beta decays. Finally, the blue values are extracted using moun lifetime, neutron lifetime and the A–correlation of neutron beta decay.

The values of V_{ud} predicted by the four neutron decay experiments in figure 1-1 do not agree with each other. Still, due to the accuracy of the most recent PERKEO 2 measurement, the average is about one sigma from the value extracted from super-allowed $0^+ \rightarrow 0^+$ decays. The errors in the values extracted from neutron decay experiments are also much higher than the other errors. Both the inconsistency and the

size of the error suggest that new neutron experiments with new and lower uncertainties should be pursued.

1.1.4 The Sensitivity of V_{ud} to Changes in the Neutron Lifetime and λ

New experiments can be done to find higher precision values for both the neutron lifetime and the value of lambda; a high precision value of lambda would have the most effect on V_{ud} at this point in time. The current error in the lifetime is about 0.1%, while the error in lambda is about 1%. Equation 1 for calculating V_{ud} from the neutron lifetime and lambda has more sensitivity to lambda than the neutron lifetime as seen in figure 1-2. Figure 1-3 shows that the error in V_{ud} is also affected more by lowering the error in lambda than the neutron lifetime. Of course, reductions in the error of both the neutron lifetime and the A–correlation are expected in the near future.[15, 16, 17]

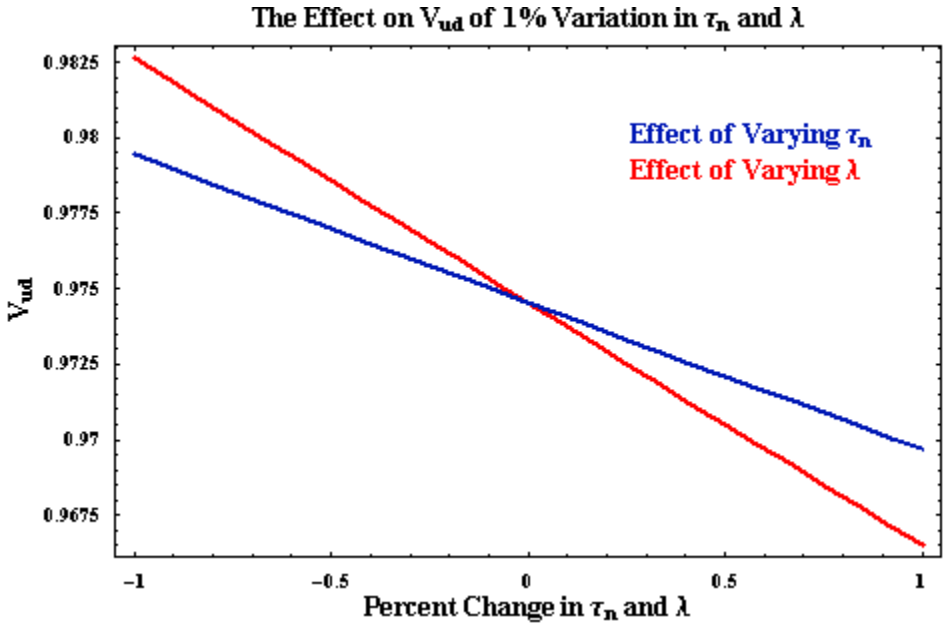

Figure 1-2 The effect on V_{ud} of 1% Variations in τ_n and λ: The steeper slope of the red line shows that variation in λ has a greater effect on V_{ud} than changes in τ_n. It should also be noted that the neutron lifetime will probably change only 0.1%, while the current spread in A–correlation values indicates λ could change by more than a percent.

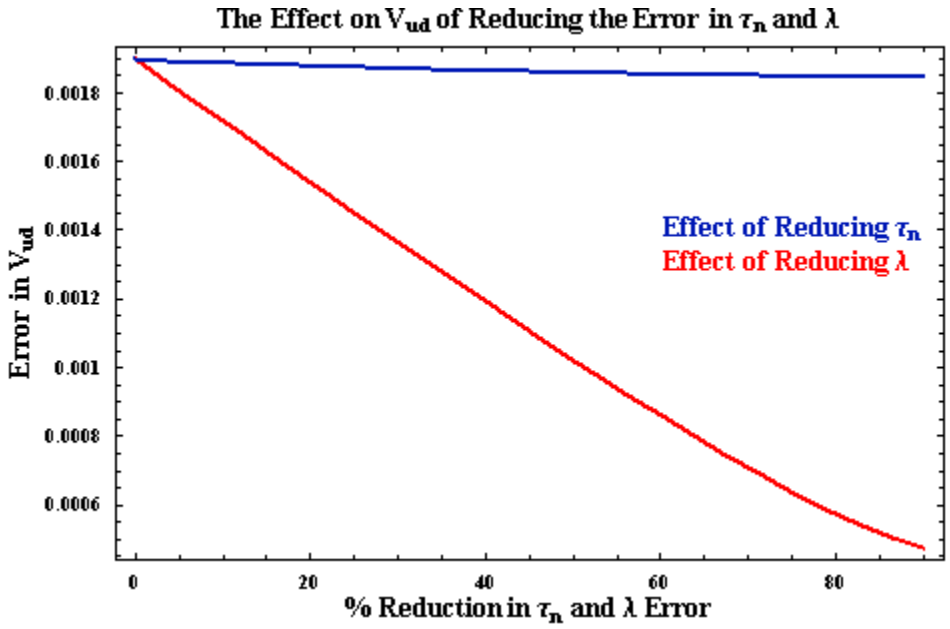

Figure 1-3 The effect on V_{ud} of reducing the error in τ_n and λ: Reduction in the error of λ will have a large effect in the error in V_{ud}. Experiments underway propose to lower both the neutron lifetime and λ errors by 80% or more.

1.1.5 The Best Correlation Coefficient for the Extracting V_{ud}

As seen in Section 1.1.1 (the final set of equations, page 4) lambda can be extracted by measuring any of the decay coefficients, but it has a different sensitivity to each. Currently the B-correlation coefficient has the lowest percent error while the D-correlation has the largest [Table 1-1]. However, having the lowest error doesn't make the B-correlation the best coefficient to calculate lambda.

PDG Values for the Neutron Decay Coefficients			
Coefficient	***PDG Value***	***Error***	***Percent Error***
a $\left(\vec{p}_e \cdot \vec{p}_{\bar{\nu}_e}\right)$	-0.103	0.004	3.88%
A $\left(\vec{\sigma}_n \cdot \vec{p}_e\right)$	-0.1173	0.0013	1.11%
B $\left(\vec{\sigma}_n \cdot \vec{p}_{\bar{\nu}_e}\right)$	0.983	0.004	0.41%
D $\left(\vec{\sigma}_n \cdot \left(\vec{p}_e \times \vec{p}_{\bar{\nu}_e}\right)\right)$	-0.6	1	166.67%

Table 1-1 PDG values for the neutron decay coefficients[3]

The sensitivity of lambda to small changes in B_0 is much greater than a_0 or A_0. This makes it a bad choice for determining lambda to a high precision [Figure 1-4]. Lambda has about the same sensitivity to both a_0 and A_0, but currently the error in A_0 is much lower making it the preferred correlation coefficient to determine both lambda and V_{ud} with.

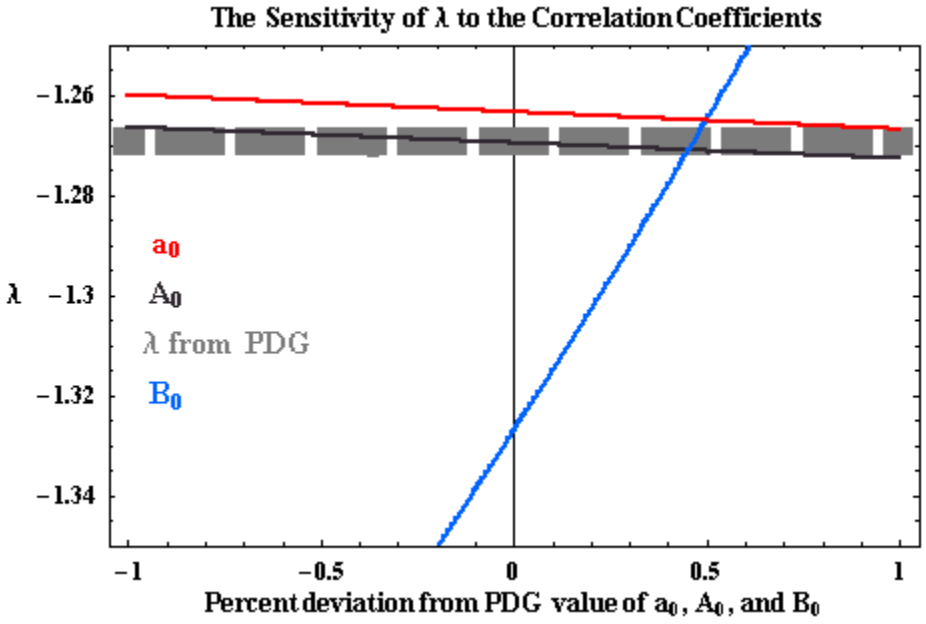

Figure 1-4 The sensitivity of λ to the correlation coefficients: This plot shows how λ is affected by changes in the correlation coefficients of neutron beta decay. Since a small change in B_0 gives a large change in λ, it is not used to determine λ. A_0 is currently used, since it has lower error than a_0.

By starting with V_{ud} (derived by demanding CKM unitarity) and using the PDG, E965 and KTeV values for $V_{us,}$ the correlation coefficients that would correspond to unity can be determined [Figure 1-5]. In Figure 1-5, both a_0 and A_0 span the predicted values (predicted by demanding CKM unitarity using various values of V_{us}) with one standard deviation errors, while B_0 does not. A_0 also has the least error relative to the unitarity predicted values. The large difference between the B-correlation and the predicted values seems to indicate that the latest precision measurement may have an error, since earlier measurements of it are more in agreement with the predicted value.

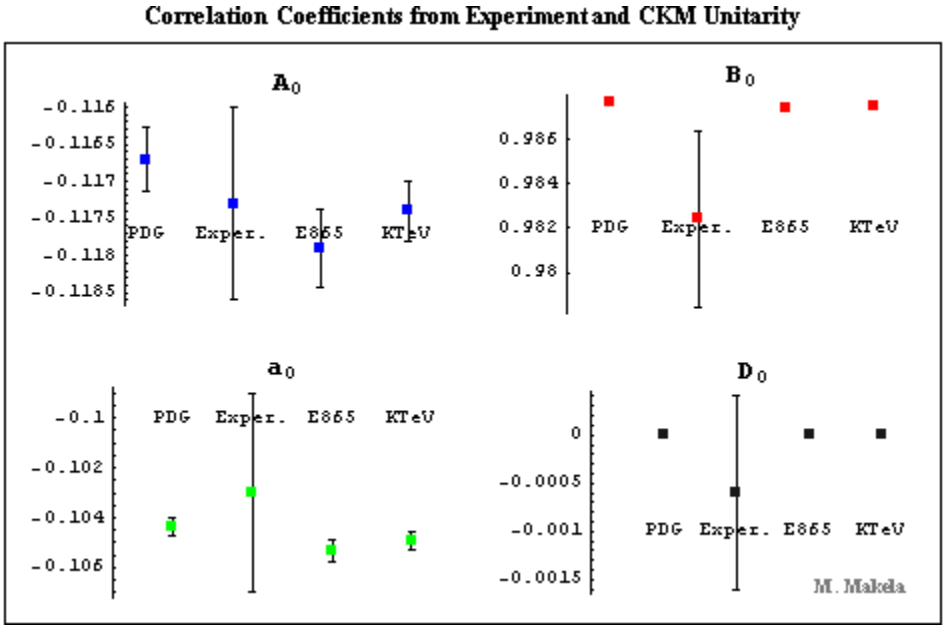

Figure 1-5 Correlation coefficients from Experiment and CKM Unitarity: The PDG experimental values (Exper.) of the four correlation coefficients of neutron beta decay are shown compared to the value calculated from V_{ud}. V_{ud} is found by demanding unitarity of the CKM matrix using various values of V_{us} (PDG, E865 and KTeV).

A new measurement of the A–correlation of polarized neutron beta decay looks to be the best way to improve the value of V_{ud} derived from neutron decay. A reduction of the error from about 1% to 0.2% will make the extracted value of V_{ud} comparable to that of super-allowed $0^+ \rightarrow 0^+$ nuclear beta decays or demanding CKM unitarity with current values of V_{us} and V_{ub}.

1.2 Effect of Proposed UCNA Measurement on A_0 and V_{ud}

The UCNA experiment is designed to determine A_0 to better than 0.2% using ultracold neutrons. Making an A–correlation measurement with UCN will also provide a different set of errors than the past neutron beam measurements. The increased precision is possible due to better polarization and lower backgrounds; this increased precision is due to a non-reactor based source and the low kinetic energy of the UCN.

1.2.1 What is different about ultracold neutrons?

Ultracold neutrons are defined as neutrons that have kinetic energies comparable to the material potential of solids. If the kinetic energy of a neutron is below the material potential of a surface, then when it strikes the surface it will be elastically reflected; so UCN can be held in a bottle made of standard materials. The energies of materials and UCN are typically below 250 neV, with a few exceptions. This energy corresponds to a few milli-Kelvin temperature.

Due to their low kinetic energy UCN are also strongly affected by the earth's gravitational and magnetic fields. The potential energy due to the earth's gravitational field ($m_n gh$) is about 100 neV per meter for the neutron; so a 3 meter high box can hold most energetic UCN without a top – that is they can be held in a bucket. UCN can also be trapped with magnetic fields; the interaction energy of the neutron's magnetic moment with an external magnetic field ($\boldsymbol{\mu_n \cdot B}$) is ~60 neV/Tesla. So if a UCN tried to pass through a 5 Tesla field region it would either slow to a stop and then be accelerated away or be accelerated into it, depending on its spin–state.

These UCN properties both allow and demand a new design for the A–correlation experiment. Since UCN are in principle 100% reflected by walls, a guide system can be used that allows the experiment to be totally shielded from the source. At a kinetic energy of 250 neV a neutron is moving about 7 meters per second; due to this slow speed a higher percentage of UCN decay in this experiment than in cold neutron beam experiments. Another major change is the method of polarization; beam experiments use magnetic super mirrors with polarization below 99%; whereas a superconducting solenoid placed around the guide can give in principle a 100% polarization for UCN.[18, 19, 20, 21] (The key is to *keep* them polarized)

Neutron Class	Velocity m/s	Critical Angle for ^{58}Ni (degrees)	Absorption Cross Section (B) for ^{58}Ni	Beam Polarization	Gravity Trap Height (m)	Wavelength
Thermal Neutrons	2000-3000	0.15-0.23	4.6@2200 m/s	80%	N/A	0.1-0.2 nm
Cold Neutrons	400-1000	0.46-1.15	25@400 m/s	99%	N/A	0.4-1 nm
Ultracold Neutrons	< 8	0	1265	100%	3	>50 nm

Table 1-2 Table of values comparing thermal, cold and ultracold neutrons

1.2.2 The UCNA experiment

The UCNA experiment has a dedicated source, state–of–the–art guides, high efficiency polarization and spinflipping, 4π beta collection, low–backscatter beta detection and low backgrounds. All of these features combine to provide a new approach to measuring the A–correlation of polarized neutron beta decay with minimal error due to uncertainties in polarization and background.

The UCNA neutron source is a super thermal solid deuterium UCN source [Figure 1-6].[22, 23, 24, 25] The source for the UCNA experiment is a scaled up version of a prototype source that achieved a world–record density of greater than 100 UCN per cubic centimeter. Neutrons are provided by a pulsed proton spallation source.[26, 27] These neutrons are trapped, elastically cooled, and finally down–scattered in the solid deuterium to become UCN. Due to the intense radiation of the interacting proton beam, the source is located inside a steel and concrete crypt; the UCN must be guided out of this crypt and into the experimental area.

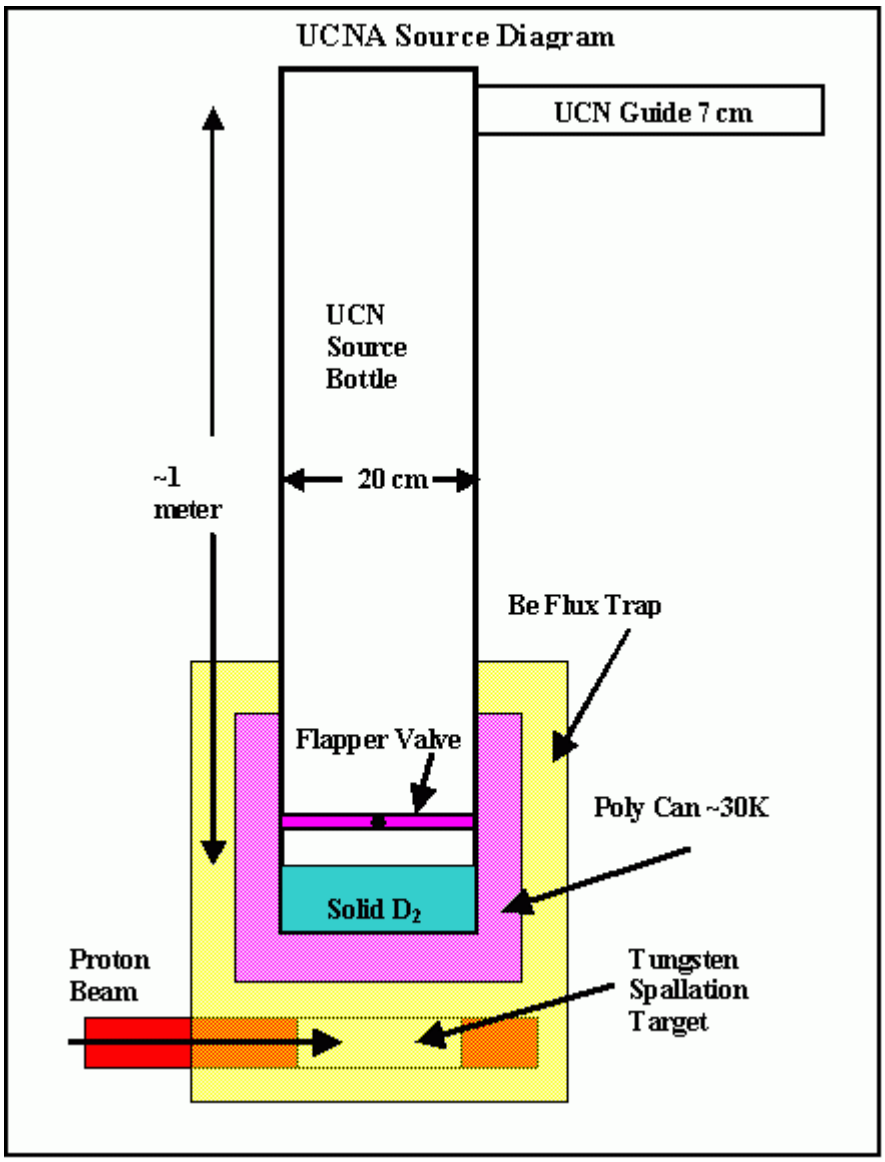

Figure 1-6 UCNA Source Diagram: The UCN source for the UCNA experiment uses three steps: First the 800 MeV LANSCE proton beam hits a tungsten rod that releases spallation neutrons. These neutrons are partially trapped by a beryllium can, where they interact with a cold (~30K) poly can and are cooled by momentum transfer with the hydrogen atoms in the poly. These cold neutrons can pass into the source bottle and through the solid deuterium inside. Some of the cold neutrons that pass through the solid deuterium are transformed to UCN by scattering off a phonon. These UCN are now trapped inside the source and guide system.[25, 27]

The guide system is made with state–of–the–art diamond coated quartz guides. There are about 12 meters of guide before the UCN enter the decay region of the experiment. Even with the high quality guides only about 1% of the UCN reach the decay region.[28]

Before entering the decay region the UCN are polarized with a 7 tesla solenoidial magnetic field. This field provides 100% polarization of the UCN. The magnetic field is tailored on the downstream side where the UCN spinflipper is located.

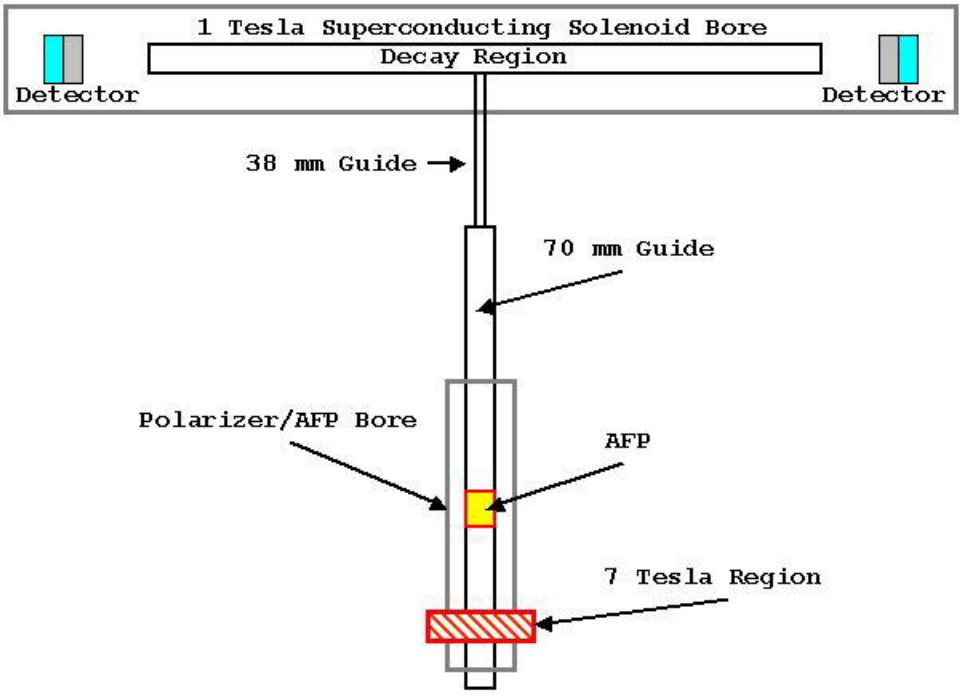

Figure 1-7 UCNA Experiment Diagram: The UCN guide leading through the Polarizer/AFP bore is about 2 meters long and .07 meters in diameter. The guide penetrating into the superconducting solenoid is square (38x38 mm) and about .6 meters long. The decay region guide is .1 meters in diameter and 3 meters long. All of these guides must be minimally depolarizing for UCN in order to make a high precision measurement of the A–correlation.

The spinflipper is of the adiabatic fast passage type (AFP) which has been shown to be over 99.9% efficient.[29] This high spinflipping efficiency combined with 100% polarization provides the highest polarization ever used in an A–correlation experiment. The diamond coated quartz guides and magnetic holding fields are needed to keep the UCN polarized while they travel into the decay region [Figure 1-7].

The decay region is a three–meter–long, ten–centimeter–diameter diamond–coated quartz tube that the UCN enter in the middle. To give 4π collection of the decay electrons this tube is inside a 1 Tesla solenoidial magnetic field.

Electron detectors at the ends of the decay region detect the beta particles. These detectors combine low backscatter wire chambers and energy monitoring plastic scintillators. The A–correlation is calculated from the difference in counts between the detectors at each end of the decay region.

Backgrounds are minimal at the detectors and have a time structure due to the pulsing of the shielded spallation target. Cosmic–ray backgrounds are minimized by surrounding the decay region with plastic scintillator. UCN that do not decay in the decay region are trapped on lithium fluoride surfaces that cause only a low energy gamma background.

1.2.3 Proposed UCNA Precision

The goal of the UCNA experiment is to make a 0.2% measurement of the A–correlation with minimal or no correction due to systematic effects. The main systematic effects are neutron polarization, and betas that backscatter off the detectors; these two effects combine to make up most of the 1.7×10^{-3} systematic effect in the measured value of the A–correlation as seen in Table 1-3. This systematic effect is well below the 6×10^{-3} systematic effect corrected for in the PERKEO 2 experiment.[30] By making accurate measurements of these systematic effects they can be separated from the measured A_0 value to give an even more accurate value. A large amount of work has already gone into

understanding these systematic errors with offline experiments and Monte Carlo work. As a result these projected errors seem obtainable.

Systematic Effect	$\Delta A/A$	σ_A/A
Polarization (including neutron spin flipping)	$\leq 1 \times 10^{-3}$	$\leq 1 \times 10^{-4}$
Depolarization	$< 9 \times 10^{-4}$	$\leq 1 \times 10^{-4}$
Spatial variations in UCN density	$< 5 \times 10^{-5}$	$< 5 \times 10^{-5}$
Temporal variations in UCN density	2×10^{-5}	2×10^{-5}
Neutron spin alignment	1×10^{-4}	1×10^{-4}
Subtotal UCN Systematic Effects	**1.4×10^{-3}**	**2.1×10^{-4}**
Backscattered betas	1×10^{-3}	$\leq 2 \times 10^{-4}$
Scattered betas - residual gas contribution	$< 1 \times 10^{-5}$	$< 1 \times 10^{-5}$
Scattered betas - wall contribution	$< 3 \times 10^{-6}$	$< 3 \times 10^{-6}$
Field nonuniformities	1×10^{-4}	2×10^{-5}
Magnetic mirror effect	$< 8 \times 10^{-6}$	$< 8 \times 10^{-6}$
Fiducial volume definition	$< 3 \times 10^{-6}$	$< 3 \times 10^{-6}$
Subtotal Electron Collection	**1.0×10^{-3}**	**2.0×10^{-4}**
Detector inefficiencies	$< 5 \times 10^{-6}$	$< 5 \times 10^{-6}$
Detector resolution function	3×10^{-4}	3×10^{-4}
Detector nonlinearity	6×10^{-5}	6×10^{-5}
Detector backgrounds - room	$\leq 1 \times 10^{-6}$	$\leq 1 \times 10^{-6}$
Detector backgrounds - beam associated	$< 1 \times 10^{-7}$	$< 1 \times 10^{-7}$
Detector backgrounds - UCN related	$< 4 \times 10^{-6}$	$< 4 \times 10^{-6}$
Subtotal Detector Effects	**3.0×10^{-4}**	**3.0×10^{-4}**
TOTAL	**1.7×10^{-3}**	**4.2×10^{-4}**

Table 1-3 Systematic effects and uncertainties. $\Delta A/A$ is the size of the systematic effect relative to A (which has a value of -0.114) and σ_A/A is the size of the systematic uncertainty relative to A. The total systematic uncertainty is determined by adding the individual systematic uncertainties in quadrature.[30]

The proposed 0.2% error in the UCNA measurement of the A–correlation is a factor of three below the error in the PERKEO 2 value [Figure 1-8]. Should this value agree with the latest value for PERKEO 2, the uncertainty in the average will drop considerably. On the other hand, if it agrees with the older experiments, the average will continue to have a high uncertainty.

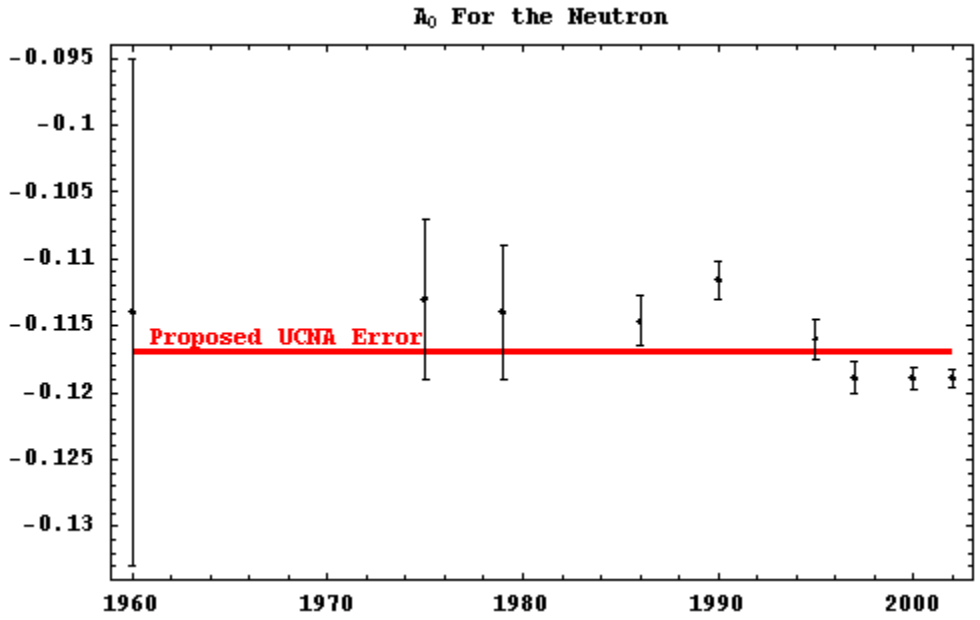

Figure 1-8 A_0 for the neutron: Experimental values found for A_0 have declined over the years. The last three values are all from PERKEOII. The proposed A_0 and error for the UCNA experiment has been placed for comparison only.

A 0.2% measurement of the A–correlation combined with the current 0.1% measurement of the neutron lifetime will give a 0.06% measurement of V_{ud} which is comparable to the 0.05% error in V_{ud} from super-allowed $0^+ \rightarrow 0^+$ nuclear beta decays and >.06% error from demanding unitarity using various values of V_{us} and V_{ub}. This is shown in figures 1-9 and 1-10 where the UCNA value of the A–correlation was picked for comparision, while the error is the proposed 0.2%. If the lifetime of the neutron were measured down to 0.1 seconds and the error in the A–correlation was lowered to 0.1%, then the error on the extracted value of V_{ud} would be 0.02%. This should be possible in the near future with the NIST neutron lifetime experiment and possible new lifetime experiments at Garching and LANL.[15, 16, 17]

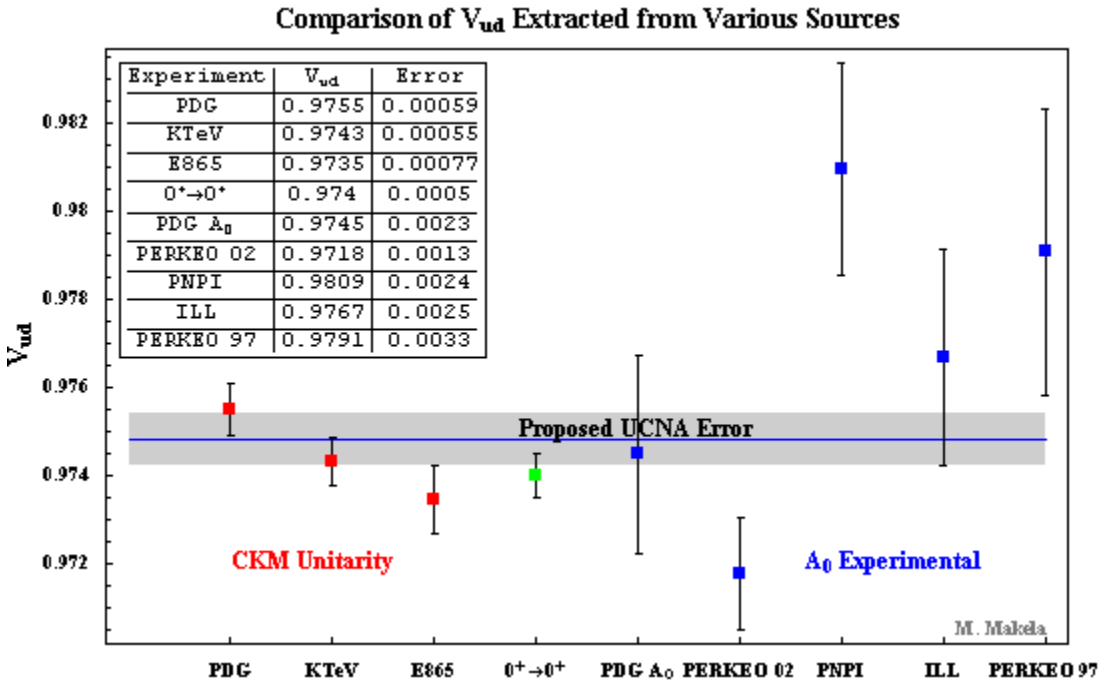

Figure 1-9 Comparison of V_{ud} extracted from various sources and the proposed UCNA error: The proposed error in the UCNA value of V_{ud} is in gray, randomly placed for comparison. The red values are from using V_{us} and V_{ub} to calculate V_{ud} assuming unitarity of the first row. The green value is the PDG value for V_{ud} from super-allowed $0^+ \rightarrow 0^+$ nuclear beta decays. Finally the blue values are extracted using moun lifetime, neutron lifetime and the A–correlation of neutron beta decay.

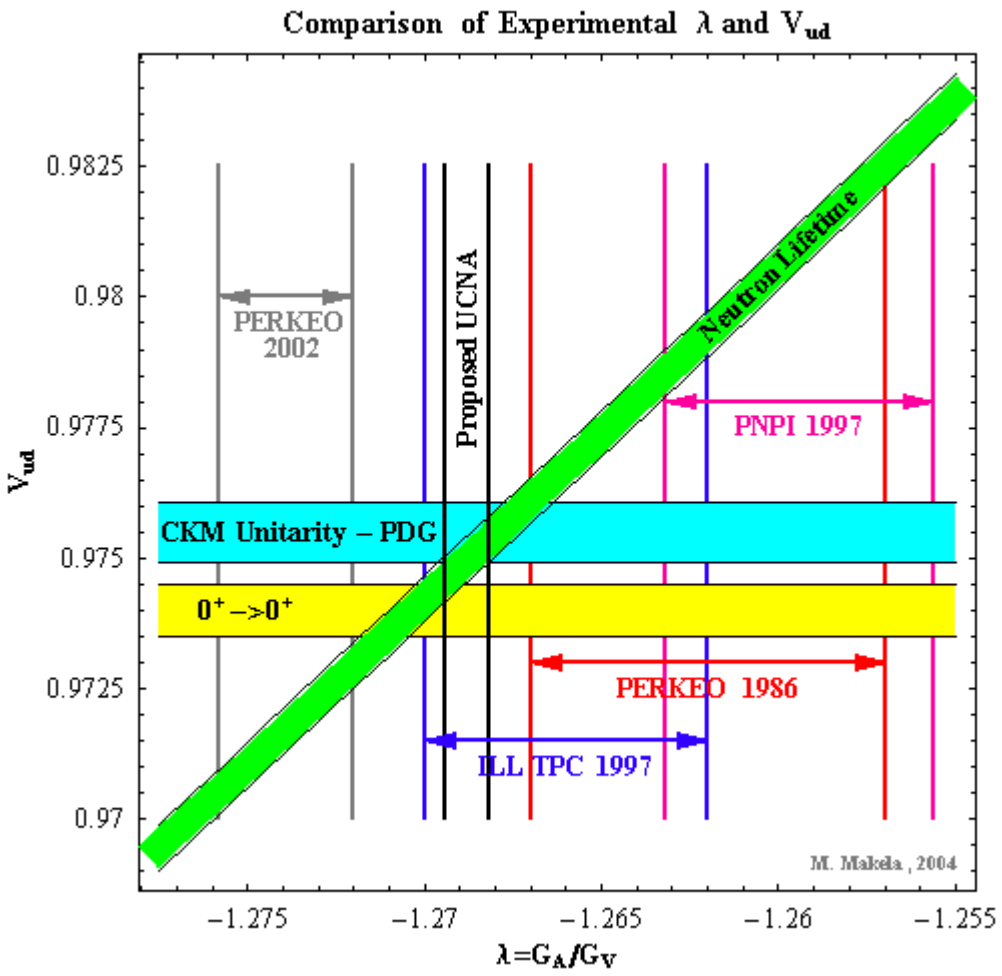

Figure 1-10 Comparison of experimental λ and V_{ud}: Values of λ can be compared to values of V_{ud} with the neutron lifetime curve. This is done by finding the intersection of say a lambda value and the lifetime curve and projecting this point over to the V_{ud} axis.

1.2.4 Possible New Physics

A precision measurement of the A–correlation of neutron beta decay can be used to look at physics beyond the standard model by testing CKM unitarity when combined with the neutron lifetime and the muon lifetime, and it can also test for new physics on its own. Tight constraints on V_{ud} and CKM unitarity put tight constraints on minimal left-right symmetric models[31], on universality in the minimal supersymmetric standard model and constraints on R-parity violating supersymmetric models.[30, 31, 32] Limits on right–handed currents can be set using precision measurements of the A–correlation in combination

with the neutron lifetime and the other decay coorelations.[33, 34] The validity of the decay correlation defined in terms of lambda can be tested with the zero sums $1+A_0-B_0-a_0=0$ and $a_0B_0-A_0-(A_0)^2=0$.[34, 35] The conserved vector current (CVC) hypothesis and second class currents (SCC) can be tested using the combination of high precision measurements of the a– and A–correlations.[11] A test of the predicted value of the weak magnetism term of the standard model may also be accessible with the low backgrounds and energy resolution of the UCNA experiment. The precision needed for these measurements is getting to the point where better calculations of the radiative corrections are needed and several groups are looking into this.[2, 10, 11, 36, 37, 38]

1.3 Polarized Ultracold Neutron Transport in the UCNA Experiment

In this section the causes of depolarization and the effect of depolarization on the UCNA experiment are discussed.

1.3.1 Mechanisms of Ultracold Neutron Depolarization

Polarized UCN can depolarize via three mechanisms: traveling through magnetic field inhomogeneities, traveling through zero field regions, and interaction with nuclear and electronic spin-states of guide–wall materials. Field inhomogeneities are generally low enough that slow moving UCN can follow the change in the magnetic field, but if the UCN is in a changing field when it hits the wall and elastically bounces away it could become depolarized.[39] Zero–field regions are avoided by adding additional field where needed in the UCNA experiment. By choosing guide materials that are non-magnetic and without unpaired spins, depolarization by interacting with the guide materials can be minimized.

By using non-magnetic guide material, field gradients can be minimized at the guide walls. Still, ferromagnetic impurities in materials will cause local regions of high field gradient. Even if the guide coating is free of impurities, ferromagnetic clusters in the

wall can produce fields that extend beyond the surface that could cause depolarization on collision.

Another possible cause of depolarization is the interaction of the UCN with hydrogen in and on the neutron guide coating. Surface hydrogen is common to most materials but the amount varies.[40] A recent study seems to show that surface hydrogen in the form of water does not cause significant depolarization – this is good since most high vacuum surfaces have water layers. These experiments also show the depolarization rate of UCN on beryllium to be below 10^{-5} per bounce.[41, 42]

1.3.2 Polarized UCN Guides

The UCNA guides are made from quartz tubing that has been cleaned, vacuum baked and coated on the inside with dense hydrogen–free diamond-like carbon. Quartz tubing is used since it is very smooth and relatively free of impurities. Carbon is a good choice for a non-depolarizing coating since it has no unpaired nuclear or electronic spins. The deposition inside the quartz tubes is done by ablating the carbon with a pulsed excimer laser; this process creates a hydrogen–free carbon layer with density near that of diamond. Due to the high critical velocity of diamond and smoothness of the quartz the UCNA guides for polarized UCN are better than the ^{58}Ni coated stainless steel guides used in most UCN experiments. This has led to the use of the guide developed for the polarized region of the experiment to be used throughout the whole experiment.

1.3.3 Depolarization Rate

The depolarization rate of a UCN in the polarized UCN guides has been tested two ways by making a bottle with one "end" being a 5 tesla magnetic field. One method is to fill the bottle with a set number of trapped UCN – any that depolarize will leave the trap through the polarizer and can be counted in a detector. By knowing the collision rate in the bottle and the number of UCN in it, the depolarization rate can be calculated. The depolarization rate deduced for the guides was below 10^{-6} per bounce. This is well below that seen in previous experiments.[41, 42] These experiments will be discussed in full in the chapters of this thesis.

1.3.4 The Effect of Depolarization on the UCNA Experiment

The depolarization due to wall collisions in the UCNA experiment can be estimated by multiplying the average number of bounces a UCN will make before leaving the decay–trap times the depolarization rate. To do this, a random velocity distribution will be assumed and transport from the polarizer to the decay–trap will be included. To get from the polarizer to the decay–trap ~2 meters of 65.5 mm ID guide and ~.6 meters of 38 mm square guide needs to be traversed. This section of will give about $\frac{200}{6.55}+\frac{60}{3.8}\approx 50$ bounces. The decay–trap has an ID of 101.6 mm and the average UCN spends 5 seconds in it with an average velocity around 5.5 m/s. This gives $\frac{5*550}{\sqrt{2}*10.16}\approx 200$ bounces. With an average of about 250 collisions the chance of depolarization is less than $1-(1-10^{-6})^{250}\approx .00025$ which is well below the 0.0009 listed in Table 1-3. At this level the depolarization will not be noticeable compared to the 99.9% initial polarization listed in the table. Online tests of the polarization will be made between data taking cycles. This will allow for any corrections that need to be made.

2 The Search for a New Ultracold Neutron Guide Coating

Several technologies had to be developed to make the UCNA experiment successful: a brighter UCN source, guides for polarized UCN transport, a high efficiency UCN spin-flipper, and low energy beta detectors with low backscatter. We (VT) decided to take the lead in developing the guides for polarized UCN transport and with this came the responsibility for the rest of the guide system.

The coatings proposed for the UCNA experiment were ^{58}Ni for unpolarized UCN guides and Beryllium or diamond-like carbon (DLC) for the polarized UCN guides. The ^{58}Ni guides were to be made by the PNPI group lead by Anatoli Serebrov, this type of guide has been the standard for our UCN source development. While the PNPI group looked into beryllium for the polarized guides Albert Young of NCSU looked into the possibility of making guides with a DLC coating.

Our first involvement with the coating development was testing samples of diamond-like carbon for surface roughness using an Atomic Force Microscope (AFM) at VT. We sent several test samples to be coated with DLC to SURMET, the coating company that had provided DLC coating for the EDM experiment.[43, 44] While researching the process they used to make these DLC films several other dense carbon coating techniques were found. Some of these other films appeared to be better than the DLC used in the EDM experiment.

To pick the best process for making DLC coated UCN guides both the process and the resulting coating must be considered. The process needs to be able to coat the inside of long tubes – not a common requirement. The coating needs to be good for polarized UCN transport. Whether or not a coating is good can be estimated by looking at its material properties.

2.1 The Material Properties Needed for UCNA Guide Coatings

The guides that transport polarized UCN in the UCNA experiment need have the same attributes as standard UCN guides (ie. near specular reflection, low loss per bounce and highly reflective for UCN). In addition they also need to have a low loss of UCN polarization per bounce and be transparent to the 30 MHz RF signal used by the AFP spin-flipper. Since UCN guides are generally made by putting a good UCN coating onto a standard substrate material like stainless steel, aluminum, or glass, the attributes needed for efficient UCN transport are a product of both substrate and coating.[45, 46] Critical velocity and loss per bounce are predominantly coating properties; whereas, specularity, depolarization and RF transmission have to do with both the coating and substrate.

The critical velocity (v_c) of a coating is defined as the velocity where the UCN's kinetic energy is equal to the coating's material potential. The critical velocity of a coating is determined by two material properties: the nuclear scattering length and the density of nuclei. The scattering length is a property of the potential well formed by the strong force around the nucleus. Since the wavelength of a UCN is very large compared to both the nucleus and the atomic spacing in a solid, the UCN can be seen as scattering off an effective potential resulting from a collection of nuclei.[47, 48, 22, 23] The strength of the scattering is therefore a function of the nuclei's scattering length and the density of nuclei in the coating. The relation between critical velocity, scattering length , *a,* and density of nuclei , N (number density) is given by $v_c = \frac{\hbar}{m_n}\sqrt{4\,\pi\,N\,a}$, this is derived by setting the neutrons kinetic energy equal to the material potential. ("a" can be negative – in this case the material potential is attractive and the formula does not hold)[22] The scattering length (bound coherent scattering length) and number density for materials can be found in various books and online (a, NIST and N, matweb). Although the tabulated scattering lengths are very accurate, the densities listed may not be correct for thin coatings; the problem with these densities is that they are for bulk samples. The density of the coating depends on the deposition method used. Since the critical velocity of a coating is unique

to neutrons, the best way to find it is by reflecting neutrons; this technique is called neutron reflectometry.[49]

The loss of UCN when they bounce off a surface is caused by several factors, some of which are direct properties of the coating and some that are not. The same nuclear potential that elastically scatters the UCN can also absorb or inelastically scatter it. The cross sections for these processes are also given in tables with the scattering length. Inelastic scattering is temperature dependent and results in loss of the UCN, since they are generally scattered into a higher energy state and are no longer UCN. Even with a good UCN coating, surface contamination can be a major cause of loss. Water, hydrogen, and hydrocarbons are common contaminates on vacuum surfaces.

Neutron scattering lengths and cross sections (ref NIST)							
Isotope	**conc (%)**	**Coh a (fm)**	**Inc a (fm)**	**Coh xs (barns)**	**Inc xs (barns)**	**Scatt xs (barns)**	**Abs xs (barns)**
H	---	-3.739	---	1.7568	80.26	82.02	0.3326
1H	99.985	-3.7406	25.274	1.7583	80.27	82.03	0.3326
2H	0.015	6.671	4.04	5.592	2.05	7.64	0.000519
He	---	3.26(3)	---	1.34	0	1.34	0.00747
3He	0.00014	5.7-1.5*i*	-2.5+2.6*i*	4.42	1.6	6	5333.(7.)
4He	99.99986	3.26	0	1.34	0	1.34	0
Be	100	7.79	0.12	7.63	0.0018	7.63	0.0076
C	---	6.646	---	5.551	0.001	5.551	0.0035
F	100	5.654	-0.082	4.017	0.0008	4.018	0.0096
Ni	---	10.3	---	13.3	5.2	18.5	4.49
58Ni	68.27	14.4	0	26.1	0	26.1	4.6

Table 2-1 Neutron scattering lengths and cross sections: This table of neutron scattering lengths and cross sections is taken from the NIST data tables. [50]

The final property that standard UCN guides need is specular reflection. UCN have a wavelength of ~50-100 nm – one tenth that of visible light – so the surfaces need to have a better than optical finish to give a highly specular reflection for UCN. This demands that the guide tube have roughness on the order of nanometers over micrometer distances.

The additional requirement that the guides be transparent to high–power RF is more of a problem for the guide substrate since very thin metal coatings can transmit RF with minimal heating. Still, a non-conducting coating would be preferred. Typical UCN reflective coatings are 100-200 nm thick and this is about one hundredth of the skin depth of beryllium for a 30 MHz RF signal [Table 2-2]. Glass is the only standard guide material that is non-conductive. The standard UCN guide coatings are all metals and therefore less than perfect for the UCNA experiment.

Skin Depth for a 30 MHz RF Signal[51]		
Temperature	Cu	Be
80K	$4.3\ 10^{-6}$ m	$2.5\ 10^{-6}$ m
293K	$1.2\ 10^{-5}$ m	$1.7\ 10^{-5}$ m

Table 2-2 Skin depth for a 30 MHz RF signal: Skin depth is the 1/e attenuation length. These values are calculated using a temperature dependent conductivity.[51]

The major source of UCN depolarization is not known, so all possible sources should be eliminated when making guides for polarized UCN. The physics however, is known and the two main causes of depolarization are spin exchange and magnetic field gradients. A UCN can be depolarized by moving through a changing magnetic field faster than its spin can precess; this can happen when a UCN hits a wall in a region of high magnetic field gradient.[39] To lower the chance of spin exchange, materials with unpaired spins should be avoided. In general, magnetic materials and impurities are to be avoided in guide construction, since they can cause field gradients and spin exchange. Surface and interstitial hydrogen is also a likely cause of depolarization since it has unpaired spins; unfortunately most materials are susceptible to hydrogen contaminations.

Beryllium meets most of the requirements of the UCNA experiment but high density carbon can meet all the requirements. The theoretical critical velocity of diamond is 7.5 m/s, which is higher than all other standard guide coatings except ^{58}Ni. The absorption and inelastic scattering cross–sections are very low – lower than beryllium. Since diamond is resistive, it should be fine in the high RF field. The depolarization rate is

unknown but expected to be low since diamond has very low magnetic susceptibility, very little surface or interstitial hydrogen, and no unpaired spins. The main problem with diamond films is that they are crystalline and very rough; but diamond-like carbon films can be amorphous, dense and very smooth [Figure 2-1].

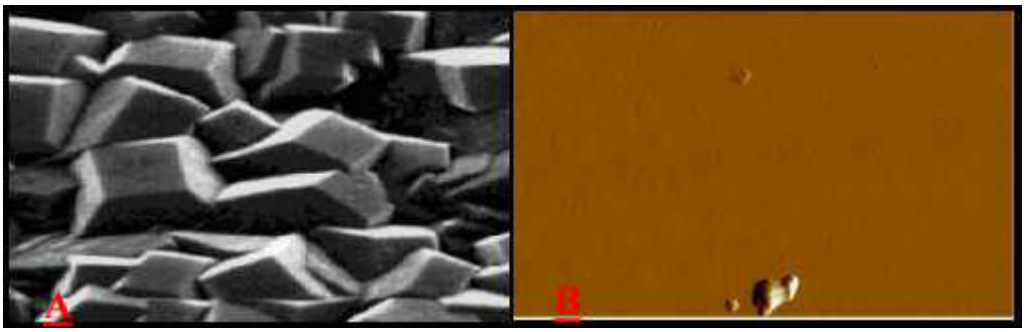

Figure 2-1 AFM and SEM images of DLC: The left image is a 5 μm across SEM image of CVD diamond; on the right is a 5 μm across AFM image of PLD DLC.

2.2 Ways to Make Diamond-Like Carbon

Diamond-like carbon is made by a number of techniques; these techniques can be divided into to groups, those that use hydrogen and those that do not. The various chemical vapor deposition (CVD) techniques used to make DLC use hydrogen and hydrocarbon gasses. The hydrogen–free processes make DLC directly from high–energy carbon atoms.

Unlike the CVD diamond film in Figure 2-1, diamond-like carbon films made by CVD techniques can be very smooth and dense. They have already been tested for UCN use and are currently used in the UCN EDM experiment to coat the electrodes. The hydrogen that is incorporated into the coating lowers the material potential and could cause increased depolarization. Since CVD DLC is commercially available it is an interesting possibility for polarized UCN guides.

Hydrogen–free diamond-like carbon is as smooth as CVD DLC and denser. There has been very little neutron testing of it and no UCN testing or use. With this lack of neutron data, the neutron properties must be estimated from the material properties of the hydrogen–free DLC.

In general the elimination of hydrogen from the coating should make a much better UCN guide coating – so if the hydrogen–free coating is as dense and smooth as CVD DLC it should be used for the UCNA experiment. Another consideration is if the techniques are possible inside of long tubes.

2.2.1 Hydrogenated Diamond-Like Carbon

Chemical vapor deposition (CVD) is used to make various carbon compounds from graphite to diamond using hydrogen and hydrocarbon gasses. DLC can be made by several different CVD techniques. Generally the hydrocarbon gas is mixed with hydrogen and/or an inert gas in the reaction chamber, where a plasma is formed by an RF or microwave source. The deposition temperature can be is relatively cool (less than 400C). This allows coating of aluminum and some plastics.[52, 53] The resulting films can be hard and smooth with densities of 1.85 g/cm^3 and a critical velocity of 5.4 m/s.[44, 49]

SURMET CVD DLC was recognized as a possible UCN coating, tested and used in the EDM experiment.[44, 49] The main problem with CVD DLC films is that the atomic concentration of hydrogen can be over 50%.[44, 49] Since hydrogen has a negative scattering length it lowers the material potential of the film. This problem can be eliminated by replacing hydrogen with deuterium, which has a scattering length very close to carbon. The resulting films have a critical velocity of 6.5 m/s and are nearly as smooth as the substrate used.[44]

There are several other techniques for making hydrogenated DLC films that have similar properties to the SURMET DLC.[52, 54] If guides were to be made using CVD one of these other techniques may work better due to the need to coat inside a tube.

Since large amounts of hydrogen are incorporated into the CVD DLC replacing the hydrogen in the processing gasses with deuterium is necessary. This replacement may also help with maintaining UCN polarization. The main problem with the SURMET

coating is the relatively low critical velocity, 6.5 m/s compared to diamond at 7.5 m/s. This problem can be partially taken care of with some hydrogen–free processes.

2.2.2 Hydrogen–free Diamond-Like Carbon

Hydrogen–free DLC films are made by depositing high–energy carbon atoms onto the substrate (high energy is relative to thermal deposition techniques). The first to appear in the literature is ion–beam deposition, followed by magnetron sputtering. About this time the first papers about laser–ablated carbon films started to come out. This was soon followed by cathodic–arc deposition. Each of these techniques makes a DLC with different properties, the density and smoothness being the most important with regard to UCN transport. Review articles by J. Robertson[54], M. P. Siegal et al.[55],and N. Savvides[56] give an overview of the techniques described below.

2.2.2.1 Ion Beam Deposition[57, 58]

Diamond-like carbon was produced in the early 70's by a extracting carbon ions from a plasma and accelerating them onto a substrate. The deposition takes place in a high vacuum region of the chamber, $\sim 10^{-6}$ torr. The typical deposition energy was 50eV, which was set by the accelerating potential. The resulting films were reported to be clear, smooth and low in stress. Since the plasma was formed with Argon, some of this was also accelerated toward the target and may have been involved in the film growth dynamics.

2.2.2.2 Magnetron Sputtering[59, 60, 61]

N. Savvides studied carbon films deposited with a DC magnetron sputtering system. The sputtering gas was Argon so the films were hydrogen free. Although these film were not very dense (2.1 g/cm^3),[61] they did show diamond-like optical characteristics. The optical characterization of the films was done with transmission and reflection spectroscopy, and is very well explained in the literature.

2.2.2.3 Pulsed Laser Deposition

Pulsed laser deposition uses a pulsed laser to vaporize a target material inside a vacuum chamber; the chamber can also have a low pressure atmosphere. This technique has several advantages over standard techniques like evaporation and sputtering. The process applies energy only when and where needed from outside the vacuum chamber via a pulsed laser beam. The basic deposition system is very simple; the target and substrate are inside a vacuum chamber. A window into the chamber allows the laser light to hit the target. Depending on the energy density needed for the deposition process a focusing lens may be needed. A laser and beam optics to get the light into the chamber are the final components needed.

The first worked published on pulsed laser deposition was by Howard M. Smith and A. F. Turner in 1965[62]. They reported on the deposition of several materials with a ruby laser. The work showed that different materials react differently to this deposition process. The first work with carbon was not so much for deposition but to look at the dynamics of the plasma plume coming from the ablation process[63, 64, 65]. One of these original groups deposited the evaporated carbon into a quartz bubble to find the amount of material in the plume. They found the resulting film inside the bubble to be "extremely uniform and very hard"; this was probably the first un-reported pulsed laser deposited DLC[65].

The first articles about laser deposition of DLC are by Susumu Fujimori et al. in the early 1980's[66]. Their films were made with a CO_2 laser and were not very dense, but did show some diamond-like qualities. The first PLD DLC films were made with a Q-switched Nd:YAG laser operating at a wavelength of 1.06 μm by C.L. Marquardt, R. T. Williams, and D. J. Nagel in 1985[67].

Excimer lasers were first used for depositing DLC in 1987 by Sato et al.[68, 69] They used a XeCl excimer laser (308 nm wavelength) with power densities of $3*10^8$ W/cm^2 at the target and heated substrates. They found the optimal substrate temperature was 50 Cº; above this the coating became more graphitic.

A group led by C. B. Collins of Texas published its first papers in the late 80's.[70] They explored laser and ion–assisted laser deposition with a Nd YAG laser. Most of their work involved very high-energy depositions, which gave very hard, relatively rough DLC films. We tried to get samples from them since they were scaling up to make flat panel displays, but the sample price was over a $1000.

The move toward shorter–wavelength excimer lasers began in the 90's; with the use of shorter wavelength excimer lasers the DLC films became smoother, clearer and harder[71, 72]. The densities of the films made with short–wavelength lasers were 3 g/cm^3 and above.[73-76] This is between crystalline graphite ~2.2 g/cm^3 and diamond ~3.5 g/cm^3.

2.2.2.4 Filtered Cathodic Vacuum Arc (FCVA)

Filtered cathodic arc deposition is done by igniting an arc between an anode and the deposition material (cathode) in a vacuum chamber. The resulting plasma creates particles with 10-30 eV of kinetic energy.[54] To reach the deposition area the charged atoms in the plasma follow a curved magnetic field; this filters out the particles and neutral atoms. Depositions rates of 1-3 nm/sec. have been obtained with a 70, ampere 25 volt arc.[77, 78] The film density can be above 3 g/cm^3 when a DC accelerating potential is used.[54, 78] The films made by this method can be rough if the filtering is not done very well.[76, 54] A related technique using an RF potential at the substrate and no filtering reported a film density of 4.1 g/cm^3 and a new form of carbon.[79-82]

2.2.2.5 Atmospheric Pressure Diamond-Like Carbon Deposition[83]

A form of DLC is currently being made without a vacuum chamber from a plasma formed with several converging laser beams and several jets of gas. There is little technical data on the resulting material, but it seem to have a good bond to metals as it is used for work surfaces. This could be a good way to cover a large bottle since the process is fast.

2.3 The Best Diamond-Like Carbon for the UCN Guides

The best coating for the UCNA experiment is the one that will get the most UCN into the experiment with the least depolarization. Losses per bounce should be similar for the hydrogen–free films, and only the inelastic scattering should be a little higher for the CVD films with deuterium replacing the hydrogen. All of these techniques produce "smooth" films but there is not enough information to decide if one will have a more specular reflection than the next. Another important unknown factor is the amount of surface and interstitial hydrogen that each type of DLC will have. The density of the DLC made by the different processes varies a lot, and denser films without hydrogen have higher critical velocities.

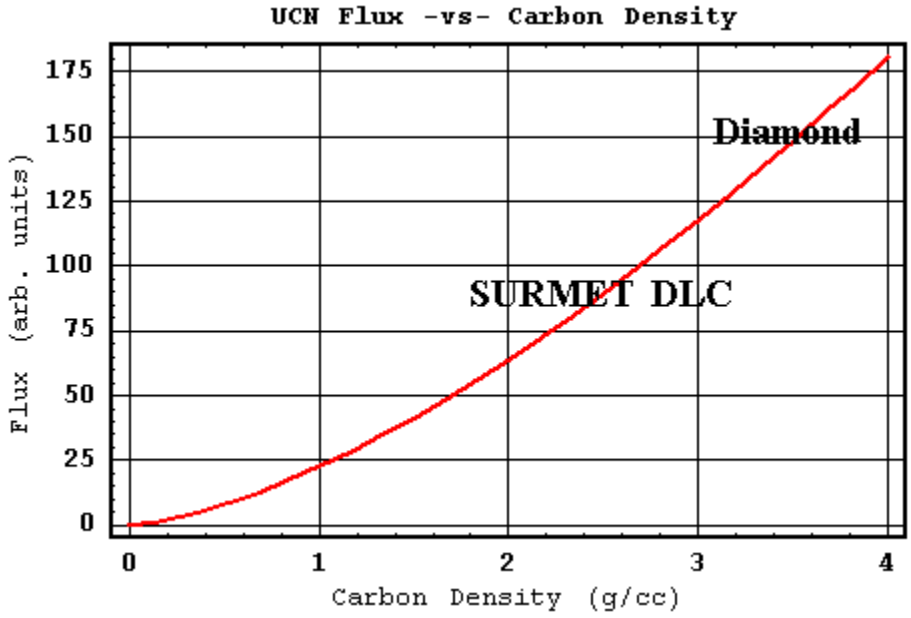

Figure 2-2 UCN flux versus carbon density: As film densities approach that of diamond the flux increases to nearly double that of guides coated with SURMET DLC.

With the other properties somewhat the same for all types of DLC, the critical velocity becomes the main property that predicts which will be the best UCN guide coating. The critical velocity is very important since the UCN velocity distribution follows the v^2 tail of a Maxwellian velocity distribution. As a result, the flux from the UCN source increases with the integral of this and is proportional to v^3. Since the critical velocity of a material increases with density so does the flux. The graph (Figure 2-2) shows a 2-fold

increase in the flux for diamond density films compared to deuterated SURMET DLC. Both the PLD and FCVA techniques give films with densities above 3 g/cm^3.

Another consideration in picking a coating system is that standard UCN guides are tubes – so the deposition needs to take place inside a tube. This seems reasonable for PLD since only the graphite target would be in the tube. It may be possible for FCVA but the system would have to be much different then the ones in the literature, which have magnetic filtering fields with half meter radii.[77] The combination of feasibility and critical velocity make PLD DLC a good choice for the UCNA experiment.

Although PLD DLC looks feasible there are no companies producing it – even on flat surfaces. Initially it looked like Tom Freidmann at Sandia National Lab might be able to produce some samples for us, but his schedule became too full. At his point we found out that there used to be a PLD system at VT. It was found disassembled, half moved and ready to go into the dumpster.

3 Diamond-like Carbon from Pulsed Laser Deposition of Pyrolytic Graphite

Pulsed laser deposited diamond-like carbon is made by ablating a graphite target inside a vacuum chamber with a high–power pulsed laser and depositing the ablated carbon onto a substrate. The interaction between the laser beam and the target is highly dependent on the laser wavelength, power, and pulse width. UV lasers with short pulse widths give the best quality films due to the material properties of graphite.

The Virginia Tech deposition system uses an excimer laser operating at 248 nm with pulse energies over a Joule and a vacuum system capable of holding low to high vacuum in the deposition chamber. The laser beam is focused onto the target with a convex lens through a fused silica window. The substrates are held parallel to the target inside the vacuum chamber [Figure 3-1]. The vacuum chamber can be held at high vacuum or a low pressure background gas can be maintained; each of these conditions produces a different type of DLC.

The best DLC for a UCN guide coating is not necessarily the best DLC coating found in the literature, so the parameter space needs to be explored to determine the best parameters for UCN guide deposition. The basic parameters are laser power per unit area that reaches the target, the vacuum conditions, and in addition the ions in the plasma and resulting plume can be affected by external magnetic and electric fields.

In order to explore the parameters and characterize the deposition system, several monitors are used. The laser energy is monitored with internal and external energy monitors. The vacuum conditions are monitored with both Convectron and ion type vacuum gauges to cover the full pressure range, 1000-10^{-9} torr. The carbon plume is monitored by watching the ion current with an ion probe. Together, these readings allow a given film to be recreated.

3.1 The Ablation of Graphite

The ablation process of pyrolytic graphite is a complex interaction of the laser beam with the graphite and the resulting plasma that ends with a forward directed plume of carbon atoms. The laser interaction is governed by the optical and thermal properties of the pyrolytic graphite. To make the best deposition the laser wavelength, pulse length and power must be matched to these properties.

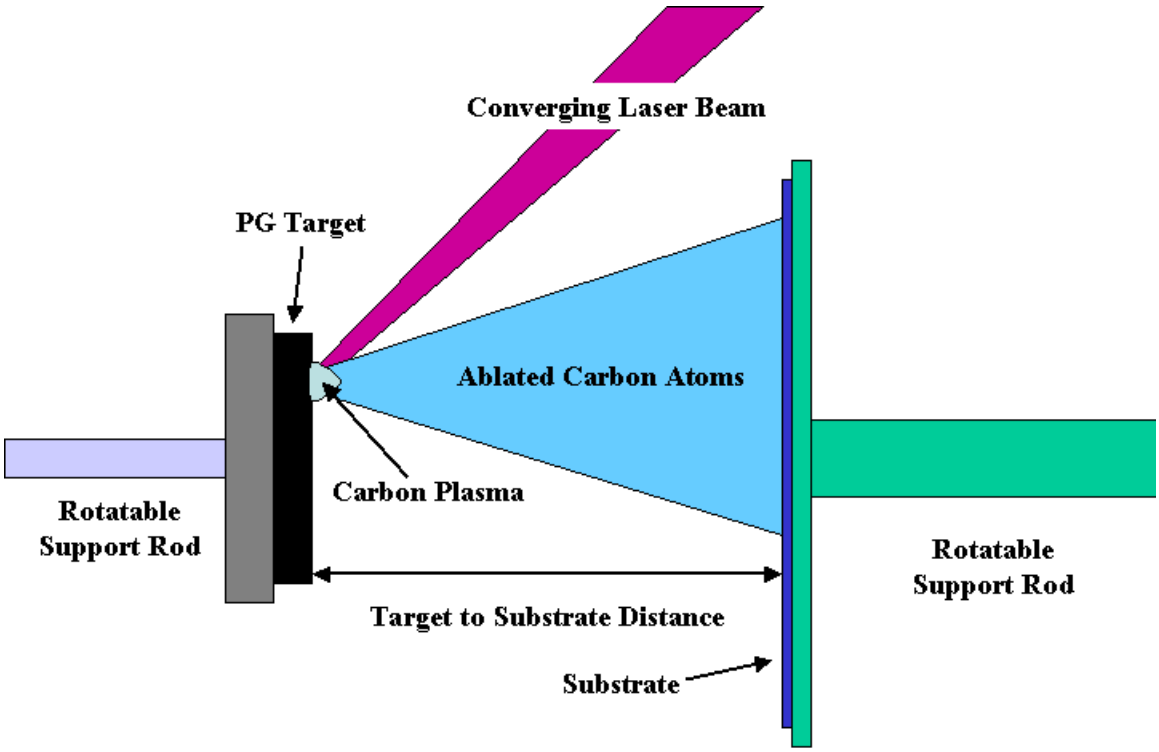

Figure 3-1 Diagram of pulsed laser deposition of graphite: This figure shows off–axis high vacuum deposition. The target and substrate are parallel and the laser beam hits the target at an angle, usually 45 degrees. Rotating the substrate off axis from ablation point allows larger areas to be coated evenly.

3.1.1 The Ablation Process [84, 85, 86]

The ablation process can be viewed as three steps: laser–target interaction, laser–plasma interaction and post laser pulse plume development. During the first step the target

surface absorbs laser energy and a very dense, highly–ionized plasma is formed. The electrons are more mobile than the ions so they move to the surface of the plasma but cannot escape due to the pull of the ions. The ions repulse each other and feel the pull of the electrons so they begin to leave the surface after the electrons. At this point the second step starts as the growing plasma starts to absorb the laser beam. This absorption causes more ionization and the break up of clusters in the plasma. After the laser pulse the plasma plume continues to grow with the kinetic energy of the electrons being transferred to the ions. If there is a background gas present, it takes part in the third step and thermalizes the plasma.

3.1.2 Ablation Properties of Graphite

The optical properties of graphite make it easy to ablate with high–power UV lasers. It only reflects about 53% of normally incident light at 248 nm[87] and about 37% at 193 nm[88]; this reflection decreases due to surface roughening during ablation. Figure 3-2 shows that the reflectivity of unpolarized light in the UV spectrum at 20 and 70 degrees from normal is near a maximum at 248 nm. This implies a shorter wavelength laser would be better. The new excimers lasers operating at 157 nm should be great for low loss of energy due to reflection, but low power, and the cost of optics and other components may make them impractical. Graphite's short attenuation length, 22 nm for λ=248 nm and 18 nm for λ=193 nm concentrates the energy in the surface of the target which lowers the amount of particulate in the plume. The attenuation length is a function of n, k, and the incident wavelength, $\delta=(n/k)(\lambda/2\pi)$[89]. After one attenuation length only 1/e of the beam is left.

The temperatures reached in the initial plasma are very high but the target and substrate are only minimally heated. The PLD plasma temperature (>10000 Cº, 10-100 atm.)[84] is significantly above the sublimation and triple points of graphite (3825 Cº, 1 atm. and 4489 C, 102 atm.)[51]. Since this is very localized, there is only minimal heating of the target, substrate or chamber.

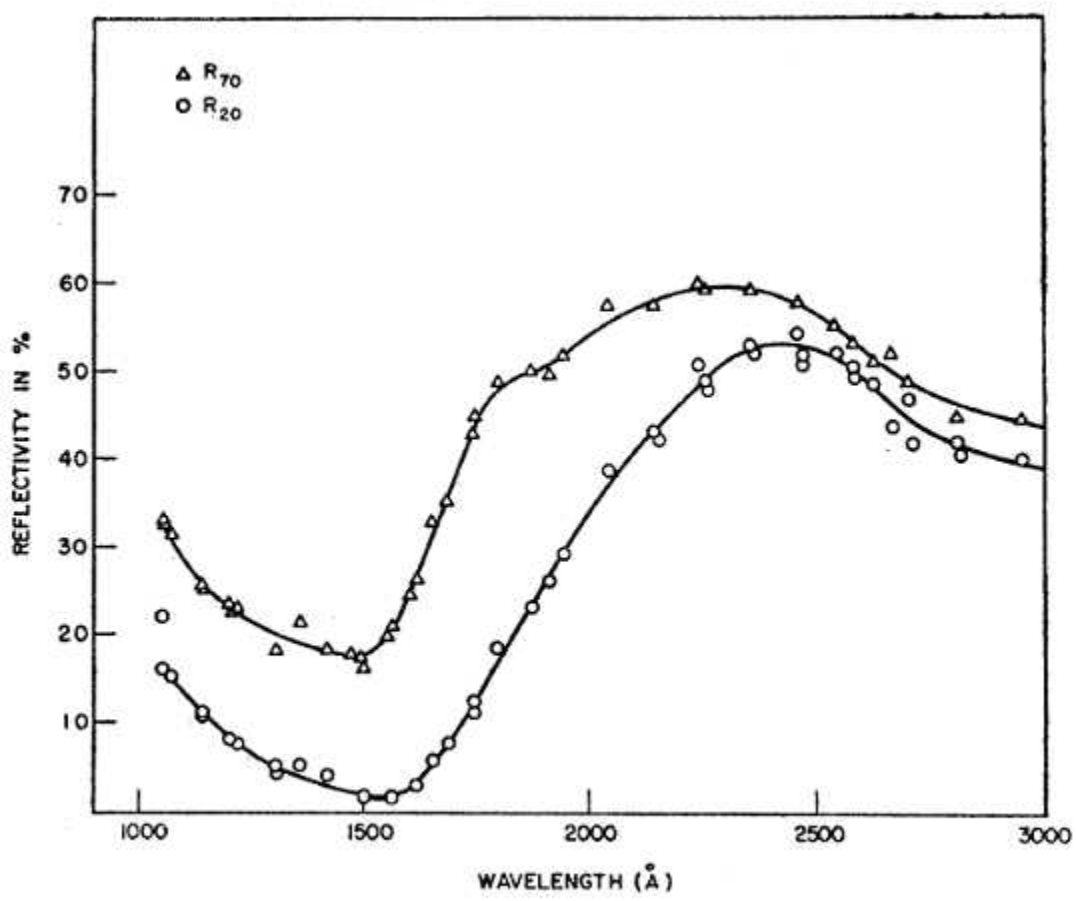

FIG. 1. Measured reflectance of unpolarized light from pyrolytic graphite for light incident at 20° and 70°.

Figure 3-2 Reflectance of pyrolytic graphite: The reflectance of pyrolytic graphite increases the laser energy needed to initiate the ablation process. As the target surface undergoes repeated ablation it roughens and this changes the reflectivity. This plot also indicates that the choice of the angle of incidence has only a small effect at 248 nm. (Figure 3-2 copyright info: Modified figure 1 with permission from J. G. Carter, R. H. Huebner, R. N. Hamm, and R. D. Birkhoff, "Optical properties of graphite in the region 1100 to 3000 Angstrom", Physical Review, Vol. 137, No. 2A, January 18, 1965, pp A639-41, Copyright 1965 by the American Physical Society)

Another interesting property of pyrolyic graphite that may effect its deposition is its thermal conductivity. The in-plane conductivity is several orders of magnitude above the plane to plane conductivity, 19.6 and 0.0573 W cm^{-1} K^{-1} at 298.2 K respectively.[51] The high in-plane conductivity should lower deep heating of the target, which in turn may lower particulate in the deposition.

3.1.3 Laser Pulse Effects on Ablation

The ablation process is very dependent on the laser pulse energy and duration. These, along with the spot size, define the watt density at the surface of the target. Ablation starts when the watt densities are well above those which cause surface melting. With a focused beam, the LPX305i excimer laser is always above this threshold. The best ablation of carbon occurs when high watt densities are achieved with very short pulses rather than high laser energy.[90] Short pulses keep the energy concentrated in the surface layers of the target. Changing the spot size changes the energy density, but this is limited to a finite spot size by the optics and laser beam divergence. Changing the spot size and shape also changes the plume shape and possibly the plume dynamics. As the spot size increases the plume becomes more forward directed.

The laser wavelength has also been reported to have a great effect on the deposition of DLC.[91, 92] It was shown that the 193 nm wavelength yielded good films at lower laser energies than the 248 nm wavelength. The energy needed was about half – which is about what the difference in reflectivity is. Also, the pulse length of the ArF laser used was shorter – this always helps make better PLD DLC.

3.2 The Virginia Tech Diamond-Like Carbon Pulsed Laser Deposition System

The pulsed laser DLC deposition system consists of a pulsed laser, laser beam optics, and a vacuum chamber with a laser grade UV window, graphite target and substrate holder. An excimer laser working at 248 nm provides the energy to ablate the graphite target. Beam optics direct the light beam into the chamber through a window, and a converging lens increases the energy density of the beam to achieve effective ablation of the target. The substrates that are coated with the ablated carbon can be held in a fixed position or rotated inside the vacuum chamber. The VT chamber is setup to allow target and substrate extraction via load–locks without breaking vacuum; this allows rapid prototyping.

3.2.1 Laser[84, 93, 94, 95]

The laser for the VT PLD system is an LPX305i excimer laser made by Lambda Physik. The excimer operates at a wavelength of 248 nm; the light is from a transition in the metastable KrF dimer. A maximum of ~1.2 joules of energy per pulse can be delivered at 10 Hz at this wavelength.

The name "Excimer" comes from the contraction of excited and dimer, and refers to the metastable excited state of the molecule that undergoes the lasing transition. The stimulated emission in the LPX type laser comes from the rare gas halides; some of these are: ArF, 193 nm; KrCl, 222 nm; KrF, 248 nm; XeCl, 308 nm and XeF,350 nm. The laser transition is between the lowest excited state and a repulsive ground state of the dimer with lifetimes of ~2.5 ns and ~.1 ps respectively for KrF. In the LPX type laser energy is provided to a gas mixture by electrical discharge across the laser tube. Some of the reaction in the KrF gas laser are show below; Ne is added as a buffer gas to aid in the reactions.[84, 95]

$Kr + e^- \rightarrow Kr^+, Kr^*, Kr_2^+$ (Kr^* denotes an excited state)

$F_2 + e^- \rightarrow F + F^-$

$Kr^+ + F^- + X \rightarrow KrF^* + X$ (X denotes a third species like Kr, F, or Ne)

$Kr_2^+ + F^- \rightarrow KrF^* + Kr$

$Kr^* + F_2 \rightarrow KrF^* + F$

$KrF^* \rightarrow KrF + Photon$ (Stimulated emission at 248 nm)

$KrF \rightarrow Kr + F$

The LPX 305i has a 50 liter tube where the laser gasses reside; the gas is circulated through the actual laser cavity so that fresh gas is used every shot. Figure 3-3 show the laser tube of the LPX305i and the inset shows a cross sectional drawing with basic electronics. Since the fluorine gas is highly reactive, the gas in the chamber has to be replenished periodically.

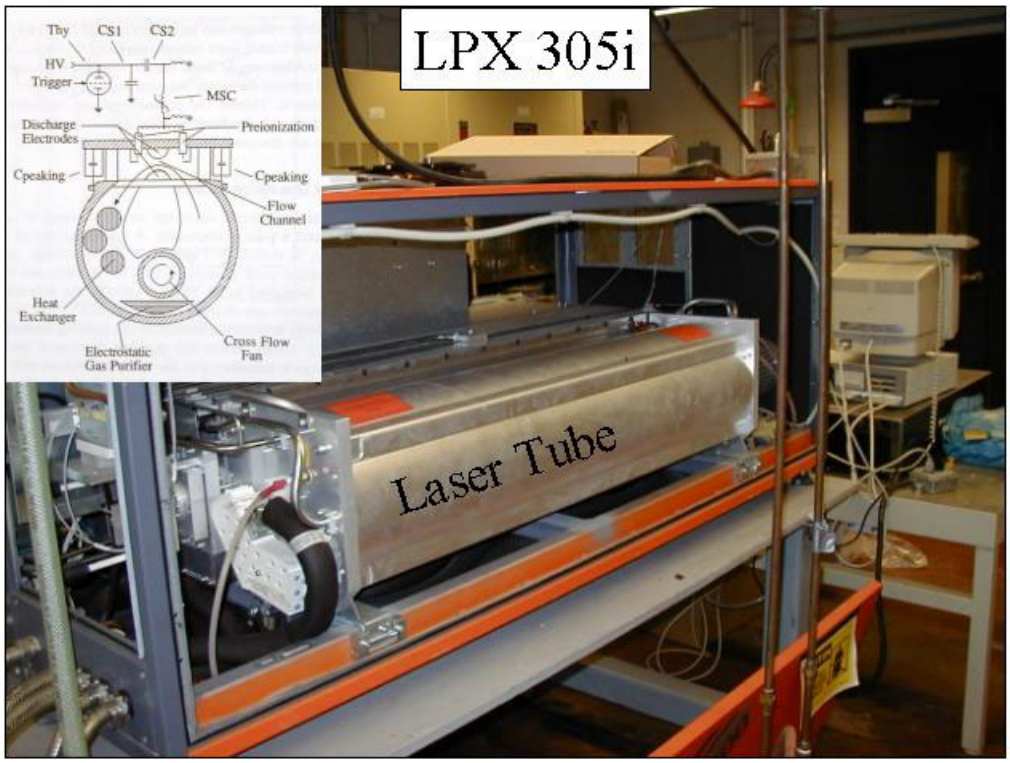

Figure 3-3 LPX 305i diagram: The LPX 305i laser tube and a cross sectional diagram of the tube. Most of the tube is a gas reservoir where the gases cool and relax.

3.2.2 Optical System

In principle, the optical system for PLD is very simple. The laser beam is focused onto the graphite target through a window in the vacuum chamber by a converging lens; beam steering is done with mirrors between the laser and chamber [Figure 3-4]. Copper, aluminum and polycarbonate sheets are used to stop the beam and secondary reflections.

The converging lens and chamber window are the two critical optical elements in the PLD system. A plano-convex UV grade quartz lens is best for focusing the beam and it should be anti-reflection (AR) coated at the lasers wavelength, 248 nm. The window should be transparent to light with a 248 nanometer wavelength and AR coated on the air–side. The window needs to be replaced from time to time since ablated carbon slowly lowers its transmission.

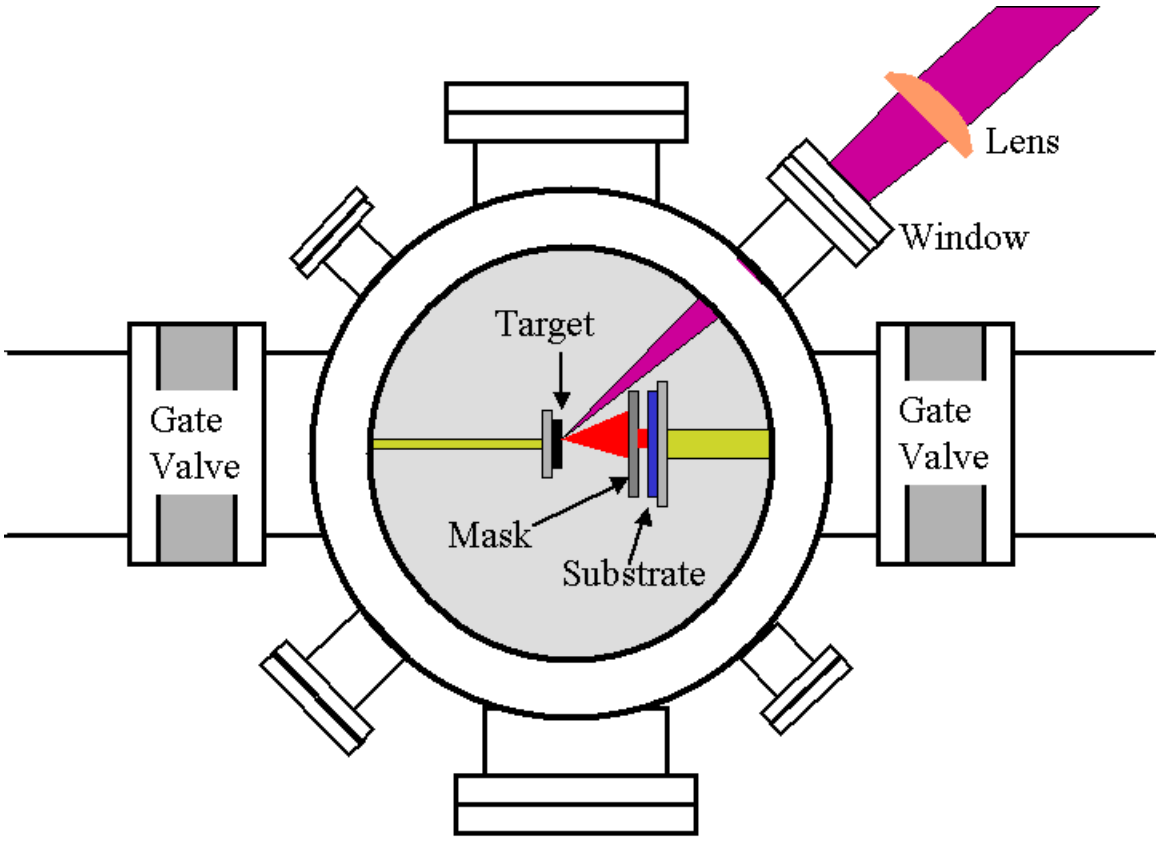

Figure 3-4 The VT PLD vacuum chamber: The window and lens are UV grade fused silica. The gate valves are part of a load lock system for target and substrate removal.

To allow for easy beam manipulation two dielectric mirrors are used. Mounting each mirror in adjustable gimbals allows the beam to be manipulated onto the target. Typically one mirror allows x-direction movement while the other moves the beam up and down. By automating these movements the beam can scan the ablation target; this allows even ablation of the target.

Copper and aluminum are used to stop the laser beam and poly carbonate can be used to stop stray beams while allowing viewing of the system. Copper absorbs about 67% of the beam at normal incidence whereas aluminum reflects 92% of the beam at 248 nm, so copper is much better at eliminating stray beams and diffuse reflections. Apertures made of copper or aluminum are used to eliminate the beam halo and reduce the beam. Quarter inch thick poly carbonate does not transmit 248 nm light so it is good for stopping stray

UV light while allowing the optical system to be monitored; it should not be used to block a direct beam since it will melt.

3.2.3 Vacuum Chamber

PLD is done in low–vacuum to high–vacuum conditions and with different background gasses so a versatile vacuum system is needed. Although the target and substrate can be statically mounted inside the chamber, mounting each on rods that pass through rotary/linear feed–throughs is best. No substrate heating is needed for making high quality DLC although it can be used to anneal the films post deposition.

The pressure in the vacuum chamber has a lot of influence on the ablation process. The effect of bad vacuum can be seen by looking into the chamber. In the range between 10^{-1} to 10^{-3} torr a plasma is formed which can extend several inches from the target. The addition of background gas allows novel compounds to be deposited or, in the case of inert gasses, lower energy particles. A vacuum below $5x10^{-5}$ torr is high enough to make high quality DLC films with PLD.

The target and substrates are generally mounted so they can be manipulated from outside the chamber. The VT system used rods that pass through o-ring seals to hold the target and substrate. This allows them to be rotated and removed via load-lock systems.

3.2.4 The Graphite Target

Both carbon and hydrocarbon targets have been ablated to make diamond-like carbon. Since we are interested in making hydrogen–free DLC, only pure carbon targets are desirable. Pyrolytic graphite (PG) is the preferred target for making DLC due to its optical and structural properties. Pyrolytic graphite targets with different amounts of impurities can be bought; the main impurity to avoid is boron due to its high neutron absorption cross section. Since graphite is tightly bound in two-dimensional planes that are loosely bound together, care should be taken machining and mounting the target so that the same crystal orientation is exposed to the laser beam with each new target.

The first target used in the VT PLD system was a 1.5 inch diameter 0.5 inch thick piece of PG from BF Goodrich. It was mounted on the end of a ¼ inch diameter rod that passed out of the vacuum chamber via an o-ring sealed feed–through. The uniform ablation of the surface was accomplished by rotating the target with an external drive while moving the laser beam in and out radially using the gimbal mounted mirrors.

3.2.5 Substrate Mounting

Several different substrate mounts were used depending on the type of sample. The best method for testing parameters without breaking vacuum is to mount the substrate to a rod that can be rotated from outside the vacuum. In front of the substrate a mask blocks all but about a one square centimeter area of the substrate from the ablation plume [Figure 3-4 and Figure 3-5]. After each deposition, the rod is rotated to expose a fresh part of the substrate. This allows 6-8 tests to be done at one time on one substrate, saving time and lowering variation due to handling.

For x-ray and neutron scattering analysis larger samples are needed. To make large samples with the same film properties across the surface, a combination of two techniques are used. By moving away from the target the central part of the plume gets wider; combined this with moving the rotating substrate off axis, and an even coating can be made over larger surfaces. The samples made for neutron reflectometry were made at 7 cm with the ablation point ~1.25 cm off the substrate's rotational axis. These samples were very even over a two-inch diameter.

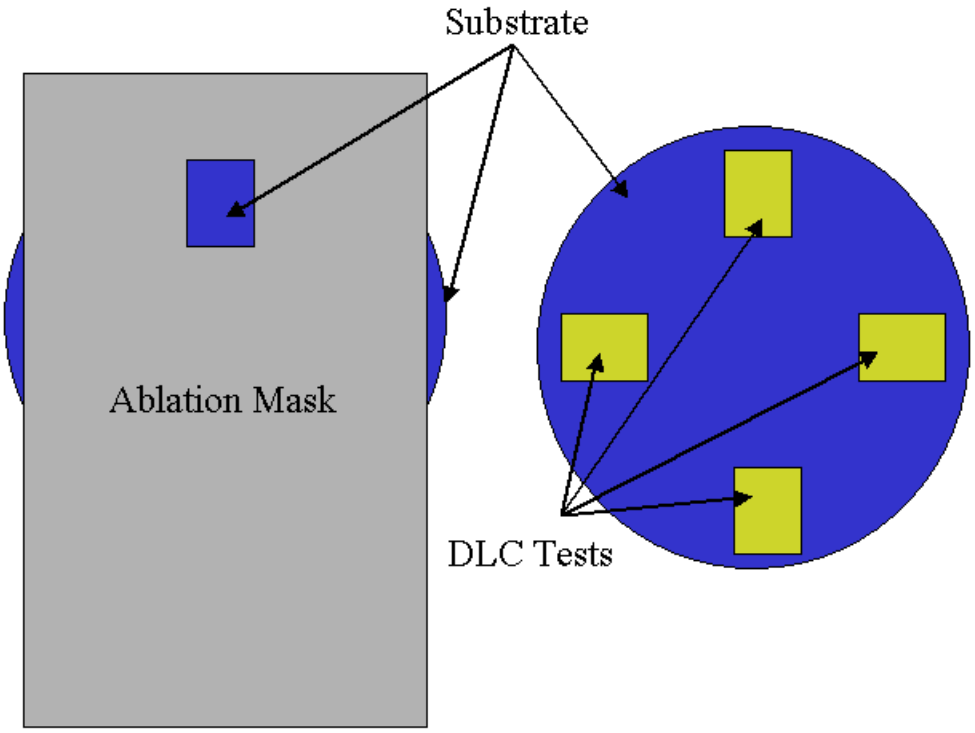

Figure 3-5 Substrate mask diagram: Substrate masks can be used to make multiple tests on one substrate without breaking vacuum. This allows several laser energies or chamber atmospheres to be tested rapidly.

3.3 Parameters

The quality of the coating that results from laser ablation is dependent on the initial plasma and the vacuum conditions. The plasma formation is governed by the laser wavelength, power and duration; the addition of magnetic fields will affect its growth since it is highly ionized. The high–energy atoms in the initial plasma interact with any gasses in the vacuum chamber as they travel to the substrate; if the mean free path is short enough, the atoms will thermalize before reaching the substrate.

3.3.1 Laser

The LPX 305i can be set to run at different wavelengths (KrF⇒248 nm or ArF⇒193 nm) by changing the laser gas and optics (dual wavelength optics can also be installed). The most desirable wavelength for PLD DLC is193 nm, but this will take a bit of work since

the beam path should be in nitrogen. This is due to the high absorption by air that results in the creation of ozone in amounts that are a health hazard.

The easiest parameter to change is the laser energy density reaching the target. This can be done by changing the laser power, attenuating the beam, masking off part of the beam or changing the focus. The first two have the same effect, but changing the laser power also changes the characteristics of the laser pulse. The latter two can both be used to change the area that is being ablated with different effects. Masking is the way to change the rectangular profile of the beam; this can make the deposition more uniform – with a loss of deposition rate.

The type of laser cavity optics used (mirrors, flat or curved) can affect the focus and spot size of the beam. The VT laser was set up with standard flat windows, these have a high divergence and allow several cavity harmonics to resonate. Both divergence and multiple modes cause a blurred focus. At short distances this is less of a problem, but with the 1.5-meter long focal length needed for in tube deposition this causes a very poor focus and large spot size. The standard cavity optics were used for all the early testing and the ILL guides. Unstable optics (Lambda Physiks name for non-flat laser cavity optics) enhance the fundamental cavity mode and lower the beam divergence; as a result the spot size is much smaller and the focus is very localized. With the change in optics it is possible to ionize the air if the beam is brought to a focus; this can be both seen and heard. The drawbacks are a 50% loss in total power, an increase laser window cost ($1000→$5000) for a pair and a decreased laser window lifetime.

3.3.2 Chamber atmosphere

PLD deposition can be done in a low-pressure gas or high vacuum. Depending on the pressure and reactivity, different amounts of the background gas are incorporated into the film. This can be used to create new compounds, like carbon nitride,[72] or to add a dopent like fluorine for increased conductivity[96].

Carbon nitride (C_3N_4) could be a very good neutron reflector since it should have density comparable to diamond with a higher scattering length due to the nitrogen. [97, 98, 99, 100] The problem with making it in a background gas appears to be the loss of kinetic energy of the deposited compound. The film density usually falls well below 3 g/cm as the nitrogen percentage gets above several percent, with about 10% being the highest.[101, 102, 71] Unless denser C_3N_4 films are made it will be of little use for UCN guides.

Another use of the background gas is to lower the kinetic energy of the ablated particles. With each collision the ablated atom loses energy until it comes to thermal equilibrium with the background gas. As the pressure of the background gas increases, the average distance an atom travels between collisions decreases as seen in Figure 3-6 (mean free path ~$1/(N\sigma)$).[103] The typical distance from the target to the substrate is 5-10 cm, which is about the mean free path of a carbon atom at 0.01 torr, Figure 3-6. By moving the substrate closer to the target different parts of the active plume can be deposited. In Figure 3-7B the substrate is just beyond the optically active part of the plume. By analyzing the plume's optical spectrum the types of reactions happening in it can be studied.[104, 91, 105]

Another advantage of background gas is that the ablated atoms are not all forward directed. This makes coverage of uneven surfaces possible, but it also allows unwanted growth structures to form. This can be seen in figure 4-6, where the background gas is nitrogen.

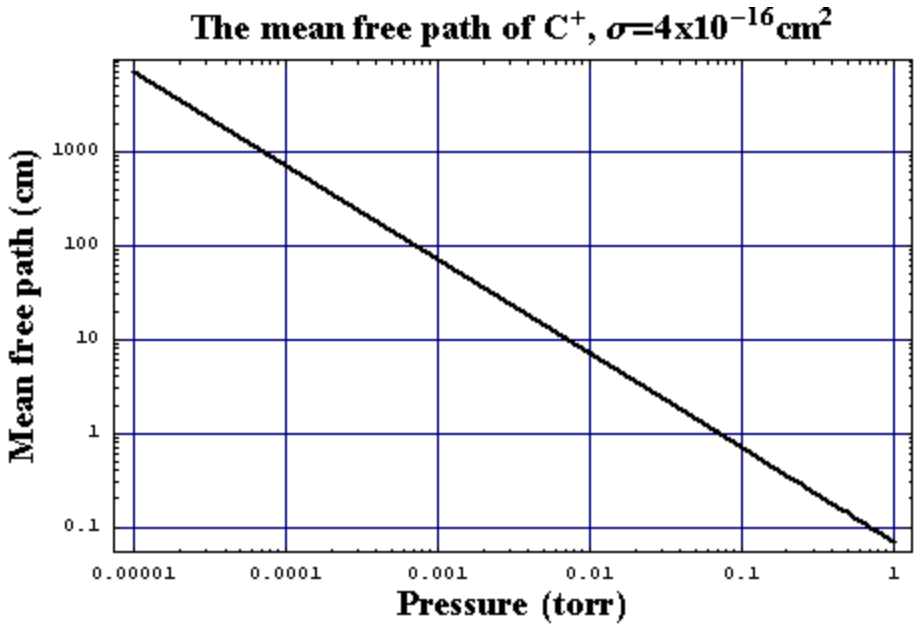

Figure 3-6 Carbon ion mean free path: This log-log plot shows that the mean free path of ablated carbon atoms decreases rapidly with increased chamber pressure. Typical distances from the target to the substrate are in the range 5-20 cm, for UCN guide depositions the range is ~5 cm.

When the ablated atoms and electrons collide with the background gas there is a chance for ionization to occur. The energy needed to cause ionization depends on the background gas used [Table 3-1]. For ionization to occur the collision must involve more energy than the ionization potential. For example, the cross section for the first ionization of Ar, by an electron, peaks at 60-80 eV with a cross section of $3x10^{-15}$ cm^2. [103]

Ionization Potentials[51]			
Element	1st Ionization (eV)	2nd Ionization (eV)	3rd Ionization (eV)
He	24.587	54.416	
C	11.260	24.383	47.887
N	14.534	29.601	47.448
Ar	15.759	27.629	40.74

Table 3-1 PLD gas ionization potentials: This table show ionization potentials for several possible chamber gasses used in the PLD of DLC.[51]

Another process that happens in the presence of a background gas is the creation and destruction of molecules. Table 3-2 show a few possible bonds that may be present in the plume with various background gasses.

Compound	Bond Energy kcal/mole	Bond Energy eV	Wavelength nm
O-NO	73	3.17	391.70
O=CO	127.2	5.52	224.80
NC-CN	128.1	5.56	223.22
C-C	144	6.24	198.57
N-O	150.8	6.54	189.62
C-N	184	7.98	155.40
N-N	226.8	9.84	126.08
C-O	257.26	11.16	111.15

Table 3-2 Table of bond energies for possible plume compounds.[51]

Figure 3-7 Pyrolytic graphite ablation: The left image shows a laser hit on the pyrolytic graphite under high vacuum. The right image shows a laser hit in a background of nitrogen gas at ~10^{-2} torr; the target also has two magnets taped on the backside.

Background gas can be added to the chamber in a static or flow–through configuration by valving off the pump. The static case is better when adding expensive, explosive or toxic gases; but the mixture is slowly contaminated with new compounds from the plasma, causing the deposition to change with time.

3.3.3 Magnetic Field

A magnetic field can affect the movement of charged particles in the ablation plume and change the resulting film. The effect varies according to the relation $\mathbf{F}=q(\mathbf{E}+\mathbf{v}\times\mathbf{B})$, known as the Lorentz force law, where **E**, **v** and **B** are the electric field, particle velocity and magnetic field, respectively. By looking at the radius and frequency of the particle's orbit the field's effects can be seen.

The frequency and radius can be derived by setting the product of the angular acceleration and the mass equal to the force due to the magnetic field: $mv^2/r=qvB$, m – mass, v – velocity, q – charge, B – magnetic field, r – radius. The orbit radius is $r = \frac{\sqrt{2mKE}}{qB}$, where the velocity has been written in terms of the kinetic energy (KE). From this the frequency of the orbit is determined to be $f = \frac{qB}{m2\pi}$, which is independent of the energy.

Looking at figures 3-8 and 3-9 it is apparent that the electron will orbit several times in the area of the initial plasma. Since the mass of the carbon is much greater than the electron its orbit is much larger than the initial plume. The orbiting electron should cause more ionization of the plasma, which will increase the kinetic energy of the resulting plume. The 100 eV energy was chosen since it is the goal energy for high quality DLC.[92] There is one paper that reports on the use of a magnetic field to aid in the PLD process for DLC; the general conclusion was that the film quality was increased.[106]

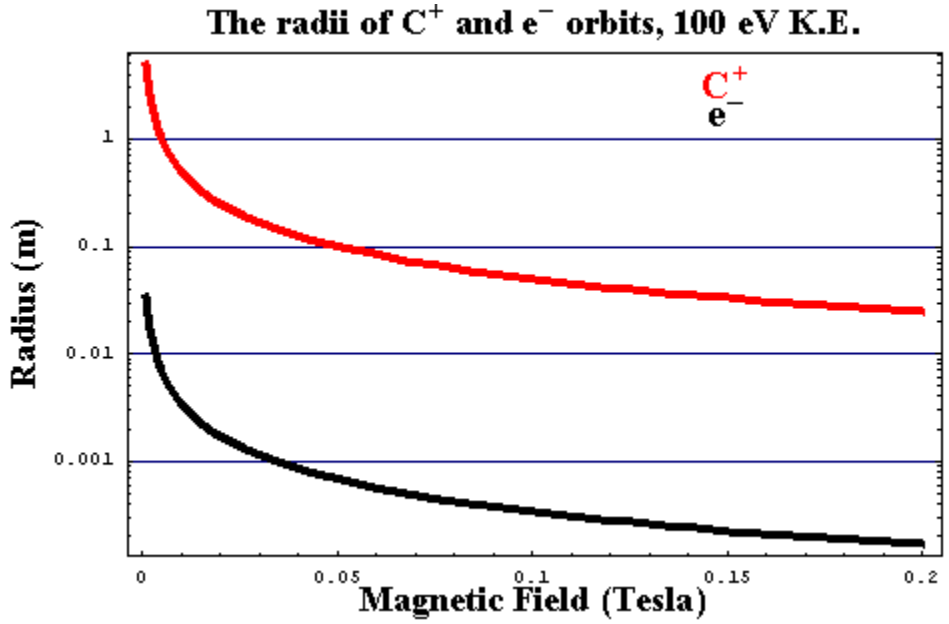

Figure 3-8 The radii of C^+ and e^- orbits at 100 eV of kinetic energy: This plot shows the radius of 100 eV C^+ and e^- particles with their velocity perpendicular to the magnetic field. The laser spot size on the target is ~.001 meters so electrons can orbit in the initial plasma causing further ionization of the carbon atoms and ions.

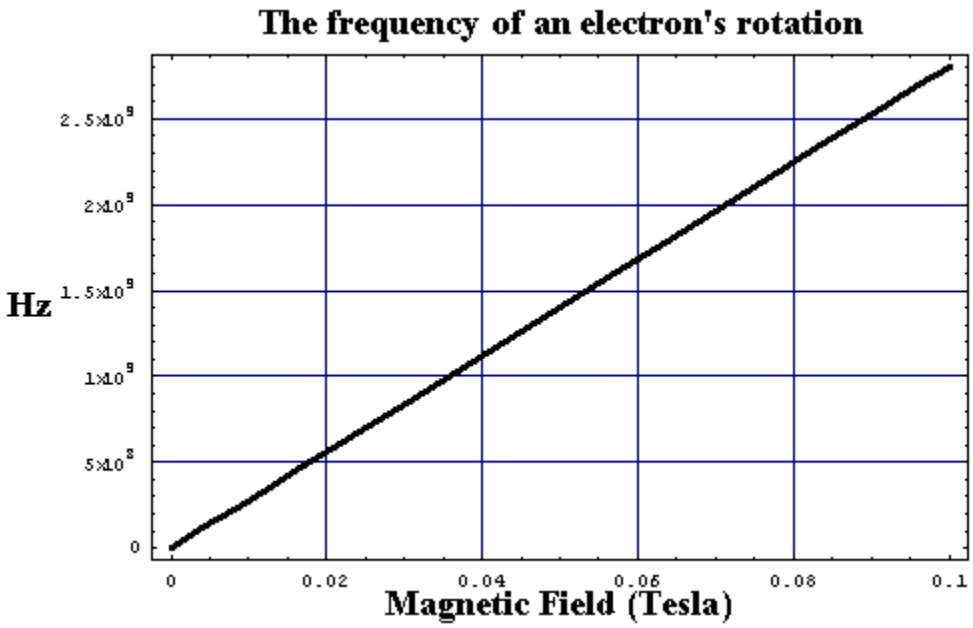

Figure 3-9 The frequency of an electron's rotation in a magnetic field: This plot shows the frequency of rotation for electrons in a magnetic field. Since the pulse width of the LPX305i is about 25 ns the electrons will make multiple orbits in the initial plasma if they do not hit anything.

3.3.4 Substrate Biasing

According to the Lorentz force, the electrons and ions are also accelerated by an electric field. The amount of acceleration is dependent on the mean free path, and in high vacuum can lead to a substantial increase in kinetic energy of the ions. If the substrate is DC biased negatively relative to the target, and the mean free path is comparable to the target substrate distance, the carbon ions will have an increased kinetic energy. Depending on the conductivity of the substrate the bias may be canceled by charge build up. For insulating substrates an RF biasing can be used; depending on the conditions a natural DC bias may build up during deposition.

Applying a DC bias in high vacuum conditions can result in arcing between the target and the substrate during deposition. The arc follows the plume back to the point that the laser hit. The DC supply used in the VT system did not have enough current for this type of deposition, but this technique has been used to make dense amorphic diamond films.[70] The films made this way are very rough.

When a DC bias of several hundred volts is used along with a nitrogen atmosphere the active part of the plume can be extended to the substrate. Again the low current limit of the power supply we used was a problem. It seems that with a better power supply this might be something to study more.

3.4 Diagnostics

Monitoring of the ablation process is needed to make repeatable DLC films. The ablation process diagnostics on the current PLD system are very simple compared to those used to study the ablation process by other groups.[86, 91] The laser power reaching the target needs to be known and kept constant. The vacuum conditions also need to be monitored – this is especially true when using background gas.

The laser energy is monitored in several ways: the LPX305i has its own energy monitor and a handheld monitor can be used to check the energy along the beam path. The

internal monitor is used to watch for changes in the laser performance and the external monitor can find optical components that are wearing out or misaligned.

The most common parameters that indicate how a film was made are the energy density at the target and the vacuum pressure, but the ion energy has been found to be a more predictive parameter to know.[92] The ion energy can be found with a simple probe and oscilloscope, and it can be monitored during deposition.

3.4.1 Laser Beam Energy Monitors

The LPX has an internal energy monitor; this is used as the primary monitor of the laser's condition. The software will shut the laser down if the energy monitor is not seeing laser pulses; it can also raise the discharge voltage to maintain a constant energy level in the monitor.

A standalone energy monitor is also used to make sure the energy reaching the target is not fluctuating due to problems with the optics or alignment. The energy before and after each optical component should be checked from time to time to make sure the components are aligned and not damaged. The chamber window is the component that needs the most checking, although the other optics do age and require repositioning of the beam to an unused section of the optical component.

The laser energy can be continually monitored using the handheld meter. For this the beam reflection off the chamber window is monitored. The window is purposely not normal to the beam so the reflection is easy to separate from the beam.

3.4.2 Energy Density at the Target

Energy density, or more correctly the power density, at the target is what controls the formation of the initial plasma that becomes the deposition plume; this is the parameter usually reported in the literature about PLD DLC films. The energy density is calculated from the spot size and laser energy at the target. The spot size can be measured by hitting

a thin sheet of copper with the focused laser beam; the resulting spot is easily measured. The energy needs to be taken at the target but since the focused beam would damage the portable monitor this is a two-step process; this is done by first finding the loss due to the lens, then with it removed the energy at the target is measured and corrected.

3.4.3 Vacuum Pressure

The vacuum pressure is monitored by Convectron type thermocouple gauges for low vacuum and an ion gauge for high vacuum. Convectron type gauges are good for the range 1000 torr to ~10^{-4} torr, this is very useful for both monitoring pumpdown and holding deposition pressures. The pressure read out from the Convectron depends on the gas in the chamber and can be very nonlinear; tables in the manual allow accurate conversion. The ion gauges used are not nude (they are encapsulated in a glass tube) so the pressure can be a bit higher than it is in the chamber. Also, as the vacuum gets better the major components of the atmosphere changes from nitrogen and water to hydrogen. Since the ion gauge reading depends on the residual gas present, the reading is not the true vacuum pressure.

3.4.4 Ion Probe

A simple ion probe made from a coaxial wire like Figure 3-10 is a good diagnostic tool for PLD.[107] An oscilloscope is used to monitor the probe. By using a negatively biased probe the ion current of the plume can be monitored (the negative bias has very little affect on the plasma, since the plasma is self shielding).[92] The best films are made at ion energies of around 100 eV[92, 90]. The energy is calculated from the velocity by assuming the major component of the ion pulse is from signally ionized carbon atoms.[91] The easiest way to get the velocity is to use two probes a set distance apart and look at the difference in the arrival time of the ion pulse peak.

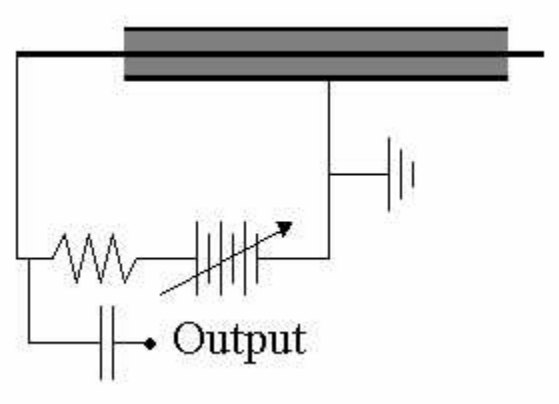

Figure 3-10 Ion probe pickup circuit: This is the circuit used to look at the ion current in the plume. The values of the resistor and capacitor depend on the pulse width of the ablation plume.

This system can also be used to focus the optical system onto the target. The best focus for a given laser energy is obtained by moving the focusing lens and maximizing the current pulse seen by the ion probe.

Figure 3-11 shows three different ion pulse shapes corresponding to three different laser energies (~250 mJ, ~500 mJ, ~700 mJ). The size of the pulse increases dramatically as does the arrival time with increased laser energy. The ion pulses have been fitted by a couple of authors with equations (Maxwellian) that give center of mass speeds and temperatures.[85, 86, 107] This is a definitely an interesting possibility with the new digital scope.

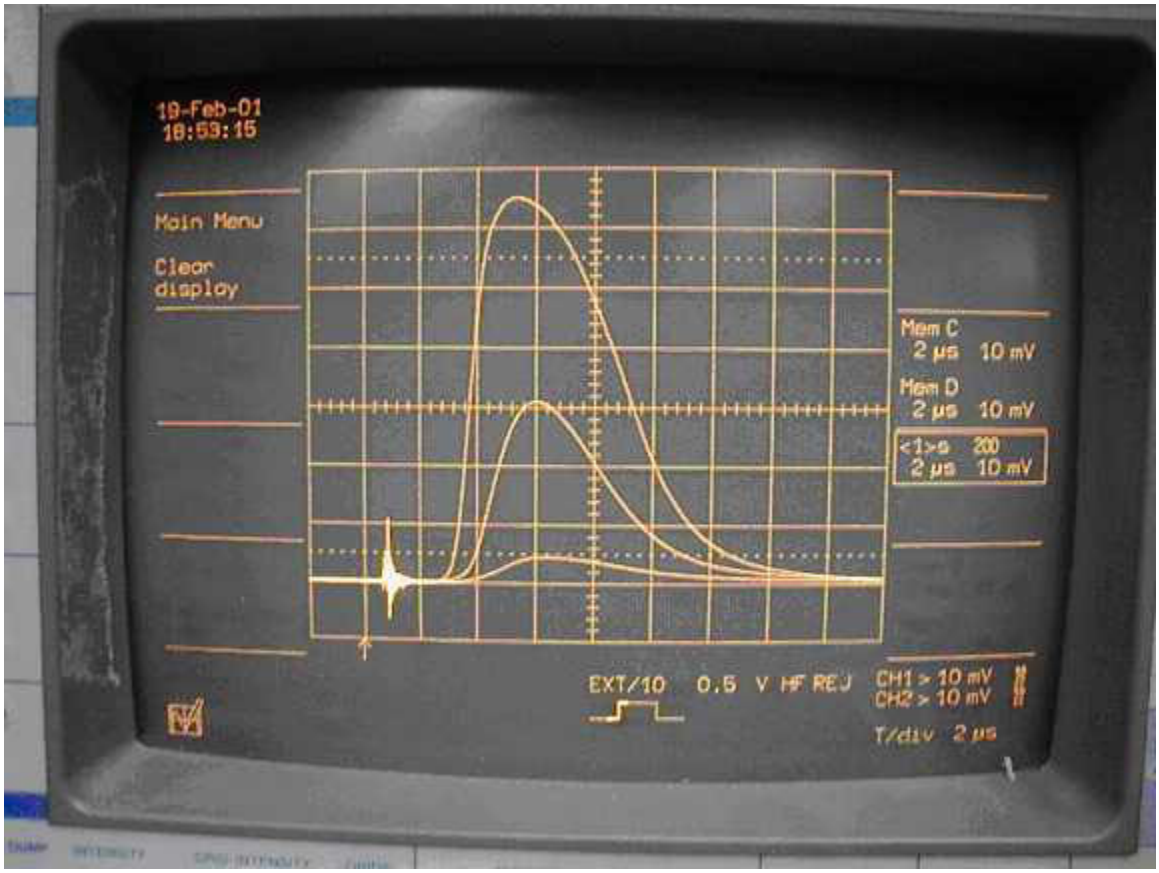

Figure 3-11 Oscilloscope image of ablation current: This picture shows the oscilloscope traces of three different ion pulse shapes corresponding to three different laser energies (~250 mJ, ~500 mJ, ~700 mJ). The arrival time decreases and the ion current increase with increased laser energy.

4 Diamond-like Carbon Coating Surface Characterization

The next step after rebuilding the VT pulsed laser deposition system was to make diamond-like carbon and test its properties, mainly those properties that relate to UCN transport. The basic technique is easy enough; focus an ultraviolet laser beam onto a graphite target inside a vacuum chamber and collect the resulting plume on a substrate. Exploring the parameter space of laser energy and beam focus was the first things to do. The literature also pointed to other parameters to explore including adding some nitrogen gas to attempt making carbon nitride, which could be better than diamond for neutron transport. The primary goal was to see if we could make smooth, dense diamond-like carbon. As a final test the coating would need to be tested for its ability to reflect neutrons. If the coating was smooth and highly reflective to neutrons we could scale up to making guides to be tested with UCN.

4.1 Substrates

To study the properties of the films made in the PLD system one first needs a well-characterized substrate. The first DLC film properties to look at would be roughness and optical characteristics. To look at the roughness of the film one needs a substrate that is very smooth and the same substrate to substrate. For optical testing one needs both transparent and opaque substrates that are very smooth. The substrates also need to be very clean, again so the surface is easy to characterize.

4.1.1 Substrates

PLD DLC was deposited on several different types of substrate. The least expensive and good for general testing was float glass; window glass is made by floating the molten glass on liquid tin. Polished fused silica disks and electronics grade silicon wafers are more expensive and were used for final testing. Float glass is generally available from hardware stores while Si wafer and fused silica must be ordered.

Glass, fused silica and silicon wafers were all cut to size by scribing with a diamond scribe and breaking. Cutting should be done before cleaning since it leaves a lot of very small particles on the sample. Wiping the dust off will scratch the surface so they should be blown and/or dip cleaned.

4.1.2 Substrate cleaning

Substrate cleaning has two goals; one is the removal of surface contamination and the second is the removal of oxides. Surface contamination is generally removed with solvents and/or soap. A more aggressive technique is to boil the substrate in a mixture of 70% H_2SO_4 (Conc.) and 30% H_2O_2 (30%) for an hour. To clean the native oxide off of Si wafers we originally used a product called Buffered Oxide Etch (BOE) and later just electronics grade HF. Another method of removing oxides and the polishing compounds that are in polished glass and Si wafer is boiling in 5 parts DI water, 1 part NH_3 and 1 part H_2O_2 for an hour. A final useful cleaning solution to remove imbedded metals is a bath of aqua regia; by boiling the substrate in a 50:50 ratio with DI water. It is best to follow each cleaning step with DI water rinses, and the excess water should be removed from the surface by blowing with clean, dry inert gas or clean low lint wipes.

4.2 Sample Deposition

Silicon, glass and fused silica samples were coated with DLC using the techniques discussed in chapter 3. The samples were usually made using a mask so that several values of a parameter could be checked quickly [Figure 4-1]. The main parameters investigated were energy density at the target, target to substrate distance and background gasses. The following sections discuss the different techniques used to characterize the samples.

4.3 Visual Inspection

Inspection of deposited films by eye and with a microscope is very helpful in tuning the system. The amount of particulate can be seen as well as any areas of delamination. A

set of samples made at various energies can be checked in seconds to find the optimal energy range.

4.3.1 Delamination , Internal Stress and Annealing

One of the early indicators that DLC was being made was the delamination of the films. This is due to the high compressive stress inherent in DLC films[71, 108]. The stress is relieved when the film buckles in one of three characteristic patterns.[109, 110] Some films will look good to the eye; but, under microscopic examination, small s-shaped snakes appear. With time these usually develop into a system of interconnecting snakes like those on the edges of Figure 4-2B. Films with more stress show visual delamination that under a microscope look like the mountain ranges of Figure 4-2A. If the stress in the film is high enough, it pops off when the vacuum chamber is vented. This is seen in the 3 o'clock part of Figure 4-1. The stress relief in PLD DLC films appears to be similar to that in CVD DLC films[109, 110]. The stress relief that results from delamination can be seen by a shift in the Raman spectrum[111]; this is a very sensitive test, and may show delamination before it is visible.

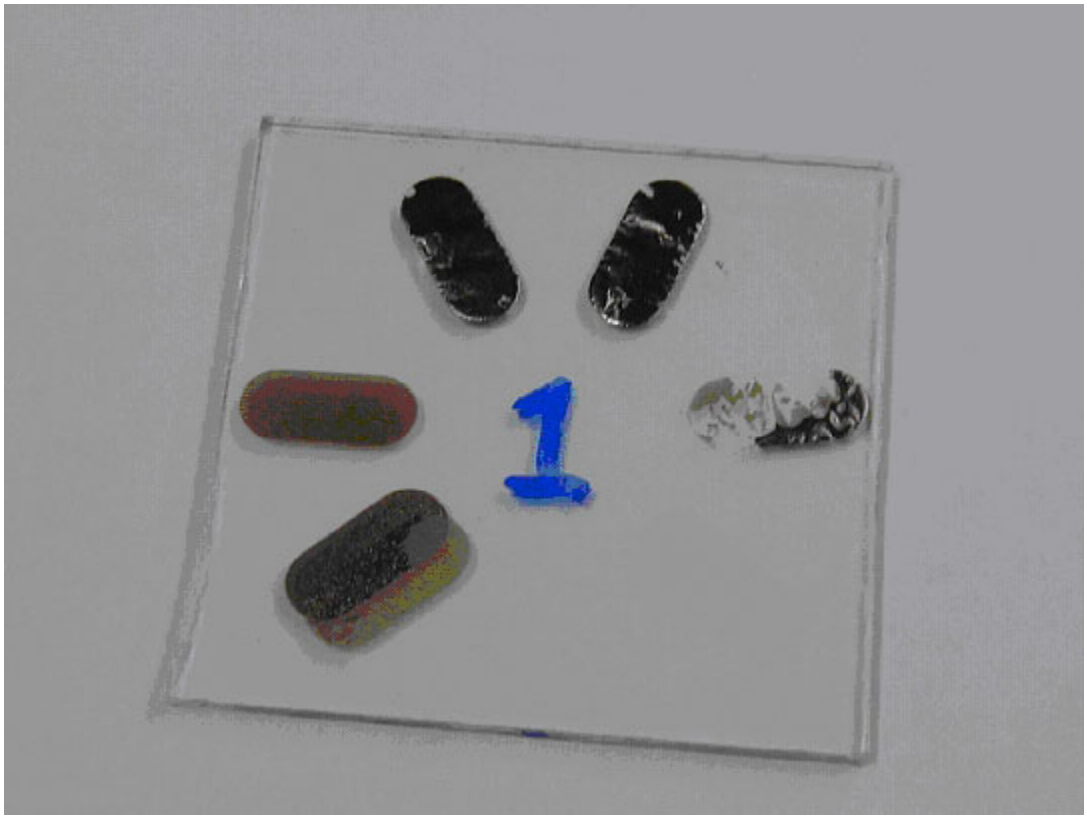

Figure 4-1 PLD sample one: This shows the first sample made with a mask. The depositions at 11, 1, and 3 o'clock were taken at 175, 270, and 400 mJ of laser power. Each had 10000 pulses at a distance of two inches from the target and all three are delaminating. The other depositions were alignment tests with lower numbers of counts.

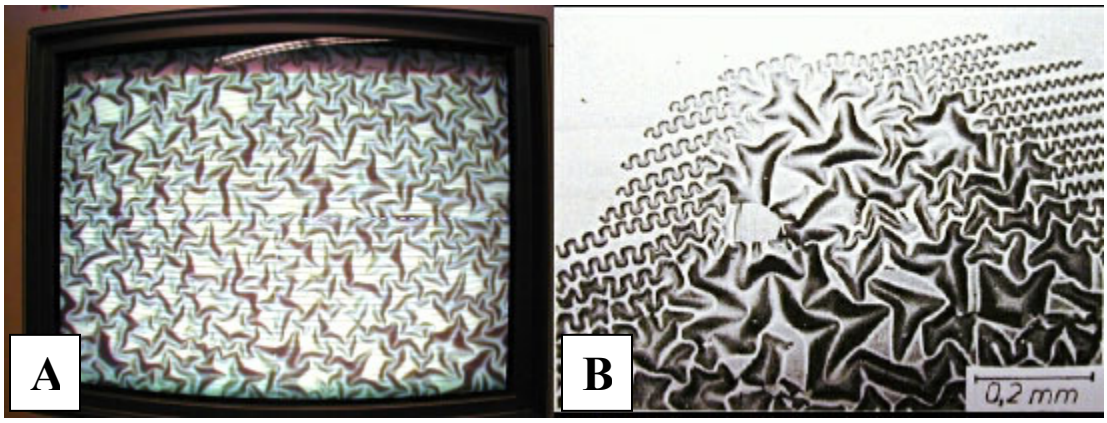

Figure 4-2 PLD DLC delamination: 'A' is a picture of the delamination in Figure 4-1. It is from the AFM alignment microscope TV monitor. 'B' also shows DLC stress relief patterns.

4.3.2 Color and Transparency

The color and transparency of deposited films vary with the film density. The densest films that were made are fairly clear on glass. As the films become less dense they become dark to the eye. The color also changes due to interference effects and wavelength–dependent absorption and reflection. Changes in color and transparency are the first sign that the process has changed. This is very easy to see if several samples are looked at side by side.

4.3.3 Particulate and roughness

When the films are inspected with a microscope, the amount of particulate can be seen. These are large pieces of carbon from the target. Fresh targets have a lot of particulate until they have been conditioned with a few thousand pulses. At higher laser energies the amount of particulate starts to increase due to deep heating of the target.

4.4 Resistivity

The resistivity of diamond is 10^{13} to 10^{15} Ohm centimeters. DLC films have resitivities that vary from 10^{5} to 10^{14} Ohm centimeters; with PLD DLC being at the lower end of this range, $10^{5} \rightarrow 10^{8}$ Ohm centimeters[112]. The resistivity of PLD DLC can decreases several orders of magnitude by annealing [113].

Several samples of PLD DLC on silicon wafers were tested using a three point probe in the MSE Department at VT. The resistivity was a little higher than the setup was designed to test, but it seemed to be above 10^{6} Ohm centimeters. The densest films were never tested; in general, this is an area that needs more work.

4.5 Surface roughness – Atomic Force Microscopy

Surface roughness is a major source of loss in UCN transport since it can result in UCN being reflected back toward the source and away from the experiment. A good UCN coating needs to be as smooth as the substrate that is used. In traditional coating techniques the roughness is a function of the deposition rate, and different for each

material and technique. To determine the roughness of PLD DLC films and substrates, an atomic force microscope (AFM) was used.

4.5.1 Atomic Force Microscope

The atomic force microscope is a device that physically scans a surface with nanometer height resolution over areas from hundreds of square nanometers to tens of square micrometers. The greatest resolution is in the vertical direction. The AFM examines a surface by dragging a small tip on the end of a flexible cantilever over the surface [Figure 4-3]. A laser beam is reflected off the back of the cantilever and into a split photo detector. As the tip moves up and down on the surface, the laser light moves across the detector. A feedback circuit energizes a piezo crystal that adjusts the cantilever height with the goal of maintaining a constant signal in the detector. The voltage applied to the piezo is proportional to the height variation in the sample. A second set of piezo crystals raster the tip in an x-y grid to map the desired surface region.

The AFM used for these studies was a Digital Instruments 3000 scanning probe microscope (SPM). Most of the data was taken in contact mode, but some was taken in tapping mode. In tapping mode the tip is oscillated with the piezo crystal and the height is adjusted to maintain a constant amplitude oscillation [Figure 4-3]. Tapping mode tips cost around $20 and often last for only one sample on the PLD DLC so most the data was taken with the $5 contact tips that could be used for many samples.

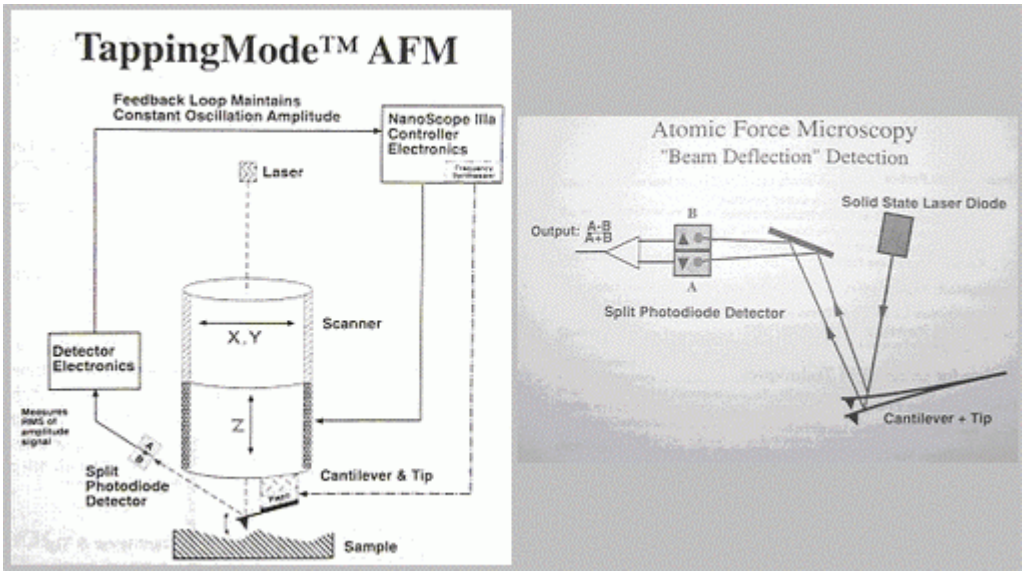

Figure 4-3 AFM diagrams: These two diagrams are from the Digital Instruments manual for the AFM. The left diagram shows the cantilever, tip and piezo assembly, the x,y piezos make the scanning motion while the z is adjustded by the feedback loop to maintain a constant distance from the surface. The right diagram shows how the tip position system works.

Typically several different sized scans were made of each sample; smaller scans have higher x-y resolution. The normal scan sizes were 20x20 μm^2, 5x5 μm^2 and 1x1 μm^2 – Figure 4-4 shows such a set. The machine can take up to 512 samples per scan so the 1x1 μm^2 scan has a data point about every 2 nanometers. Quartz tubing usually has about the same roughness at all three resolutions, whereas stainless steel tubing has decreasing roughness with decreasing scan sizes due to uneven grinding and polishing patterns.

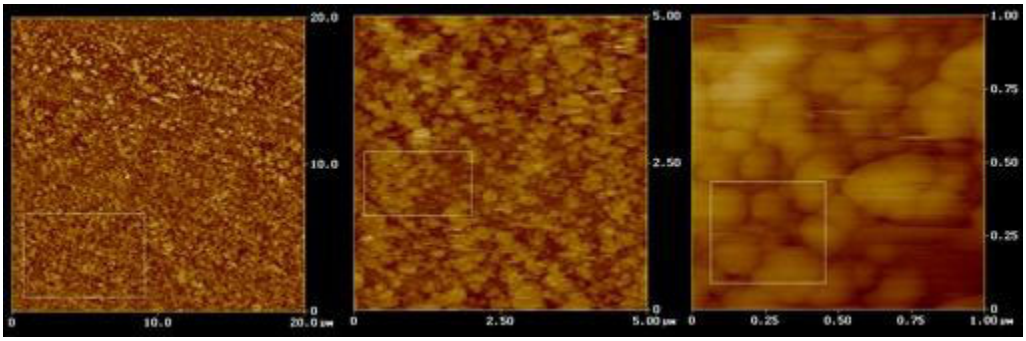

Figure 4-4 Three different resolution images of quartz tubing: The images are 20x20, 5x5 and 1x1 μm^2 in size from left to right, each with a z and y resolution of 512 points. The cloud like structure is typical of the quartz tubing scanned. This sample is from one inch ID quartz tubing from the CWU glass shop.

One problem that is encountered when scanning insulating surfaces is the build up of static charge. PLD DLC on quartz is definitely not very conductive and the image often is lost part way through a scan due to charge build up. Charge build up is eliminated by putting a small radioactive source near the AFM tip, this ionizes the air and seems to work most of the time.

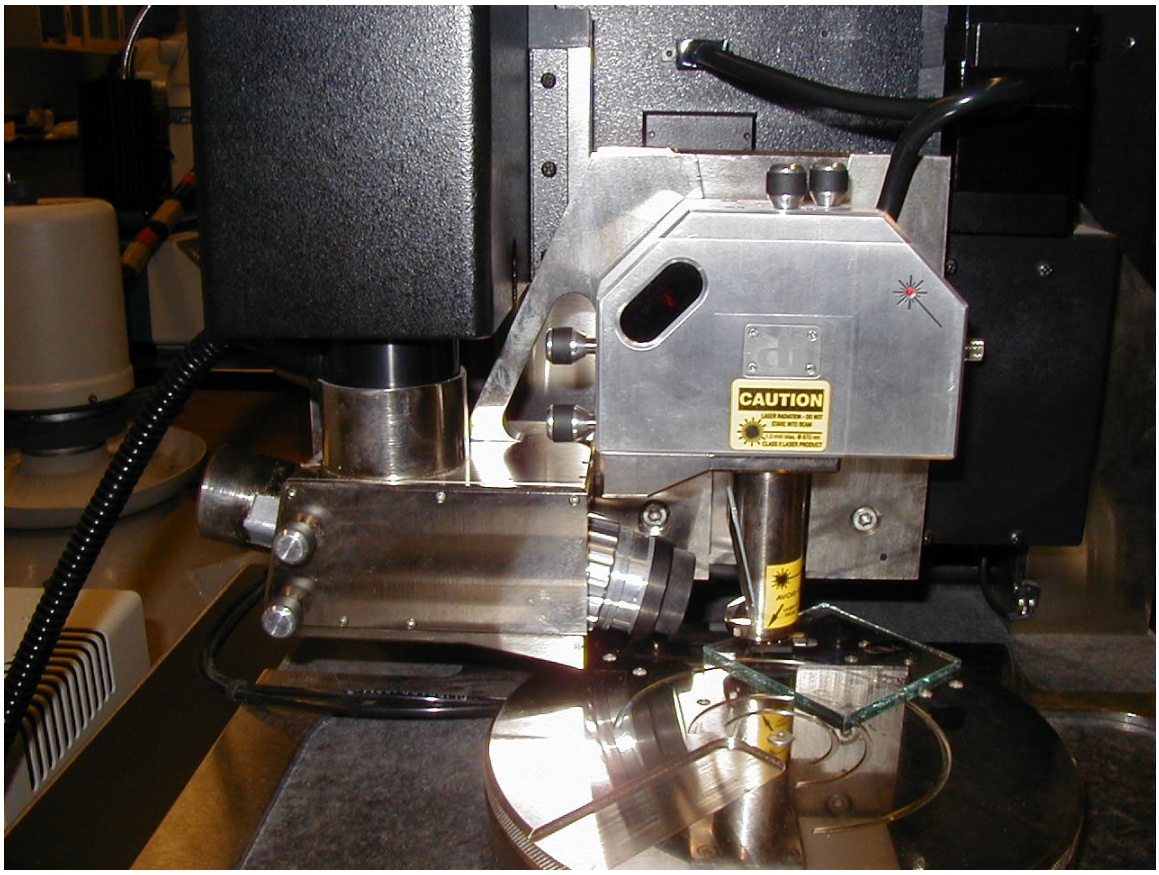

Figure 4-5 Digital Instruments 3000 photo: The photo shows a float glass sample like figure 4-1 being scanned by the AFM. The laser and piezo crystals are in the part labeled "CAUTION" and the tip in the section just above the sample. The lens at the left of the sample is part of the video monitor used to position the tip on the sample; figure 4-2A was taken with this camera.

4.5.2 Roughness Studies of Carbon and Carbon-Nitrogen Films

AFM studies of PLD DLC showed that there are two types of surfaces that result from changing the vacuum conditions and that a well–used target puts less particulate contamination onto the substrate. In general, the surface of vacuum PLD DLC is very smooth. As nitrogen is added to the chamber the DLC surface begins to have increased structure and roughness [Figure 4-6]. The initial sets of PLD DLC samples were made

after the target had been cleaned by removing a layer of graphite with sand paper and then blowing it clean; this is a common practice in the literature, but it results in a lot of particulate hitting the substrate.

The increased roughness shown in the right image of Figure 4-6 is due to preferential growth of the film, this is possible since the ablated carbon has been thermalized by the background gas in the chamber. It is not present in the vacuum deposition (left image) since the energetic atoms destroy any preferential growth as they burrow into the film. The surface structure is also seen in the bulk as columns that extend to the substrate [Figure 4-7]. Figure 3-6 shows that the mean free path is a few centimeters at the chamber pressure of the right image, this allows the carbon atoms and ions to thermalize.

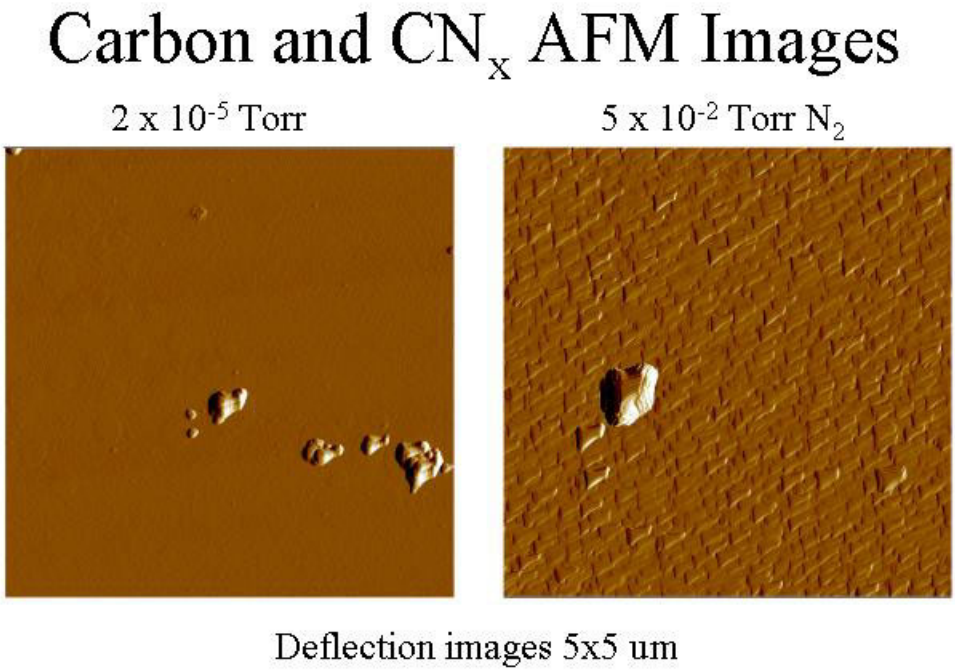

Figure 4-6 AFM images of carbon and carbon with nitrogen: The left image of vacuum PLD DLC is smooth except for the islands that are probably chunks of carbon from the target. The right image shows the triangular growth structures of CN_x that start to show up when the ablated graphite thermalizes before it reaches the substrate.

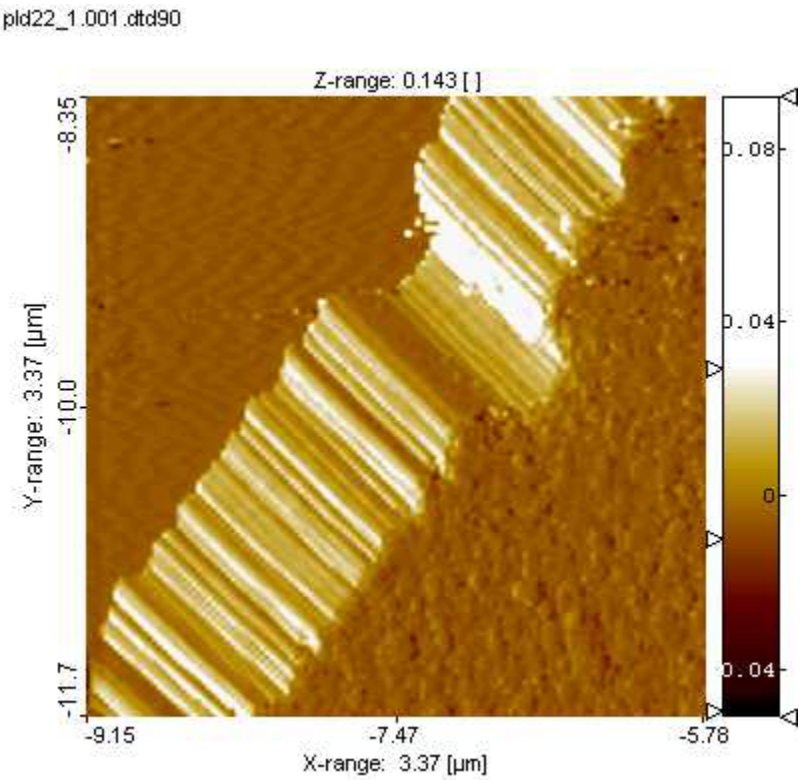

Figure 4-7 Columnar structure of a CN_x film: The upper left of part of the image is the Si wafer and the lower right corner is the top of the CN_x film. The columnar structure is showing on the diagonal. The film is ~700 nm thick with a roughness of 15 nm.

The goal of using nitrogen background gas is to increase the critical velocity of the coating by incorporating a large amount of nitrogen into the film; the scattering length of nitrogen is 1.5 that of carbon. The amount of nitrogen in the film should increase with the nitrogen pressure in the chamber. Even if the critical velocity of the film is increasing, the increased roughness lowers the specular reflectivity of the coating, so this is not a good coating for a UCN transport guide. The increased roughness caused by using the background nitrogen gas might make a good diffuse coating for a UCN bottle if the surface has a decent critical velocity or if it is coated with vacuum PLD DLC.

The AFM can also provide direct measurement of the films thickness. This is done by removing the coating in an area and making a scan across the resulting step. Figure 4-8 shows an example of this. This thickness information can be used to check the thickness found with optical ellipsometry (explained later).

The effect of target conditioning was found by looking at multiple samples made on the same wafer as described in chapter 3. Starting with a freshly cleaned target, the first sample shows more chunks then the final sample. There are also noticeable fireballs leaving the target. The cleaning was done the same way as in the literature; first the surface is sanded then it is blown clean with argon. In addition to getting less particulate the samples taken after conditioning have slower film growth rate.

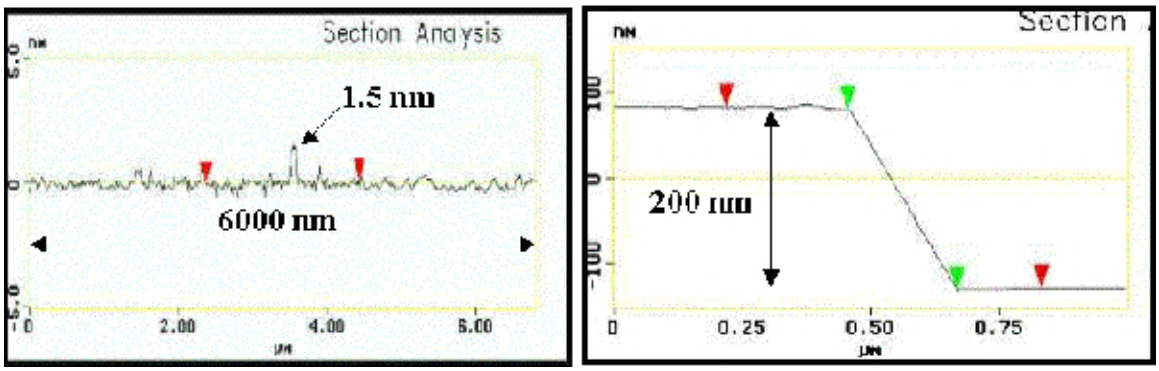

Figure 4-8 AFM cross sections of PLD films: The left cross section is of a PLD DLC sample with roughness Ra = 0.15 nm. The right cross section shows the thickness of a PLD DLC film; the edge was created by scratching the coating off the wafer.

4.5.3 Guide Surfaces

Since PLD DLC can be nearly as smooth as the substrate, using a very smooth substrate will result in a very smooth guide. The AFM was used to compare several types of tubing for possible use in the UCNA experiment. The standard Serebrov UCN guide was scanned as a reference. A sample of the ^{58}Ni coating made by evaporation at Princeton was also scanned.

Quartz tubing was the preferred choice for the polarized guide sections, but the roughness, although thought to be low, was not known. Initial AFM scans showed some scrap quartz to be similar to Serebrov tubing in roughness. The first scans of large diameter GE quartz tubing showed it to be smoother than Serebrov tubing, but it had some angular patches on the surface [Figure 5-2]. After talking with several people in the quartz industry it was decided to try etching the quartz to see if the patches could be

removed[114, 115]. They did disappear with etching in 5% HF solution for ten minutes and the resulting surface was considerably smoother [Figure 4-9]. The etching of tubing is discussed in Sections 5.1.2 and 5.1.3.

Stainless steel tubing is a much stronger product to build UCN guides with, but it has to be polished to make a UCN guide. The commercial process has a final grind at ~320 grit that is followed by electropolishing. The final surface quality is very dependent on the quality of tubing that is used. Serebrov tubing is polished with a special system at PNPI, but the availability is poor so a replacement source would be useful. Rath Manufacturing is one of the main US suppliers of high quality electropolished stainless steel tubing; their tubing has a 10Ra (microinch) finish and is available in ½ to 4 inch diameters.[116] AFM scans of Rath tubing have shown that it is comparable to the finish of the Serebrov guide that was scanned [Figure 4-9]. The AFM results indicate that it should be tested with UCN, but this has not occurred yet.

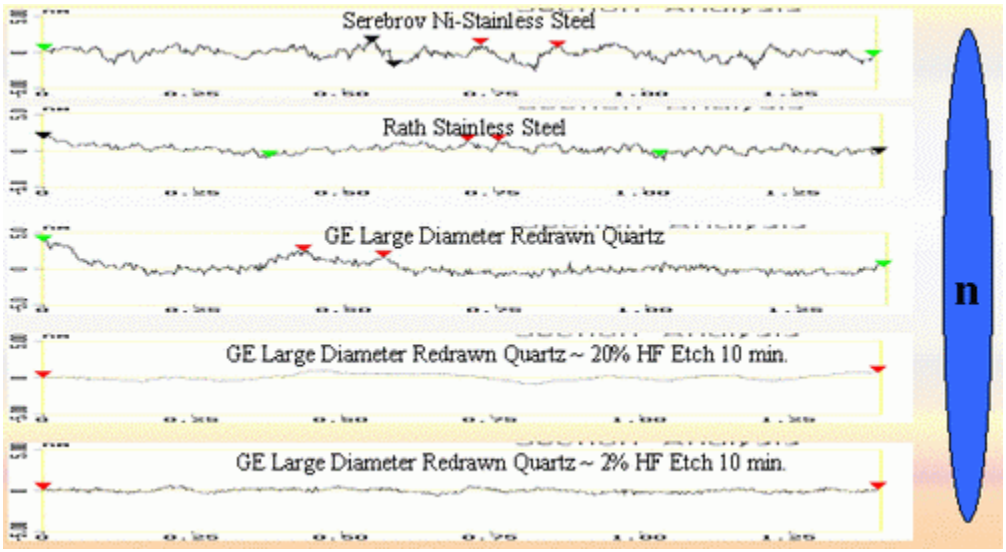

Figure 4-9 AFM tubing cross sections: This image shows a cross section of standard Serebrov ^{58}Ni coated stainless steel UCN guide and several tubes that are commercially available. The blue ellipse shows a 50 nm circle drawn to the distorted scale used in the cross sections. Each cross section is 10 nm full height and about 1.3 μm long.

Some of the parts used in the source development were coated with ^{58}Ni by thermal evaporation at Princeton; a test slide was made on a Si wafer and scanned with the AFM, [Figure 4-10]. The AFM results for the four scans are shown in Table 4-1; the roughness is due to the film since the Si wafer roughness in below 0.5 nm. The islands formed during the deposition are similar in size to the wavelength of a UCN, 50-100 nm.

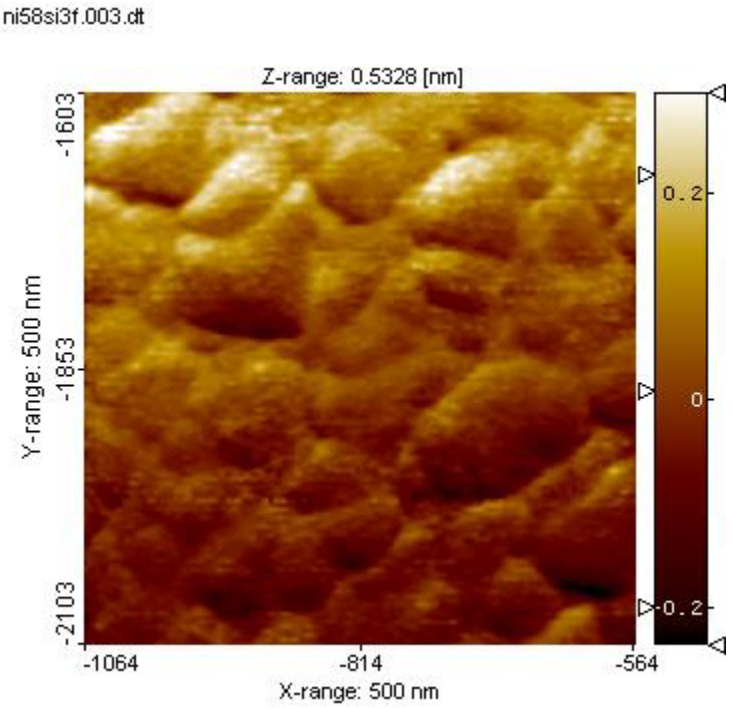

Figure 4-10 Evaporated ^{58}Ni film: Thermal evaporation like PLD DLC with a background gas is a low energy deposition process and the film exhibits preferential growth. The image is not a height map but rather a tip deflection map; deflection images usually show structure better than height images. The average peak to peak height is ~17 nm and the roughness is 1.85 nm. The image size is 500x500 nm^2.

AFM Scan Results for Evaporated ^{58}Ni				
Sample	Size	Roughness (nm)	Peak to Peak (nm)	5 P-P Average (nm)
Ni58si1f	1x1 μm^2	2.61	29.5	23
Ni58si2f	5x5 μm^2	2.92	59.9	48
Ni58si3f	0.5x0.5 μm^2	1.85	17.8	16.7
Ni58si5f	5x5 μm^2	2.74	35.4	30.6

Table 4-1 AFM scan results for evaporated ^{58}Ni: 5 P-P Average is the difference between the average of the 5 highest point and the 5 lowest. The 0.5x0.5μm^2 scan of Ni58si3f is shown in Figure 4-10.

4.5.4 The Effect of Surface Roughness on UCN Reflection and Loss

The effect of surface roughness on UCN reflection and loss has been studied by several authors with similar results[117, 118, 22, 23]. The treatment follows that of acoustic and electromagnetic wave reflection. The rough layer is assumed to be thin enough to be treated as a perturbation, that is the wavelength of the UCN in the material is much larger than the surface roughness. This is generally true of UCN guides, which are either mechanically and electrolytically polished or made of smooth glass where the average surface roughness is 1-3 nm and the UCN wavelength is greater than 50 nm.

The formula for the relative intensity of the non-specularly scattered wave is given as:[117]

$$I_{ns}(\theta_i,\theta_s,\phi_s) = \frac{3G}{2\pi} Cos\theta_i\, Cos^2\theta_s\, Exp[-\frac{w^2k^2}{2}(Sin^2\theta_i + Sin^2\theta_s - 2\,Sin\theta_i\, Sin\theta_s\, Cos\phi_s)]$$

$$G = \frac{4k^4\, w^2\, b^2}{3}$$

$$P_{ns}(\theta_i) = \int_{\theta_s}\int_{\phi_s} I_{ns}(\theta_i,\theta_s,\phi_s)\, Sin\theta_s\, d\theta_s\, d\phi_s$$

In the formula the wave is incident at angle θ_i (φ_i=0) relative to the surface normal and the diffusely scattered wave leaves at angle θ_s, φ_s. b and w are the average surface

roughness and correlation length and $k=2\pi/\lambda$. $P_{ns}(\theta_i)$ is the probability of non–specular scatter. These equations are only good for roughness below ~5 nm for UCN.

The probability of non–specular scatter is dependent on the guide surface and the incident UCN wavelength and angle. In general, the probability of non–specular scatter increases with the guides roughness and correlation length, while it decreases with increased wavelength and angle of incidence. Figures 4-11 and 4-14 show these affects for variations around a reasonable set of parameters: roughness average of 1 nm, correlation length of 25 nm, an 80 nm wavelength (~ 5 m/s), and a 45 degree angle of incidence. As shown in Figure 4-11 the roughness below 1 nm will greatly reduce non–specular scatter, while reduction in the correlation length of the guide surface has a lesser effect.

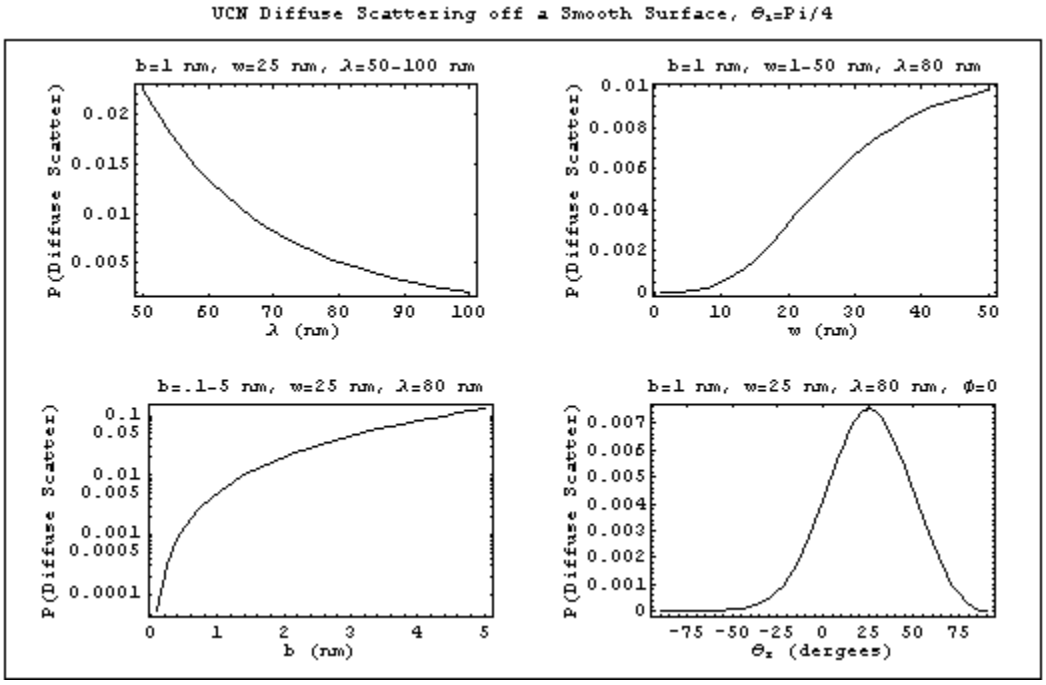

Figure 4-11 Probability of diffuse scatter at a 45–degree angle of incidence: Three of the plots show the effect of changing λ, w, and b on $P_{ns}(\pi/4)$; while the fourth shows the forward directed scatter at $\varphi_i=0$ using $I_{ns}(\pi/4, \theta_s, 0)$. The plot showing the effect of varying the roughness parameter b is on a log scale.

The effect of diffuse scattering on UCN transport through a guide system depends on where the UCN are scattered. If the scattering is distributed around the normal to the guide surface the chances of reaching the end of the guide system is greatly reduced. On

the other hand if the scattering is forward directed the UCN still has a good chance of reaching the end of the guide. Figures 4-12, 4-13 and 4-14 show the distribution of scattered UCN for different values of the guide parameters, incident UCN wavelength and angle.

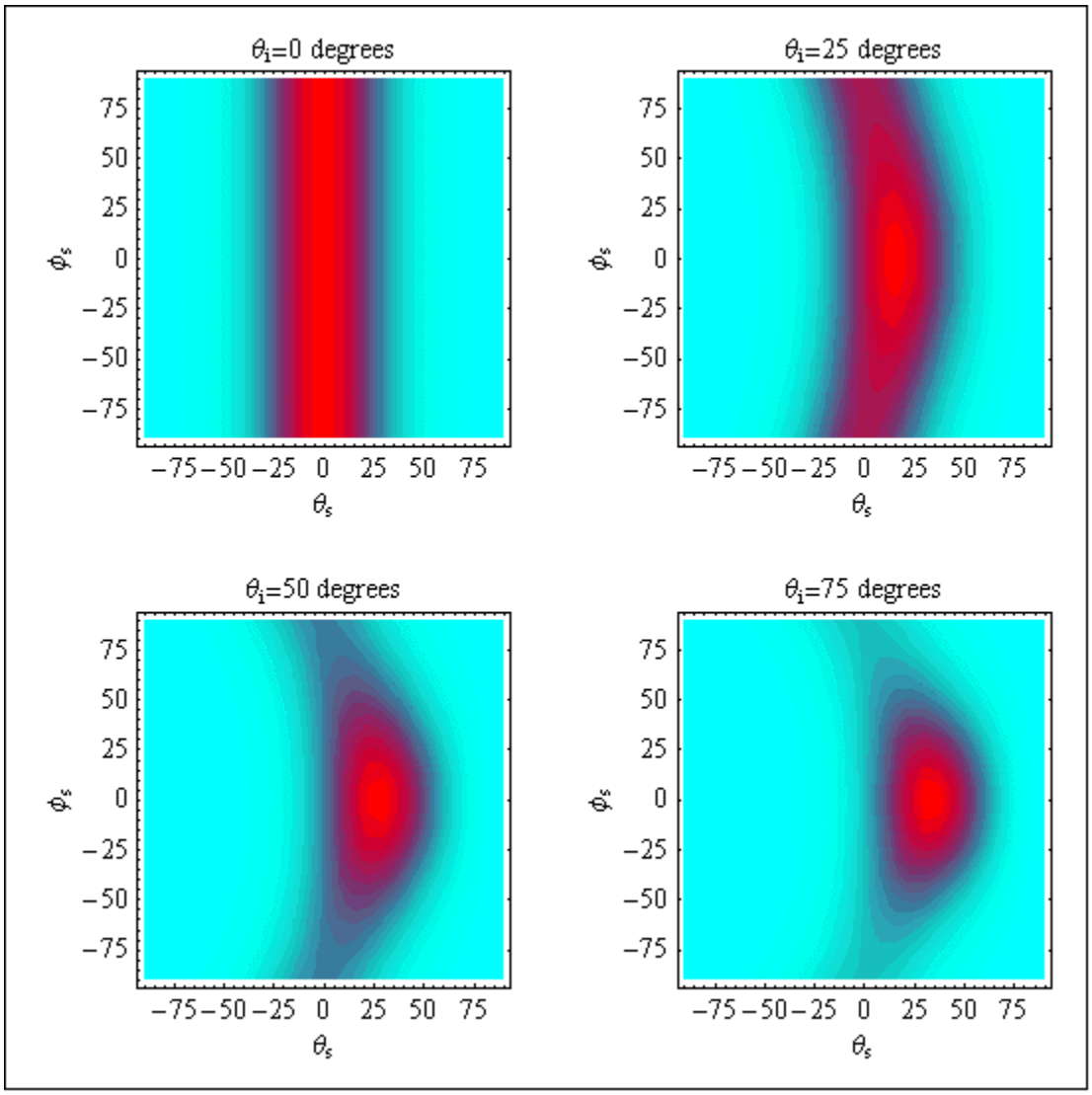

Figure 4-12 The distribution of scattered UCN for several incident angles: The plots show the distribution of diffusely scattered UCN with changing angle of incidence for b=1 nm, w=25 nm and λ=80 nm. The scattered UCN become more forward directed as the angle of incidence approaches the surface. The intensities of the contour plots are not related; Figure 4-14 shows that the intensity decreases as the angle of incidence approaches the surface.

Quartz tubing has a roughness below 1 nm after etching and a correlation length over 25 nm. Figure 4-12 shows the angular scattering distribution for UCN from a surface with these parameters. As the UCN become forward directed the diffuse part of the scattering also becomes forward directed, and the intensity decreases as shown in Figures 4-12 and 4-14. An increase in the correlation length also leads to a highly forward directed diffuse scattering, but the intensity of the scattering also increases [Figures 4-13 and 4-14].

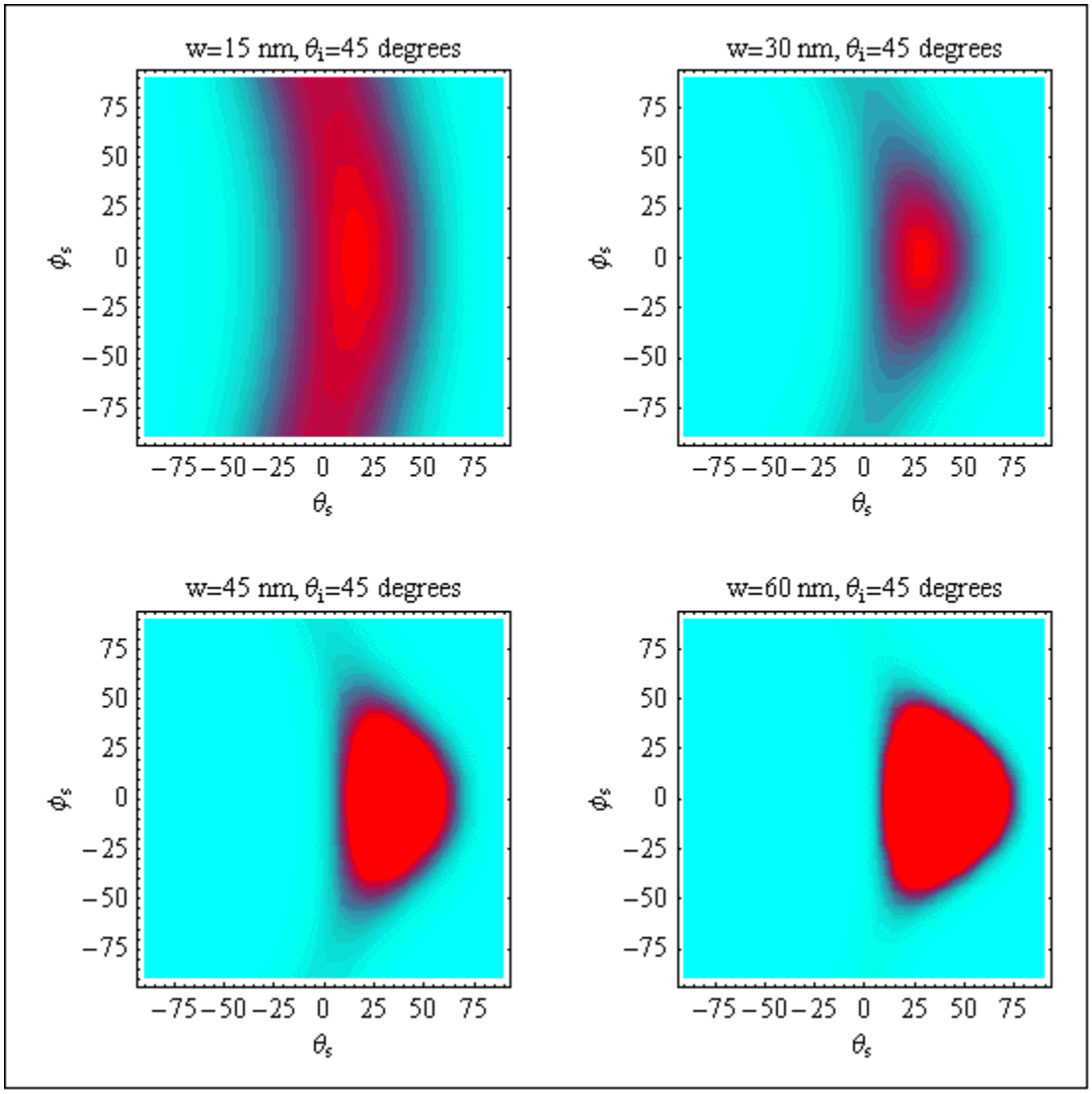

Figure 4-13 The distribution of scattered UCN for several correlation lengths: As the correlation length w increases the diffusely scattered UCN become very forward directed. These plots are for b=1 nm, θ_i=45 degrees and λ=80 nm. Referring to Figure 4-11 the intensity also increases with the correlation length. This does not show since the intensities of the contour plots are not related.

Scattering into the φ direction can increase losses in a circular cross section tube since this causes helical trajectories; helical trajectories are lossy due to an increased number of wall collisions. Rectangular cross section guides do not have this problem.

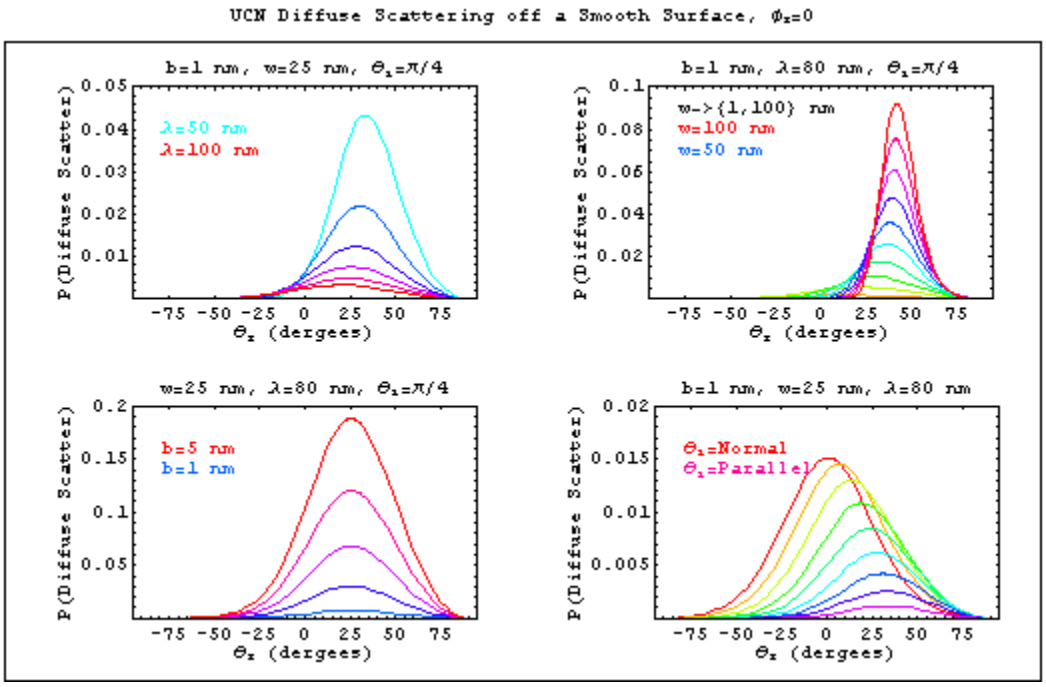

Figure 4-14 Forward directed (φ_s=0) scatter as a function of λ, w, b and θ_i: Increases in λ, w and θ_i increase the probability of a diffusely scattered UCN being forward directed. Increases in roughness lead to increased scattering without noticeable change in direction.

The roughness of a guide surface can also cause increased losses. If the roughness is assumed to be triangles, the surface area will increase by a factor of more than the square root of 2 for 45–degree slopes. The increased surface area holds more hydrogen and other impurities that can upscatter and absorb UCN. Roughness can also cause an increase in loss by absorption in the bulk material; this increase over a flat surface is due to a smoothing of the potential barrier. Using formulas derived by Igantovich and Luschikov the loss increase due to a rough surface over a smooth surface is at most 25%.[22]

4.6 Optical Ellipsometry

The optical properties of carbon films are very different for graphite and diamond and these differences can be used to test the diamond-likeness of a film [Figure 4-15]. As the amount of graphite increases in a DLC coating the extinction coefficient increases, this is seen as a darkening of the coating [Figure 4-16]. Optical ellipsometry can be used to find the optical properties of a solid, thin film or multilayer coating.

Optical ellipsometery was the most used tool in the development of the UCNA guide coating due to the availability, low cost and amount of information gained from a sample. Aside from the optical constants that show which films are more diamond-like and potentially better neutron reflectors, ellipsometery also gives a measurement of the film thickness. Calibration of the thickness is needed since the compressional stress increases with the film thickness until it delaminates; also, due to the large surface that needs to be coated, unnecessary thickness is wasted time and causes extra equipment wear.

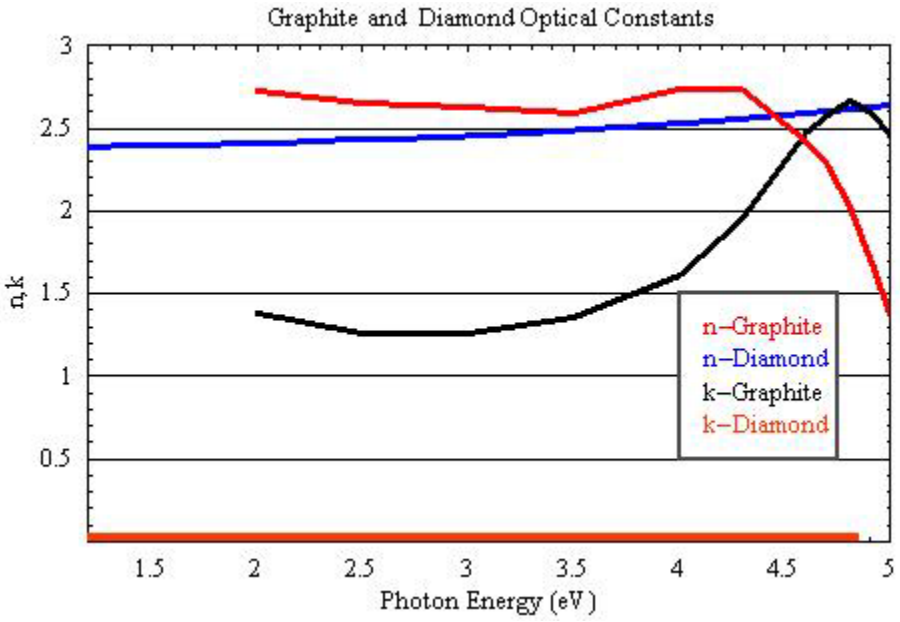

Figure 4-15 Graphite and diamond optical constants: This graph shows the differences between optical constants of graphite and diamond.[51, 119, 120] In general, diamond is a clear solid with a high index of refraction and graphite is a dark opaque material with a high index of refraction. The optical properties of both are relatively constant in the visible light region, but the optical constants of graphite change rapidly in the UV region around 5 eV.

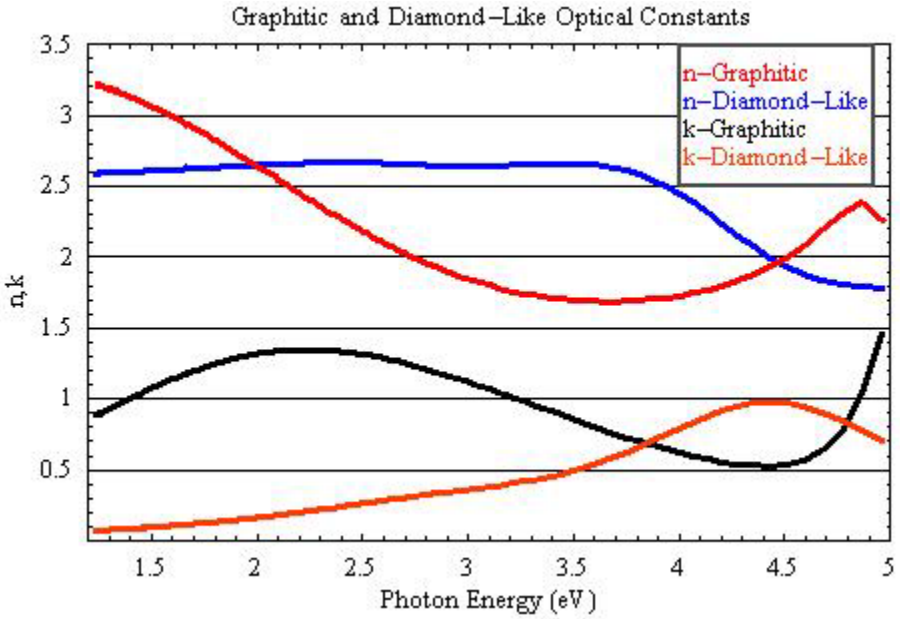

Figure 4-16 Graphite-like and diamond-like optical constants: These are optical properties of PLD DLC films made at low energy resulting in dark, low density films. The lower the deposition energy the more graphitic the films are. The diamond-like sample has optical properties similar to low temperature CVD DLC.

4.6.1 Basic Principle of Optical Ellipsometry

Optical ellipsometry is a non-destructive technique for characterizing thin films. Polarized light is reflected from the film surface into a detector that measures the resulting polarization. This data is then compared to that predicted by an optical model prepared by the data taker. When the real data and the data from the model agree to some level, the optical constants from the model are accepted as those of the sample. Typical information extracted from the model are film thickness, index of refraction (n), extinction coefficient (k), and sometimes surface roughness.

4.6.2 VASE Ellipsometer[121]

The ellipsometer used to study the PLD DLC films belongs to the MSE department. It is a Variable Angle Spectroscopic Ellipsometer (VASE) made by J. A. Woollam Co. The

light source is a monochromator that delivers 250-1000 nm wavelength light; the range 250 – 340 nm is usually very low intensity unless the bulb is new. Samples are mounted on a vertical plane and held in place with a vacuum chuck.

4.6.2.1 VASE Data[122]

The monochromatic light is polarized by a rotatable polarizer before being reflected from the sample. The light is reflected at an angle between 20 and 90 degrees from vertical through a spinning analyzer-polarizer and into a detector. The detector signal varies as the analyzer spins unless the light is circularly polarized. The intensity of this signal can be represented by Equation 4-1; A is the analyzer angle.

$$I_D \propto 1 + \alpha \cos(2A) + \beta \sin(2A) \qquad \textbf{Equation 4-1}$$

Using the relations from Equation 4-2 the optical parameters Ψ and Δ can be determined from the data; P is the polarizer angle.

$$\tan\Psi = \sqrt{\frac{1+\alpha}{1-\alpha}\left|\tan P\right|} \quad \cos\Delta = \frac{\beta}{\sqrt{1-\alpha^2}}\frac{\tan P}{\left|\tan P\right|} \qquad \textbf{Equation 4-2}$$

The Ψ and Δ from the data can then be related to those predicted by the optical model and are related to the Fresnel reflection coefficients by Equation 4-3.

$$I_D \propto 1 + \frac{\tan^2\Psi - \tan^2 P}{\tan^2\Psi + \tan^2 P}\cos(2A) + \frac{2\tan\Psi\cos\Delta\tan P}{\tan^2\Psi + \tan^2 P}\sin(2A) \qquad \textbf{Equation 4- 3}$$

4.6.2.2 Optical Modeling[122]

An optical model for the sample is needed to generate Ψ and Δ values to compare to the data. To do this the optical constants and layer thickness from the model are used to find the Fresnel reflection coefficients for each polarization[89]. These are converted to Ψ and Δ values with Equation 4-4 for comparison to the data; where the subscripts p and s stand for light polarized in the plane of incidence and perpendicular to it, respectively. The

WVASE32 software can find the optimal optical constants and thickness for the model and data supplied.

$$\frac{R_p}{R_s} \equiv \tan\Psi e^{i\Delta}$$ **Equation 4-4**

The optical model used to fit the PLD DLC films on various substrates is the Lorentz oscillator model[122, 123]. The Lorentz oscillator model is derived by treating the material as a set of harmonic oscillators coupled to the electric field of the incident light.[123] In general, a material can be treated as a mixture of several different oscillators.

The Lorentz oscillator function is related to the complex dielectric function in Equation 4-5, both are functions of photon energy (E_γ),

$$\varepsilon\left(E_\gamma\right) \equiv \varepsilon_1\left(E_\gamma\right) + i\varepsilon_2\left(E_\gamma\right) = \varepsilon_{1\infty} + \sum_k \frac{A_k}{E_k^2 - E_\gamma^2 - iB_k E_\gamma}$$ **Equation 4-5**

where $\varepsilon_{1\infty}$ is a positive, real valued, dimensionless constant, and A_k, E_k, and B_k are positive, real valued constants that have the dimension of energy. Since the complex dielectric function is related to the complex index of refraction by $\varepsilon_1\left(E_\gamma\right)+i\varepsilon_2\left(E_\gamma\right)=\left(n+ik\right)^2$, $\varepsilon_1\left(E_\gamma\right)=\varepsilon_{1\infty}=n^2$ when the film has no absorption. This can be a useful starting point for fitting parameter $\varepsilon_{1\infty}$. A_k is the amplitude of the oscillator. E_k is the position of the oscillator or absorption peak. And, B_k gives the absorption peak width. The WVASE32 software that is used to analyze the data allows up to seven oscillators per layer in the model, so k in the summation can be from zero to seven.[124]

Other models can also be used, but standard ones like the Cauchy model can be represented by a Lorentz model. A new model that is not included in the VASE software is designed for semicomductors like DLC[125, 90]; this Tauc-Lorentz model can be defined in the VASE software and compared to the standard one used. This has not been fully implemented yet.

4.6.3 PLD DLC on Si Wafer Model

A three oscillator model is used for the Si wafer without an SiO_2 layer, since the wafer is usually etched first. The PLD layer is usually fit well with a two oscillator model. The table shows typical parameter values for Si wafer and two different DLC films

Sample	oscillator	$\varepsilon_{1\infty}$	A_k	B_k	E_k
Si wafer	1	2.271600	23.470000	0.437700	3.663000
	2		19.870000	0.258900	3.401000
	3		102.500000	0.772800	4.205000
PLD Tube	1	2.627300	107.300000	5.618000	4.947000
	2		1.487000	2.127000	2.125000
Fg57	1	4.359000	33.792000	0.001000	5.349000
	2		1.835800	1.324000	3.064200

Table 4-2 Parameters for Lorentz oscillator models:

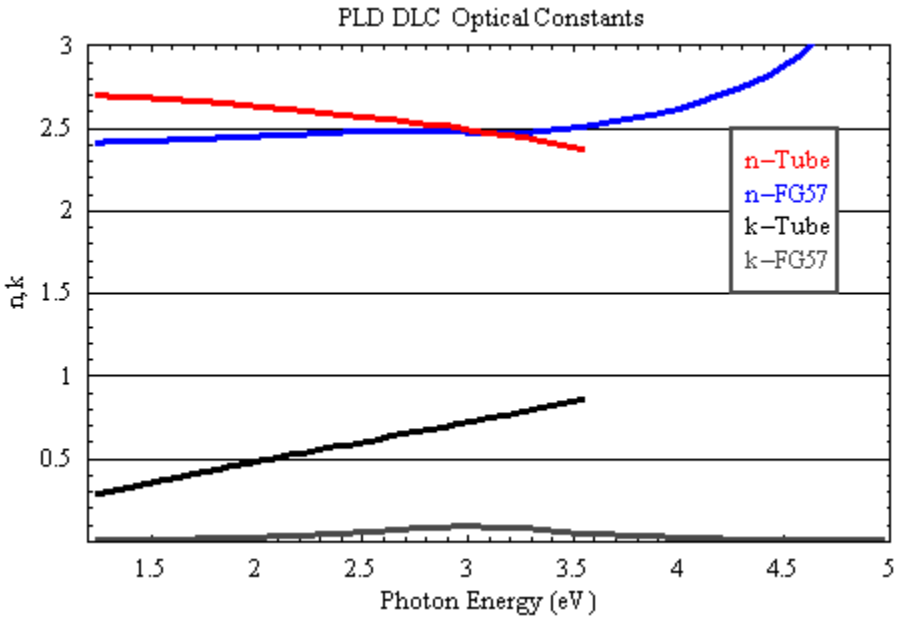

Figure 4-17 PLD DLC optical constants: The "Fg57" sample has more diamond-like properties than the "PLD Tube" sample.

The large amplitude and width of the oscillator at 4.9 eV in the "PLD Tube" model results in the large and increasing extinction coefficient seen in Figure 4-17. The slight rise in extinction coefficient [Figure 4-17] of the "Fg57" model is from the oscillator at 3 eV [Table 4-3]. In general, the n and k values for the "Fg57" model are much more diamond-like than the "PLD Tube" model and the film appears much clearer to the eye.

4.6.4 Float Glass Modeling

The PLD DLC samples for neutron reflectometry were made on float glass – very flat glass that has floated on molten tin. The resulting glass has optical constants that change with depth due to diffusion of the tin into the sample. The modeling of the float glass used for the reflectometry studies was difficult. There is a lot of literature about using ellipsometry to study float glass, but this float glass seems to have been old, so the surface was further changed by aging.[126, 127, 128, 129, 130, 131, 138] The best model was a bulk layer with a single Lorentz oscillator and a surface layer with two or three oscillators. Sample "Fg57" was modeled on this type of a substrate.

4.6.5 Sample 25 Modeling

Sample 25 is a Si wafer with six different energy depositions on it, also included for comparison are a "Fg57" and a sample made with nitrogen atmosphere and a – 300 Vdc bias. The index of refraction values for all but the low energy deposition are decreasing with energy in a uniform way; this trend shows the films to be more diamond-like with higher deposition energy. The 50 mJ sample does not look like diamond or graphite, this is what was seen for all low energy depositions. Although the trend is in the correct direction, even at 1000 mJ per pulse, the index of refraction is always above 2.5, whereas the "Fg57" sample that was deposited at 300 mJ is below 2.5 until ~3 eV, much like the diamond graph [Figure 4-18].

This difference is because "Fg57" had a much shorter focal length lens system giving a much better and smaller focal spot. Sample 25 was made with a 33 cm focal length lens and due to the divergence of the laser this gives a spot that has a halo of lower energy density around it. As the laser pulse energy is increased this halo starts to ablate more

material so the resulting deposition is a mixture of low and high–energy carbon. This effect can be lowered by masking off part of the beam or using a shorter focal length lens. The other way to fix this is to use lower divergence laser cavity optics. This beam divergence seems to be one of the variables that causes differences between various published works. The ion probe can be used to minimize this problem by changing the mask or focus to get a narrow ion peak at the desired energy.

The N_2 biased sample is very different from the other films. It has a glassy black appearance and does not delaminate. The index of refraction is very low compared to the other films, but the extinction coefficient is about the same.

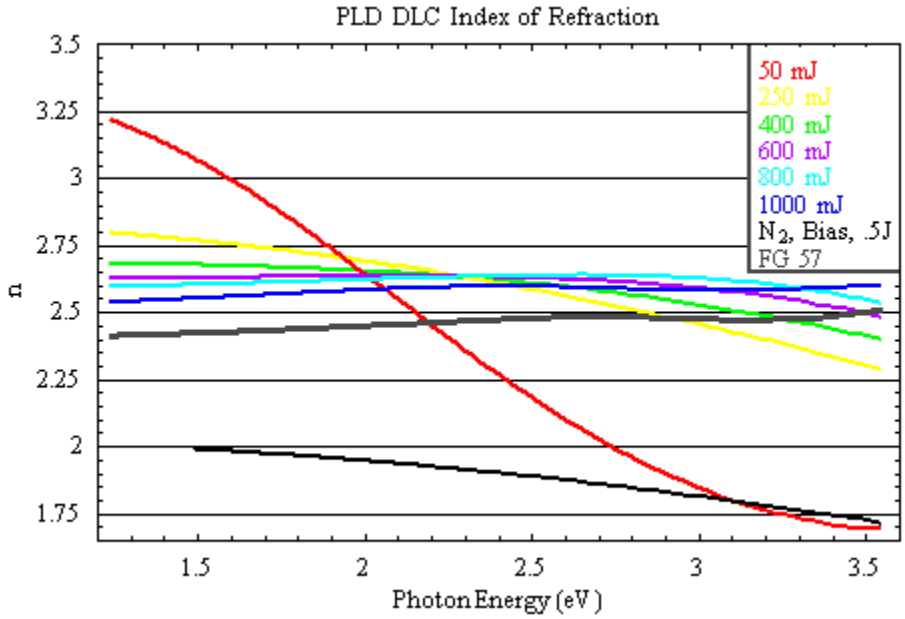

Figure 4-18 PLD DLC index of refraction: The samples have more of a diamond-like index of refraction with increased deposition energy. The CN film has a much lower index of refraction; it is not like diamond or graphite.

The extinction coefficient of the sample 25 films is going down until the laser energy reaches 1000 mJ [Figure 4-19]. This is an indication that the best deposition energy is probably around 800 mJ since the film is the most diamond-like there.

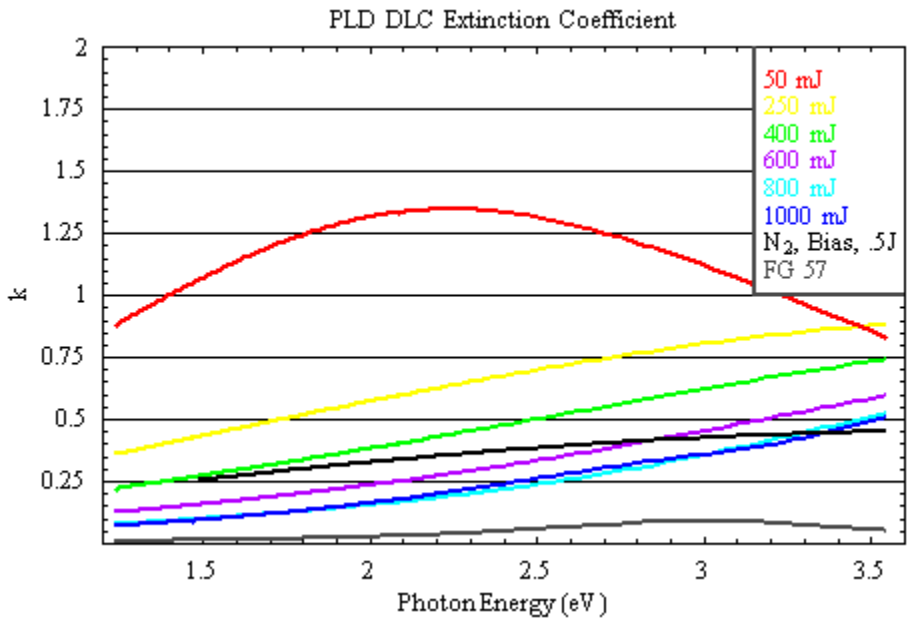

Figure 4-19 PLD DLC extinction coefficients: The extinction coefficient decreases with increased deposition energy. The CN film behaves similarly (unlike with the index of refraction).

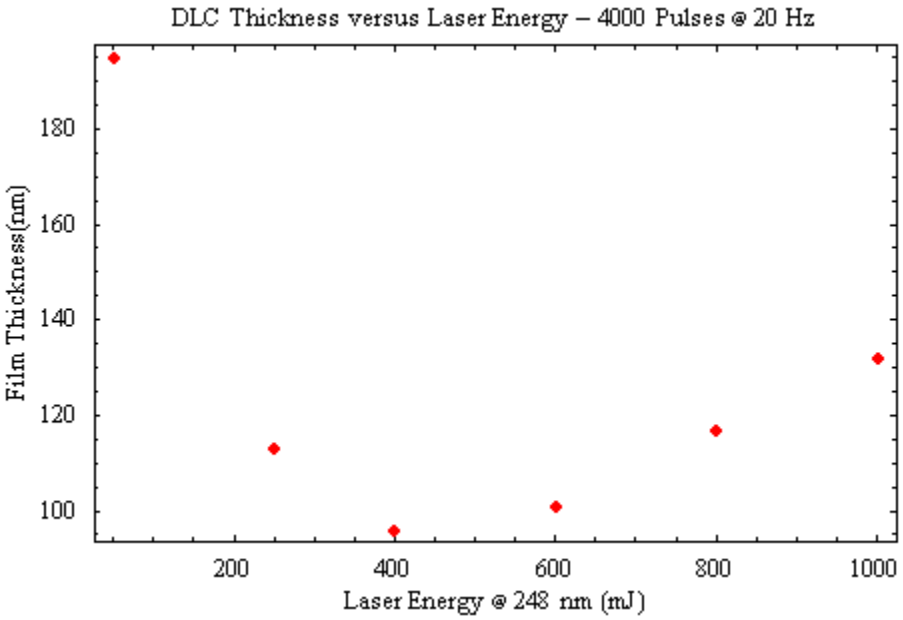

Figure 4-20 DLC thickness versus laser energy – 4000 pulses @ 20 Hz., 5.5 cm target to substrate: The minimum in the film thickness is due to the increase in density of the coating which is countered by the increasing amount of ablated material. The density may also start to decline at higher energies due to increased particulate and disorder in the coating.

The film thickness for a set number of pulses is dependent on two things: the amount of carbon deposited and the density of the film [Figure 4-20]. The low energy deposition makes a thick low-density film. As the film density increases the thickness goes down. The increase in thickness at higher energies could be due to the increased amount of ablated material or the lowering of density due to the low energy halo and increased disorder in the coating from the higher-energy ions. The increased disorder due to the high–energy ions could also cause an increase in the extinction coefficient.

4.6.6 Conclusion

In general, ellipsometry showed the film made at VT were similar to the ones in the literature and that with increased energy they became more diamond-like. Ellipsometry also showed the need to lower the amount of halo around the beam. The only method for doing this at a long focal length is masking off part of the beam.

In general, the films made with nitrogen atmospheres were not dense. This was determined by the thickness found from ellipsometry and the number of pulses.

4.7 Neutron Reflectometry

The best tool for checking the neutron reflectivity of a coating is a neutron reflectometer. For single component films like DLC a neutron reflectometry study will give information about the coating's density, thickness and roughness.

4.7.1 Basic description of SPEAR and neutron reflectometry

The Surface Profile Analysis Reflectometer (SPEAR) is located at the Los Alamos Neutron Science Center in the Lujan Center.[132] SPEAR is primarily used to study surfaces by finding the grazing angle that total reflection occurs at. The intensity of the reflection around the angle of total reflection is fit to a model to determine the material properties of the sample. The neutron wavelength is resolved by time of flight, since the neutron source is a pulsed spallation target. This means the sample does not have to be rotated as it does with a monochromatic beam.

4.7.2 Sample Prep

SPEAR has a wide beam, so to take advantage of this the samples need to be large. For this reason the samples were made on 2 x 2 inch float glass. Prior to coating, the float glass was cleaned with windex, acetone, ethanol and DI water. They were then dipped in Buffered Oxide Etch, rinsed in DI water and dried with Argon. Part of the samples were on 3/16 inch float glass and the other were on ¼ inch float glass. All of the ¼ inch samples were coated on the same side, which was probably the tin side.

The first set of samples coated were on 3/16 inch float glass squares. The laser beam reflected off one mirror then went through a 33 cm focal length lens and the vacuum chamber window before hitting the rotating target. The optical energy that reached the target was 34% of the reading on the laser. The focus of this system was about 1x2 mm with a strong halo; as a result the power density is not a very accurate measure. The target to substrate distance was 7 cm. These samples were numbered 39-49.

The second set of samples were coated using the same setup with the addition of a second lens. This provided a much better focus so the power density should be more accurate. These samples were on ¼ inch float glass and a blank sample was included in the samples to be measured. The target to substrate distance was ~5 cm and the vacuum pressure was 2-4x10^{-5} torr. These samples were numbered 54-61 with 61 being uncoated.

4.7.3 Modeling Neutron Reflectometry Data[74]

Reflectometry data is used to create a model that represents the neutron reflecting properites of the sample. This is done about the same way as modeling in optical ellipsometry. The neutron is treated an incoming wave with its DeBroglie wavelength given by $\lambda_n = \frac{h}{p} \approx \frac{4x10^{-7}}{\mathrm{v}}$ (v in m/s). The index of refraction of the material is given by $n = 1 - \frac{\lambda_n^2 Na}{2\pi} - i\frac{\lambda_n N\sigma}{2\pi}$, where σ, N and a are the absorption plus incoherent scattering cross section, the density of nuclei and the bound coherent scattering length respectively. The index of refraction is generally less than one so total reflection is

possible. For a bulk sample the angle of total reflection is given by $\theta_c = \sqrt{\frac{Na}{\pi}}\lambda_n$. This point is easy to see for a smooth bulk sample but if the sample is layered it is not possible [Figure 4-21]. Reflectivity plots are usually made as a function of $Q = \frac{4\pi \sin\theta}{\lambda_n}$ rather than the incident angle as in Figure 4-21 and the other plots in this section. Figure 4-21 shows a periodicity in the decaying reflection for the thin diamond films on float glass. This is due to interference since the wavelength is comparable to the film thickness.

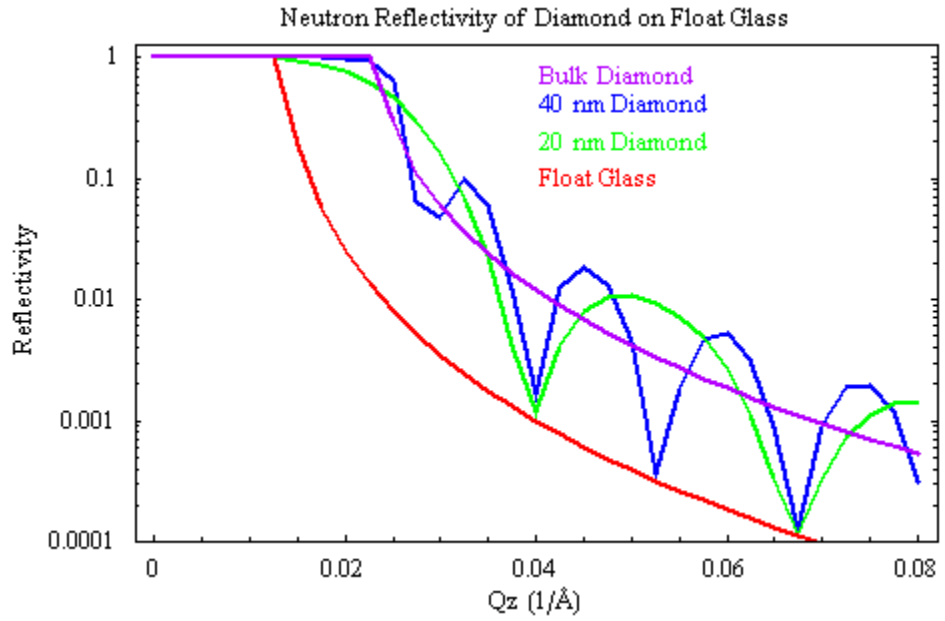

Figure 4-21 Neutron reflectivity of diamond on float glass: The reflectivity of a layer of diamond on float glass depends on the thickness.

The model used to represent a sample is called a scattering length density (SLD) profile. To model the wave reflected off multiple layers the Fresnel reflection is found for the set of layers.[133] There is locally developed software on the SPEAR computer to model and fit the data, but due to ease of use most of the analysis was done with Parratt32 software.[134] For an overview of modeling and fitting reflectivity data see Parratt and Russell.[133, 135]

4.7.4 Results

The fit to the substrate needs to be good so that in later fits the sample layer parameters do not help fit the substrate. The ideal substrate would have a uniform density and be very flat and smooth. Freshly etched Si wafers are like this, but due to the stress of the coating it would have to be rather thick to stay flat; this increases the cost by a large amount. Float glass was used since it is inexpensive and highly available. The SLD profile of float glass is complex and different for the each side. From the literature both surfaces have impurities that decrease in concentration with depth[136, 137, 138, 139, 140, 141]. As the glass ages it takes on water, which also affects the SLD of the surface.[138] With the literature as a guide, the float glass was modeled as a bulk material with a less dense surface layer [Figure 4.22]. Some roughness was added and the result was a very nice fit to the data, [Figure 4.23].

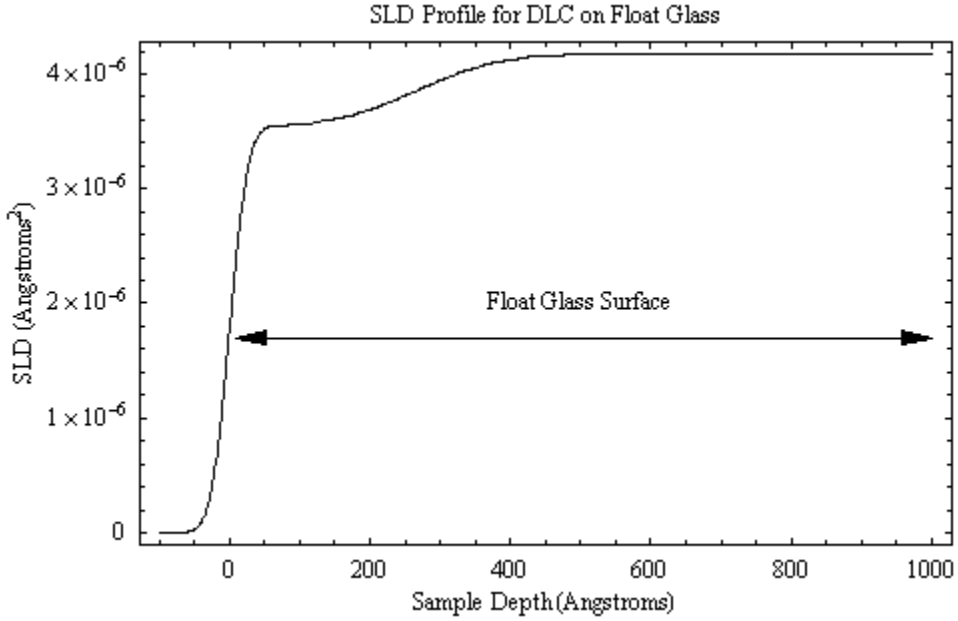

Figure 4-22 SLD profile for float glass: This profile has a decreasing density near the surface of the float glass. The decrease is due to impurities near the surface.

To model the DLC samples several different approaches were tried. The simplest is to fit the data with a bulk layer, this is shown in Figure 4-24. The data fits between the curves for graphite and diamond and the best fit is an SLD of 1.004E-5 $Å^{-2}$. This corresponds to a critical velocity of seven meters per second. To fit the periodic part of the data a layer or layers need to be added to the float glass model.

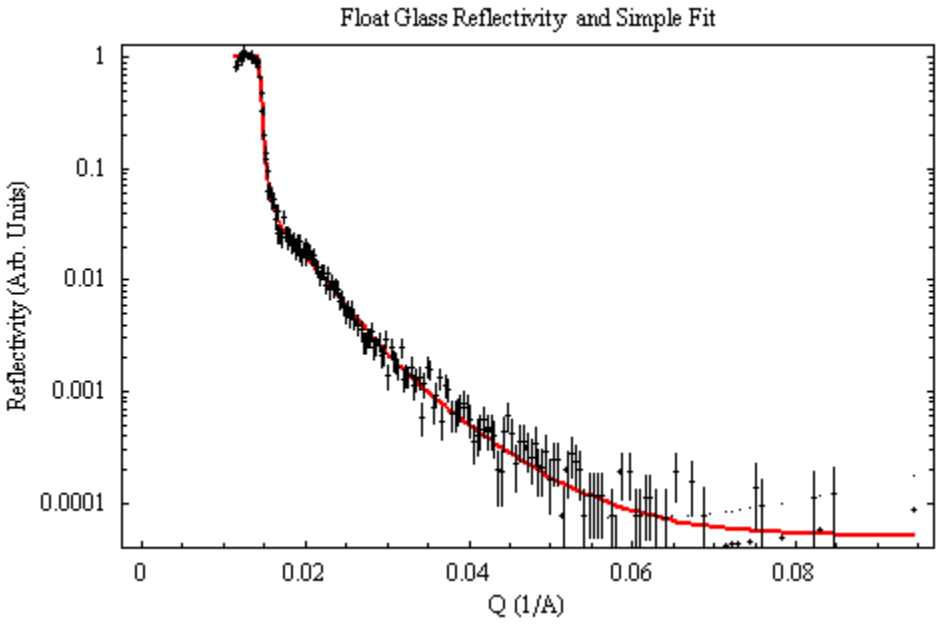

Figure 4-23 Float glass reflectivity and simple fit: The red line is the reflectivity for the model SLD profile in figure 4-18. The data taken on SPEAR is in black.

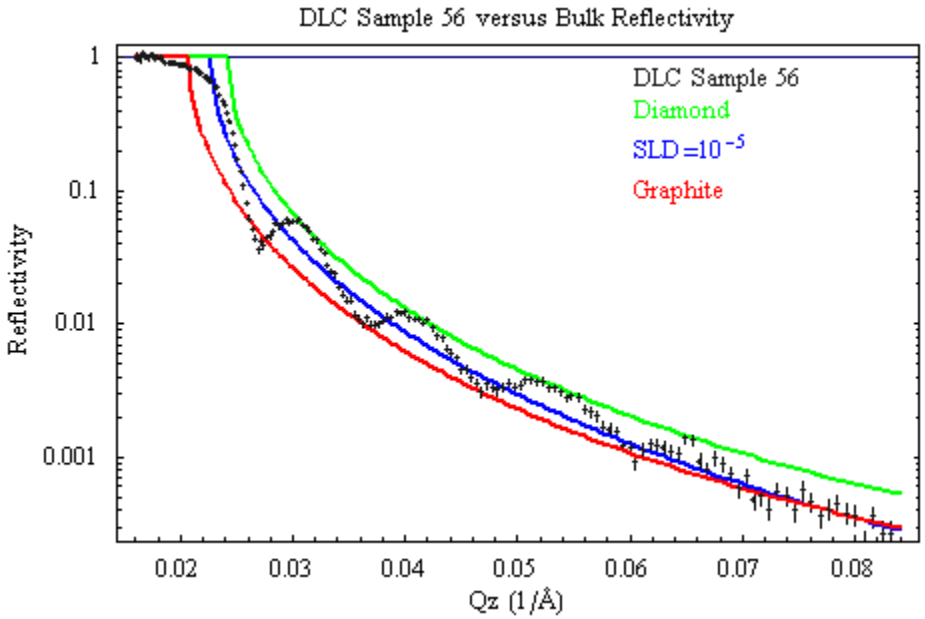

Figure 4-24 DLC sample 56 versus bulk reflectivity: The black data for sample 56 is bracketed by the reflectivity for graphite and diamond. The periodic nature of the data is due to the layer thickness.

A simple one layer model with some roughness was fit to all the samples. The results are shown in Figure 4-25 along with data points for glassy carbon, graphite and diamond. The data is grouped to show trends. The first group shows the effect of increased laser

energy with a poor focus. The second group shows the decrease in critical velocity with increased nitrogen pressure in the vacuum chamber. The fourth group shows the increase in critical velocity with laser energy with a good focus. Adding interface layers to this single layer results in better fits.

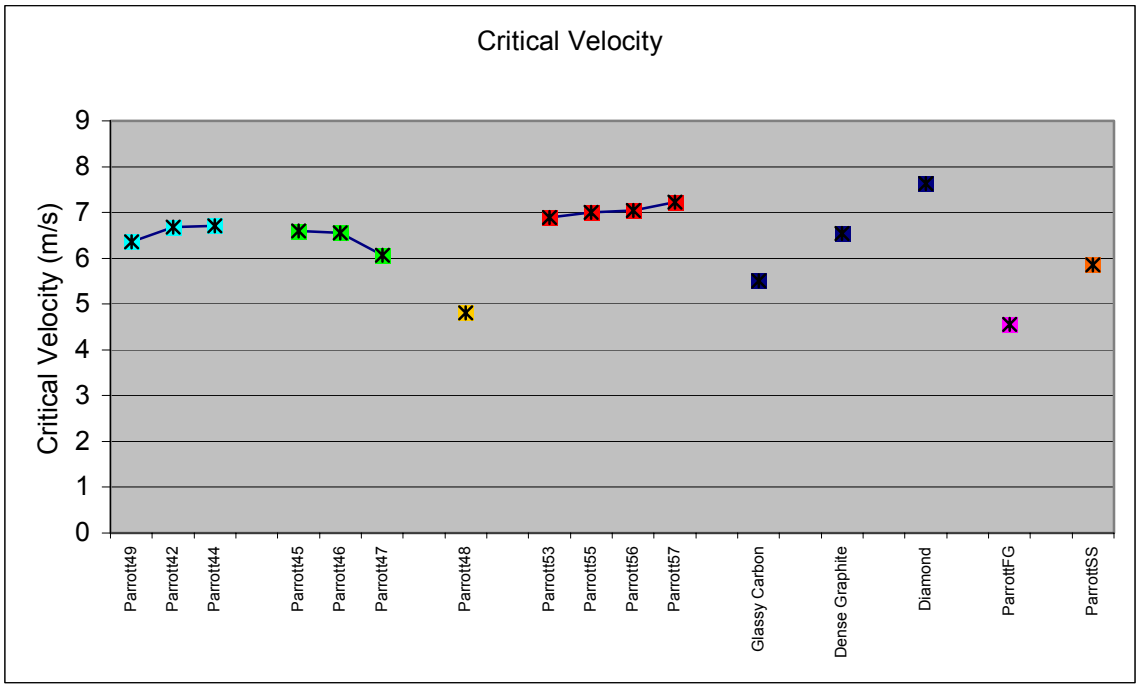

Figure 4-25 Critical velocity of PLD DLC tests: The first series (light blue) is in vacuum with increasing laser energy; the laser spot is fairly diffuse. The second series (green) shows the effect of increasing the nitrogen background gas pressure. The very low critical velocity coating (yellow) is the result of ~$5x10^{-2}$ N_2 with a biased substrate. The series with the highest critical velocity series (red) was made in vacuum with a short focal length lens system resulting in a sharp laser spot; further increased laser power may have resulted in even higher critical velocity. Ideal carbon critical velocities (blue) are shown for comparison. And the final two data points are the float glass substrate and a Sandia sample respectively.

If an interface layer is added between the float glass and the DLC layers the fit of the data is greatly improved, see Figures 4-26 and 4-27. Adding a similar layer on the air side of the DLC is not as effective and only improves the fit a little if used in conjunction with the float glass interface layer. Better fits of the data are possible, but several different layer systems give about the same result. By making a model that is derived from the literature about PLD DLC a little more confidence can be gained.

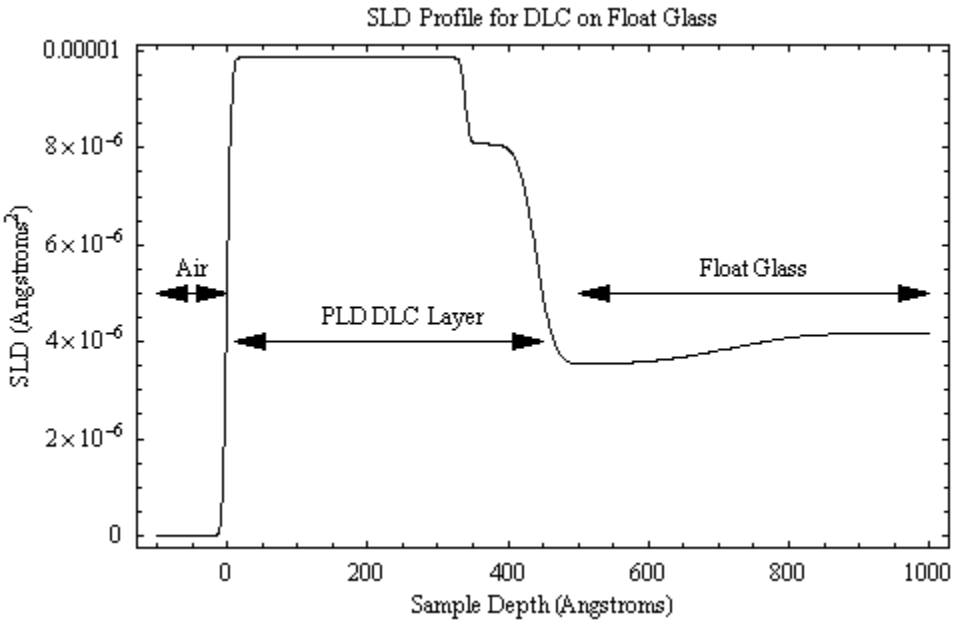

Figure 4-26 SLD profile for DLC on float glass: This simple model of DLC on float glass has a region of reduced scattering length density reflecting the disordered interface between the glass and the bulk of the film.

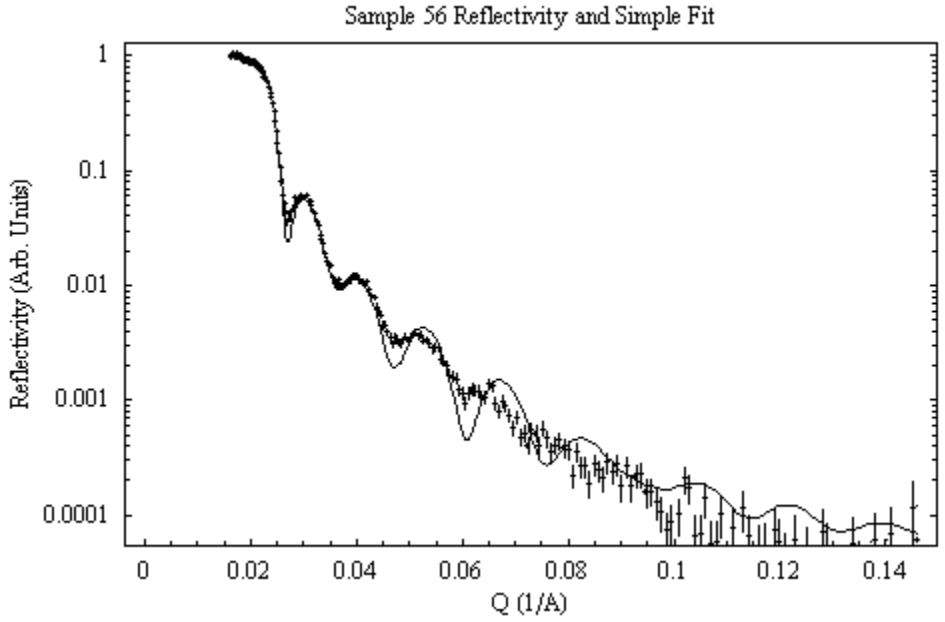

Figure 4-27 Sample 56 reflectivity and simple fit: The fit of the model in figure 4-22 is fairly good, but it is not complete.

Articles by the Sandia group show that PLD DLC films have structure and that this structure changes with deposition energy[142, 55]. Their work shows low energy films to have 3 distinct layers: a low density interface to the substrate, a higher density central

region and a lower density surface. At higher laser energies a fourth layer appears which has very high density; it is located between the interface layer and central layers. A multilayer model was made that incorporated this structure information, [Figure 4-28], and the fit to the high–energy deposition film "Fg56" was very good [Figure 4-29]. The best fit model has a layer with density greater than diamond.

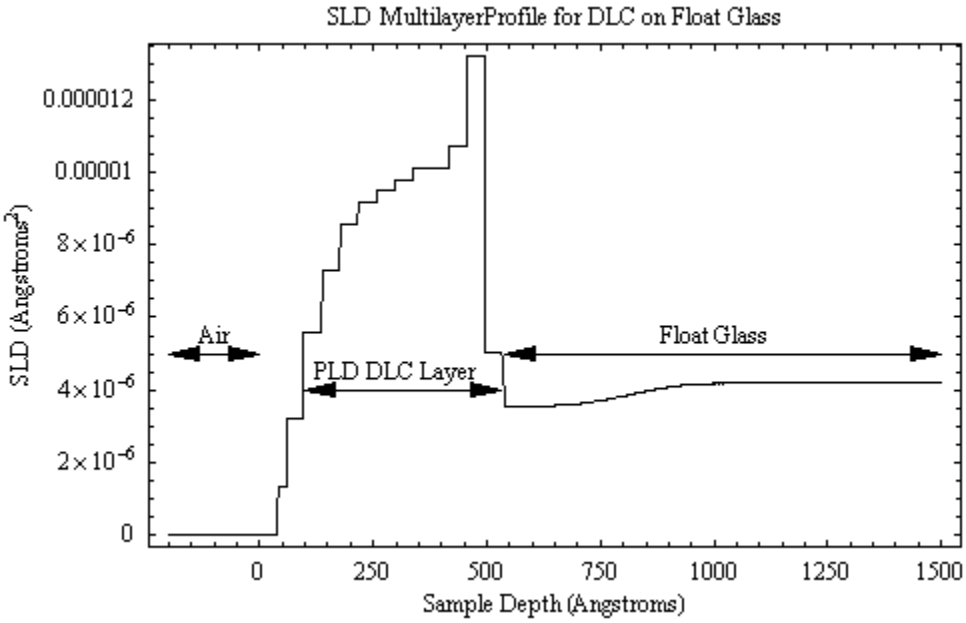

Figure 4-28 SDL multilayer profile for DLC on float glass: This model is inspired by the literature.

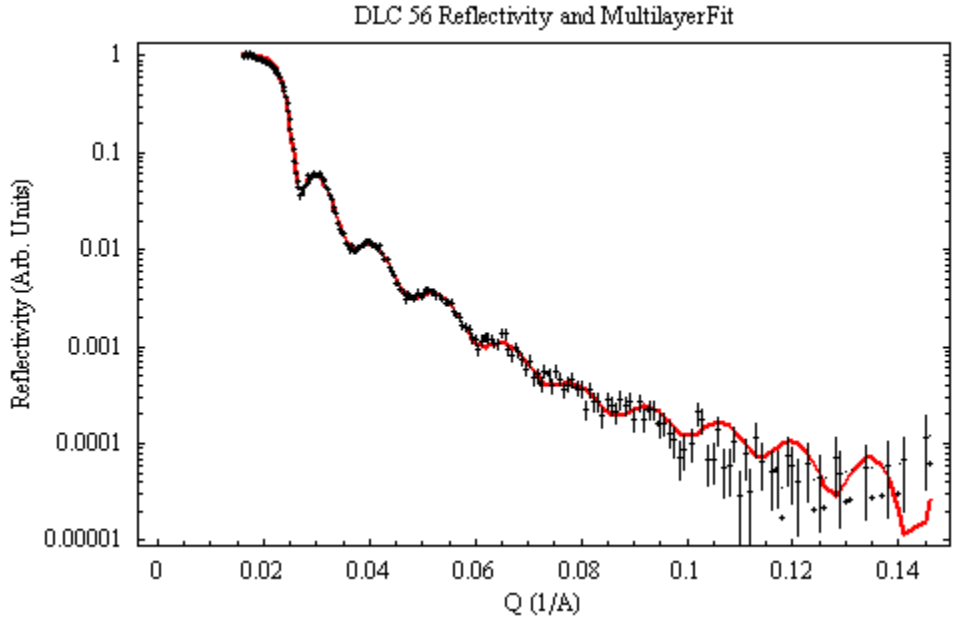

Figure 4-29 DLC 56 reflectivity and multilayer fit: The fit of the model in figure 4-24 is very good and more data would be needed to go farther.

One of the most useful relations to get from the neutron data is that between laser energy and the resulting critical velocity of the coating. The samples 54-60 were made with a good focus and similar vacuum conditions. Unfortunately there was not time to get data on all the samples. The trend shown in Figure 4-30 shows the critical velocity increasing with laser energy. This could probably only continue to 7.5 m/s unless some of the super dense carbon seen by N. N. Matyushenko et al. is deposited in the film[81]. The work by the Sandia group does seem to say this is possible[142, 55]; as does some of my modeling. This appears to be an area that could use another study with neutrons and also x-rays to determine the structure and density of the PLD LDC as a function of laser energy.

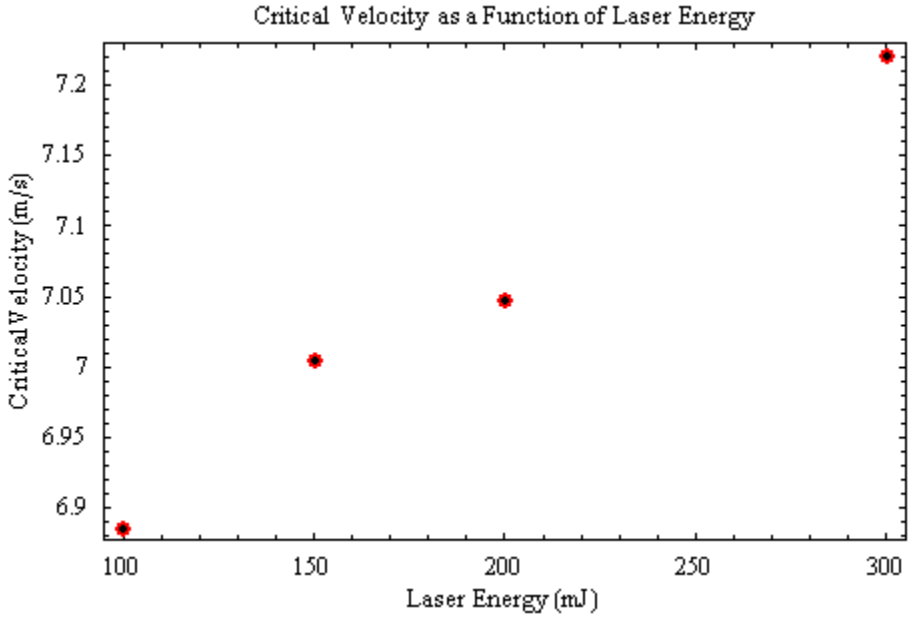

Figure 4-30 Critical velocity as a function of laser energy: The four samples of this series ("Fg53", "Fg55", "Fg56", "Fg57" the red series in Figure 4-25) show an increasing critical velocity with laser energy. There were several other samples in this series at higher energies but there was not enough time take data on them.

4.8 Raman Spectroscopy

The Raman spectra of diamond and graphite are very different and this makes Raman spectroscopy a good tool for studying carbon films. Crystalline diamond has one peak at 1332 cm^{-1} while single crystal graphite has one peak at 1580 cm^{-1}. This is complicated when disorder is added to the graphite crystal, which causes a second peak at 1350 cm^{-1}.

As DLC coating become amorphous the peaks become very wide and shift, but there is still a lot of information that can be obtained from careful analysis.

Raman spectroscopy is sensitive to the small changes in DLC coatings and has been used to show the effects of heating and cooling. During heating in vacuum the DLC films begin to turn into graphite films. This effect is not seen in hydrogen–free films until above 600 C^{o} [108, 113, 143]. By rapidly cooling the coating delamination can occur, this relieves some of the stress in the film and this can be seen by the shifting of the Raman peaks[111].

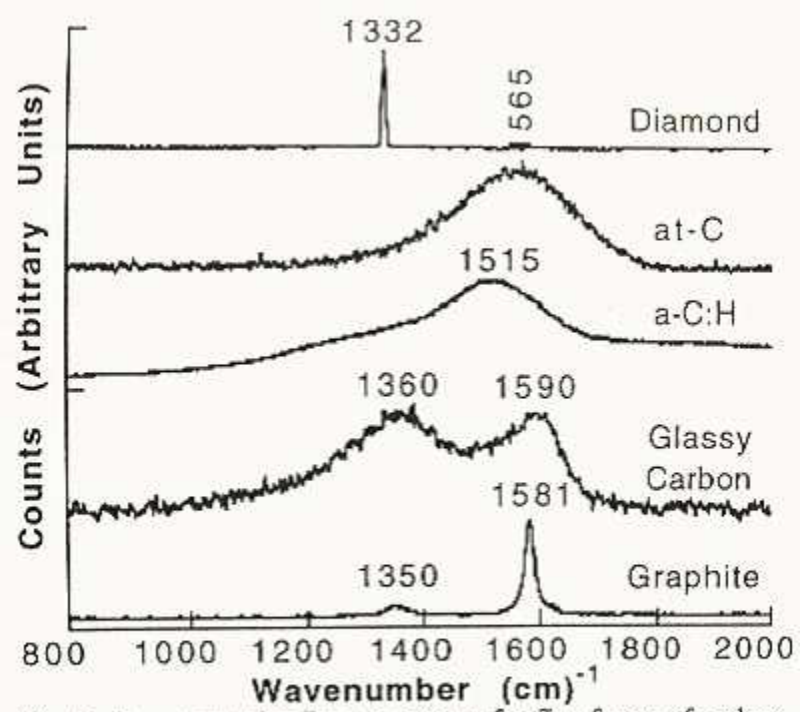

Fig. 2 Representative Raman spectra for five forms of carbon. Note the difference in peak position and shape between the at-C and a-C:H spectra.

Figure 4-31 Raman spectra of several carbon forms: This image shows the diamond, graphite and glassy carbon Raman spectra in comparison to vacuum PLD DLC (at-C–amorphous tetrahedral carbon) and hydrogenated DLC (a-C:H–amorphous hydrocarbon).[71]

When looking at Raman spectra of DLC the excitation wavelength should be taken into account. The disordered and graphitic modes are more active than the diamond-like

modes in the IR and visible spectra; the diamond-like modes become very strong in the UV range[144, 145, 54].

Only one set of VT made PLD DLC was tested by Raman spectroscopy. This was done on a Raman system in the Geosciences Department at VT. The scans are shown in Figure 4-32. The excitation wavelength was 514 nm, which is the most common in the literature. Although the basic shape agrees with spectra in various articles the relative intensity between the vacuum and nitrogen atmosphere deposited films is reversed, compare to Figure 4-33.[71]

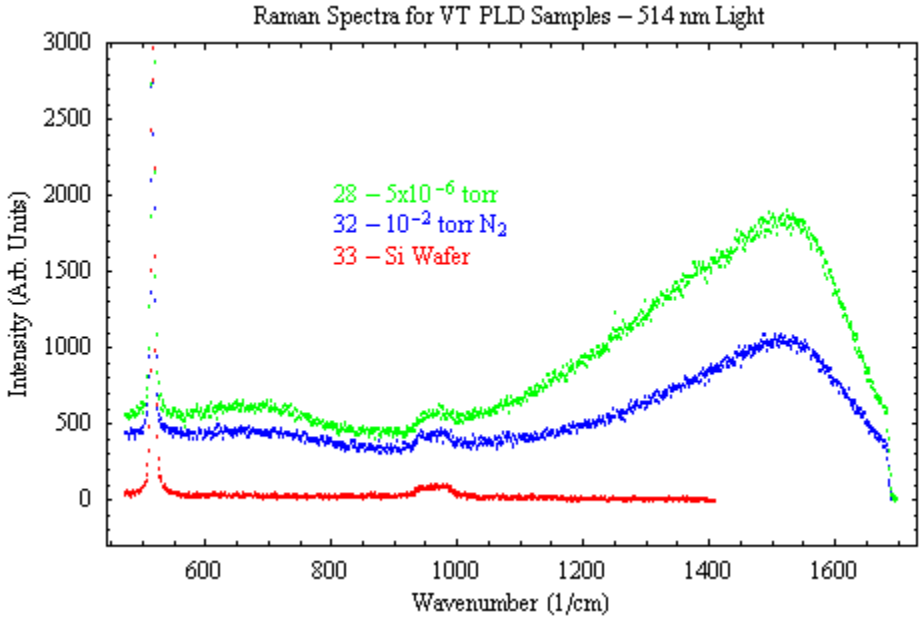

Figure 4-32 Raman spectra for VT PLD samples – 514 nm light: The Raman spectra of the Si wafer is present in the other two spectra since the laser penetrates the thin film and interacts with the Si wafer substrate. The height of the major peak should be reversed; that is the N_2 background peak should be higher.

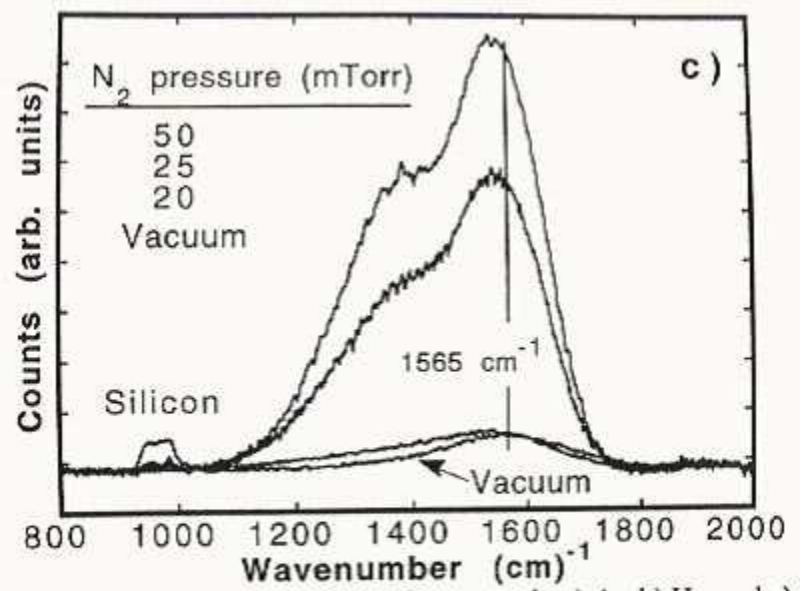

Fig. 5 Raman spectra for samples grown in a) Ar, b) H_2, and c) N_2 background ambients. Note that the spectrum for the sample grown in vacuum is plotted with the same intensity on each graph.

Figure 4-33 Raman spectra for PLD deposition in background gases: This graph is of the same type as figure 4-28, but from the literature. The peak grows with increased nitrogen pressure.[71]

4.9 X-ray Scattering, Diffraction and Reflectometry

4.9.1 Setup and Data

Samples for x-ray diffraction were made on n-type Si wafer that was cleaned with acetone, alcohol and DI water; they were also etched in BOE. The series, samples (28-32) were made with varying laser energy and amounts of nitrogen background gas. Part of the laser beam was masked off with an aluminum aperture so the energy reaching the target was reduced. These samples are similar to the 40 series used for neutron reflectometry. The laser power and nitrogen pressure are shown on the plot [Figure 4-34].

The old x-ray diffraction machine in the Geosciences Department at VT was used to take the data. The machine was set up for powder diffraction so to be able to do thin films special holders were made out of Delrin[tm]; they replaced the powder holder. For a reference one piece of wafer was covered with corundum (Al_2O_3) powder and one was

left bare. The corundum peaks were shifted by 0.03 Å, which does not affect the plots in figure 4-34, since the peaks are so broad.

The PLD DLC films are thin and carbon has a low cross section for scattering x-rays. As a result the Si wafer provides most of the signal in the data. To see the effect of changes in the film the Si wafer scan is subtracted from the PLD DLC scans. The mass attenuation coefficients (μ/ρ) for C, N and Si are 4.576, 7.562, and 64.68 cm^2/gm for 1.5418 Å x-rays [146]. The drop in intensity from passing through the carbon can be calculated with the formula $I = I_0 Exp(-(\mu/\rho)x)$ where x is the mass thickness (density times film thickness), for the ~40 nm thick films this gives an attenuation of 0.005% [147].

4.9.2 Results

The goal of using the x-ray diffraction is to find which films are dense and/or diamond like. Since the films are amorphous or nano-crystalline they should only show broad peaks. In figure 4-34 data for all the samples is shown with the background subtracted.

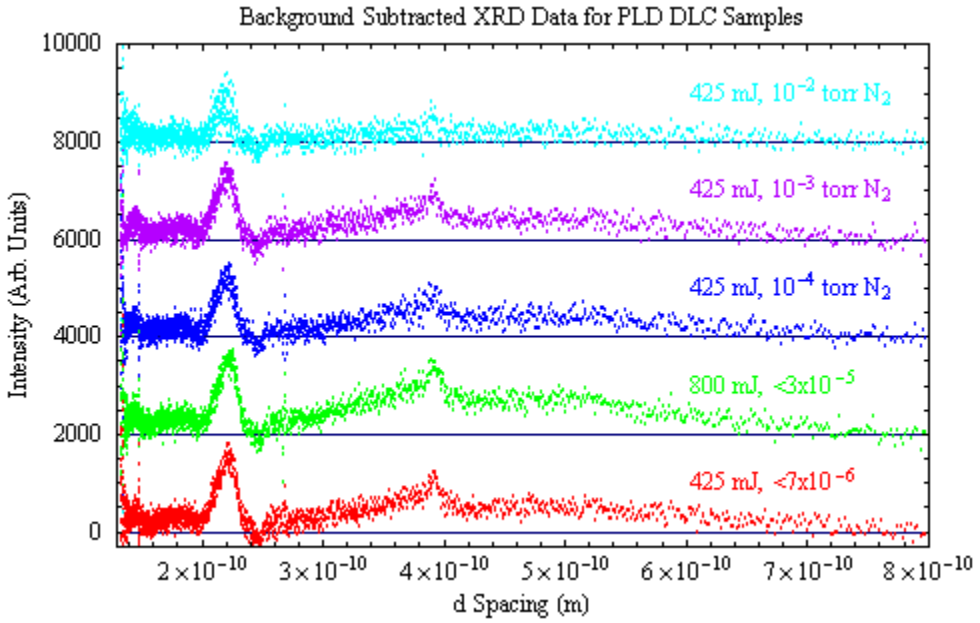

Figure 4-34 Background subtracted XRD data for PLD DLC samples:

There are several structures that change from trace to trace, but understanding how to interpret them is a problem. Table 4-3 shows the peaks and intensities for silicon, several types of carbon, and the scanned samples. The main peak in our samples is close to the

main peak of diamond, but the second peak does not come close to anything. It appears that the data should have been taken for shorter d (in a crystal d is the spacing between the atomic planes) spacings. Lonsdaleite and Chaoite are both diamond density forms of carbon that form due to meteor impacts. The C_8 form of carbon was identified by this x-ray method.[81]

Compound	d (Angstroms)	Intensity	d (Angstroms)	Intensity	d (Angstroms)	Intensity
Silicon[148]	3.134	1	1.917	0.5	1.644	0.1
Graphite[148]	3.35	1	1.675	0.08	1.541	0.6
Diamond[148]	2.06	1	1.261	0.25	1.0754	0.16
Lonsdaleite[148]	2.06	1	2.19	1	1.26	0.75
Chaoite[148]	4.26	1	4.47	1	4.12	0.8
C8[81]	3.02	1	2.13	0.87	1.352	0.69
S28	2.2	1	3.9	0.7		
S29	2.2	1	3.9	0.9		
S30	2.2	1	3.9	0.7		
S31	2.2	1	3.9	0.8		
S32	2.2	1	3.9	0.6		

Table 4-3 X-ray diffraction peaks for known carbon forms and PLD samples:[148]

4.9.3 Other X-ray Techniques

X-rays can also be used in other ways to study PLD DLC films. X-ray Photon Spectroscopy (XPS) can be used to study the composition of the first 5 nm of a surface. Since this is similar to what a UCN sees, this is very useful in looking for surface contamination; but is not any good at looking for hydrogen (although it is useful for hydrocarbons). X-rays can also be used for reflectometry studies.[133, 135] In the case of pure carbon films the analysis is straightforward. For nitrogen rich films it can be used in parallel with neutron reflectometry to find the amount of nitrogen in the film. Since the critical scattering vectors for neutrons and x-rays depend on different parameters, it is possible to find the number densities of some mixed depositions. Hydrogen and carbon concentrations were done by this method in both PLD and CVD DLC films [73, 74]. To make a 1% measurement of the nitrogen concentration in a CN_x film, the measured neutron and electron SLD's would have to be at the 0.1% level.

4.10 Surface Studies

The UCN reflectivity of materials is greatly affected by the surface of the material since UCN have very low energies. Many materials build up a surface layer of water when exposed to air. Hydrogen also sticks to exposed surfaces and migrates into the bulk of some materials. A good UCN and vacuum surface is hydrophobic and low in hydrogen.

4.10.1 Hydrophobic

Graphite and diamond are both hydrophobic in their natural state. Freshly cleaved graphite is hydrophobic, but fresh diamond surfaces have dangling bonds that have to be terminated. If hydrogen, fluorine, or chlorine atoms terminate these bonds the resulting surface is hydrophobic; if they are terminated with oxygen the surface is hydrophilic.[149]

The surface of PLD DLC has a lower density than the bulk and is probably a mixture of graphitic and diamond carbon. This is due to the high-energy atoms that continually disrupt the surface. The surface is still hydrophobic as are DLCs in general. This is determined by the contact angle of a drop of water with the surface.

4.10.2 Hydrogen

Hydrogen on the surface of UCN reflecting materials is thought to be the reason that UCN losses in experiments are much higher than predicted. An experiment by Lanford and Golub found surface hydrogen on copper, glass and aluminum surfaces that had been prepared for UCN experiments.[40, 22] Losses by this amount of hydrogen were consistent with that seen in experiment.[22, 23]

PLD DLC has been shown to have very little hydrogen on the surface and in the bulk. Hydrogen Forward Scattering (HFS) studies of PLD DLC films show hydrogen at both the interfaces, Si/DLC and DLC/Air, this is seen in Figure 4-35. The substrate layer hydrogen is thought to be a result of the HF etching process, while the surface layer hydrogen is from exposure to atmosphere before testing. The resolution of the HFS scan is 50 nm so this scans does not imply any penetration of the hydrogen into the bulk.

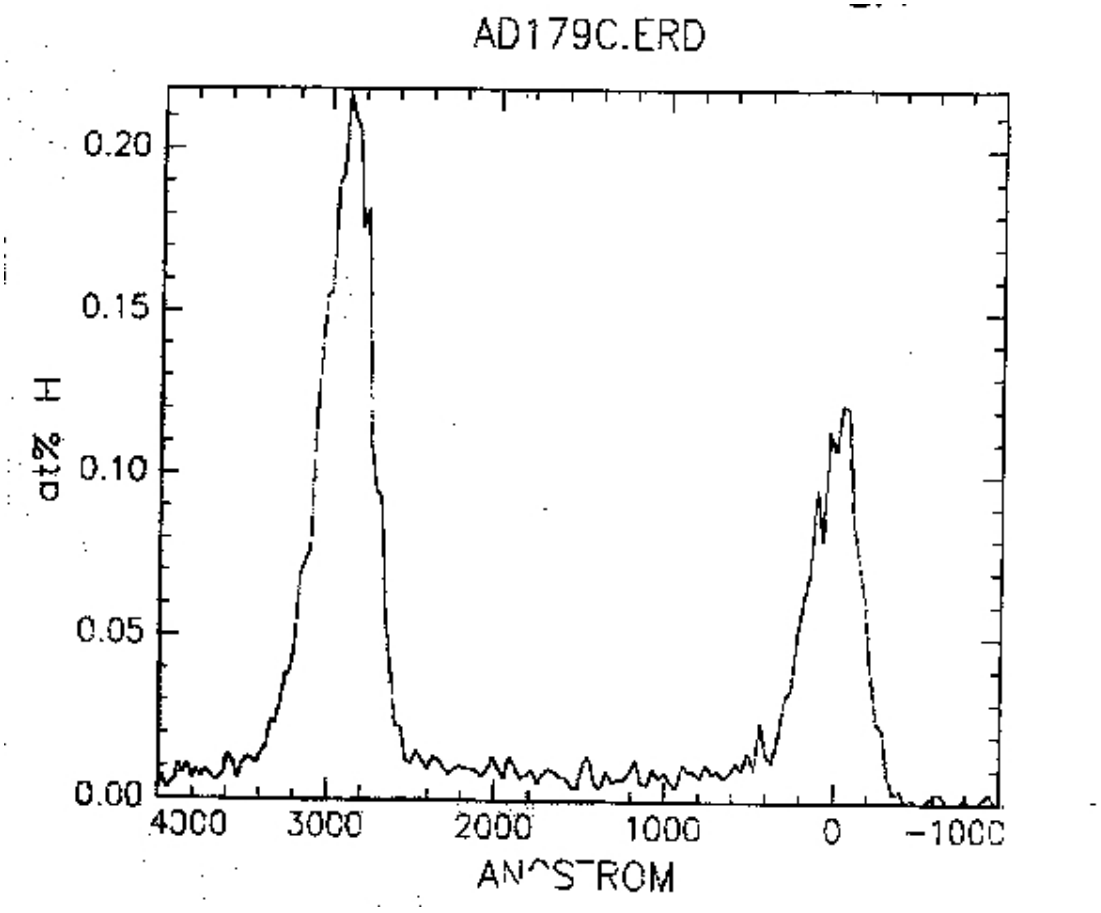

Figure 4-35 Hydrogen forward scattering (HFS) off PLD DLC film: This graph shows that there is a hydrogen layer at 0 Å, which is the interface between the silicon wafer and the PLD DLC. The airside of the PLD DLC at 3000 Å shows a greater amount of hydrogen. This HSF scan is of PLD DLC was made at Sandia.

The Sandia group produced the PLD DLC samples that are present in the Genesis solar wind probe. These samples were studied in detail by the Caltech/ JPL group lead by Dr. Burnett. Secondary Ion Mass Spectrometry (SIMS) studies of the films showed less that 2 ppm of hydrogen in the bulk of the PLD DLC films[150, 151].

To lower the amount of hydrogen below the levels seen, replacement with deuterium can be attempted. The amount due to etching can be lowered by using DF in place of HF. To eliminate the surface hydrogen layer deuterium can be introduced to the vacuum chamber after the deposition process. The lifetime of the deuterium on the surface is not known, but it will be decreased by baking.

4.11 Overall results of initial testing

The studies of PLD DLC show that it has the properties to be a good UCN guide coating. The roughness is on the order of the substrate that is used and this is better than other types of UCN coatings. The critical velocity is above 7 meters per second, this is better than beryllium although well below ^{58}Ni. There is also very little hydrogen in the bulk of the film and less than a monolayer on the surface, this should lower the depolarization rate. In general, the results indicate that PLD DLC should be tested as a UCN guide coating.

5 Pulsed Laser Deposition Ultracold Neutron Guides

Glass and quartz tubing have been used for UCN guides in past experiments.[45] The extremely smooth inside wall yields near specular reflection for UCN. The problem is that the low material potential gives it a critical velocity around 4 m/s. Attempts at coating tubing with a good neutron reflector have resulted in a lowered specularity. The reason for this varies with the technique used, but usually involves the deposition of chunks or the building of islands and voids. Since glass and quartz tubing are electrically and thermally insulating many deposition techniques will not work. Adhesion to the smooth surface can also be a problem.

PLD DLC makes a coating with surface roughness near that of the substrate so depositing it on the inside of quartz tubing should make a specular guide with a high reflectivity. Since PLD is a low temperature, non-electrical process, depositing PLD DLC inside glass tubing should not be a problem. And adhesion should not be problem due to the high kinetic energy of the deposition, at least the problem should not be worse than normal.

5.1 Quartz Tubing (Fused Silica Tubing)

Quartz tubing is the ideal substrate for the transport of polarized UCN since it is very low in impurities that can cause depolarization.

5.1.1 Surface impurites [152, 153, 154, 114, 115]

The inside surface properties of quartz tubing vary depending on the production technique, amount of post processing, time in storage, and parts used in the fabrication process. Fused silica tubing is pulled from melt of SiO_2 that is heated by electricity or burning gas in a large graphite crucible; each of these imparts different impurities to the bulk of the tubing. The hot tubing is shaped by pulling it over or through a pyrolitic graphite mandrel that can also introduce surface contamination. As the tubing cools the surface crystallizes and impurities from the air are incorporated into it. After the initial pull the tubing may undergo post processing steps which involve reheating in a furnace which will lead to further contamination of the surface by the furnace walls and heating

elements or gas. After production, storage and manufacturing of the final product may introduce more contamination.

The impurities due to production and post processing are concentrated near the surface, and the concentration decays quickly with depth until the bulk levels are reached. Work by Leko and Komarova shows the decline in the impurity level over the first 20 micrometers [Figure 5-1].[152, 153] The tails of these graphs tend to agree with the bulk values given by GE Quartz for their type 214 tubing shown in Table 5-1.

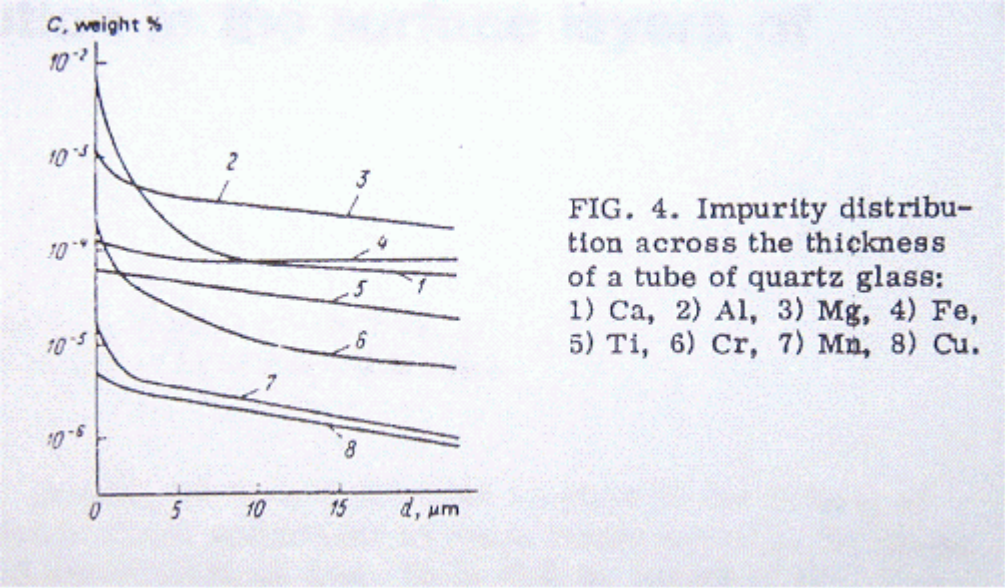

FIG. 4. Impurity distribution across the thickness of a tube of quartz glass: 1) Ca, 2) Al, 3) Mg, 4) Fe, 5) Ti, 6) Cr, 7) Mn, 8) Cu.

Figure 5-1 Depth profile of impurities in quartz tubing:[153]

Typical trace element composition (ppm by weight) **Analysis via direct reading spectrometer (GE Quartz)**									
Type	Al	As	B	Ca	Cd	Cu	Fe	K	Li
214 LD	14	<0.002	0.4	<0.01	<0.05	<0.05	0.2	0.6	0.6
Cont.	Mg	Mn	Na	Ni	P	Sb	Ti	Zr	Total
214 LD	0.1	<0.05	0.7	<0.1	<0.2	<0.003	1.1	0.8	<19

Table 5-1 GE Quartz tubing trace element composition: This study was done by atomic absorption spectroscopy.

To make guide components from fused silica, heat forming, machining, grinding, and polishing steps are used and each of these steps can increase the surface contamination [114, 115]. When heating the part in an oven the refractory walls and hot wires or burning fuel evolve gasses that interact with the surface. The torches used to heat fused silica slowly wear out since they are continually spitting small pieces onto the work they are heating. Machining and cutting is often done with diamond tools, but the diamond is in a nickel matrix and some of this is left in the machined part. Grinding and polishing compounds get stuck in the surface; some of these compounds contain ferrous elements. If parts are machined then worked with a flame, the impurities will be locked deep in the surface. To lower the amount of impurity on the surface the fused silica, parts can be etched in 5-10% HF solutions between steps.

One of the most common impurities on fused silica is silica monoxide (SiO), commonly known as bloom. SiO forms on the surface anytime the fused silica is heated for working and may grow during storage. Bloom makes the surface look dull or foggy. It can be eliminated with a short HF etching.

Another impurity that is on and in the fused silica is water. Water goes into solution with the quartz, so over time the amount can increase. The water can be removed by vacuum baking the fused silica.

Experiments with UCN have shown that etching of the tubing results in increased lifetime of trapped UCN [23]. This is very likely due to the elimination of surface impurities.

Standard techniques like XPS and SIMS can be used to study surface impurities, but Atomic Absorption Spectroscopy (AAS) gives much better results, accurate into the PPM level. To do AAS the sample is etched in HF for a set time; then the solution is analyzed by AAS. A depth profile of the impurities can be made by repeated etching in new HF solutions. The depth of each etching can be calculated by weighing the sample after each

etching to see how much of the surface was removed. This type of study is possible at VT with the AAS machine in the environmental sciences department.

The rate that the surface is removed with HF depends on the concentration and temperature of the etching solution [155]. Etching at room temperature in a 5% HF solution should remove 70-100 nm of material per minute [153, 155]. Assuming there is enough acid, the etch rate is constant, so a ten minute etch will remove nearly a micron of material. Etching away the surface layer will eliminate the surface contamination, but it also changes the surface morphology.

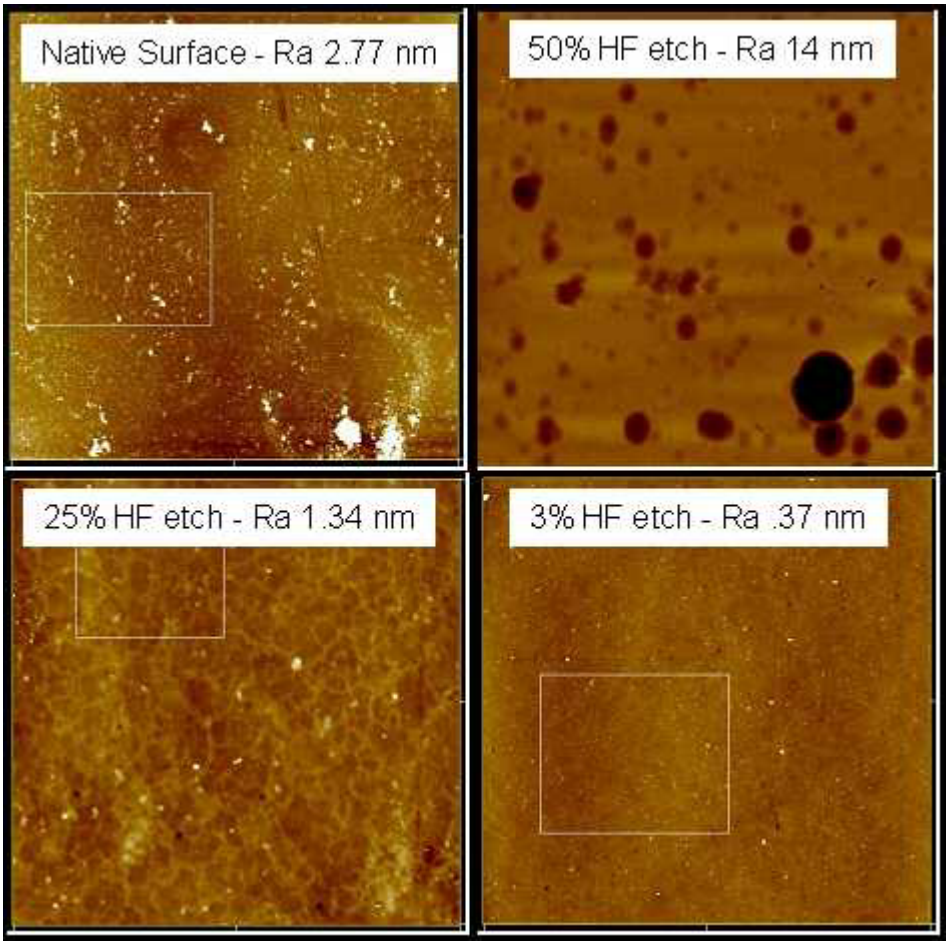

Figure 5-2 AFM images of etched quartz tubing: Each sample of tubing was etched for ten minutes in the solution listed in the image.

5.1.2 Tubing roughness

The roughness of quartz tubing varies from tube to tube. This is probably due to the fact that the tubes we get are from different batches and have been etched a different number of times during processing. The quartz surface with some bloom has a roughness average (Ra) below 5 nm. Etching the tubing in HF can change this as shown in the figures 5-2.

The images are of GE type 214 large diameter (LD) tubing were made with an AFM in contact mode. LD tubing is made by reheating and expanding smaller diameter drawn tubing. This etching study showed that short periods of etching ~10 minutes in low concentrations of HF (3-25%) result in lowered roughness and etching in full strength (50%) results in pitting which increases the roughness. A ten minute etch is the upper limit that the quartz processors use [114, 115], but longer etching may not increase the roughness if low concentrations are used.

As a result of this study, all the quartz guide tubes are etched before coating with DLC. A study of the transport properties using UCN and uncoated etched guides would be helpful in understanding what amount of etching is optimal for transport. Using the formulas from Section 4 on diffuse scattering, the 3%, ten minute etching should give a 99.9% specular reflection.

5.1.3 Surface roughening of the decay–trap

To increase the density of UCN in the decay region the last half meter of guide on each end needs to give a diffuse reflection for UCN. The surface can either give a true diffuse reflection or a random specular reflection; surface features that are large compared to the UCN wavelength tend to give a specular reflection, while smaller features give a diffuse reflection. As the surface roughness increases so does the surface area, and with this the amount of hydrogen and other depolarizing contaminates. The coating quality is also affected since PLD is a line–of–sight deposition process; this will cause shaded areas where the coating is thin or non-existent. A surface that has features that are longer than the UCN wavelength and rounded will have less surface contamination and be easier to coat evenly.

A number of factors need to be taken into account when deciding how to roughen the tubing. As discussed above, the type of features that give the roughness are very important. Ferromagnetic impurities like nickel can be introduced by machining. The process needs to be repeatable for each section made, or asymmetries may be introduced to the UCN population in the trap. If the surface has deep features the UCN can be trapped in them for a time; this can increase the amount of depolarization and loss. And the resulting surface needs to be coated with PLD DLC that tends to have very high internal stress that can cause delamination.

Since etching cleans the surface and can add roughness it could be reasonable method [Figure 5-2]. The most likely way of doing it would be a long etch in dilute HF. The pits formed when etching with 50% HF need to be avoided since they could trap UCN. From Figure 4-11 a roughness average of 5 nm should give about 10% diffuse reflection; 5 nanometers is the limit that can be used with the equations of Section 4.5.4. It should also be noted that for shorter correlation lengths the diffuse scattering is normal to the surface, not in the direction of specular reflection, see figure 4-13.

Machining or sandblasting a pattern into the surface causes definite roughness, but it will also imbed particles into the surface and cause micro fractures that trap gasses like hydrogen. To eliminate this problem, the surface can be etched after sand blasting. GE Quartz has done research into processes similar to this to make a tubing that is easier to coat. They may have this product on the market by now, so maybe it should be looked into.

Another possible way to add roughness is the by depositing a rough layer over the tubing. This could be done with the e-beam system or the laser. SiO_2 is a natural material to try and it can be deposited with the e-beam system or by ablation. Ablated Al seems to give a very rough coating to the eye, but we didn't test it further. The main concern other than the type and amount of roughness produced is the how well the coating adheres to the surface; this is tested by coating it with PLD DLC and seeing if it delaminates.

The quality of the diffuse guides is best tested with UCN and this is the only way to test for a increased depolarization rate of the UCN. Offline testing like XPS, SIMS and AAS are good at finding impurities. The scattering of light is a good indicator of the diffuseness for larger features. Offline vacuum testing with a residual gas analyzer (RGA) and heating will tell something about the surface contamination. But a quick transport and storage experiment followed by a depolarization measurement is the only way to know how the guides will affect the UCNA experiment.

5.2 Guide Coating System

With all the initial tests of the PLD DLC coating being positive and the tests of quartz tubing showing it to be a great substrate; the design, fabrication, assembly, and testing of a guide coating system could begin.

5.2.1 Concept

To coat the inside of tubing with laser, the target needs to be translated inside the tube and the entire surface of the tube needs to spend equal time in the deposition area. A combination of translation and rotation is needed to accomplish this. Due to the high divergence of the excimer–laser beam, moving a fixed focus system through the tube is not an option. To keep the focus constant the lens and target are fix, while the tube is rotated and translated past. To evenly ablate the target, the laser beam is scanned over it by moving the positioning mirror.

5.2.2 Optical System

The goals of the optical system are to deliver the beam to the target, provide low energy loss and to scan the beam around the target. Two gimbal mounted dielectric mirrors are used give up-down and right-left beam motion [Figure 5-3]. Using two mirrors allows the beam to be moved and remain parallel to the beam leaving the laser. The mirrors are 99% reflective at a 45–degree angle of incidence. The converging lens is anti-reflection coated for the 248 nm excimer light, as is the front surface of the window into the PLD chamber. The beam is moved around the target by moving the second mirror. The

mirror was moved first by an electromagnetic drive then by a stepper motor drive; the later provides better control but takes more time to adjust due to the programming needed.

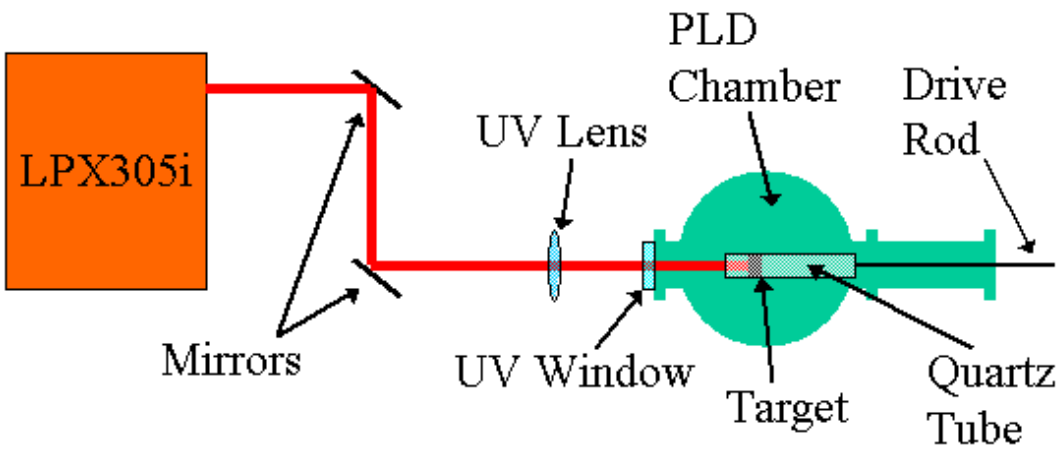

Figure 5-3 Tube deposition PLD optics system: The two dielectric mirrors allow easy positioning of the beam onto the target. The beam was manipulated during deposition by moving the second mirror with an electromagnetic drive.

5.2.3 Prototype Coating System

The prototype coating system was constructed using the PLD deposition chamber with an additional 4–inch vacuum tube attached to the central chamber. The tube being coated was translated and rotated by a coaxial rod that entered the chamber through an o-ring seal. In the first system [Figure 5-4], motion was accomplished with one motor so the rotation and translation rates were locked. This was improved by using separate motors for rotation and translation in the next system. The tube being coated rode on Delrin bushings that slid along three stainless steel rods [Figure 5-5]. Since the drive was coaxial, the target support had to be mounted from the beam entrance end; the support was tubular and the beam passed through it to the target [Figure 5-6].

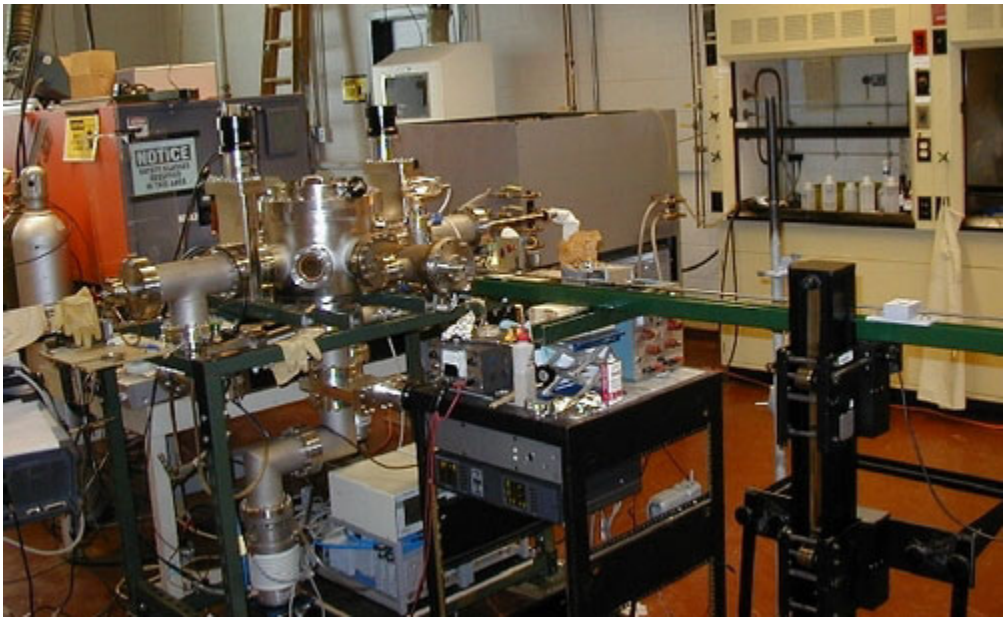

Figure 5-4 Prototype tube coating system: The first tube coating system used the two six inch conflat ports perpendicular to the load–lock ports. The one seen in the image has a short extension added to allow 10 inch tubes to be coated. The drive is on the green unistrut exiting the right of the image.

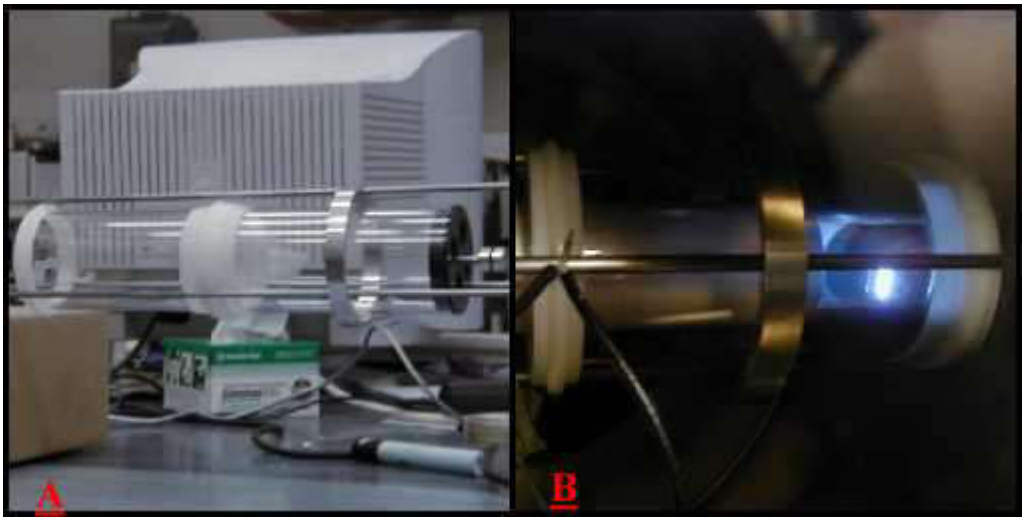

Figure 5-5 Guide support rods: The left image shows a short tube ready to be coated; it is the section between white Delrin rings that ride on the support rods. The section between the right ring and the black plug is to allow the target to pass the end of the tube for complete coating of the tube. The quarter inch drive rod attaches by the flexible coupler at the right edge of the photo. The right image shows the same tube being coated; the bright blue/white spot is a series of laser hits on the graphite target. The target is held by a tube coming in from the left that can be seen inside the quartz tube.

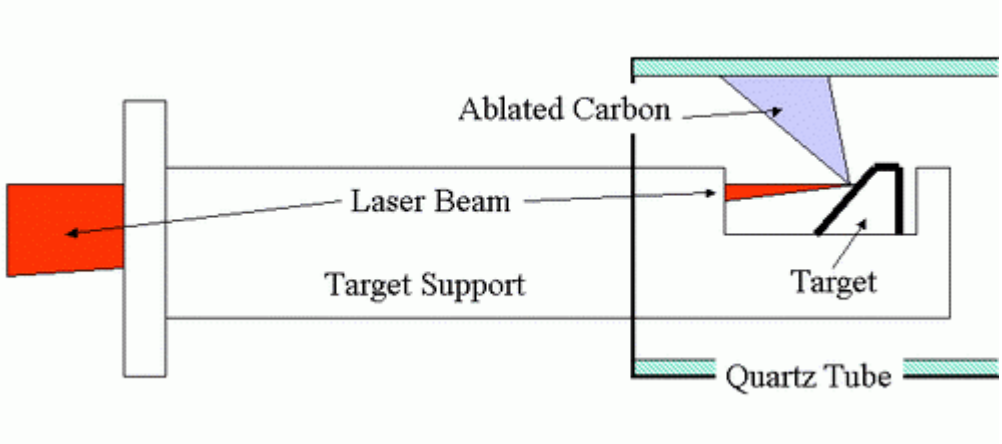

Figure 5-6 Target support tube: The target is held inside the tube being coated by a tube that is attached to the beam entrance window. The target support tube has to be longer than the tube being coated.

5.3 Institut Laue-Langevin Guide Production

After we had a tested diamond-like carbon coating (PLD DLC), a very smooth substrate (quartz tubing – fused silica) and a guide coating facility, an experiment to determine the UCN depolarization rate in our guides could be planned. The only UCN source in the world was the reactor at the Institut Laue-Langevin (ILL) in Grenoble, France, so the depolarization experiment was designed around this UCN source. The following sections describe the making of the guides used in this experiment.

5.3.1 Cleaning and Vacuum Baking

The fused silica that was used in the depolarization experiment went through two cleaning steps before coating. The first step was to remove surface impurities from processing and the second was to remove water from the fused silica bulk. The two steps combined took around one and a half days.

The cleaning process is different for ground fused silica than the guide tubing. The ground plates used for apertures and endplates have small amounts of grinding compound imbedded into the surface that needs to be removed, whereas the tubing should be free of imbedded impurities on the inside. The cleaning of the apertures and endplates starts with a 30-120 minute bath in a boiling mixture of (30% H_2O_2(30%) + 70% H_2SO_4(Conc.)

+ H_2O), this is to remove the grinding compound base. This is followed by a 30-120 minute bath in boiling (1 H_2O_2(30%)+1 NH_3(28%)+5 H_2O) which is to remove the grinding compound imbedded into the surface; it also removes some of the silica [Figure 5-7]. The next step was a 30 minute bath in boiling aqua regia (1 HNO_3 + 1 HCl + 2 H_2O), this is to remove ferrous and non-ferrous metals that might be imbedded into the surface from the grinding or cutting processes. A final 10 minute etch in HF and several rinses in DI water and the parts were ready for vacuum baking. The cleaning of the tubing was done with one ten minute etch in 1% HNO_3(Conc.) + 3% HCl(Conc.) + 5% HF(50%) + 91% H_2O followed by several rinses in DI water [Figure 5-7] Excess water was removed from inside the tubing with lens paper on a Nylon rod – this was to prevent any spotting from impurities in the water. At this point the tubes were loaded into the vacuum oven.

Figure 5-7 Tube and aperture cleaning: The left photo shows apertures and endplates being cleaned in boiling H_2O_2+NH_3, prior to this they were cleaned in boiling H_2O_2+H_2SO_4. The right photo shows the HCl+HNO_3+HF quartz tube cleaning station; the small tube holds the acid mixture and the other tubes are for rinsing after cleaning.

The oven is large enough to bake two meter–long guide tubes at a time; it is ~48 inches long with an ID of 5.75 inches [Figures 5-8 and 5-9]. The vacuum is provided by a sixty liter per second dry turbo, backed with a diaphragm pump. After the whole system is baked pressures below 10^{-8} can be reached. The residual gas in the system is analyzed

with an RGA, this allows monitoring of the water outgassing from the quartz; it also shows if the system has other contamination or a leak.

The vacuum baking of the quartz pieces was done in two steps: step one was to remove any organic materials from the surface and the second step was to remove water from the bulk. The first step is done by heating the oven to 200 C° for 12-24 hours, this allows any volatile organics to leave the surface. The second step is to rapidly heat the oven to above 400 C° and hold it there until the vacuum pressure returns to around 10^{-6} torr; this takes several hours. After this the heat is turned off and the oven cools; when it is cool the pressure is typically below 10^{-7} torr. Without vacuum baking the oven will only reach ~10^{-6} torr due to water coming out of the fused silica; the water is in solution with the glass. After vacuum baking the parts are removed into clean plastic bags and moved to the coating chamber.

Figure 5-8 Vacuum baking oven: The 48 inch long vacuum oven has a 5.75 inch ID and can reach temperatures over 400 C°. The vacuum is provided by a 60 liter per second dry turbo pump backed by a diaphragm pump. The vacuum is monitored by thermocouples, an ion gauge and an RGA. The amount of water coming out of the baking quartz is monitored with the RGA.

Figure 5-9 Tube and aperture baking: The left photo shows two Hereaus Amersil quartz tubes ready to be baked and the right one shows the apertures and endplates on quartz spacers ready to bake. The typical baking cycle took over 24 hours.

5.3.2 Coating

The coating of the guides and other parts for the ILL experiment were done in the standard PLD chamber with the extra four–inch vacuum tubing added to the load/lock ports. The bushing and rail type tube support system used in the prototype tube deposition setup was used again. The drive system for the tube was changed to have two separate motors, one for rotation and the other for translation of the tube. A system was added to allow a higher pressure at the beam entrance window; this was to lower the amount of ablated carbon that deposited on it. The chamber was also setup to coat the plates and aperture with the same optics system. The chamber with these added features is shown in Figure 5-10.

A rail and bushing system like the one in Figure 5-5 was used to guide the tubes through the four–inch vacuum tubes and the chamber. This rail system performed well throughout the coating period of about one month. Setscrews were used to hold the rail support rings in place inside the tubes. The rails were unsupported across the gap in the chamber, but this did not cause any problems.

The drive system was much more flexible with two separate drive motors, but there were more failure points. Having two motors allowed more rotations per inch than the original 28 thread per inch screw drive; this allowed very slow feed rates without risking uneven deposition. The main problem was one of the motors stopping while the coating process continued. This was mostly due to a problem with the power supplies. The o-ring that sealed the vacuum chamber to the drive rod was lubed with Fomblin grease – without this grease the motion became erratic and the o-ring started to show wear.

An inlet for argon or nitrogen was added at the beam entrance window, this was monitored with a Convectron gauge also at the window. In general, the pressure was at the bottom of the scale of the Convectron gauge. Nitrogen was used for all the ILL depositions and a chamber pressure of $5\text{-}7 \times 10^{-5}$ torr was maintained during deposition. The flow of gas may have lowered the amount of ablated carbon that stuck on the entrance window, but it still needed cleaning every couple of tubes.

To coat the flat aperture and endplate pieces one of the 45 dergee ports was fitted with a vacuum feed–though that allowed a ¼ inch drive rod to hold the flat pieces. This was driven with a belt drive by an electric motor that can be seen on the left side of the chamber in Figure 5-10 under the ion gauge. The graphite target was held at 45 degrees to the beam with an optical table mount and ring stand 90–degree holder [Figure 5-11].

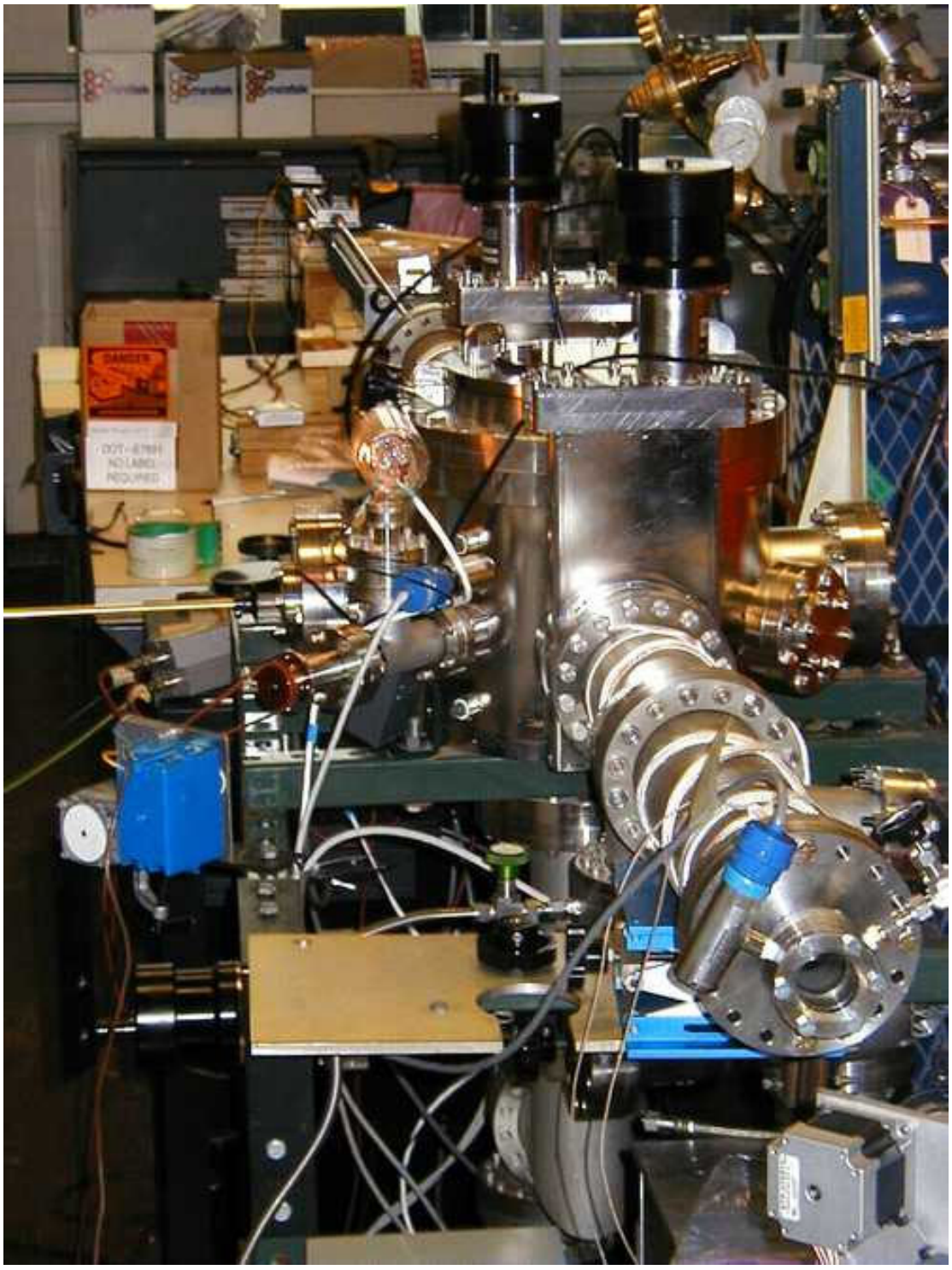

Figure 5-10 ILL tube coating chamber: The PLD chamber with two extensions off the load–lock ports was used to coat the 37 inch long tubes for the ILL depolarization runs. The beam entrance window is in the right foreground and the drive is in the rear of the photo. One of the mirror drive stepper motors is showing in the lower right corner.

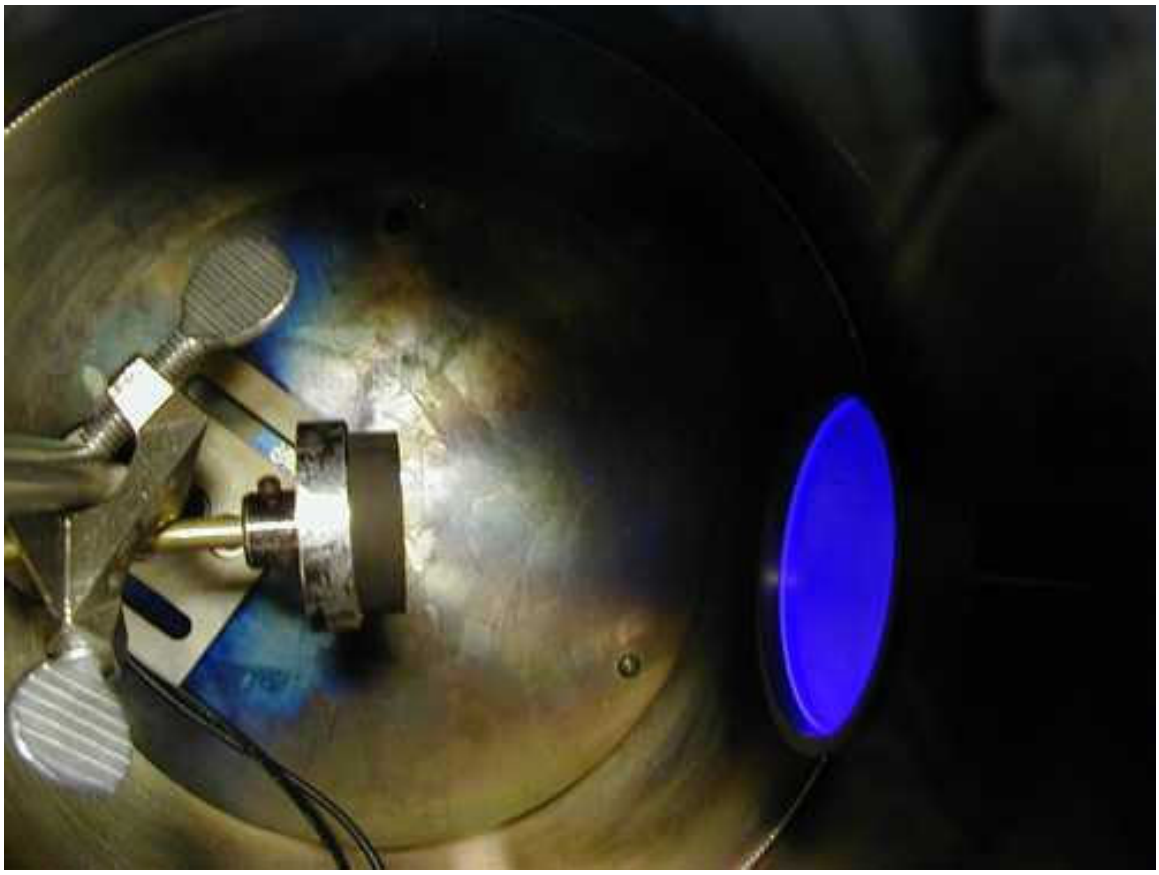

Figure 5-11 ILL endplate coating: The endplates and apertures for the ILL run were coated in the chamber that was setup to coat the guide tubes. The rail system and target support were removed and the graphite target was held in the beam path. The image shows the fluorescing endplate that is being rotated on a shaft that extends out of the vacuum chamber.

The main problem with the deposition system was getting the laser energy to the target. This problem was caused by beam divergence and deposition on the entrance window. The beam divergence is due to the flat cavity optics of the laser and causes a poor focus with the 1.5 meter focal length lens. This can be solved by the use of special cavity optics that lower the laser output energy but make a low divergence beam. The problem of coating the window with ablated carbon cannot be eliminated, but using an aperture so that only part of the window gets coated allows the window to be turned to a clean area between tubes.

About 20 pieces were coated for the ILL depolarization run. Six 37–inch long sections of guide were coated. The shutter had two sets of quartz parts for a total of six tubular and 2

flat pieces. There were two apertures, two endplates and two short guide sections for the elbow. Finally there was one 34–inch guide to the LANL detector.

5.3.3 Table of Guide Coating Parameters

Tube	Pressure (10^{-5} torr)	Laser Rep. Rate (Hz)	Laser Energy (mJ)	Duration (min.)	Thickness (nm)
H8 (ILL H1)	6-7	20	1200	56	30
H5 (ILL H2)	6-7	15	950	~110	60
GE1	6	15	940	~110	
Ge2	6-7	15	882	~110	
DT1	6-7	15	600	~110	80

Table 5-2 Deposition parameters for ILL guides

5.3.4 Packing and Shipping

The goal of packing the coated parts for the depolarization experiment was to minimize contamination during shipping and storage. The tubes were removed from the coating chamber and places into long plastic bags; these bags were then filled with argon and tied shut. They were then carried back to the physics building for packing. In the clean room the bags were opened and purged with argon before they were heat sealed. The sealed bags were than wrapped with bubble warp and placed inside four–inch diameter cardboard tubes. These tubes were packed into foam lined cardboard boxes and shipped to the ILL via DHL and UPS.

6 Ultracold Neutron Depolarization in Pulsed Laser Deposition Diamond-Like Carbon Coated Quartz Guides

The UCN depolarization in the UCNA experiment should be low enough that it does not need to be considered to obtain the desired precision in the A–correlation measurement. That is, the depolarization rate must be low enough that UCN traveling through the polarized sections of the experiment remain 99.91% polarized.[30] To determine the depolarization rate of UCN during transport through pulsed laser deposition (PLD) diamond-like carbon (DLC) coated quartz guides an experiment using UCN is necessary.

Prior to the UCNA depolarization experiment two experiments had already been done at the Institut Laue-Langevin (ILL) to determine the depolarization rates of UCN on several different surfaces; the results of these experiments looked promising but were insufficient to predict the success of our guides. Beryllium seemed to have a depolarization rate below 10^{-5} per bounce, this is in the range needed. Although carbon was tested, it was graphitic and not PLD DLC like we intended to use in the UCNA experiment. The previous experiments showed that the depolarization rate may be low enough, but a new experiment was needed to test the UCNA guide concept.

The only user facility for UCN research in the world is the ILL in Grenoble, France, so an experiment was designed to utilize this facility and find the depolarization rate for our guides. The experiment to test the Virginia Tech (VT) PLD DLC coated quartz guides was designed and built during 2002 with the data collection occurring during October 2002 at the ILL. The depolarization rate was found to be below 10^{-6} per bounce – this is low enough to satisfy the design criteria of the UCNA experiment.

This chapter will cover three topics: previous UCN depolarization experiments, the design of the UCNA depolarization experiment, and the data analysis of the UCNA depolarization experiment. In the first section the two previous experiments looking at

UCN depolarization will be described and the results discussed. The second section will show how estimates of the UCNA's sensitivity were made – these estimates were used in the designing of the experiment. The third section covers how some of the experiment's components performed, the extraction of needed parameters from the data and the calculation of the UCN depolarization rate.

6.1 Previous UCN Depolarization Experiments

A group led by Anatoli Serebrov ran the two previous experiments that looked at the depolarization rate of UCN on various surfaces. The first experiment collected data in 1998, while the second ran in 2000. The two experiments had different designs and their results were not in total agreement. The data was published in references 41 and 42.

The first experiment looked for depolarization rates on several materials including beryllium, copper and carbon. The rates were all at or below 10^{-5} per bounce.

The second experiment looked at the same materials and added a cryogenic insert to look for temperature dependence in the depolarization rate. In general, the depolarization rates were higher and in the 10^{-5} per bounce range, and no temperature dependence was found.

6.1.1 The first depolarization experiment [41]

The first depolarization experiment was motivated by two questions: can polarized UCN be used to make a precision measurement of the neutron's beta decay asymmetry and could spin incoherent scattering cause the anomalous loss of UCN during storage in various material traps. Knowing the polarization is one of the main systematic uncertainties for polarized beta decay experiments. So if UCN have a sufficiently low probability of depolarizing while in a material trap they would be ideal for a β-asymmetry experiment, since the 100% polarization of UCN is possible with a high magnetic field gradient. With regard to anomalous losses, spin incoherent scattering would not only provide depolarized UCN to the trapped population, but also losses since they could scatter into 4π, leaving half the scattered UCN in the wall. The experiment was designed to look for depolarization on various surfaces that could be placed in a large vacuum trap.

The experimental apparatus shown in Figure 6-1 was built at Petersburg Nuclear Physics Institute (PNPI).[163] It consisted of two symmetric traps separated by a 4.5 Tesla superconducting solenoid magnet (PNPI SCS). The traps were made of copper and coated with beryllium. With a maximum field strength of 4.5 Tesla, the magnet can polarize UCN with kinetic energies up to 270 neV. This is above the material potential of the beryllium coated trap (252 neV). The residual magnetic field from the PNPI SCS provided the holding field for the polarized UCN in the traps; the holding field was an average of 300-400 G in the traps.

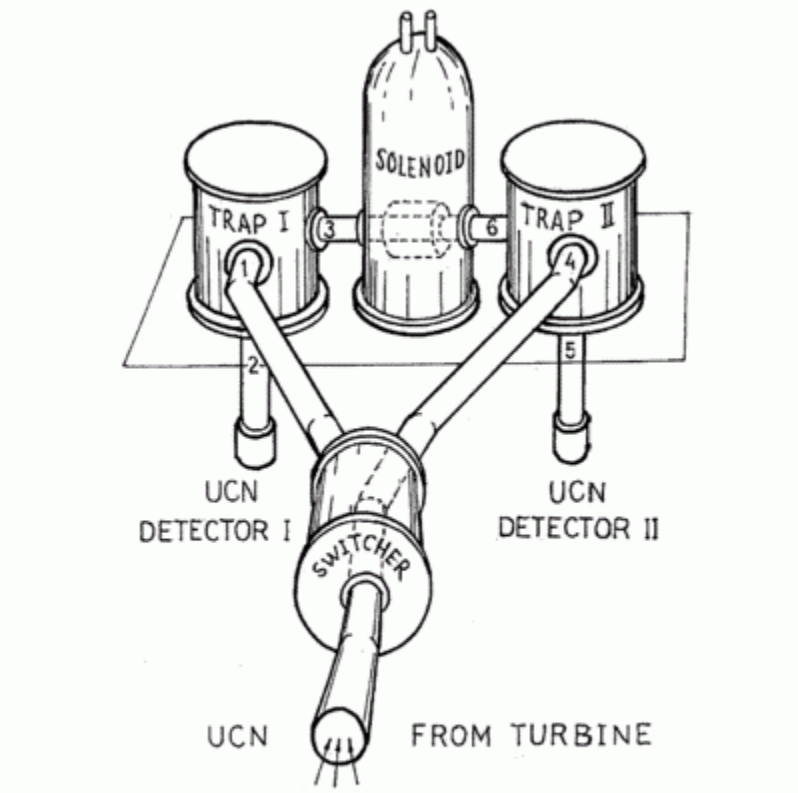

Fig. 1. Scheme of the apparatus. 1, 2, 3: shutters of trap I; 4, 5, 6: shutters of trap II.

Figure 6-1 1998 depolarization experiment diagram: This diagram of the first UCN depolarization experiment is from reference 41.

Depolarization was studied two different ways with the apparatus: one counts the number of UCN in a population that depolarize after a set time, the other watches a population of trapped UCN for any that depolarize. In the first method, one of the traps is filled with

polarized UCN by flowing UCN into the other trap and then through the polarizer into the trap to be studied. After filling the trap under study it is sealed off with the shutters and the other one is drained into its detector. After the polarized UCN are held for a set time the shutters between the traps are opened and the UCN that are still in their original polarization flow back into the other trap and are counted with its detector. After the signal in the detector drops to about zero the other detector shutter is opened and any UCN remaining in the test trap are counted and labeled as depolarized. For the second method a trap full of polarized UCN trapped by the magnetic field are needed. To do this, one of the traps is filled with unpolarized UCN. Then the filling shutter is closed and the shutters to the other trap are opened. One polarization passes through the magnet into the other trap and is counted in the detector. If the UCN maintain their polarization in the trap only half will leave and the signal will fall to zero. UCN that depolarize in the test trap will be able to pass through magnet and be detected. This effect can be seen by using the shutter to block the magnet after the free spin–state is drained; after opening the shutter a pulse of depolarized UCN should be seen by the detector.

Both techniques showed that UCN were depolarizing; but to get a value for the depolarization rate the lifetime in the traps has to be known, as does the frequency of wall collisions. The collision frequency was estimated using the kinetic theory of gas flow, $\nu = Sv_{av}/4V$ where S is the surface area, v_{av} the average velocity, and V the volume of the trap. The lifetimes for UCN in the two traps were 175 and 130 seconds for traps 1 and 2 respectively; no reason for the difference was given. The reported depolarization per bounce and loss per bounce are given in Table 6-1.

To test other materials for depolarization they were loaded into the trap and the same type of experiments were performed. The addition of materials causes a change in the frequency of collisions due to changes in geometry and possibly the average velocity. Materials with low critical velocities like glass and Teflon eliminate all of the higher energy UCN after a few scatters; this makes it harder to determine the total number of bounces in the trap since the rate is changing with time. The results from these samples are also shown in Table 6-1.

Since UCN interact with the atoms on the surface of the material, knowledge of the surface composition is very important. The surface of the traps is beryllium coated copper; this type of surface has been shown by the Paul Scherrer Institute (PSI) group to have exposed copper at the 0.01-0.001% level [164, 156]. Figure 6-2 show holes in the Be coating as seen by an optical microscope. Since copper has a lower critical velocity than beryllium this will cause the velocity spectrum to shift during storage and will make the total number of bounces harder to predict. Also, if the coating is missing, due to surface contamination, this could add an unknown source of depolarization. In addition to the exposed copper, using XPS and SIMS studies, the PSI group found the surface (the depth of an XPS scan is about 5 nm) to be 47% Be and BeO, 30% O including oxygen from BeO, and 22% C. The depth of the BeO layer was about 3 nm thick and the C layer was about 4 nm thick according to SIMS studies. The effect of the carbon layer depends a lot on how much hydrogen is attached to it; there was no information on this since XPS cannot measure the hydrogen concentration.

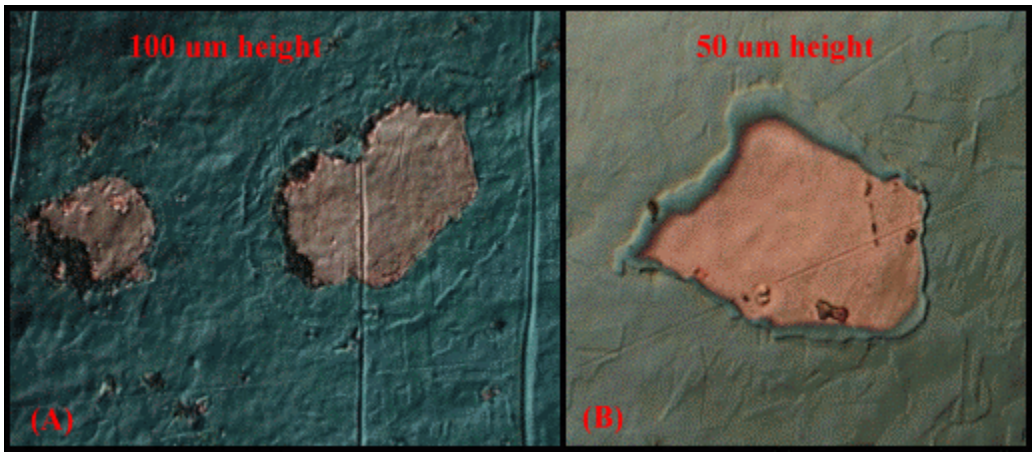

Figure 6-2 Holes in beryllium coatings: [156] These two photographs of beryllium coated copper show exposed copper. The left image is ~100 μm across while the right one is ~50 μm across. The ratio of exposed copper to beryllium is between 10^{-4} and 10^{-5}.[156]

The results of this first experiment appeared promising, but due to problems with establishing the number of bounces and defining the actual surface properties the experimental errors seem too low. It is possible that a Monte Carlo analysis of the

experiment could increase the understanding of the data. This experiment does show depolarization, but where it comes from is not obvious.

6.1.2 The Second Depolarization Experiment [42]

The second depolarization experiment was motivated by the same reasons as the first, with the hope of getting a more precise measurement of the depolarization probability per bounce (DPB) and a better understanding of the incoherent scattering mechanism. To improve the depolarization measurement a gravitational spectrometer was used to condition the UCN spectrum before the trap was loaded. This allowed a more accurate estimate of the number of bounces per second in the trap. To better understand the incoherent scattering, a cryostat was added to look for any temperature dependence of the depolarization rate. Due to these and other changes the second experiment was very different from the first and came up with different results.

The second depolarization experiment by the Serebrov group was done with a new experimental apparatus, shown in Figure 6-3. The same polarizing magnet was used, but the geometry and components were changed. To get a better value for the average UCN velocity, a gravitational spectrometer was used to condition the UCN velocity spectrum from the turbine. The conditioned UCN were then polarized and loaded into a graphite coated copper trap. A liquid nitrogen filled cryogenic insert could also be installed into the trap; it was also made of copper and coated with graphite. Both the gravitational spectrometer and the trap had 49 cm inside diameters; the spectrometer was 2.2 meters high and Be coated, while the trap was 49 cm high. The guide between the spectrometer and the trap was made of polished copper coated with beryllium.

The depolarization rates found in this experiment were higher than those found in the first experiment and no temperature dependence was seen. The gravitational spectrometer made estimating the collision rate more accurate; and in general, the collision rates were found to be lower than predicted in the first experiment. Using the new collision rates, the previous results were corrected and re–published. The new values for various materials are listed in Table 6-1; new loss rates were not published. In general, the rates seen were

higher in this experiment and a partial explanation suggested that the beryllium surfaces had a different amount of oxidation than in the previous experiment. The use of the cryogenic insert showed that depolarization rates on Be, BeO and C had no temperature dependence. This indicates that depolarized UCN that scatter into the surface do not return to the trap. The depolarization rates in this experiment are probably more accurate than those of the previous experiment due to the characterization of the velocity spectrum.

The cryogenic insert was also used to study the effect of varying amounts of water condensed on its surface; the loss probability increased with the amount of water but the depolarization rate remained constant. This result seems to exclude hydrogen and oxygen as major factors in UCN depolarization. The details of how it was known that water was deposited on the insert were not given in the article so this result might be questionable.

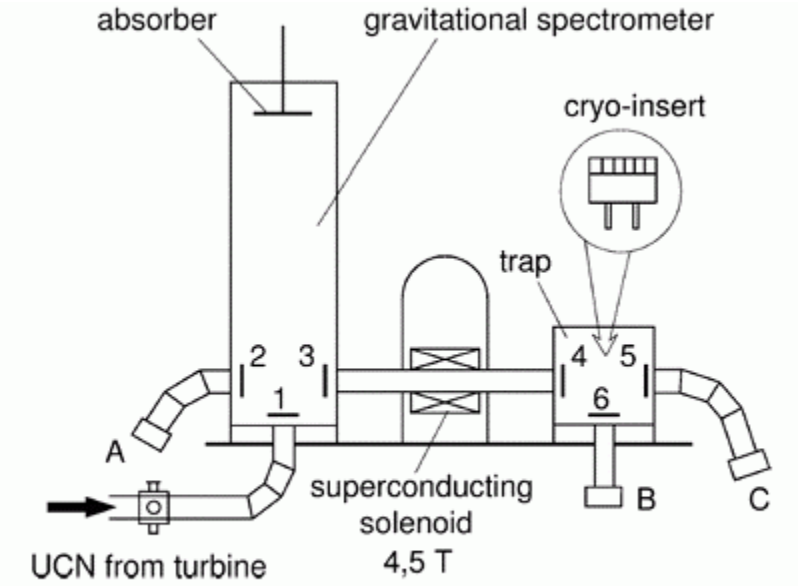

Fig. 1. The experimental setup. 1, 2, 3, 4, 5, 6 are UCN valves. A, B, C are UCN detectors.

Figure 6-3 2000 depolarization experiment diagram: The second depolarization experiment used a gravitational spectrometer to condition the UCN velocity spectrum. This helped to determine the number of bounces a UCN undergoes while in the trap.[42]

Material Tested	P[spin flip] (10^{-6})	P[loss] (10^{-5})	V_c (m/s)
1. Be – trap	7.2±0.7		6.89[23]
2. Be – trap and foils	7.7±0.7 , 21.7±2	7.1±1.1	6.89[23]
3. SiO_2 - quartz	14±1	59.8±6.0	4.26[23]
4.BeO before outgassing	48±5	168±15	6.99[23]
5. BeO after outgassing	44±4	74±7	6.99[23]
6.Glass: SIO_2 -81%, B_2O_2-13%, Na_2O+K_2O-4%, Al_2O_3-2%	95±9	315±30	
7. C – graphite foil	1.9±1.0 , 5.9±1.0	18.6±2,0	6.11[23]
8. Brass: 63% Cu, 37% Zn	1.1±1.0	19.3±2.0	5.24
9. Cu	-1.2±1.0 , 7.3±1.4	20.0±2.0	5.66[23]
10. Teflon: CF_4	1.8±1.0 , 6.0±2.4	23.5±2.0	4.85[22]

Table 6-1 Depolarization, loss per bounce and critical velocity table: This table shows values for the depolarization rate from the two Serebrov experiments. Where there are two numbers the first is from the first experiment (as published in ref. 41) and the second from the second experiment (as published in ref. 42). The probability of loss is from the first experiment.

6.1.3 Conclusions

In general, the spin flip probability increased by a factor of three for beryllium, graphite, copper and Teflon in the second experiment. These are probably all due to the use of the incorrect collision frequency in the first experiment. In both experiments surface roughness and complicated geometries make the exact value for the collision frequency hard to determine. The Serebrov trap surfaces that we saw were very rough; to the point that trapping in the scratches might be possible. Temporary trapping in a small volume would greatly increase the number of collisions seen by the trapped UCN. Also ferromagnetic impurities from machining would be very hard to remove from these rough surfaces. During the second experiment Albert Young determined that ferromagnetic impurities from a polishing plate caused a significant amount of depolarization on high purity copper plates.[165]

Due to the unknown surface purity and collision rate, the quoted depolarization rates for the quoted surfaces are questionable. Perhaps they are a good upper limit or at least those from the second experiment are, but it seems a more controlled experiment is needed. The study that shows water having no effect on depolarization should also be questioned since no evidence is given that the condensate was water and not nitrogen or some other contaminate. The surface studies done at PSI suggest that perhaps all the surfaces tested need to be studied in order to see what surface the UCN are actually interacting with. In general, an experiment with well known surfaces and vacuum conditions is needed to determine the depolarization rate for materials planned to be used in a beta decay asymmetry experiment.

6.2 UCNA Depolarization Experiment Design

The previous two experiments looking at the depolarization rate of UCN on various materials showed that in general the rates were a little higher than what is needed to make a precision measurement of the beta decay parameter "A" without corrections for the UCN polarization. To see what the polarization would be in an actual experiment, the materials for the experiment need to be tested in the correct geometry and vacuum conditions. For this purpose the UCNA depolarization experiment was undertaken by the UCNA collaboration.

The experiment was built around several existing components: the PNPI gravitational spectrometer, the PNPI SCS, and the LANL UCN switcher. Estimates of the detector rates and trap lifetimes for the experiment can be made using the basic experiment design. From these estimates, the sensitivity appeared to be good enough to see depolarization below 10^{-6} per bounce.

6.2.1 Overview of the Experiment

The design of the UCNA depolarization experiment is similar to the second Serebrov experiment with the trap being replaced by a section of diamond coated quartz guide, see Figure 6-4; several other changes were also made. To guarantee known vacuum conditions, the vacuum system upstream of the quartz guide is separated by an aluminum

foil. The vacuum downstream of the foil is maintained by a pumping tower. The addition of the adiabatic fast passage (AFP) spin flipper lowered the number of detectors needed to monitor the experiment to two – the PNPI and LANL detectors shown in Figure 6-4 and 6-5.

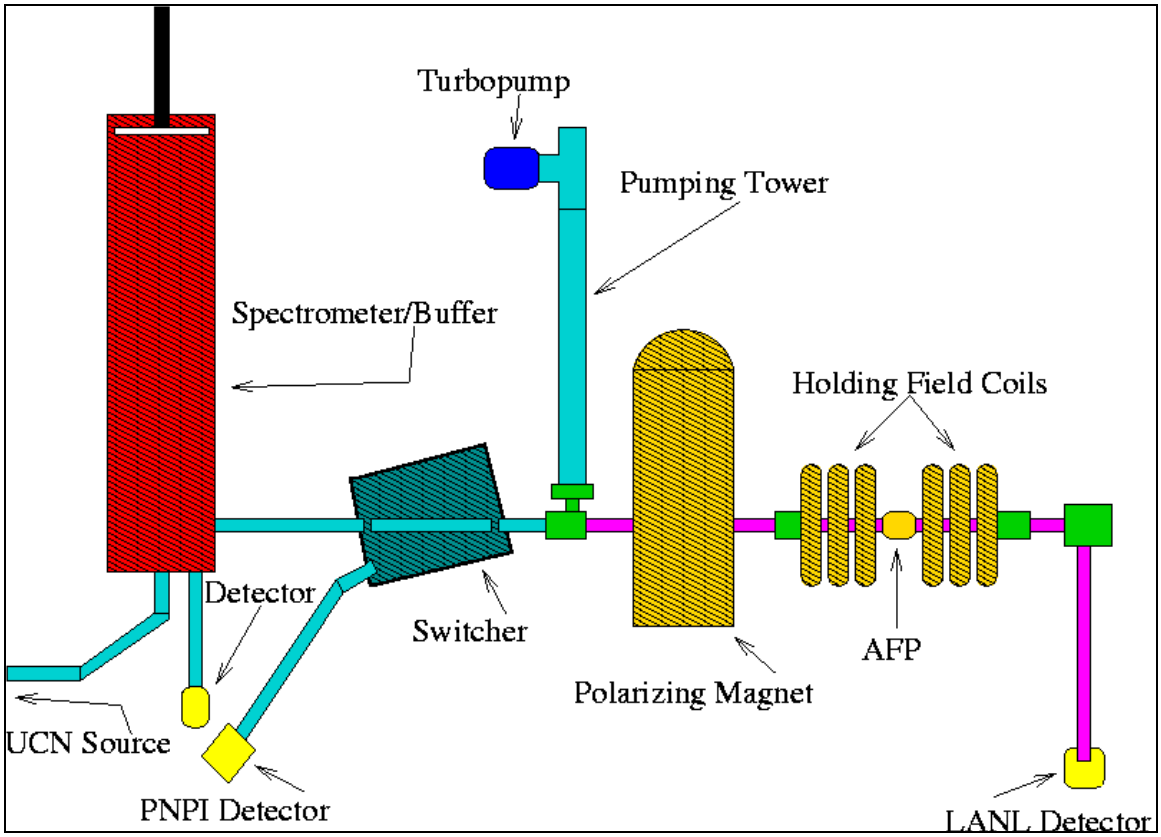

Figure 6-4 UCNA depolarization experiment diagram: In this drawing of the UCNA depolarization apparatus the quartz guides are shown in purple and steel guides are light blue.

To look for UCN depolarization the trap is filled with polarized UCN. Any UCN that depolarize in the trap are free to exit and be counted in a detector. To load the trap UCN flow in from the gravitational spectrometer via the switcher (that allows either filling of the trap or draining of the trap into a ^{3}He proportional detector, the PNPI detector – Detector 2). As they flow through the PNPI SCS they are polarized so only one spin–state can enter and leave the trap. The trap walls are the UCN guide to be tested; the magnet forms one end of the trap (for depolarized UCN) and a PLD DLC coated quartz plate with an aperture forms the other end. The aperture leads to another ^{3}He proportional detector (Detector 3) and is used to monitor the UCN density in the trap. To

unload the trap of free UCN the flow from the spectrometer is stopped and the switcher is moved to allow the UCN into the Detector 2. To unload the trapped UCN the AFP is cycled; the AFP can also be used to load the trap if it is cycled during the filling period.

Depending on the AFP efficiency different percentages of the trapped UCN can be unloaded. Assuming the AFP is 100% efficient the trapped UCN in region 2 [Figure 6-5] undergo a spin-flip when passing through it and then leave the trap; assuming a sufficiently long on period, when the AFP is turned off the UCN, which where in region 1, that are now in region 2 can exit the trap. Assuming the AFP is in the middle of the trap and that the remaining trapped population regains an equilibrium distribution before the AFP is turned off ¾ of the trapped UCN will exit the trap in an AFP cycle. Similarly ¾ of the inflowing UCN density can be trapped if the AFP is cycled during filling. Both of these numbers assume the UCN density is constant throughout the trap; which is not true since the magnetic field forms one end of the trap. As the AFP efficiency decreases more UCN that were in region 1 escape the trap during the AFP on cycle, this leads to more that 75% unloading of the trap. Hence the AFP can unload 75% or more of the trapped UCN assuming it is located in the center of the trap and that the UCN are equally distributed in the trap.

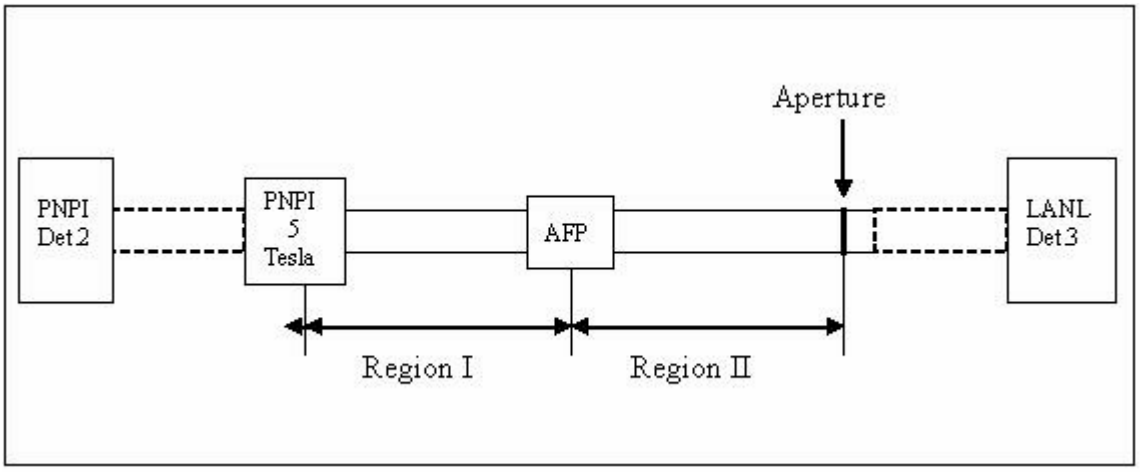

Figure 6-5 Depolarization trap diagram: This is a schematic representation of the depolarized UCN trap (Region 1 and 2 make up the trap); the dashed regions represent the guides that lead to the detectors.

Two basic experiments can be done with this setup to find the depolarization probability per bounce (DPB) of UCN in the guide. In the first, UCN of one spin-state flow through

the polarizer into the trap while interacting with the walls and flow out if they are not depolarized in the trap. After allowing this to proceed for some time an equilibrium will be reached with as many UCN being trapped as are lost by other mechanisms. At this point the inflow of UCN is stopped and the switcher set to drain the trap into Detector 2. After a period of time the trap will be populated almost entirely with depolarized UCN; using the AFP these can be drained into Detector 2 and counted. In the second method the AFP is used to load the trap with depolarized UCN. This is done by switching the AFP on after the trap has reached an equilibrium density, then it is turned off after a new equilibrium is reached. The switcher is then used to drain the non-trapped spin-state leaving the trap full of UCN. Any UCN in the trapped population that undergoes a spin-flip can exit the trap and be detected by Detector 2. Using the AFP the trapped UCN can then be drained and counted to find the population that the depolarized UCN came from.

Many more UCN are depolarized during the filling of the trap than are finally unloaded by the AFP since they are continually lost from the trap to Detector 3, so the probability of surviving until the trap is unloaded is a function of the trap lifetime. The DPB is found by solving the equation:

$$\int_{start}^{dumptime} \mathrm{DPB} \times \mathrm{BPS} \times \mathrm{UCNF(t)}\, \mathrm{e}^{(\mathrm{t-dumptime})/\mathrm{TrapLifeTlme}}\, dt = \textit{Depolarized UCN}\,,$$

(BPS, Bounces per Second is the collision rate per UCN, UCNF(t) is the number of free UCN in the trap as a function of time, and dumptime is when the trapped UCN are unloaded using the AFP). Since UCNF(t) and the *Depolarized UCN* are found using Detector 2, the efficiency of transport and detection drop out of the calculation. The number of UCN in the trap and the trap lifetime are found by monitoring a large number of trapped UCN similar to what is done in the second type of depolarization measurement. The BPS rate can be also be estimated using data from the second method or it can be estimated with theory and Monte Carlo simulations. Although this method can show if there is depolarization, information from the second experiment is needed to extract the DPB; since two different experiments are being used care must be taken to ensure their UCN populations are similar.

Using the second method, the DPB calculation is made without using data from the first method. The depolarization signal is just the rate in Detector 2 after the trap has been drained of the free spin–state minus any background. The average number of collisions that caused depolarization of the UCN is calculated by multiplying the number of UCN unloaded from the trap, using the AFP, times the theoretical collision rate. Since the trap cannot be unloaded instantaneously some of the UCN are lost before they are counted. To adjust for this the lifetime of the trapped UCN needs to be known. The trap lifetime is obtained by fitting the Detector 3 signal after the signal in Detector 2 drops to near zero. The DPB is the ratio of the UCN seen per second before the trap is emptied divided by the product of the number of trapped UCN and the wall collision rate. The effect of transport from the trap to the detector is eliminated by the ratio since Detector 2 counted both depolarized and trapped UCN.

6.2.2 Physical Description of the Experiment Components

Each component of the experimental apparatus, and the vacuum conditions, starting at the source and ending at the detectors has an effect on the final number of depolarized UCN that are counted. To better understand the experiment, each major component and its effect from the source to the detectors will be discussed.

6.2.2.1 ILL UCN Source [157]

The UCN source at the ILL combines three techniques to obtain UCN from the high–flux reactor. The process starts when neutrons near the reactor core interact with a 25 K liquid deuterium cold source. Neutrons cooled in the cold source are guided upward 5 meters to a double zirconium window that connects to an additional 13 meters of nearly vertical guide. After the initial moderation and gravitational cooling, the neutrons enter a Garching-turbine [158] where they are Doppler-shifted off the receding turbine blades to UCN velocities. Initial studies at the turbine exit showed a bottled density of UCN to be 36 per cm^3.

UCN exit the turbine into 4 guides that feed various experiments. Looking at the turbine from above, the guide closest to the reactor guide leads to the NESSIE platform, which held the Russian neutron lifetime apparatus. The UCNA depolarization experiment was located on the platform next to this, which is called the Mamba [159] platform. Next to this is the EDM platform and the last UCN guide is called the test beam. The pervious depolarization experiments also took place on the Mamba platform.

6.2.2.2 The PNPI Gravitational Spectrometer

The PNPI gravitational spectrometer conditions the UCN velocity spectrum that enters the experiment; this eliminates the high energy part of the velocity spectrum. Conditioning of the UCN spectrum is done by holding the UCN in a large bottle with a movable UCN absorber for a top. Neutrons with higher energy than the material potential of the bottle or that can reach the absorbing top are lost from the spectrometer. By lowering the absorber the maximum velocity UCN in the trap can be lowered below the material potential of the trap.

The PNPI gravitational spectrometer is cylindrical with a diameter of 49 cm and a height that depends on the number of sections added. The sections are made of copper and are coated with beryllium. UCN enter the spectrometer from the bottom and can exit via two ports at 90 degrees to each other, that are 25 cm above the bottom of the spectrometer. The polyethylene absorber that forms the movable top of the spectrometer can be lowered to within nine centimeters of these exit guides.

For the depolarization experiment the spectrometer was connected to the turbine on the MAMBA platform with a PNPI ^{58}Ni coated stainless steel guide. To stop the flow of UCN from the turbine into the spectrometer there is a ball valve in the guide. The spectrometer also has three shutters as shown in Figure 6-3. For the UCN depolarization experiment, shutter one was at the bottom, shutter two was on the experiment guide and shutter three leads to a PNPI UCN detector. The shutters are pneumatic and operate in two steps: step one moves the shutter away from the guide and the second step rotates it

clear. As a result of this two-step process it takes several second for the shutters to fully open or close.

In the UCNA depolarization experiment the spectrometer height was about 2 meters. Since the UCN guide exits the spectrometer 25 cm from the bottom, the energy spectrum of the UCN was cutoff at about 175 cm (179 neV, 5.86 m/s) by the absorber. Using data provided by the PNPI group for the UCN energy spectrum exiting the spectrometer at the MAMBA position and the foil transmission data from the spectrometer at the NESSIE position, velocity spectra can be generated [Figure 6-6].[160] The average velocity of UCN entering the UCNA depolarization experiment is found to be 5.1 m/s if this data is used. The actual UCN velocity spectrum exiting the spectrometer depends on the how long the UCN are held in the spectrometer.

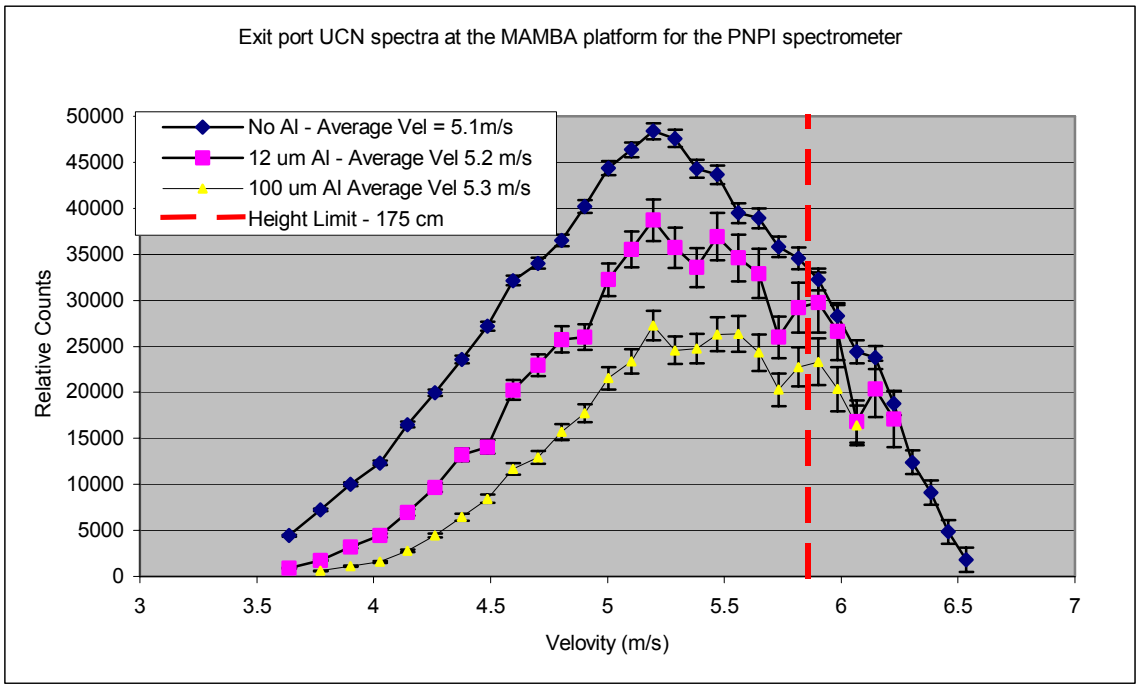

Figure 6-6 Exit port UCN spectra at the MAMBA platform for the PNPI spectrometer: This figure shows the UCN velocity spectra for UCN exiting the spectrometer: without a foil (blue), through a 12 μm thick foil and through a 100 μm thick foil. The average velocities correspond to the absorber being 175 cm above the UCN exit port.

During the UCNA depolarization runs the spectrometer was used in two different ways. In the first method the spectrometer was filled for 50 seconds, then the shutter to the experiment guide was opened for 120 seconds while the spectrometer continued to be filled. After this, the open shutters were closed and the shutter to the PNPI detector was opened to count the UCN in the spectrometer. This filling method was used in the 140 second hold, method one depolarization runs. A second method was used to fill the trap for the Serebrov AFP loading runs – depolarization method two used this method. In this second method the spectrometer was not pre-filled, instead UCN were allowed to flow into the spectrometer and guide for 90 seconds after which the spectrometer was dumped into the PNPI detector as before. The trap density reached equilibrium much faster in the first method than the second as can be seen in Figure 6-28 and by comparing Figures 6-31 and 6-38.

The PNPI spectrometer was used in a flow–through configuration so the actual spectrum and average velocity are probably different than shown in Figure 6-6. The average velocity should shift upward which will make the depolarization rates lower than predicted. The difference in the spectrum between the two filling methods is also an unknown, but it can be assumed that the second method has a higher average velocity. It should also be noted that the velocity spectrum in the trap would be cooling due to UCN lost to the aperture. This is a small affect; at 100 seconds the average velocity will drop about 2% and at 200 seconds it will have dropped 4%. Wall losses will also cool the spectrum but to a lesser extent.

6.2.2.3 LANL Switcher

To allow both filling and emptying of the trap though the polarizing magnet, a switcher is located between the PNPI spectrometer and the magnet. The switcher was designed and built at LANL. It is designed to allow straight through flow or a 30-degree bend. This is accomplished by rotating a section of guide inside the switcher housing. The actuation is pneumatic and has a 0.5-1 second switching time. To allow the rotation, gaps are needed at each end of the rotating guide; these gaps are a source of loss.

In the experiment the straight through position fills the experiment and the 30–degree bend is used to empty the trap into Detector 2. The gaps were about 2 mm each. During filling, some of the UCN that leak through the gaps reach the detector on the 30–degree port. This allows monitoring of the UCN density in the guide during filling as seen in Figure 6-7 (in the region before the tall unload peak).

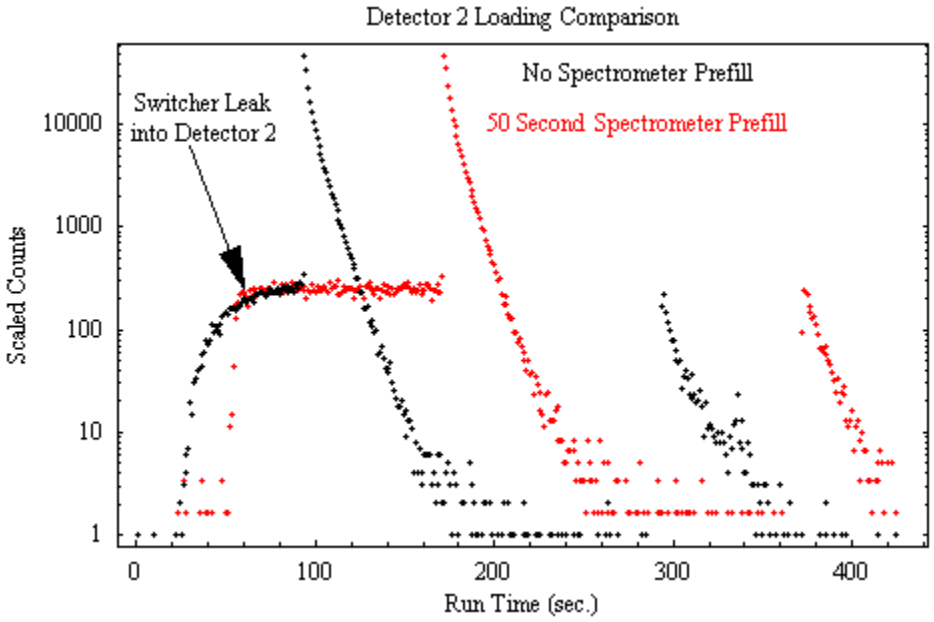

Figure 6-7 Detector 2 loading comparison: Some of the UCN that leak through the gaps in the switcher guide reach Detector 2. The signal of Detector 2 before the tall peaks in the figure is a monitor of the UCN density in the guide.

6.2.2.4 Aluminum Foil Holder/Pumping Port/Metal to Quartz Junction

A special coupler connects the PNPI guide coming from the switcher to the quartz guide and the pumping system. In addition to mechanically coupling these guides, the coupler can separate the PNPI guide from the quartz guide with a thin aluminum window. The window is there to separate the vacuum into semi-clean and clean vacuums, and the pumping port is on the quartz guide side of the window to pump the clean side. There is an area of exposed stainless steel in the coupler with unknown UCN transport properties. Also, UCN can enter the vertical pumping port and be partially trapped there. The PNPI guide has an OD and ID of 81 and 78 mm, respectively, while the quartz guide has an OD and ID of 70 and 64 mm, respectively.

The aluminum window separating the two systems increased the drain time of UCN from the trap, as did the vertical pumping port. To eliminate these problems, the window was removed and a valve was installed that allowed the pumping port to be blocked during runs. Eliminating the window connected the vacuum system of the switcher and PNPI spectrometer to the quartz test guides; this resulted in a poor vacuum for the depolarization runs of about 10^{-4} mbar. Also, the valve in the pumping port was not used in the data taking runs.

6.2.2.5 Quartz Guide

The experiment used four quartz guide sections to get UCN from the foil to Detector 3. Two 94 cm long PLD DLC coated quartz guides were used in the test section. The first guide started at the coupler and went through the PNPI polarizing magnet; at the end of the second guide a quartz plate with a 0.94 cm diameter hole in its center formed the end of the test guide and trap. After the aperture, two sections of guide led to Detector 3; an additional DLC coated quartz plate was also used in this section.

Only one set of guides was tested in the depolarization experiment, although several others were on hand. Both guides were made from Heraeus Amersil quartz tubing. The first guide was H1, which was coated with less than 50 nm of DLC and not terminated with deuterium. H2 was the second guide and its coating was thicker than 50 nm and terminated with deuterium. The aperture coating was also terminated with deuterium as were the guides to Detector 3.

6.2.2.6 Guide Monitoring Port

The 9.4 mm aperture at the end of the trap is the monitoring port for the UCN trap. UCN that leave the trap via this port enter a 20 cm long horizontal guide beyond the trap. This guide has a PLD DLC coated quartz plate at the far end and a square hole in the bottom near the plate. This square hole leads downward to a vertical PLD DLC coated quartz guide; at the bottom this guide is a special copper coupler with a pumping port that connects the guide to the LANL ^{3}He detector. The hole in the bottom of the horizontal section has an area of about 9 cm^2, but due to misalignment this was reduced to ~4 cm^2. The remainder of the hole was blocked with a piece of Be/Cu foil. Since the surface area

of the aperture is 1/6 that of the hole leading down to the detector, there is about a one in six chance for UCN entering the horizontal section to re-enter the trap rather than the hole down to Detector 3. It should also be noted that, UCN that depolarize on the Be/Cu foil, can reenter the trap (via the aperture) and be counted as depolarized UCN.

6.2.2.7 Magnetic Field

The PNPI superconducting solenoid magnet used in the previous depolarization experiments was used again in this experiment. With the power supply provided by Oliver Zimmer a 5 Tesla field was achieved. At five Tesla, UCN with energies up to 300 neV can be polarized; this is well above the average energy of UCN stored in the spectrometer (150 neV) but still below the ^{58}Ni critical velocity (335 neV). This difference allows UCN of the trapped spin–state to enter the trap through the field; these high–energy UCN should be lost since the material potential of the trap is below 300 neV.

A set of six copper coils were used to make a holding field tailored for the AFP spin flipper. The coil spacing was designed by Jun Hua at CalTech. The actual positions of the coils are given relative to the center of the PNPI magnet in Table 6-2 and shown in Figure 6-8. Two HP 50 amp DC power supplies were used to power the coils. A set of light bulbs in parallel with the fifth and sixth coils allowed fine-tuning of the field at the AFP position near the fourth coil. The measured field strength at the AFP resonance point (76.5 cm from the 5 Tesla point) was 521 G, and the gradient was 1 G/cm.

Magnetic Coil Positions							
Coil	PNPI	6	5	4	3	2	1
Position (cm)	0	55.5	66.7	81.5	104.7	119.1	130.7
Turns	~3000	~100	~150	~150	~150	~150	~100
Amps (A)	~300	~34	~34	~40	~40	~40	~40

Table 6-2 Magnetic Coil Positions: This table lists the position, number of turns, and current for the coils used to produce the magnetic field in Figure 6-8.

The axial field strength shown in Figure 6-8 was obtained by using the coil spacings, currents and geometries in Table 6-2 and fitting the resulting field to the 521 gauss measurement at the AFP resonance point. The axial field profile shown in this figure is used to make estimates of trap length and high field trapping; while a 3-D calculated field is used in the Monte Carlo simulations. A full mapping of the field was not possible at the ILL, but measurements were made (with a handheld probe) in regions with a field strength below 1.5 Tesla.

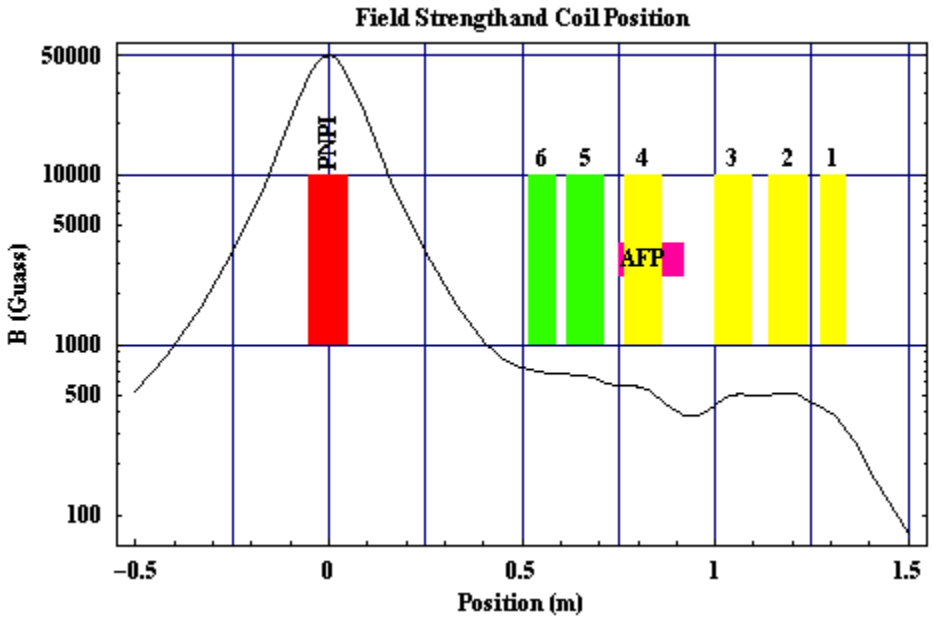

Figure 6-8 Field strength and coil position: The tall colored rectangles represent the magnetic coil positions used to calculate the axial magnetic field shown. The red coil is the PNPI SCS, the current in the green coils was adjusted to lower the field gradient at the AFP. This profile was only fit to the field strength quoted at the AFP resonance point.

6.2.2.8 AFP [161]

The adiabatic fast passage spin-flipper (AFP) is a birdcage resonator design RF oscillator.[162] The 17 cm long AFP was made on a Teflon sheet so it could be wrapped around the 7 cm OD quartz guide. The AFP was operated at 1.52 MHz and positioned as shown in Figure 6-8. The resonance point was about 76.5 cm from the center of the PNPI solenoid.

The longitudinal field gradient was about 1 G/cm, but no information on the radial gradient was recorded. From a set of measurements taken at the top and bottom of the guide (with the PNPI SCS at 2.5 Tesla and no holding field) a difference of about 5 Gauss across the guide could be measured.

6.2.2.9 Vacuum

The initial goal of the vacuum system was to have a pressure of $<10^{-6}$ torr in the trap and to have this vacuum separated from the switcher and spectrometer vacuum. To accomplish this, the systems were separated by a thin aluminum foil window at the junction of the PNPI and quartz guides. The spectrometer side of the vacuum was pumped by a turbo at the top of the spectrometer; this turbo was backed by a scroll pump. A 4-stage diaphragm pump provided differential pumping for the absorber rod feed–through at the top of the spectrometer. The vacuum on the trap side of the experiment was maintained by three dry turbo systems.

The trap was pumped at the PNPI/quartz junction and at Detector 3. In addition, differential pumping of the guide couplers was done by a third dry pumping station. The primary trap pumping was done by a dry, 500 l/s turbo, backed by a 600 l/s scroll pump. The pressure was monitored near this turbo with a cold cathode gauge. Secondary pumping of the trap was done through the aperture by a dry turbo station connected to a port on the copper coupler between the quartz guide and Detector 3. A second cold cathode gauge was also located at this port.

All the joints on the trap side of the guide system were designed to have differentially pumped double o-ring seals. The coupler used for connecting the quartz guides is shown in Figure 6-9. The small KF connections on the coupler provided differential pumping between o-rings and were connected to a second Varian Minuteman pumping station.

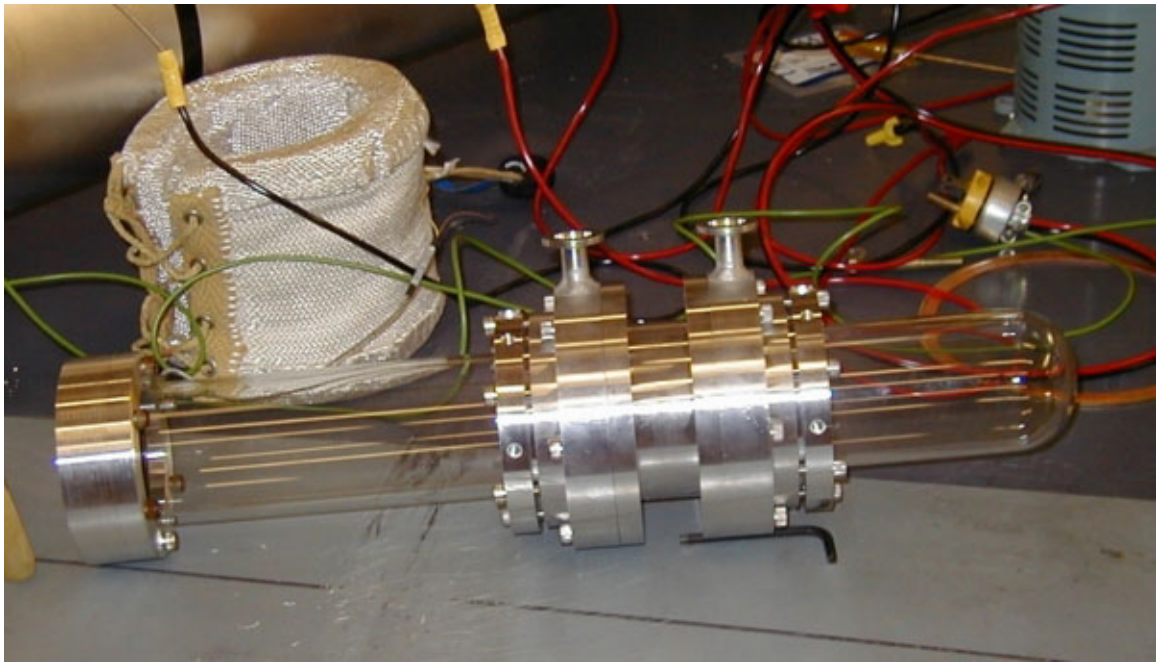

Figure 6-9 VT and LANL quartz guide coupler photo: The large coupler with differential pumping ports is the design used to couple the quartz tubes in the UCNA depolarization experiment. The coupler on the left is a VT guide coupler.

The two sides of the vacuum system had to be pumped down at the same time so that the 12 μm thick aluminum window would not break due to a pressure differential. This was done by connecting the two main scroll pumps, until a pressure under 100 Torr was reached. At this point the connection between the systems was valved off.

The vacuum in the trap side was good with all three turbos, but there were leaks. At various times there were leaks between the differential and main vacuum systems. Still a pressure of below 10^{-6} mbar was achieved. Without the Detector 3 turbo, the pressure at Detector 3 was about two orders of magnitude higher than at the main turbo.

After the vacuum separating foil was removed the vacuum got much worse. Just before the foil was removed the vacuum was at $7x10^{-6}$ and $6x10^{-6}$ mbar at the main pump and Detector 3 respectively. After removal of the foil, the same two gauges read $1.5x10^{-4}$ and $2.5x10^{-4}$ mbar. The gauges were calibrated just before this measurement by the ILL

vacuum shop. The pressure in the trap remained in the low 10^{-4} mbar range for all the depolarization measurements.

6.2.2.10 Detectors

Three ^{3}He neutron detectors were used to monitor the depolarization experiment. Detector 1 monitored the spectrometer; it was provided by the PNPI group, as was Detector 2. Detector 2 counted the UCN coming out of the trap; it had the lowest background rate of the three detectors. Detector 3 counted the UCN that exited the trap through the aperture; it was a LANL designed detector. Detector 3 ran in proportional mode with a gas mixture of ^{3}He and CF_4; the CF_4 provides gain with low neutron absorption.[166]

The rates seen by the three detectors varied during the experiment due to constant adjustment by the collaborators. Some of the adjustments are listed in the logbook, but some are missing. The adjustments were made in an attempt to lower the background in the detectors. Detector 3 received the most adjustment during the experiment. Detector 1 was prone to random rate changes, but is not needed for the depolarization analysis.

6.2.3 Estimates of Rates and Sensitivity for the UCNA Depolarization Experiment

In this section estimates will be made of how well the UCNA depolarization experiment will perform. First the quantities needed to calculate the depolarization rate will be presented (Number of UCN in the trap, bounces per second, lifetime in the trap, and trap filling and draining times), followed by determination of what sensitivity the experiment will have on determining the UCN depolarization rate. Finally the magnetic field's affect on the experiment will be estimated. Studies of this type must be done in order to design UCN experiments.

6.2.3.1 Number of UCN in the Trap [41, 42]

Trap densities from the first and second Serebrov depolarization experiments can be used to estimate the density of UCN in the UCNA depolarization experiment. The only

density given in the first experiment is 6 UCN/cm^3. In the second experiment, assuming a constant UCN density throughout the spectrometer (neglecting gravity), the density was again 6 UCN/cm^3; and the density of polarized UCN in the trap was 1.7 UCN/cm^3 for UCN with less than 100 neV of kinetic energy. Since our experiment uses the same setup as the second experiment we expected between 1.7 and 3 polarized UCN/cm^3 in the trap.

The number of UCN in the trap can be estimated using this density range and the trap volume. The depolarization guide between the magnet and the aperture is ~140 cm long, this gives a volume of 140 π 3.2^2~4500 cm^3. Using a density of 2 UCN per cm^3 there would be 9000 polarized UCN in the trap. These UCN are free to enter and leave the trap, but ~9000 will be in the trap region after equilibrium is reached.

The trap density will increase and decrease rapidly during filling and emptying, the time constant of this density change can be estimated using kinetic gas theory. The time constant for filling or emptying the trap through an aperture is the ratio of the volume/conductance; using the quartz guide volume and the conductance of an 6.4 cm diameter aperture the 1/e time is ~1.5 seconds (1/e~6500 cm^3/((510 cm/s*π*3.2^{2}cm^2)/4).[167] This does not take into account the transport down the meter of PNPI guide, which lowers the conductance and raises the 1/e time to ~12 seconds. Since UCN are not an ideal gas and tend to have specular collisions in the guide these are only upper and lower limits.[22]

6.2.3.2 Bounces per Second

The bounces per second (BPS) in the trap can also be estimated using kinetic gas theory or by making assumptions about the velocity distribution in the guide. Kinetic gas theory says that the flux is V_{av} times the cross sectional area divided by 4. Multiplying this by the UCN density gives the UCN per second that pass this area. The BPS rate in the trap is estimated using this method to be about 7x10^5, (BPS=2*UCN/cm^3*510*cm/s*(140*cm*π*6.4*cm*+Pi* 3.2^2*cm^2)/4). The BPS rate can also be found looking at the average UCN from the velocity distribution: if we assume a average path length in the guide to be $\sqrt{2}\,diameter \approx 9\,cm$ and the average velocity to be

510 cm/second, then the average time between collisions is $9/510=18x10^{-3}$ seconds. Using the 9000 UCN calculated to be in the trap there would be about $5x10^{5}$ BPS in the trap. The bounces per UCN per second would be 81 and 56 for the first and second methods respectively.

6.2.3.3 Trap Lifetime

The lifetime of a trapped UCN is much lower than the lifetime of a neutron (~887 seconds), this is the result of several loss mechanisms. The aperture to Detector 3 is a large source of loss but other smaller sources also contribute and estimates of these loss rates can be made.

The lifetime due to the aperture can be estimated using kinetic theory of gas flow through an aperture to be 49 seconds, $(1/E=TrapVolume/510*\pi*(.94/2)^2)$. If the conductance through half of the trap is added to the aperture conductance, the lifetime increases to 61 seconds.

Typical loss per bounce probabilities seen on various surfaces range from a 10^{-3} to 10^{-5}; for the average UCN in the trap this would give a lifetime of 96 seconds – assuming the loss for graphite in Table 6-1 and 56 BPS.[22, 23]

There are two joints between the quartz in the trap region, if the gap area is assumed to be 100% lossy then a lifetime due to the gap area can be estimated using an equal area aperture and kinetic gas theory. The lifetime due to gap is 0.88 (s)/GapLength (cm). Assuming a rather small total gap of 0.01 cm the lifetime would be 88 seconds.

Trapped UCN that depolarize also are lost from the trap. Assuming the depolarization probability for graphite from the second experiment in Table 6-1 and 56 BPS the lifetime would be 3027 seconds.

If these lifetimes are independent, they can be added like resistors in parallel – $TrapLifeTime=(1/3027+1/88+1/96+1/61+1/887.)^{-1}$. So, using these predicted lifetimes,

the trap lifetime would be 25 seconds (To compare to the best one could conceive of achieving lower the loss per bounce to the level of beryllium and the total gap size to 0.0025 cm (0.0025 cm ~ 0.001 inch) and the lifetime increases to 41 seconds – TrapLifeTime =$(1/3027+1/346+1/255+1/61+1/887.)^{-1}$).

6.2.3.4 Trap Drain Time

The lifetime (drain time) of free UCN in the trap can be estimated by using kinetic theory; assuming the PNPI guide gives zero resistance to flow will give a lower bound and assuming normal gas conductance in it will give an upper bound. The minimum conductance is calculated by assuming it is only due to the section of quartz guide between the trap and the PNPI guide; This gives a 1/e time of TrapVolume/TubeConductance~2 seconds; adding the conductance through the PNPI guide this increases to 10 seconds. This does not take into account the bends in the PNPI guide or the time spent in the pumping port – doing this would increase the drain time.

6.2.3.5 The Sensitivity of the Depolarization per Bounce Measurement

The sensitivity of the depolarization measurement depends on the lifetime of trapped UCN, the depolarization rate, and the emptying time of the trap. The ratio of the signal (depolarized UCN) to the noise (non-depolarized UCN remaining in the trap) is a measure of the experiment sensitivity. If this noise can be subtracted without uncertainty, very low depolarization rates can be measured. Detector backgrounds also affect the sensitivity if they have much uncertainty. In the following sections it will be assumed that the noise cannot be subtracted from the signal and the detector background will be neglected in the signal–to–noise ratio.

If in the first depolarization method (Section 6.2.1) the 1/e fill time of the trap is short compared to the fill time, then the number of UCN in the trap can be represented by this evolution equation $\frac{dN_t[t]}{dt} = N_f \times P_d - N_t[t] \times P_l$ ($N_t[t]$, is the number of trapped UCN; N_f, the number of free UCN in the trap; P_d, the probability of depolarization per second; P_l, the probability of loss from the trap; depolarization of trapped UCN has been

neglected). This has solution a $N_t[t] = (P_d/P_l) \times N_f \times (1 - E^{-P_l * t})$, so the number of trapped UCN is limited to $N_t[\infty] = N_f * P_d/P_l \sim 120$ UCN for a 40 second trapped lifetime and P_d=6x10^6. Now, if the filling is stopped and trap is drained into Detector 2, there are 9000 UCN to drain while the trapped UCN are slowly lost; the ratio of the number of trapped UCN divided by the number of free UCN still in the trap is a signal–to–noise ratio. After this ratio has reached around 1%, the trap can be drained using the AFP; the evolution of this ratio, $\frac{9000 \times \mathrm{Exp}[-t/9]}{120 * e^{-t/40}]}$, is shown in Figure 6-10, this assumes a 9 second 1/e drain time for the free UCN in the trap.

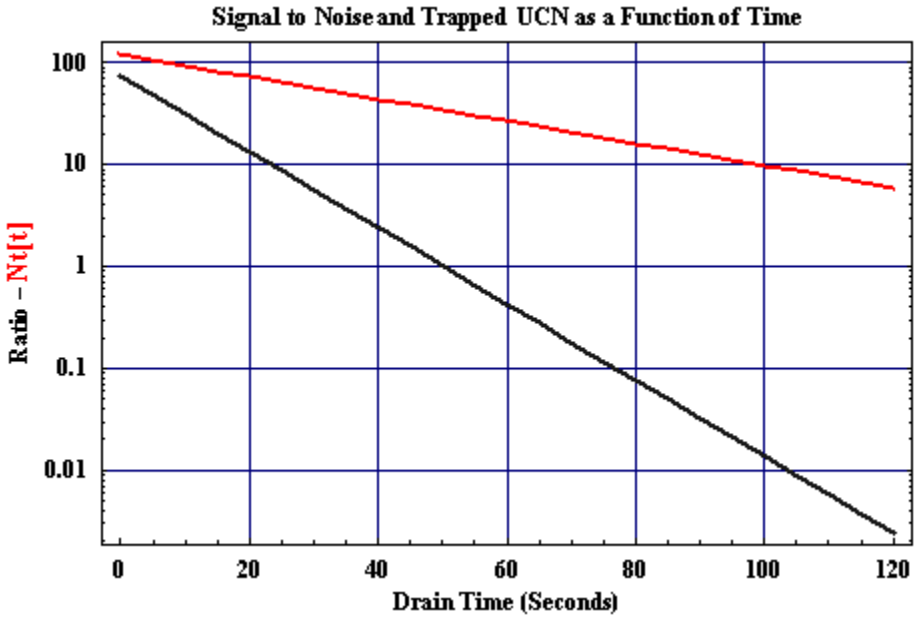

Figure 6-10 Signal to noise and trapped UCN as a function of time: In the first method to find the depolarization rate, a few UCN are trapped and held (red line) until most of the free UCN drain from the trap. The black line shows the ratio between the number of free and trapped UCN. This ratio is an estimate of the signal–to–noise ratio that the experiment will have at various dump times. After 100 seconds of draining the trapped UCN will outnumber the free UCN by 100 to 1.

Assuming that 75% of the trapped UCN can be emptied by the AFP, a 90% transport efficiency, a 50% detection efficiency and a 105 second drain time, about 3 depolariaized UCN will be counted. As the depolarization rate increases, the sensitivity of the experiment goes up, Figure 6-11 shows this for a 100 second drain time. From the graph, at a depolarization per bounce probability of 2x10^{-6}, about 1 UCN will be seen per run

with a 5% background from remaining free UCN. Since the AFP emptying of the trap takes some amount of time, the background noise in the detector can also be a problem. If the AFP emptying time is 50 seconds and the detector background rate is 0.02 Hz, the detector background will equal the signal. Subtraction of these backgrounds will increase the error in the number of depolarized UCN and the final rate. This will be covered further in the analysis of the data.

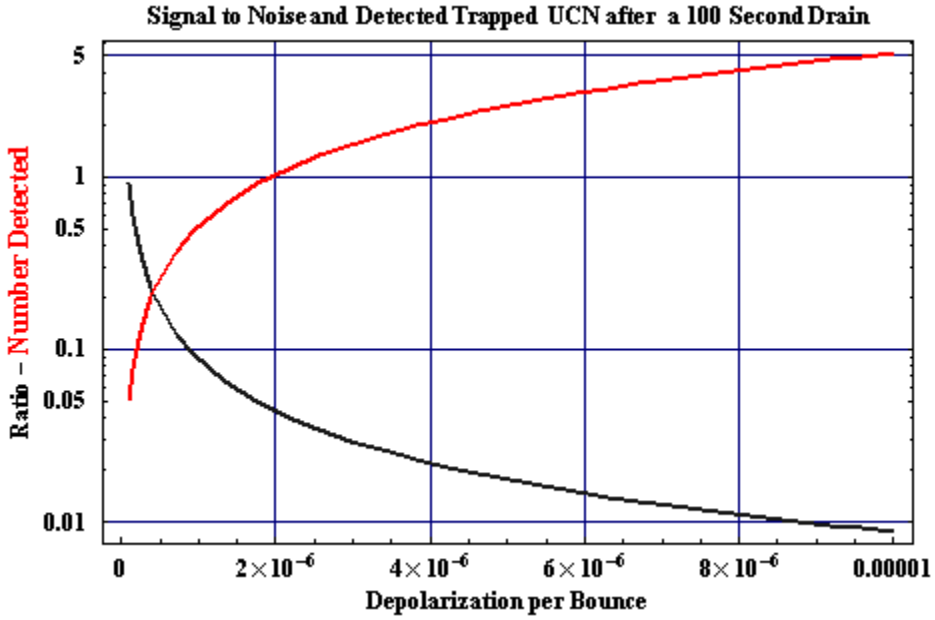

Figure 6-11 Signal to noise and detected trapped UCN after a 100 second hold: In this figure the drain time is set at 100 second. The signal–to–noise ratio and the total number of detectable, trapped UCN are plotted for various depolarization rates. For a depolarization rate of 10^{-6} the ratio is at 10%, that is one in ten counted UCN will be a free UCN, and less than one trapped UCN will be counted per cycle.

The sensitivity of the second method (where a large trapped population of UCN is monitored to see if any that depolarize) is limited by the number of UCN that can be trapped, the drain time, the efficiency of the AFP, and the efficiency of the transport. The number of UCN trapped depends on the efficiency of the AFP, but for this example it will be assumed to be 100% efficient (and located in the middle of the trap). If the trap has 9000 UCN in it when the AFP is turned on one half of them will be trapped; these will reach an equal density in the trap after a few second, and the number of free UCN will again reach ~9000 after a few 1/e filling times. At this point there will be 4500, trapped plus 9000 free UCN equally distributed in the trap; when the AFP turns off, half of each population will be trapped, (4500+9000)/2=6750. As before, the populations in

the trap decay with different lifetimes; 40 and 9 seconds will be used for the trapped and free UCN respectively. The time to achieve a 1% signal–to–noise ratio is given by solving $(6750\ e^{-t/9})/(DPB\ BPS\ 6750\ e^{-t/40})=.01$ for t. Using a depolarization per bounce of $5.9x10^{-6}$ and 56 BPS this will take about 150 seconds.

At 150 seconds there will be about $6750\ e^{-150/40}=159$ trapped UCN. Using the same DPB and BPS as above there will be 159*DPB*BPS=.05 UCN depolarized per second. Assuming as before, 0.9 and 0.5 transport and detection efficiencies it would take 40-50 seconds to see one depolarized UCN in Detector 2. Again the background noise in the detector would be about the same assuming a 0.02 Hz rate. Figure 6-12 shows that the signal–to–noise ratio is lower in this method for a given DPB, and assuming a 10 second sampling period the signal is about the same.

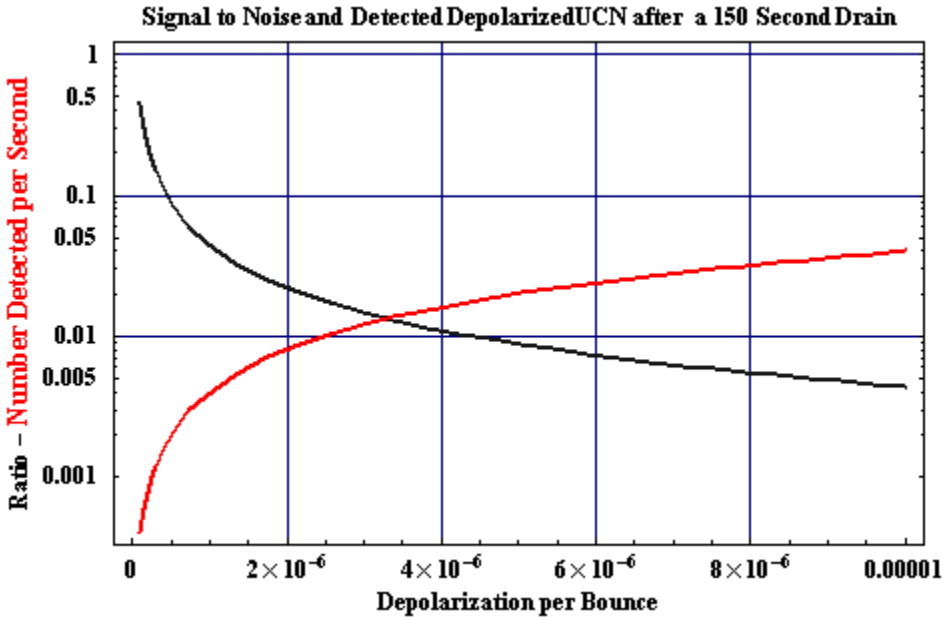

Figure 6-12 Signal to noise and detected depolarized UCN after a 150 second drain: This figure is similar to Figure 6-11, it shows that the second method has a lower signal–to–noise ratio.

After collecting this 10 second signal, the trap must be dumped and counted. This is done with the AFP as with the first method. The number that the AFP removes from the trap depends on its efficiency. Unlike the first method, the efficiency does not drop out in the ratio determining the DPB, since the depolarized UCN are not dumped with the

AFP. Of course, just counting the trapped UCN (and taking into account losses due to the aperture) an upper limit on the DPB will be found.

With the estimated UCN density of 2 polarized UCN per cm^3 in the trap, both methods appear to be able to see depolarization at or below the methods used in the previous depolarization experiments. Assuming the unloading efficiency of the AFP can be determined, the second method offers a better signal–to–noise ratio due to the fewer free UCN remaining in the trap. Still, since the first method requires the second to predict the number of UCN in the trap during filling, both will need to be done (or only the second).

6.2.3.6 UCN Density Asymmetry in the Trap Due to the Magnetic Field

The density of UCN is not constant along the length to the trap even after equilibrium is reached; this is due to the magnetic field gradient that forms the trap. This gradient accelerates the free spin–state into the trap; and it decelerates and stops the trapped spin–state. Since the acceleration and deceleration occur over some distance, the density of UCN in this region is affected. Estimates of the density gradient of each spin–state can be made by looking at the affect of the longitudinal magnetic field on the average velocity UCN. For this, the field in shown Section 5.2.2.7 will be used with an average UCN velocity of 510 cm/second.

The density distribution of trapped UCN is proportional to the time spent in different parts of the trap. To calculate the time spent in different parts of the trap the following energy relation can be used: $E_f=V(x)+E_k(x)$, E_f is the UCN's kinetic energy when it is free of the magnetic field, $V(x)=\pm\mu_n \cdot B(x)$ is the potential energy due to the magnetic field, and $E_k(x)=1/2\ m_n v(x)^2$ is the kinetic energy of the UCN. This can be solved for the velocity as a function of position, which in turn leads to an integration that gives the time spent in the region integrated over:

$$E_f = V(x) + E_k(x)$$

$$E_f = \mu_n \cdot B(x) + \frac{m_n\, v(x)^2}{2}$$

$$v(x) = \frac{dx}{dt} = \sqrt{\frac{2}{m_n}\left(E_f - \mu_n \cdot B(x)\right)}.$$

$$t_1 - t_0 = \int_{x_0}^{x_1} \frac{dx}{\sqrt{\frac{2}{m_n}\left(E_f - \mu_n \cdot B(x)\right)}}$$

The length of the trap for a given UCN depends on its velocity in the direction of the field. Solving the equation E_f=V(x) for x gives the turning point for a given kinetic energy UCN; the length of the trap for 50 and 175 neV UCN are shown in Figure 6-13. Using the equation above, the time spent in various sections of the trap can be found; the density distribution of UCN in the trap with a given energy is proportional to this time. Figure 6-14 shows the density distribution for UCN with 135 neV of kinetic energy outside the trap; both trapped and free spin–states are shown, and they show opposite trends.

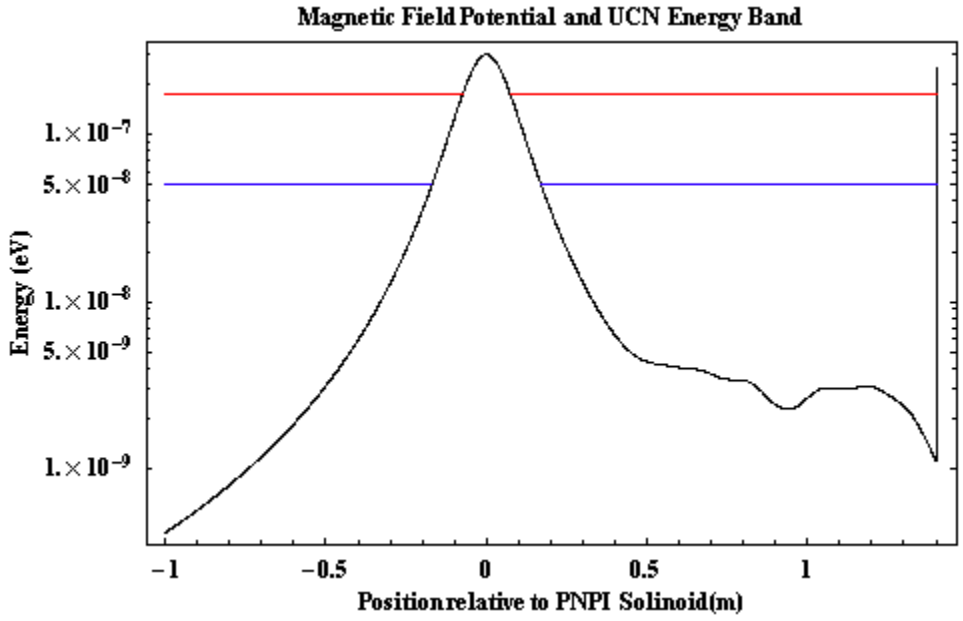

Figure 6-13 Magnetic field potential and UCN energy band: The trap length is longer for higher energy trapped UCN. The red line on the right of the peak shows the region of the trap accessible for 175 neV UCN, and the blue line is for 50 neV UCN. The black line shows the barriers due to the magnetic field and the aperture plate.

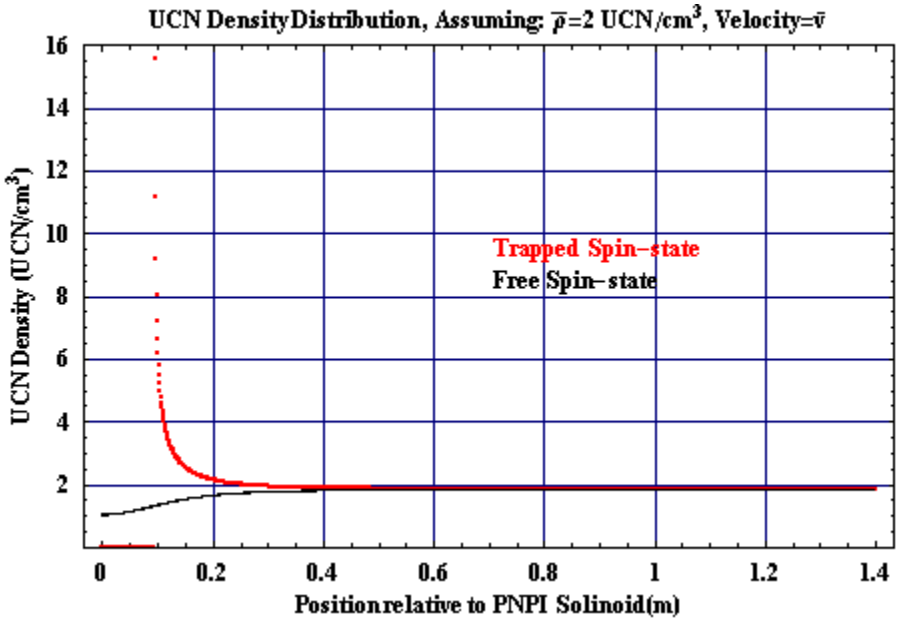

Figure 6-14 UCN density distribution, assuming 2 UCN per cm^3 and average velocity: This figure shows the density variation along the axis of the trap. The red line shows the distribution of trapped UCN being greatest near the PNPI SCS where they slow, stop and accelerate away. In this same region the free UCN show a deceased density due to increased kinetic energy from the attractive potential due to the PNPI SCS.

The most important value for loading/unloading the trap is the number of UCN on each side of the AFP; the percent of UCN in the trap region on the aperture half of the trap is shown in Table 6-3 for various energies. The number of trapped UCN is about equal on

Asymmetry in the UCN Population due to the Magnetic Field		
UCN Energy	Percent of UCN on the Aperture Side of the AFP	
neV	Trapped	Free
60	51.6	57.7
87.5	50.7	56.3
136	49.6	54.8
175	48.8	54
250	47	52.7

Table 6-3 Asymmetry in the UCN population due to the magnetic field: This table shows the asymmetry in the number of UCN in the trap on each side of the AFP. The percentage is the number on the aperture side of the AFP compared to the whole trap. The trap length is defined by the trapped spin–state at each energy.

each side of the AFP; this is very true of the average energy UCN, 136 neV. The free UCN spend more time on the aperture end of the trap, this will increase the number that can be loaded by the AFP above the constant density estimate used in Section 1.2.3.1.

6.2.3.7 Trapping in the High Field Region

It is possible to trap UCN of one spin-state in the high magnetic field region inside the PNPI solenoid; depending on the lifetime of these trapped UCN they may effect the depolarization measurement. The affect on the depolarization measurement depends on both the number trapped and the time they are trapped. For example, in the second depolarization method, if the PNPI well lifetime is comparable to the trap lifetime, the signal seen by Detector 2 could be due to UCN escaping the well rather than depolarization in the trap. Of course, the effect depends on the number trapped in the well. Both spin–states can be trapped in the well; the free state can only be temporarily trapped, while the state that is stopped by the field can be trapped for long periods of time.

The magnetic field gradient forms an attractive potential well for the free spin–state [Figure 6-16]; this well can trap free UCN that undergo a non–specular collision while in the high field region. UCN that are attracted toward the well gain velocity in the axial field direction; if the UCN then undergoes a non–specular scatter such that its kinetic energy in the axial direction is not greater than the potential due to the field at that point it will become trapped. The total energy of UCN is still greater than the trap depth, so by another non–specular scattering it can leave the trap at some later time. Since UCN in the trap have increased kinetic energy, there is a high probability a trapped UCN will not be reflected by the wall and be lost before it scatters out of the trap. An estimate of the number of UCN that are trapped by this mechanism can be made by looking at a special case.

To estimate the probability of trapping and the trap lifetime, the average velocity UCN (5.1 m/s at 45 degrees to the guide axis) can be used. For the case where UCN sees the high field region as an attractive potential (the free spin–state) the probability of trapping

is less than the probability of non–specular scattering. The number of bounces in the high field area is reduced from 100/6.5~15 per meter since the forward velocity is increased [Figure 6-15], so 15 bounces per meter is a conservative number. If the high field region is defined as above one Tesla then it is ~0.3 meters long and there would be on average less than five bounces in this region, so the probability of trapping would be less than $1\text{-}0.995^5$ ~2.5% for a 99.5% specular surface. Only scatters that result in the sum of the axial kinetic energy and the potential energy being negative result in trapping. Assuming the diffuse scattering is random around the direction of travel, half the UCN will lose axial kinetic energy. Further, if all of these are assumed to be trapped (an over estimate) then less than 1.25% of the UCN passing the region will be trapped. The flux through the region is $\frac{\text{density velocity CrossSection}}{4} = \frac{2\text{UCN}}{\text{cm}^3}\,\frac{510\text{cm}}{s}\,\frac{\pi\,3.2\,\text{cm}^2}{4} = 8203$ UCN per second, so about 8203x0.0125~100 or less UCN will be trapped per second. Since the average transverse velocity is unchanged by the field, there will still be 56 wall collisions per second. Assuming 99.5% specularity and 50% probability of untrapping per diffuse collision the trap lifetime would be 7 seconds. This would lead to an equilibrium population in the trap of ~750 after 40 seconds of filling UCN. This estimates does not take into account that some of the trapped UCN will have too much kinetic energy to be stopped by the DLC coating. Since the lifetime is comparable to the predicted drain time of the free UCN from the trap, the effect should not cause background above the normal draining.

There is a possibility that half the UCN in the well that depolarize will leave and be caught in the trap, but since 750 is less than 10% of the predicted number of UCN in the trap they will add at most 5% to the depolarized population in the trap. This number is further decreased by the fact that free UCN that depolarize in the well gain up to 300neV of kinetic energy which will make some untrappable.

UCN that see the potential due to the field as a barrier can become trapped when they non-specularly scatter and/or depolarize in the high field region since the barrier turns into an attractive potential. These depolarized UCN can be trapped temporarily like the

free spin-state or for a long period of time depending on the amount of energy they have when they depolarized. For example, if a UCN loses all of its kinetic energy to the field and then depolarizes it will drop into a negative energy state in the well, see Figure 6-16. In this case the UCN will be trapped until it depolarizes again or is lost. UCN that have more kinetic energy than potential energy when they depolarize can only be trapped temporarily in the high field trap, whereas UCN with less kinetic energy than potential at the point of depolarization will be trapped until they depolarize again or are lost.

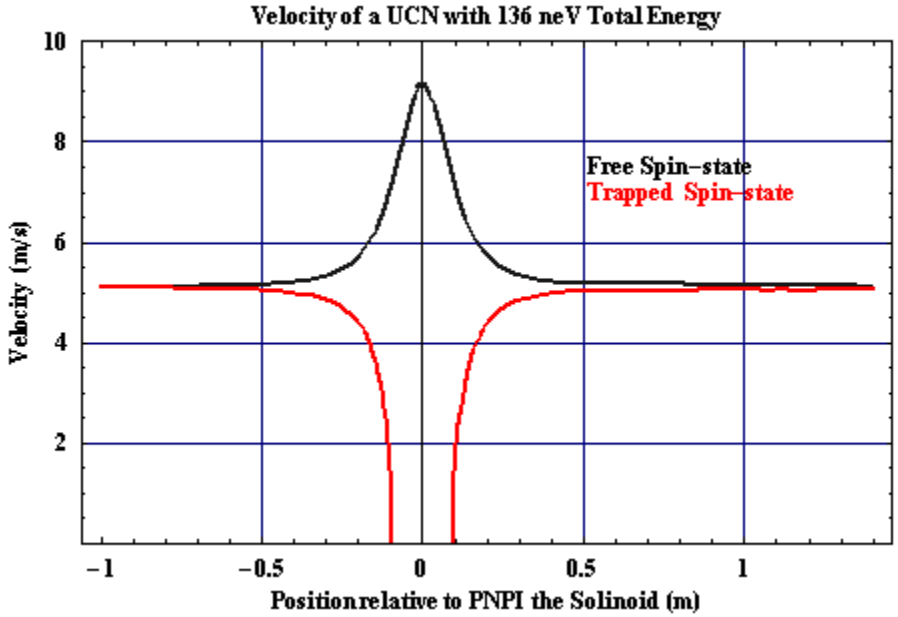

Figure 6-15 Velocity of a UCN with 136 neV total energy: This plot shows the velocity of a UCN, that has an initial velocity of 5.1 m/s outside the well, as it passes through the well. One spin–state is stopped while the other is accelerated to nine m/s; this is well above the 7-7.5 m/s critical velocity of the DLC coating.

The trapping of UCN that see the field as a barrier by depolarization is different than in the free UCN case. The probability of depolarization is much smaller than the probability of a non–specular scatter (1 in 10^6 compared to 1 in 100). The number of bounces is also harder to determine since the UCN is losing axial velocity. Using the integral from Section 1.2.3.6 for the average UCN (510 cm/s at 45 degrees off axis) the time spent in the high field region is 0.046 seconds per cycle, which gives 2.6 collisions per cycle in the trap. 2.6 collisions is 7% of the collisions per cycle in the main trap, so less than 7% of the UCN that depolarize in the main trap will be trapped in the PNPI solenoid trap. Only a fraction of the UCN that depolarize in the high field region can be

trapped long term; these are the ones that have less kinetic energy than potential energy at the time of depolarization. Half of the UCN in the trap have more radial than axial velocity. These never have less kinetic than potential energy while in the high field region, so less than half of the 7% can be trapped long term. UCN that come from the spectrometer and are stopped by the polarizing field can also depolarize and be trapped in the high field region. The number of UCN entering the high field region can be calculated using kinetic theory as follows: $rate = \frac{density\, V_{av}\, area}{4} = 2\frac{UCN}{cm^3}\frac{510\,cm}{\sec\sqrt{2}}3.2^2\,\pi\,cm^2\,\frac{1}{4} \sim 1850\ UCN/\sec$. Assuming the same conditions as for the trapped UCN, there will be 2.6 collisions per stopped UCN. Over a hundred–second filling time there would be $1850(2.6)10010^{-5} \sim 5\ UCN$ that depolarize, and, as before, half of these could be trapped long term.

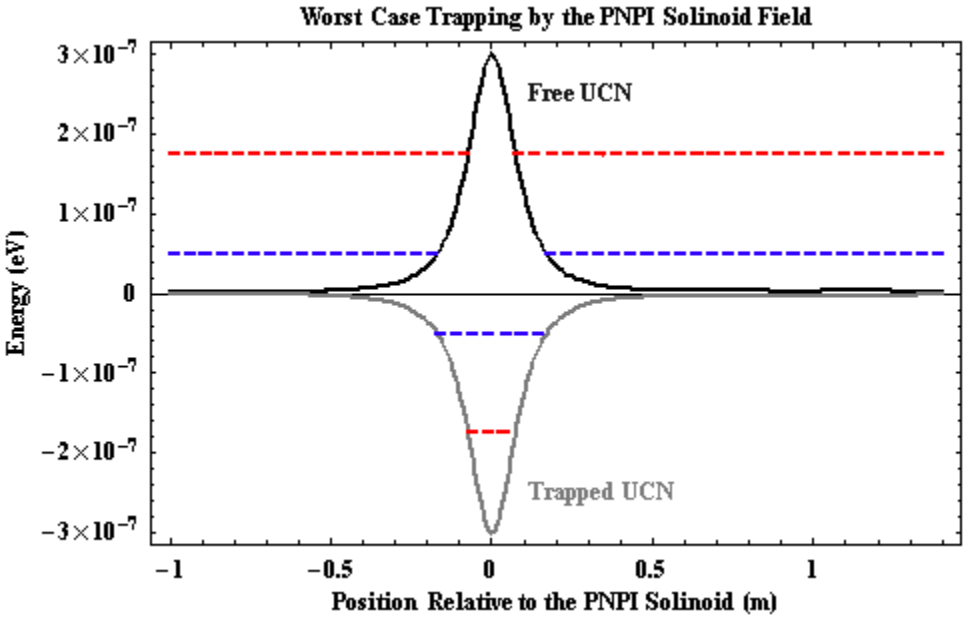

Figure 6-16 Worst case trapping by the PNPI solenoid field: The red and blue dashed lines on the top represent 175 and 50 neV free UCN, and the corresponding lines below represent UCN that depolarized when stopped by the potential and become trapped in the SCS potential well. The 50 neV UCN now has 250 neV of kinetic energy in the center of the well and the 175 neV UCN has a 125 neV max while trapped. UCN trapped in the well this way can only escape by depolarization or upscattering.

The short term trapping time is 7 seconds or less as in the case of the free UCN trapping. The long term trapping time is about 1800 seconds for a depolarization probability per

bounce of 10^{-5} and 56 bounces per second. This lifetime is greater than the 887 second lifetime of the neutron and that due to surface losses.

The effects of trapping in the high field region on the experiment can be estimated using these numbers. Since the filling and draining 1/e times for free UCN from previous sections are estimated at 2-10, seconds the 7 second short term trapping should not have much of an effect. The long term trapping of depolarized UCN from the main trap will cause at most a 3.5% effect on the depolarization rate seen. The long term trapping in general should be seen as a loss of UCN since they have a low probability of leaving the trap. In general, short and long term trapping should have very little effect on the depolarization measurement.

6.3 UCNA Depolarization Experiment Data Analysis

The UCNA depolarization experiment ran in two phases: the first phase was dedicated to lowering the trap emptying time, which ended with the removal of the aluminum foil; the second phase was dedicated to making runs to calibrate the system and looking for depolarization. Numbers for the BPS, trap lifetime, AFP efficiency and the number of UCN in the trap can be extracted from the data. Using these parameters the DPB can be found by both method one and two.

The effect of the aluminum foil on the trap filling time, draining time and maximum density was very noticeable. The foil position was definitely a design flaw in the experiment. The values for the BPS, trap lifetime, AFP efficiency and UCN density were close to agreement with the predicted values, although the density was a bit low at under one UCN per cubic centimeter.

Both method one and two provided values for the depolarization per bounce that were below 10^{-6}, which is better than reached in the previous experiments. The uncertainties of the two methods were about the same since there were many more cycles of data for the first method.

6.3.1 General Results for the UCNA Experiment

In this section the data from the experiment will be analyzed to look at how some of the components performed and to calculate the parameters needed to determine the depolarization rate. The vacuum separating foil and AFP will be analyzed to see how they worked. The wall collision rate, trap lifetime and number of UCN in the trap will be calculated for us in the depolarization calculation.

6.3.1.1 The Effect of Removing the Aluminum Foil

The aluminum foil in the pumping port worked well at separating the two vacuum systems, but it also increased the filling and draining times of the trap and lowered the density in the trap. The effect of the foil can be seen by comparing two identically timed runs in Figure 6-17, one before and one after the foil was removed; the timing of these runs is shown in Table 6-4.

5tlXXX-Oct. 24, 2001 and nf1XXX-Oct. 26, 2001			
Pre Fill (sec.)	Filter (sec.)	Trap Fill (sec.)	Drain (sec.)
2	50	30, 100	200

Table 6-4 5t1 and nf1timing table: This timing table show two times for the filling, but only the 100 second fill was used in this section. The XXX refers to some number of cycles.

The plots clearly show that the 1/e time for draining is decreased, as shown by both Detector 2 and 3 signals, and that the density in the trap is increased as shown by the Detector 3 signal before the peak. In addition to faster draining, the long tail due to partially trapped UCN is gone. Partially trapped UCN are ones that have just enough energy to pass through the foil if their velocity is forward directed – they can only escape the trap if they again hit normal to the foil surface. The trap density increased by 2.4 times when the foil was removed.

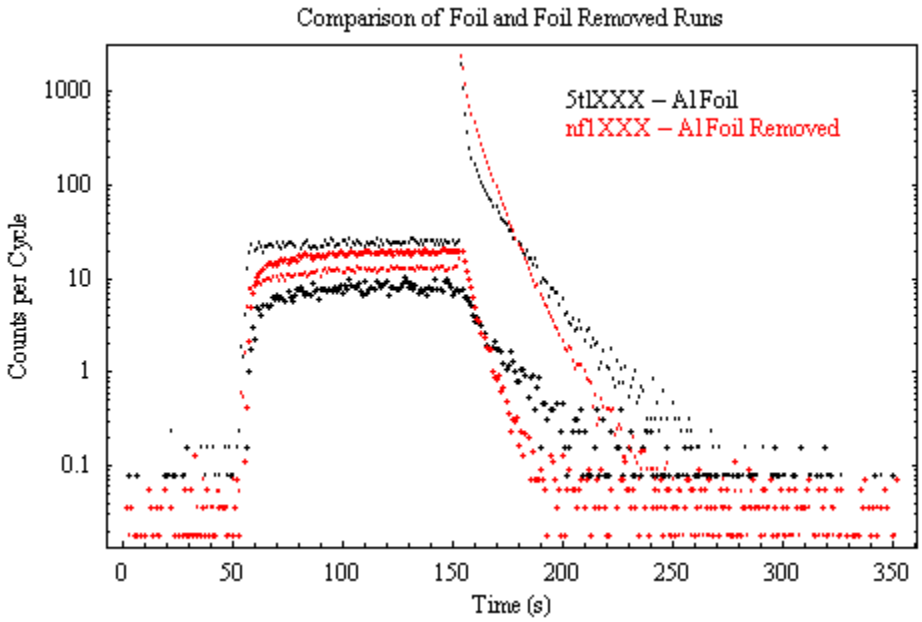

Figure 6-17 Comparison of foil and foil removed runs: This plot compares the signal from Detector 2 and 3 with and without the aluminum foil in place. The Detector 2 signal (small dots) shows a decrease before the tall peak with the removal of the foil; this is because the foil reflects many of the UCN – increasing the density of UCN in the switcher guide. The Detector 3 signal (larger dots) that monitors the trap density shows a UCN density increase of 2.4 with the removal of the foil. Both Detector 2 and 3 signals show that free UCN drain faster from the trap after the foil is removed (the region after the tall peaks).

6.3.1.2 Trap Collision Rate

In principle, the collision rate with the wall – or at least the end wall – can be obtained by looking at the rate in Detector 3, which monitors a known area of trap wall (the aperture). The difficulty comes in finding the efficiency of Detector 3 at monitoring the aperture. To get around this problem, an experiment can be done using an AFP loaded trap. If the trap is then drained of the free spin–state and the trapped UCN are unloaded using the AFP at two different times, then the difference in the number of UCN unloaded is due to losses in the trap. Figure 6-18 shows AFP unloading peaks from 140 and 200 second holding times. The aperture to detector two is the major source of loss; wall losses and the neutron lifetime are other sources of loss. If the wall loss is estimated, then the loss due to the aperture can be found using the neutron lifetime. Once the loss rate is known, the bounces per second (BPS) for the average UCN can be determined.

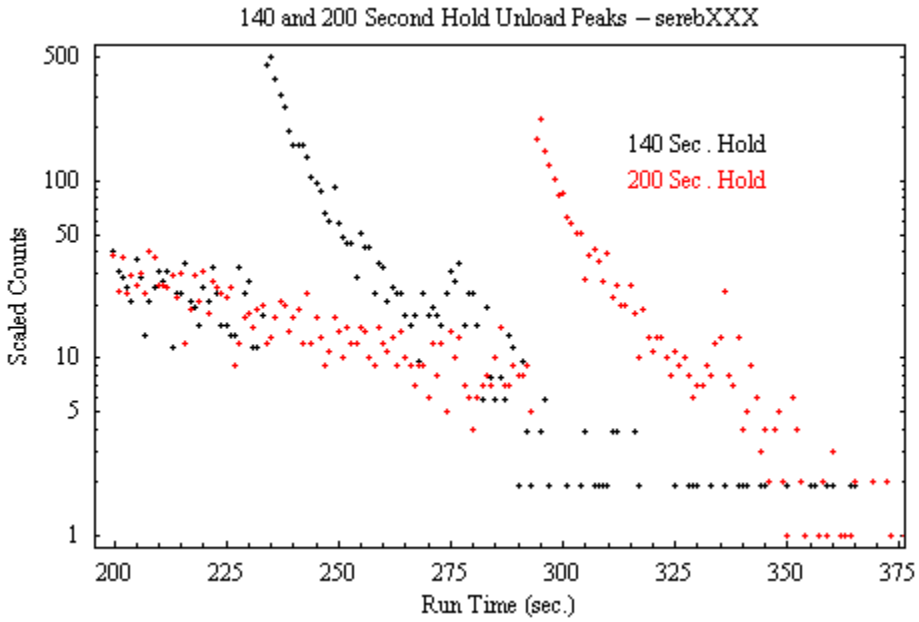

Figure 6-18 140 and 200 second hold unload peaks – serebXXX: This plot compares the number of UCN in the 140–second–hold unload peak (black) and the 200–second–hold unload peak (blue). Since the 140 second peak had only 12 cycles of data compared to the 23 cycles of the 200 second peak, the data was scaled by the number of free UCN seen by Detector 2 in the first 40 seconds of the unload. The difference in the number of UCN in the two peaks is the number lost from the trap during the additional hold time.

The first step in finding a BPS rate is to find the bounce per second rate at the aperture, BPSA. This rate is a function of time, since the number of UCN in the trap is declining. Since the aperture monitors the trap density, a good estimate of the rate is $\mathrm{BPSA(t)} = \mathrm{BPSA(0)}\, e^{-t/57}$, where 57 seconds is the trap lifetime determined in the next section. If it is assumed that the only loss mechanism is the aperture then $Peak1 - Peak2 = \int_{to}^{to+\Delta t} BPSA(t)\, dt$; other loss mechanisms can be incorporated by adjusting Peak1. For example, to take into account the neutron lifetime Peak1 is multiplied by $e^{-\Delta t/886}$. The next step is to change this bounce rate for the aperture to a bounce rate for the average UCN.

To find the BPS rate it has to be assumed that the wall rate is the same everywhere in the trap so that that the total bounces per second in the trap can be divided by the number of UCN in the trap, UCNT[t]. The number of UCN in the trap during the time between the

peaks is $UCNT(t) = UCNT(0)\, e^{-t/57}$ and $UCNT(0)=Peak1$. With this determined the bounce per second rate is $BPS[t] = \frac{BPSA(t)x(Trap\ Area)}{(Aperture\ Area)xUCNT(t)} = \frac{BPSA(0)x(Trap\ Area)}{(Aperture\ Area)xUCNT(0)} = \text{Constant}$. By calculating the BPS rate after different holding times, any change in the rate due to velocity spectrum softening can be seen. The series of runs made to test for depolarization via the second method has data of the type needed for this calculation.

The runs sereb000-sereb122 (serbXXX, XXX is used as a general cycle number for the sereb run/experiment) from October 28, 2001 were used to find the BPS rate. The timing of the these runs is shown in Table 6-5, and Figure 6-38 shows the 200 second holding time data. The series loads the trap using the AFP, then the trapped UCN are held for various times before dumping; during this time the free UCN drain from the trap. The number of runs at each holding time varies, so scaling is required to compare the runs. The holding times of 40 to 140 seconds have 11 or 12 runs each, while the 200 second holding time has 23 runs. The scaling is done by comparing the number of UCN counted in Detector 2 and 3 during the first 40 seconds of the holding time for each holding time.

sereb000-sereb122 October 28, 2001					
Spectrometer Fill (sec.)	Trap Fill (sec.)	AFP on Trap Fill (sec.)	Holding Time (sec.)	AFP on Drain (sec.)	Drain (sec.)
2	50	40	40, 60, 80, 100, 120, 140, 200	40	100

Table 6-5 Timing table for serebXXX runs: This table shows the timing for the "sereb" runs. The holding time varied as shown.

From the serebXXX runs multiple sets of consecutive unload peaks can be studied, but the shorter holding times still have a significant amount of signal in Detector 2 from free UCN draining from the trap. This is removed by fitting the Detector 2 signal before the dump and subtracting it from the peak sum [Figure 6-19]. Six measurements of the BPS rate will be made using the seven unload times.

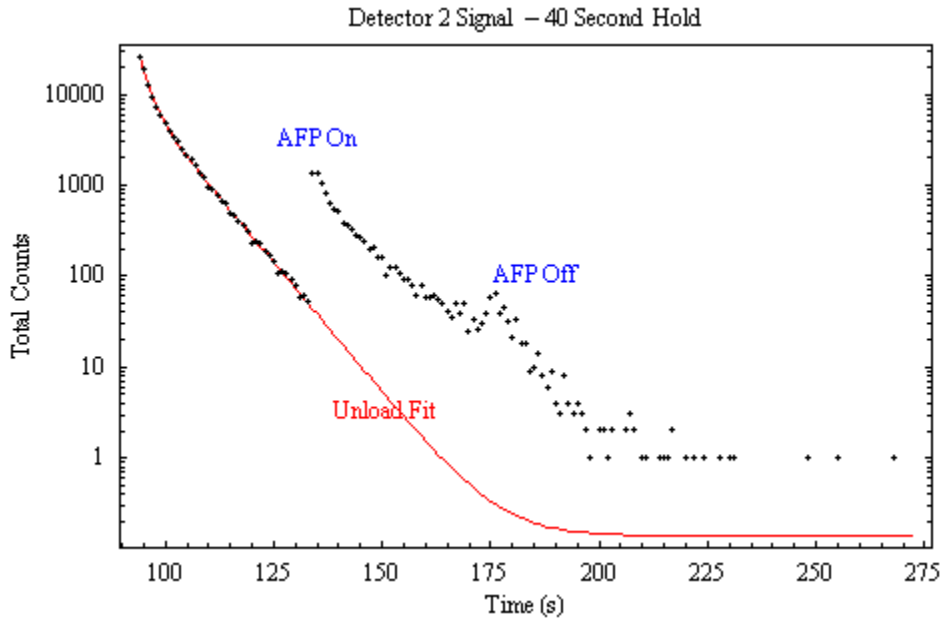

Figure 6-19 Detector 2 signal – 40 second hold: At the time of the 40–second–hold unload peak there are still free UCN draining from the trap. They can be removed from the data by fitting the pre–peak data with an exponential (the red line) and subtracting this from the peak region.

If wall losses are included in the BPS calculation, the rate is coupled to the wall loss and an iterative approach is needed to find the BPS rate. Taking into account the neutron lifetime and a wall loss of 10^{-5} per bounce, the BPS rate for the different holding times is shown in Figure 6-20 and Table 6-6. The fourth and fifth columns (Corrected BPS, CBPS) of the table are higher since they take into account that some of the UCN that enter the region beyond the aperture return to the trap since the exit to the detector is only five times the size of the size of the aperture. The errors are standard deviations from 10000 Monte Carlo runs with a trap lifetime of 57±7 seconds (peak counting errors included).

The BPS rate does appear to be changing with time, but it reaches a constant state after 80 seconds. A possible explanation of this is that UCN with more kinetic energy than the material potential of the DLC coating are tunneling out of the trap. After they are gone the velocity spectrum stabilizes. This apparent constant BPS rate is a good indicator of a low wall loss since the faster UCN hit the wall more times and are lost faster (which will lower the average velocity of UCN in the trap).

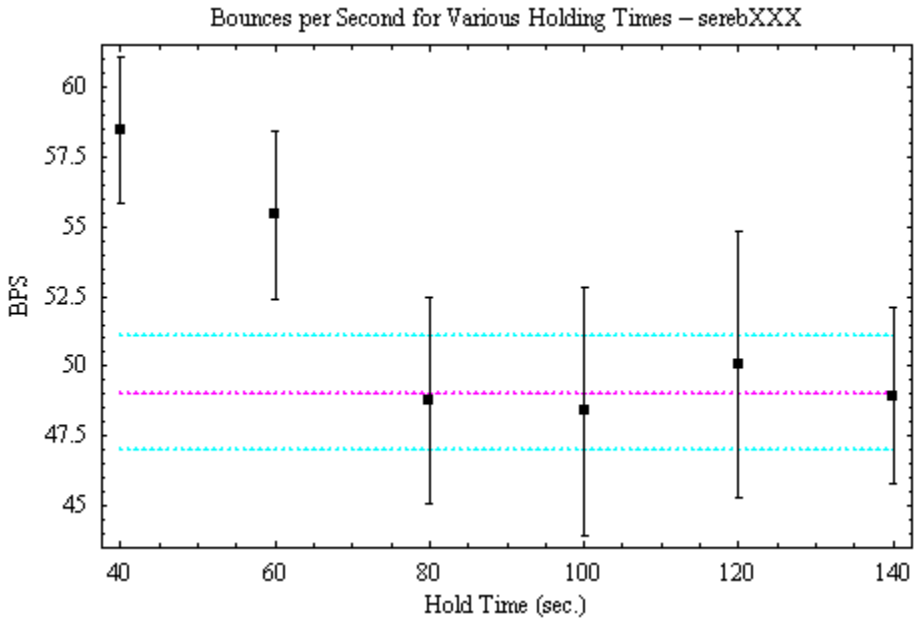

Figure 6-20 Bounces per second for various holding times: This figure shows that the calculated BPS drops for the first 3 data point and then remains constant. The purple line shows the mean of the final four points and the blue lines are the error in the mean. The loss per bounce used in the calculation was $1x10^{-5}$.

Time	BPS	BPS Error	CBPS	CBPS Error
40	58.5	2.7	68.1	3.1
60	55.4	3.1	64.5	3.6
80	48.9	3.7	57.	4.3
100	48.2	4.3	56.1	5.1
120	50.3	5.	58.6	5.8
140	48.7	3.2	56.7	3.7

Table 6-6 Bounces per second: This table corresponds to Figure 6-20. The CBPS columns have been adjusted to take into account that some UCN that leave via the aperture return to the trap.

By using different loss per bounce rates different BPS rates are found, Table 6-7; a limit can be put on the loss per bounce rate by looking at the effect on the 140 second data point since it has a different inter peak time. If we assume that the last four data points in Figure 6-21 are measures of the same BPS rate then the last data point (which has a sixty second time difference between the unload peaks) should be within a standard deviation of the other. As the loss per bounce rate is raised, this fourth data point drops until it is over a standard deviation from the others. Figure 6-21 shows the effect of a 10^{-4} loss per bounce rate; the last data point is over one standard deviation from the mean.

Bounces per Second for Different Loss Rates						
Loss per Bounce	$1x10^{-6}$	$1x10^{-5}$	$5x10^{-5}$	$1x10^{-4}$	$5x10^{-4}$	$1x10^{-3}$
BPS/CBPS	51/60	49/57	42/48	36/40	17/18	10/11

Table 6-7 Bounces per second for different loss rates: This table shows the BPS and CBPS rates with different loss probabilities.

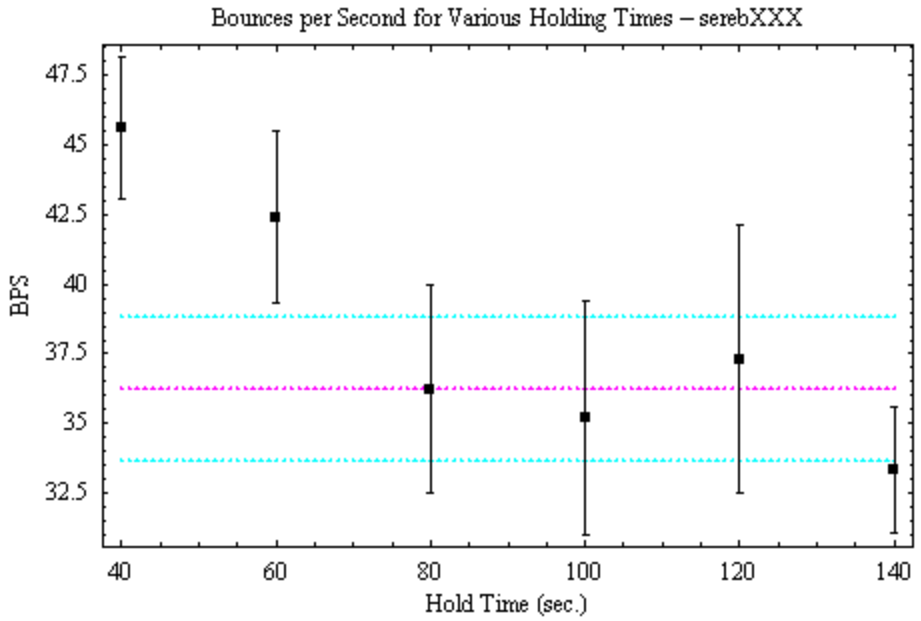

Figure 6-21 Bounces per second for various holding times – serebXXX: In this figure the purple line is the average of the 3rd , 4th and 5th data points. The loss per bounce is 10^{-4} and this causes the last data point to drop out of the error range of the mean. If the last four data points are from the same BPS rate the assigned 10^{-4} loss rate could be to high. The last data point leaves the error range when the loss rate is at $7x10^{-5}$.

A conservative estimate of the BPS rate would be to use a loss rate of $5x10^{-5}$, since this will give the lowest rate and keeps the last four data points consistent [Figures 6-20 and 6-21]. This would give a BPS rate of 42 to 48 depending on the number of UCN that reenter the trap (Section 6.2.2.6 estimates 1 in 6 will reenter the trap after leaving via the aperture); adding the errors onto each of these the range would be 40-50 BPS.

This bounce rate is comparable with those estimated in Section 6.2.3.2, 56 and 81 BPS. The 56 BPS value takes into account the geometry and the average UCN velocity; whereas, 81 BPS is calculated using kinetic gas theory and uses the average velocity but

not the geometry. For another comparison a loss rate of $5x10^{-4}$ is typically used in Roger Hill's UCN transport calculations. This rate also gives a BPS value outside the average.

6.3.1.3 Trap Lifetime

The lifetime of UCN in the trap can be found using two different methods with the data from the serebXXX runs. The first method is very direct; it uses the signal from Detector 3 that monitors the trap density. The density in the trap changes rapidly as the free UCN leave the trap, once several 1/e drain times have passed Detector 3 monitors predominantly the trapped UCN populations. The Detector 3 signal can be fit with either one or two exponentials depending on which part of the decay curve is fit. A second and more involved method fits the number of UCN left in the trap after various holding times; these UCN are emptied with the AFP and counted with Detector 2.

To obtain a lifetime by monitoring the UCN density in the trap, runs with long holding times are needed; the serebXXX runs with 140 and 200 second holding times are ideal for this, although longer would be even better. The 200 second holding time will be used since it has 23 runs (the 140 second holding time has only 12 runs) and more data points to fit due to the longer holding time. Fitting the Detector 3 signal for the entire 200 second holding period with the sum of two lifetimes is straight forward and results in a 57 second lifetime [Table 6-8]; the errors are calculated in the same way as the single exponential case that will be presented next.

To fit the density decay with a single exponential the first part of the data has to be eliminated since there is a large population of free UCN still in the trap. The plot in Figure 6-22 shows the signals from Detector 2 and 3 and their ratio for the 200 second holding time. To determine the effect of the free UCN on the Detector 3 signal the ratio of the apertures to each detector should be considered. The aperture to Detector 2 is the guide while Detector 3's aperture is a 0.94 cm diameter so the ratio is $(.47^2/3.2^2)=0.02$, and the rate in Detector 3 relative to 2 looking at the same population is 0.02xDet2Hz=Det3Hz. So after about 50 seconds the contribution of the free UCN to the trapped UCN signal is less than 2%. If the first 50 seconds of the holding time are

eliminated then the remaining data can be fit with a single exponential. The Mathematica NonlinearRegress routine is used to fit the data, which is weighted by $\sigma = \sqrt{\text{"\# in the bin"}}$.

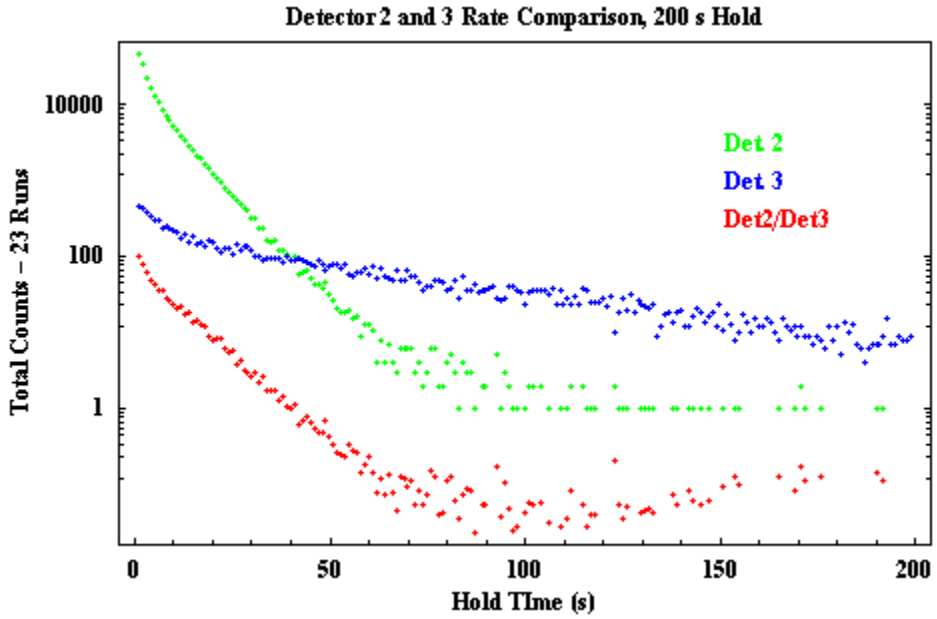

Figure 6-22 Detector 2 and 3 rate comparison, 200 second hold: The plot shows the number of UCN seen by Detector 2 and 3 when the trap is loaded with trapped UCN. To find the trap lifetime the Detector 3 signal is fit with an exponential decay curve; most of the free UCN need to have left the trap before this is possible. By looking at the ratio of the two signals the optimal time to start the fit can be determined. The straightness of the Detector 3 signal on the semi-log plot after 50 seconds of draining looks like an exponentially decaying population.

The fit of the exponential function to the data is done with a reduced chi square test. A one sigma error on a parameter in the fitting function can be established by adjusting that parameter until the reduced chi squared fit increases by one [168, 169]. The graph in Figure 6-24 shows the change in chi squared as the lifetime is adjusted away from the optimal 58 second value. The best fit and one sigma fits to the data are shown in Figure 6-23.

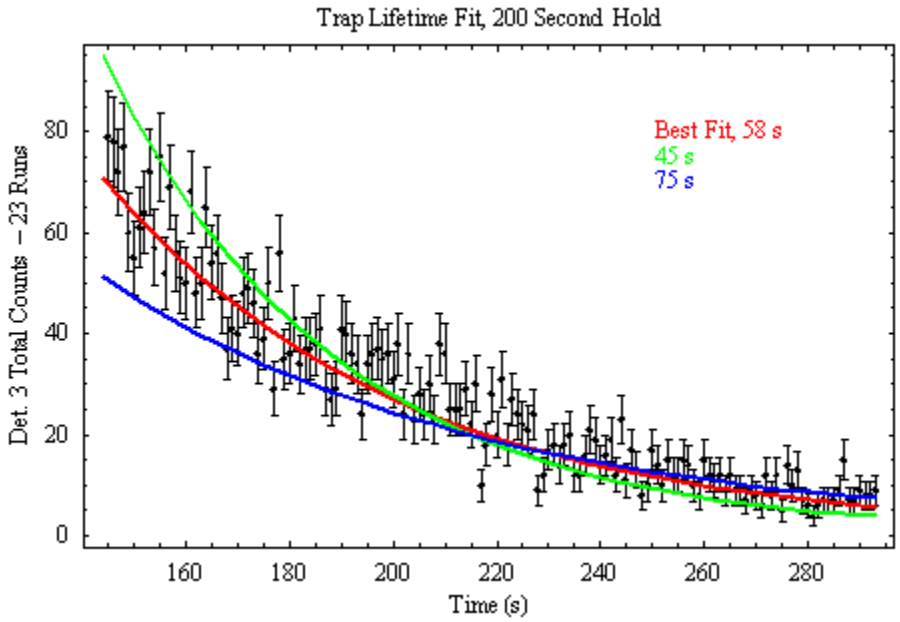

Figure 6-23 Trap lifetime fit, 200 second hold: This plot shows the best fit to the Detector 3 signal and the one sigma fits. The one sigma fits do not represent the signal very well.

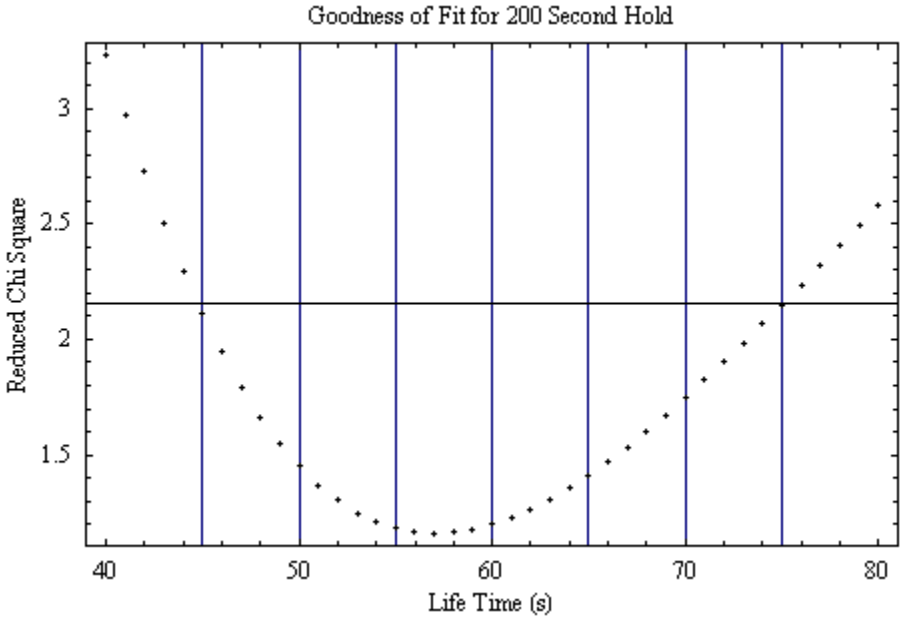

Figure 6-24 Goodness of fit for 200 second hold: This plot show the reduced chi square for fits with various values of the lifetime. The one sigma range of the fit is determined by how far the lifetime can be moved before the reduced chi square increases by 1; this is shown by the black horizontal line.

The trap lifetime can also be found by fitting the number of UCN in the trap at the seven dump times; 40, 60, 80, 100, 120, 140, and 200 seconds. To do this, the counts in detectors 2 and 3 are summed for 60 seconds starting at the time of the AFP unload. The

number of UCN that are counted includes both trapped and free UCN; this is especially true of the 40 second hold time where the signal before the AFP dump is all free UCN [Figure 6-19]. This can be taken into account by fitting the pre-dump decay curve and subtracting it from the peak, or by eliminating the 40 second data point, see Section 6.3.1.2 and Figure 6-19. Alternatively a second exponential can be added to the fit to take into account the short lifetime of the free UCN.

The seven data points could not be fit very well with a single exponential with or without the free UCN component subtracted. A better fit to a single exponential was made by eliminating the first data point without subtracting the free UCN from the other unload peaks; in this case a reduced chi square of 3.5 was achieved. This fit with a 69 second lifetime can be seen in Figure 6-25, and it looks good for the last three data points.

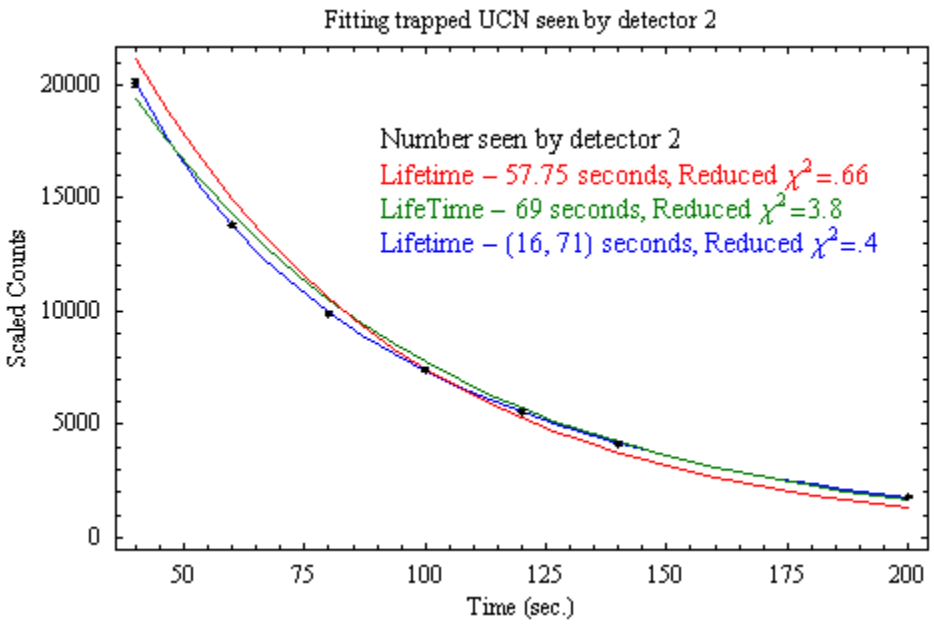

Figure 6-25 Fitting trapped UCN seen by Detector 2: The plot shows the number of trapped UCN unloaded from the trap after various holding times; the error bars represent one sigma errors. Only the two exponential fit (blue line) hits all the data. And, the 57.75 second lifetime obtained from fitting the Detector 3 data does not fit well at all.

Using the sum of two exponentials to model the seven data points, a very nice fit can be made with a reduced chi square of 0.4 [Figure 6-25]. Adjusting four parameters to fit 7 data points seem justified by the large reduction in the reduced chi-square from 3.5 to 0.4.

It should be noted that there was very little difference when fitting the raw peaks or the free UCN subtracted peaks. The lifetimes from the exponentials were 16 and 71 seconds, these are both longer than the two exponential fits of the Detector 3 data. The one sigma range for the 71 second lifetime is 69-73 seconds, which is much tighter than the best Detector 3 range [Table 6-8].

Data and Fit	Short Lifetime	Long Lifetime/χ^2	One Sigma Interval
200-50 second hold – single exp		58s / 1.2	45-75s
Sereb200 +f200 – single exponential		57s / 1.1	51-64s
200 second hold – double exp	6.6s	57s / 1.1	47-65s
fr140+f200 second holds double exp	5.2s	57s / 1.3	48-67s
60,80,100,120,140,200 single exp		68s / 3.8	67-69s
40,60,80,100,120,140, 200 double exp	16s	71s / 0.4	68.8-73.4s

Table 6-8 Trap lifetime: This table shows trap lifetimes for various runs. The longer lifetime is generally used as the trap lifetime and the shorter lifetime is attributed to the free UCN.

There is a large difference between the long decay constants in the two different methods. If this is due to the velocity spectrum getting softer, then fitting the Detector 3 data with different starting cuts (the fit neglects the beginning of the time series) should show a increased lifetime as less of the early data is fit. Figure 2-26 shows a only slight increase in the lifetime that peaks around 60 seconds, so the spectrum does not seem to be softening enough to explain the difference.

The lifetimes obtained by fitting Detector 3 data and the "unload peaks" do not agree with each other or the estimate made in Section 6.2.3.3. The reason for the difference between the two experimental methods is not obvious, so each lifetime will be used where appropriate. The ~57 second lifetime will be used most places, since it is a conservative measurement; the unload peak lifetime will be used where information about the unload peaks is needed. Both of these lifetimes are longer than the 41 second estimate in Section 6.2.3.3; this can be partially explained by the use of a BPS rate of 56 instead of the observed 45 and eliminating the gap loss.

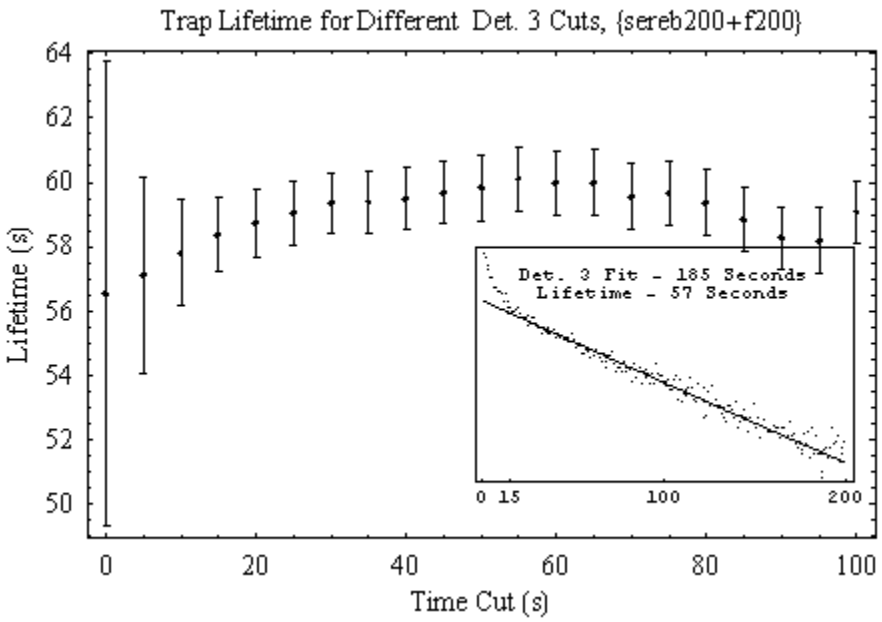

Figure 6-26 trap lifetime for different Detector 3 cuts, sereb200 and f200 combined: The main plot shows best fits of Detector 3 data using a single exponential with the first 0 to 100 seconds of data removed. The error bars are the reduced chi square of the fit. The inset shows the fit with the first 15 second of the hold time removed.

6.3.1.4 AFP Efficiency

The AFP efficiency can be expressed in two ways: the AFP spin-flipping efficiency and the AFP efficiency at loading and emptying the trap. As the flipping efficiency increases, the trap loading and unloading efficiency decreases. This can be seen by thinking of a 100% efficient spin-flipper with equal number of UCN on each side; turning it on will empty half of the UCN if they are allowed time to exit before it is then turned off, and half of the remaining UCN will now be able to exit the trap. At 100% efficiency only ¾ of the trap would be emptied. If the efficiency is below 100%, then the trap can be fully drained by leaving the AFP on for a long time. The spin flipping efficiency will be calculated four ways, three using the AFP unload peaks [Figure 6-27] and one using the AFP loading data [Figure 6-28].

Using the data in the AFP unloading peaks of the serebXXX runs, three tests of the AFP flipping efficiency can be made. First, since the Table 6-3 shows the number of trapped UCN on each side of the AFP to be about the same, the AFP "on" peak should be 4 times

as large as the AFP "off" peak, corrected for the 57 second trap lifetime. To get a reasonable amount of data the 60,80,100,120 and 140 second unload peaks will be combined [Figure 6-27].

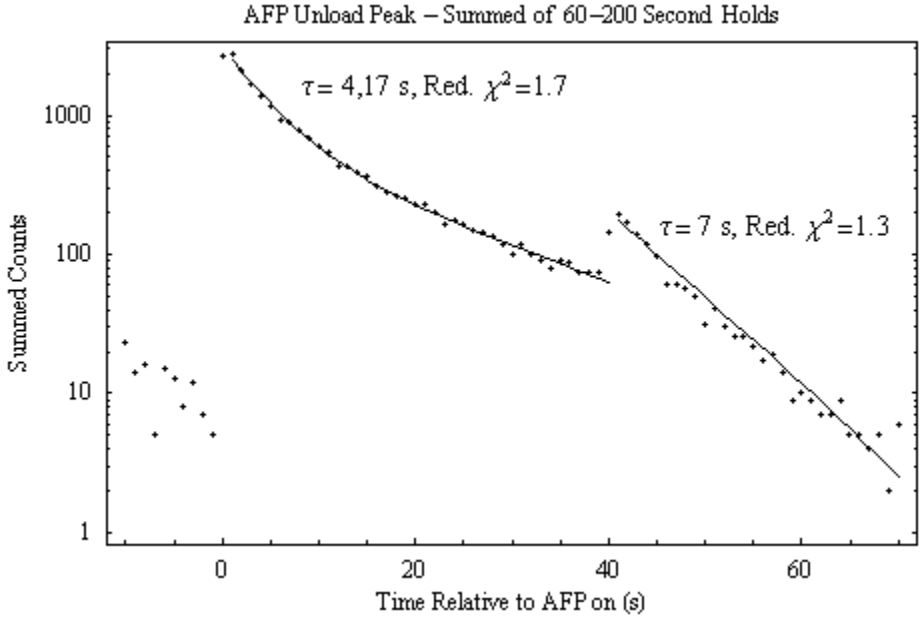

Figure 6-27 AFP unload peak – summed of 60-200 second holds: This plot shows data from the combined AFP unload peaks and the best fit with reduced χ^2 for each segment. The need to use two exponentials to fit the first peak is evidence for a less than 100% efficient AFP.

The maximum value in the AFP "on" peak is 2727 and the AFP "off" peak has a maximum of 192; this has about ~73 background counts from the AFP "on" peak giving 119 counts. Using a 57 second lifetime the 119 is equivalent to 240 at the time of the AFP "on" peak. This is 35% of the of the expected value of ¼ the peak and implies a less than 100% efficient spin-flipping. The efficiency can be estimated by using the number of times the average UCN would pass through the AFP in 40 seconds to compute an efficiency: $\text{Efficiency}^{\text{NumberOFPasses}}=.35$, for NumberOfPasses=79 the efficiency is ~.987±.002 assuming an average axial velocity of $\frac{510}{\sqrt{2}}$ cm/sec. To compute the error the full formula,

$$\frac{\text{Peak2}\, e^{40/\text{tau}}}{(1/4)\times \text{Peak1}} = Efficiency\text{^} \sum_{t=1}^{39} \frac{Velocity\, e^{-t/tau}}{TrapLength\sqrt{2}}$$

$$ErrorPeak1 = \sqrt{Peak1}$$

$$ErrorPeak2 = \sqrt{Peak2} \quad ,$$

$$tau = 57 \pm 7 \sec.$$

$$Velocity = 510 \pm 50\, cm/\sec.$$

$$Traplength = 128 \pm 4\, cm$$

was solved for the efficiency and then the efficiency was calculated 1000 times with the parameters chosen from a normal distribution around the stated value with the error used as the width. From this set of efficiencies the mean and standard deviation was computed to give the stated value and error for the efficiency; this method of determining the value and error will be called the Monte Carlo Error Method (MCEM) in this chapter.

Another approach is an iterative one where the population in the trap is written as the old population in the trap minus the number lost to AFP inefficiency and minus the trap losses. The trap losses are known, so solving this for a second peak height of 119 give a value for the AFP efficiency. The iterative equation is

$$UCNT[t] = UCNT[t-1] - UCNT[t-1] \times \left((1 - AFPeff^{NOP}) + (1 - e^{1/tau})\right)$$

$UCNT[t]$: The number of UCN in the trap

$AFPeff$: The AFP efficiency .

NOP : The number of passes a UCN makes through the AFP per second

tau : The trap lifetime ~ 57 seconds

This gives a value of .984±.001 for the AFP efficiency – where the errors in the lifetime and counting were included using the MCEM.

If the AFP were 100% efficient at flipping UCN spins, the slope of the two peaks in Figure 6-27 would be the same; it is easy to see that the slopes are not the same. The slow component of the decay in the first peak is due to UCN continuing to be freed from the trap by the less than 100% efficient AFP. To obtain a 16.5±4 second lifetime using the average UCN in the previous example, the AFP efficiency would be 0.977±.007; that

is $1/e = .977^{17x510/\sqrt{2}/128}$ – 128 cm is the trap length for the average trapped UCN. The uncertainty was found via the MCEM as before.

The efficiency of unloading can be found by assuming that as many UCN remain in the trap as escape in the AFP "off" peak. To get the number in the AFP "off" unload peak, the trap lifetime must be considered in the sum: $\sum_{i=40}^{70} Det2[i]e^{(i-40)/57} = 1543$. Similarly, the sum for the whole unload peak is found to be 28080 and the unloading efficiency from these is 1-1543/28080=.945, which is higher than 75% (a perfect AFP would unload 75% of the trapped UCN in a cycle) and also supports the less than 100% efficient AFP.

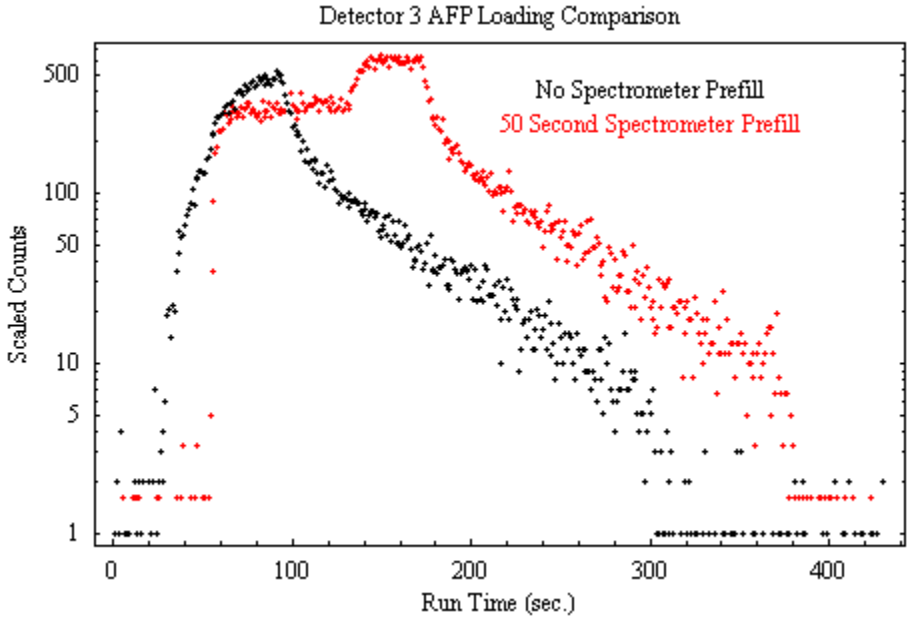

Figure 6-28 Detector 3 AFP loading comparison: These plots of Detector 3 data for the two different filling cycles show the effect of turning on the AFP during filling. It is most obvious in the signal that has reached equilibrium (red) before the AFP turns on. The increase and new higher equilibrium, after the AFP is turned on, is evidence of AFP inefficiency.

The efficiency of the AFP can also be found by looking at the filling of the trap [Figure 6-28]. The AFP loading of the trap is a function of the number of UCN in the trap, the AFP efficiency, and the trap lifetime. When the AFP cycle starts all the free UCN (UCNF) on the aperture side of the trap become trapped UCN (UCNT). If the AFP is not 100% efficient, the number of trapped UCN continues to increase during the cycle. At the end of the cycle the trapped UCN on the magnet side of the AFP remain trapped and

the free UCN on the aperture side of the AFP become trapped. If the AFP is 100% efficient after "turn on", first the trap density would increase, then it would decline with the trap lifetime until the end of the cycle. If the trap comes to equilibrium above the start value during filling, the AFP cannot be 100% efficient. The efficiency of the AFP can be determined by looking at the number of UCN that accumulate in the trap during the cycle [Figure 6-28].

When the AFP fails to flip a UCN it becomes trapped, these trapped UCN are continually lost to the aperture and other loss mechanisms. The number of trapped UCN while the AFP is on can be expressed as:

$$UCNT[t] = UCNT[t-1] + FUCNF \times P[\overline{Flip}] - UCNT[t-1] \times P[\overline{Flip}] - UCNT[t-1](1 - e^{-1/tau})$$

$$FUCNF = \frac{UCNF \times Velocity \times TrapCrossSection}{TrapVolume}; \quad \text{flux of free UCN}$$

$$FUCNT[t-1] = \frac{UCNT[t-1] \times Velocity \times TrapCrossSection}{TrapVolume}; \quad \text{flux of trapped UCN}$$

$$P[\overline{Flip}] = (1 - AFPeffciency); \quad \text{Probability of not spin - flipping per pass through the AFP}$$

tau = trap lifetime

$UCNT$[t] = the number of UCN on the aperture side of the AFP

The efficiency of the AFP affects both the density evolution and the final density reached in the trap; this can be seen in Figure 6-29. Comparing this to Figure 6-28 it is obvious that the efficiency is not great since equilibrium is reached quiet fast. The density of the trap comes to equilibrium during the fill cycle so the equation for the number of UCN in the trap can be solved to find the AFP efficiency since at equilibrium UCNT[t]=UCNT[t-1].

$$P[flip] = \frac{(1 - e^{-1/tau}) \times TrapLength \times (UCNS1 - UCNS2) + (2 \times UCNS1 - UCNS2) \times Velocity}{(2 \times UCNS1 - UCNS2) \times Velocity}$$

$UCNS1$ = Average signal in Detector 3 before AFP cycle

$UCNS2$ = Average signal in Detector 3 at the end of the AFP cycle

Doing this for the data from f200 plotted in Figure 6-28, an efficiency of 98±1% is found, while an efficiency of 98.6±.3% in found using data from fr1400. The combination of these data sets yield an efficiency of 98.1±.4%.

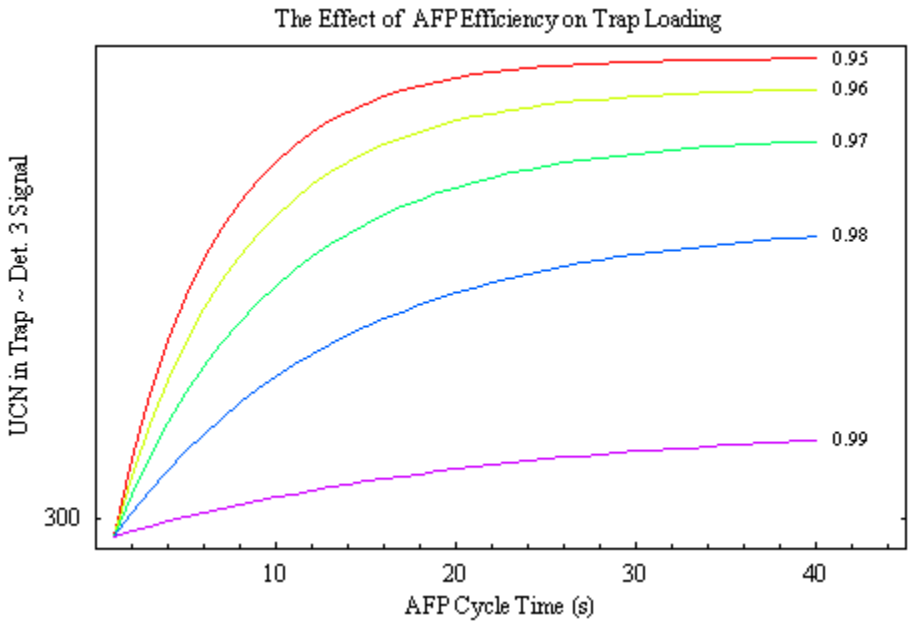

Figure 6-29 The effect of AFP efficiency on trap loading: This figure shows the effect of decreasing AFP efficiency. As the efficiency decreases, the number of UCN in the trap increases and the time to reach equilibrium decreases. The start point of the plot is the number of UCN before the AFP turns on plus half this number that are trapped by the turn on. If the AFP efficiency is high enough, the trapped UCN will be emptied by the aperture faster than they are created by AFP inefficiency, and this initial population will decline – instead of increase as seen in the figure.

The calculation of the efficiency and its uncertainty was done by using a range of values for the parameters involved. The numbers of UCN in the trap were found by taking 5 and 10 second averages at the ends of the fill (UCNS1) and AFP fill times (UCNS2); the standard error of each number was used. The trap lifetime (tau) was assigned a value of 57±7 seconds and the trap length was 128±4 cm. The variation in trap length is due to an unknown average velocity. Finally, the velocity was given a mean of 510 cm/second and a standard deviation of 50 cm/second. 1000 trials were used for each efficiency stated. It was assumed that both spin–states were in equal density on each side of the AFP; this is not true for the free spin–state.

Using Table 6-3, the free spin–state has more asymmetry in the number on each side of the AFP as the average velocity declines. If this is taken into account the number of free UCN should be lowered, since Detector 3 over estimates the number in the trap region. Using a 55% value and adding an uncertainty of 1%, the AFP efficiency, of the two runs summed, changes to 97.4±.6%. This is not much of an effect, but it does lower the efficiency a little; 10000 trials were used to find this number.

AFP efficiencies			
Method	Efficiency %	Error	Runs
Comparing AFP On/Off Unload Peaks	99.3	±0.2	Summed serebXXX Runs
Comparing AFP On/Off Unload Peaks, Peak2-PrePeak2	98.7	±0.2	Summed serebXXX Runs
Iterative fit to Peak2	98.44	±0.1	Summed serebXXX Runs
Slope of AFP "on" – Det. 2 - Unload	97.7	±0.7	Summed serebXXX Runs
AFP Load – Detector 3	98.1	±0.4	f200 + fr140
AFP Load – Detector 3 with Free UCN Asymmetry	97.4	±0.6	f200 + fr140

Table 6-9 AFP efficiencies: This table shows the AFP as being below 99% efficient in all but the uncorrected serebXXX calculation. The first four calculations were done using the unload peak of the combined "sereb" runs. The summed f200 and fr140 AFP loading data was used to calculated the last two values.

All four methods of determining the AFP efficiency show the AFP to be less than 100% efficient. The weighted average of the AFP efficiency is 98.3±.2%. The inefficiency of the AFP can be attributed to field inhomogeneity and/or being off resonance. The efficiency may have dropped between the serebXXX runs on October 28th and the f200+fr140 runs on the 30th. The resonance point did shift according to the logbook. The inefficiency of the AFP actually worked to the advantage of the experiment since it allowed filling to higher densities and more efficient unloading of the trap.

6.3.1.5 The Number of UCN in the Trap

Detector 3 monitors the number of UCN in the trap, but it needs to be calibrated to accurately give the number of UCN in the trap. The basic idea is to compare the rate in Detector 3 – before an AFP trap dump – to the number seen in a dump by Detector 2. The actual method used is defined by the following equation:

$$Calibration = \frac{\sum_{t=t0}^{to+60}(Det2(t) - Det2Background)\,e^{(t-to)/tau}}{\frac{1}{21}\sum_{t=t0-20}^{to}(Det3(t) - Det3Background)}$$, where t_0 is the time of the AFP unload. The data appears to be linear for the various holding times [Figure 6-30]. The calibration increases with time – this can be seen as a cooling of the velocity spectrum due to aperture and wall interaction losses. The error bars are from errors in the sums and backgrounds, but the error in the trap lifetime was not included. The trap lifetime is taken to be 57 seconds.

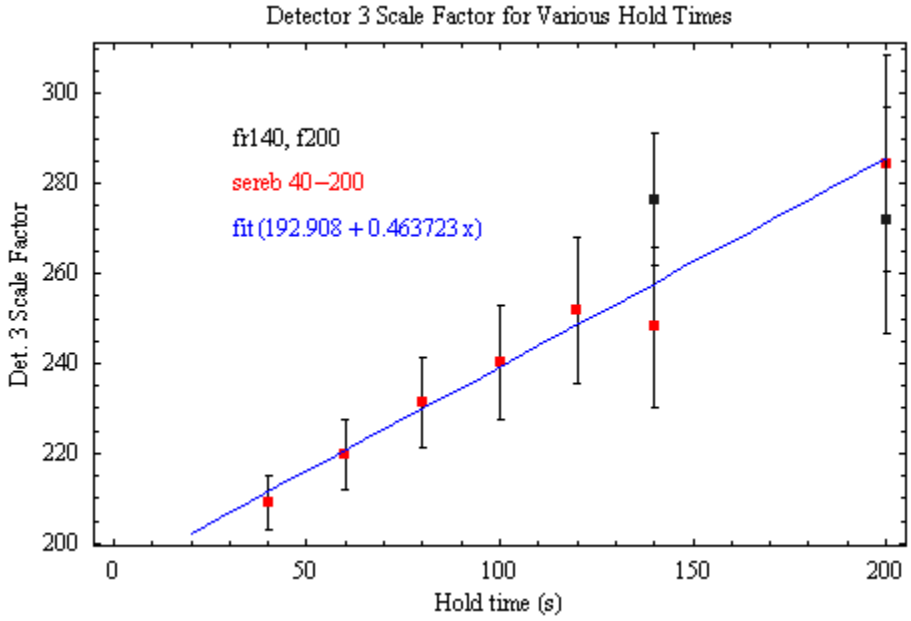

Figure 6-30 Detector 3 scale factor for various hold times: This plot shows the calibration between Detector 3 signal and the number of UCN that would be seen by Detector 2 if the trap were unloaded. The red data points seem to be linear with the exception of the 140 second point; the black points were taken on a different day and the detector electronics may have been changed.

To calibrate Detector 3 for the filling period the fit can be extrapolated to zero; this value will be used to calculated the number of UCN in the trap during filling for the DPB

measurements. Table 6-10 shows the number of UCN in the trap and density predicted by using 193 for the calibration. To calculate the error in density, a calibration of 193±5 and a trap length of 128±4 cm were used.

The Number of UCN in the Trap for Various Runs			
Run	Max. Number of UCN	UCN Density UCN/cm^3	Error in Density UCN/cm^3
5t1XXX	1572	0.38	0.04
nf1XXX	3715	0.90	0.07
serebXXX	2209	0.54	0.03
fr140+f200	4960	1.2	0.05

Table 6-10 The number of UCN in the trap for various runs: This table shows UCN density for several different runs. It shows that the 5t1XXX runs – with the foil in place – had a low density, and that the serebXXX runs without a pre–fill also had a low trap density. The density is for a single cycle in each case, so direct comparison is appropriate.

The trap density was increased by the removal of the foil and the use of the AFP. The density of the serebXXX runs were below the fr140 and f200 runs due to the fast filling scheme used, it would appear the runs could have had twice as much data if the longer filling scheme were used.

6.3.2 The Depolarization Rate in the UCNA Experiment

Using the parameter analyzed in the previous sections the depolarization rate will be found two ways. The two techniques (Methods 1 and 2) were discussed previously in Section 6.2.3.5.

6.3.2.1 Depolarization Rate via Method 1

The first method for finding the depolarization rate analyzes the number of UCN that depolarize during the filling cycle. These depolarized UCN are unloaded from the trap using the AFP *after* the free spin–state UCN have been drained from the trap. To accurately determine the number of UCN that were originally depolarized during the filling, the trap lifetime needs to be known; 57±7 seconds will be used, longer lifetimes would lower the DPB so this is a safe estimate. The calibration derived in Section 6.3.1.5

will be used find the number of UCN in the trap using the signal from Detector 3; the errors will also be used. The depolarization per bounce is found using the following equations:

$$\sum_{t=0}^{t\,dump} DPB \times BPS \times UCNT[t]\, e^{(t-t\,dump)/tau} = \sum_{t=t\,dump}^{t\,dump+60} (Det2[t] - Back[t])\, e^{(t-t\,dump)/tau}$$

$$DPB = \frac{\sum_{t=t\,dump}^{t\,dump+60} (Det2[t] - Back[t])\, e^{(t-t\,dump)/tau}}{\sum_{t=0}^{t\,dump} BPS \times UCNT[t]\, e^{(t-t\,dump)/tau}}$$

$$UCNT[t] = Det3Calibration \times (Det3[t] - Det3Back[t])$$

The error in the DPB measurement is found by a Monte Carlo method. To do this, the DPB is calculated many times using different values of the parameters; the values are chosen from a normal distribution around the mean value with a standard deviation equal to the error in the parameter.

Method 1 Run Timing				
Clean (s)	Fill (s)	Drain (s)	AFP Drain (s)	End (s)
50	120	140	40	60

Table 6-11 Method 1 run timing: This table show the timing used for all runs used for the method 1 DPB measurement.

Runs looking for depolarization via method one were taken at various times between Oct. 28 and Oct. 31, 2001. The timing of the runs is shown in Table 6-11, and Figure 6-31 shows the data from "me140" – a 150 cycle run made on October 29, 2001. The depolarized UCN signal can be seen in the AFP region of the plot; less than one depolarized UCN is seen per cycle.

To compare the various runs, the cycle totals are compared. The cycle totals for all three detectors are shown in Figure 6-32. Since, detector 1 is not used, changes in its rate are not considered reason to question the run. However, the drop in Detector 3 counts in the

second region is a possible problem. The second region is from the run "meas" on October 28.

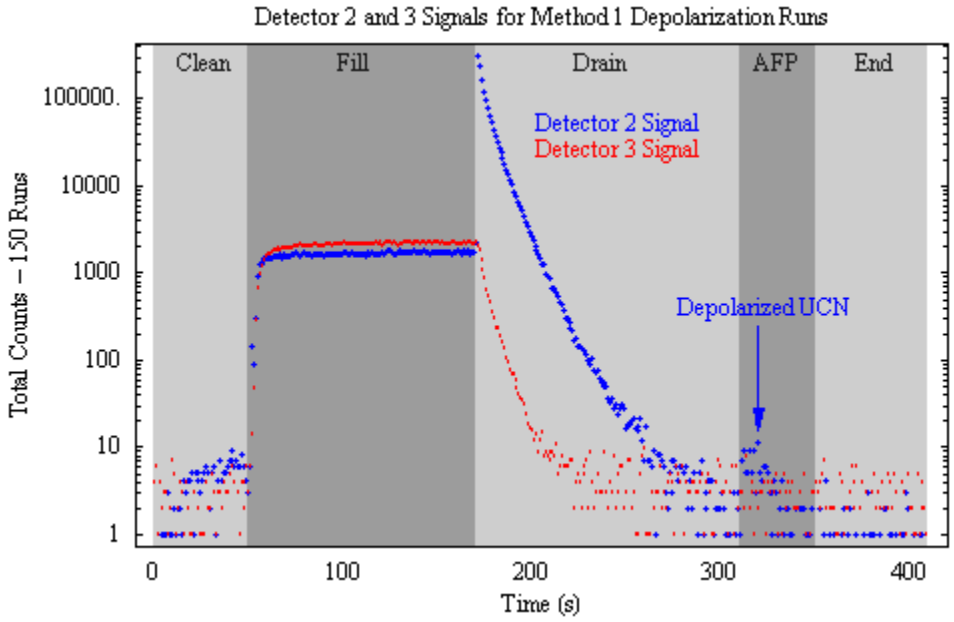

Figure 6-31 Detector 2 and 3 signals for method 1 depolarization runs: This plot show the Detector 2 and 3 data from the 150 cycle me140 run. The peak in the Detector 2 signal after 300 seconds is the trapped UCN being unloaded by the AFP. The Detector 3 signal is used to estimate the number of UCN in the trap using the calibration from Section 6.3.1.5.

Since the number of depolarized UCN is so low, the characterization of the background is very important. The background rate is extracted from the last 40 second of data taking. To look for noisy runs, the cycle totals of the last 40 second can be compared; this is done in Figure 6-33 and again the "meas" region shows a problem. Detector 2 is very noisy and this makes it difficult to count the depolarized UCN.

As a final check the cycle totals of the AFP unload region and following 20 seconds can be compared [Figure 6-34]. In this comparison, the Detector 2 total compare well in all but the second region. Since the "meas" run shows problems in all the plots, it will not be included in the analysis.

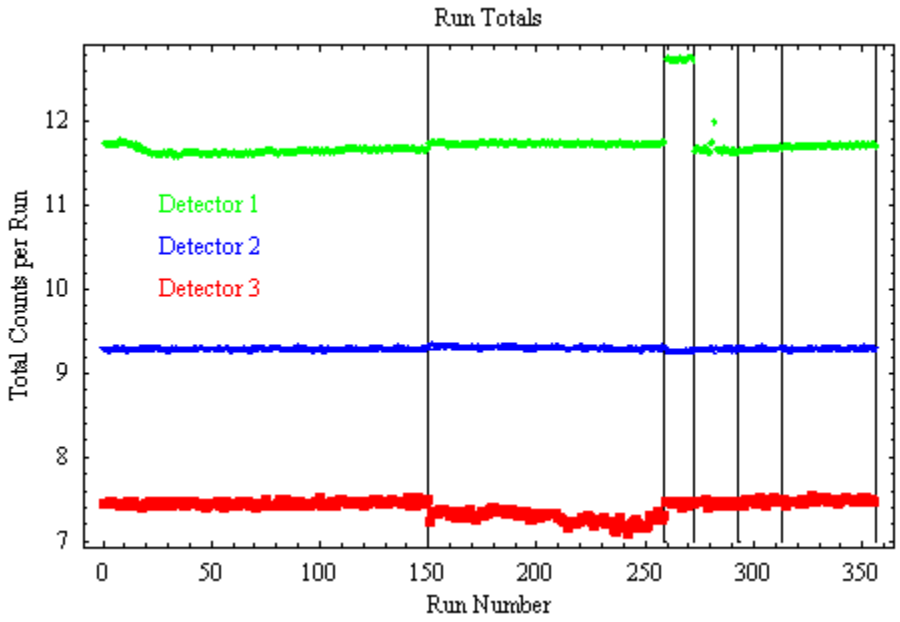

Figure 6-32 Run totals for each detector: This plot shows the total number of UCN seen by each detector for each cycle. The drop in Detector 3 signal in the second region shows a possible problem with the run. The regions from left to right correspond to runs "140me", "meas", "heat", "last", "bac31", and "fnlrn".

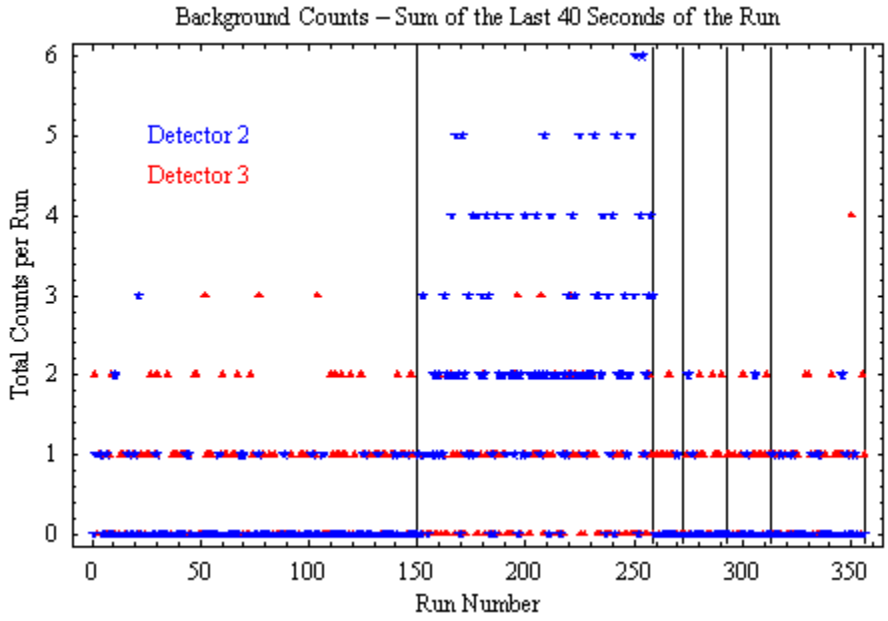

Figure 6-33 Background counts – sum of the last 40 seconds of the run cycle: This plot shows the number of UCN seen by detectors 2 and 3 during the last 40 seconds of the cycle; this region is used to determine the run background. Again the second region shows a problem. In the first set of cycles (0-150) the noise in detector three looks a little high; this is not a problem since the detector three signal is very

large. The regions from left to right correspond to runs "140me", "meas", "heat", "last", "bac31", and "fnlrn".

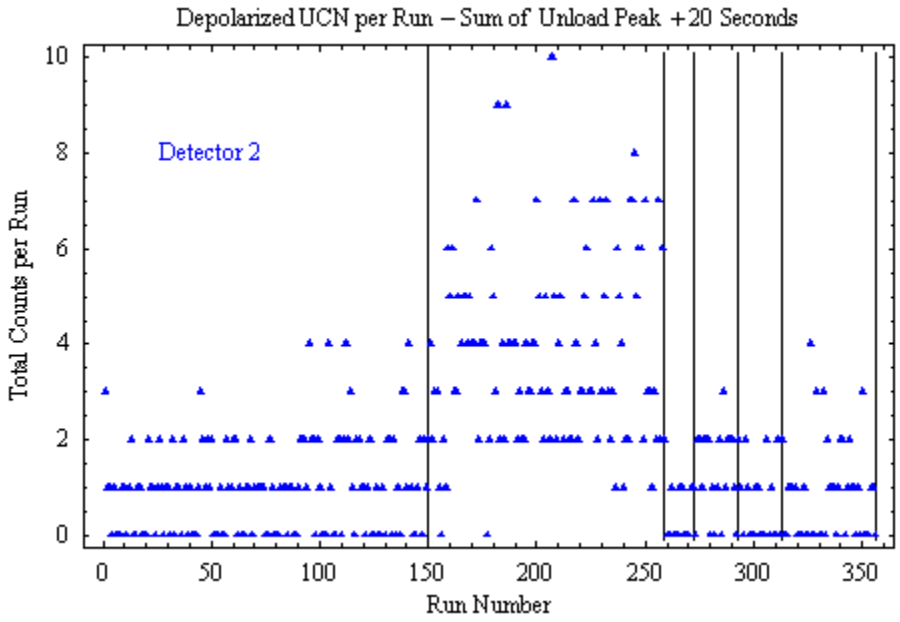

Figure 6-34 Depolarized UCN per run – sum of the unload peak plus 20 seconds: This plot show the number of UCN seen by Detector 2 in the AFP dump region. Once again the second region looks bad. The regions from left to right correspond to runs "140me", "meas", "heat", "last", "bac31", and "fnlrn".

The depolarization rate DPB was calculated for the "140me" data run and the combined data runs (less the "meas" run), [Table 6-12]. The data was put into ten second time bins to improve the statistics where the background was subtracted, this is mainly for summing the unload peak [Figure 6-35]. The background that was subtracted from the peak was obtained by fitting the average rate in Detector 2 before the peak and the background after the peak with an exponential decay. The error in the background was also obtained by fitting the "before" and "after" errors the same way. The number used for the BPS was 45±5 and the lifetime was 57±7 seconds. The square root of the bin sum is used as the error in the bin. In each case, the DPB was calculated 10000 times, as described earlier, and the quoted values are the mean and standard deviation of this data set.

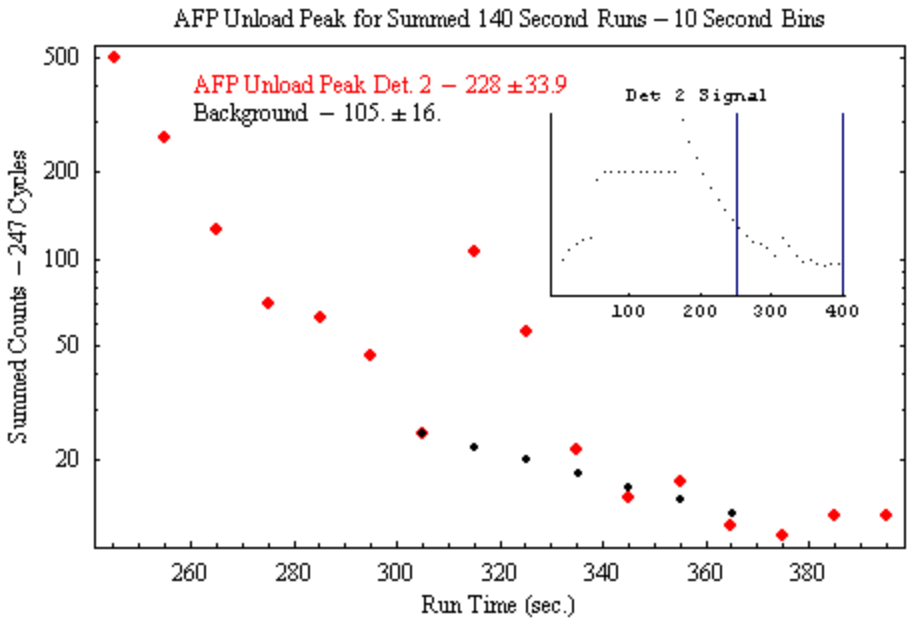

Figure 6-35 AFP unload peak for summed 140 second runs – 10 second bins: This plot shows the Detector 2 signal in the region of the AFP unload peak. The data has been put into 10–second time bins to aid in the error analysis. The black dots show the background that was subtracted from the peak to obtain – the number of depolarized UCN. The data is from the combination of all the 140–second hold runs (except the ”meas” run).

DPB Rates for Method 1 via MCEM					
Run	Number of Cycles	Trapped UCN	DPB	Error DPB	Trails
me140	150	68	$7.7\text{x}10^{-7}$	$4.4\text{x}10^{-7}$	10000
All 140 less “meas”	247	123	$6.4\text{x}10^{-7}$	$3.4\text{x}10^{-7}$	10000

Table 6-12 DPB rates for method 1 via MCEM: This table shows that using the combined run from several different days did not effect the DPB measurement.

The uncertainty in the trap lifetime has the largest effect on the uncertainty in the DPB rate; a decrease from 7 to 3.5 seconds will change the rate and error to $6.0\pm2\text{x}10^{-7}$. Increasing the lifetime to 68±3.8 second decreases the DPB rate to$3.8\pm1\text{x}10^{-7}$. Both of these are for the larger data set.

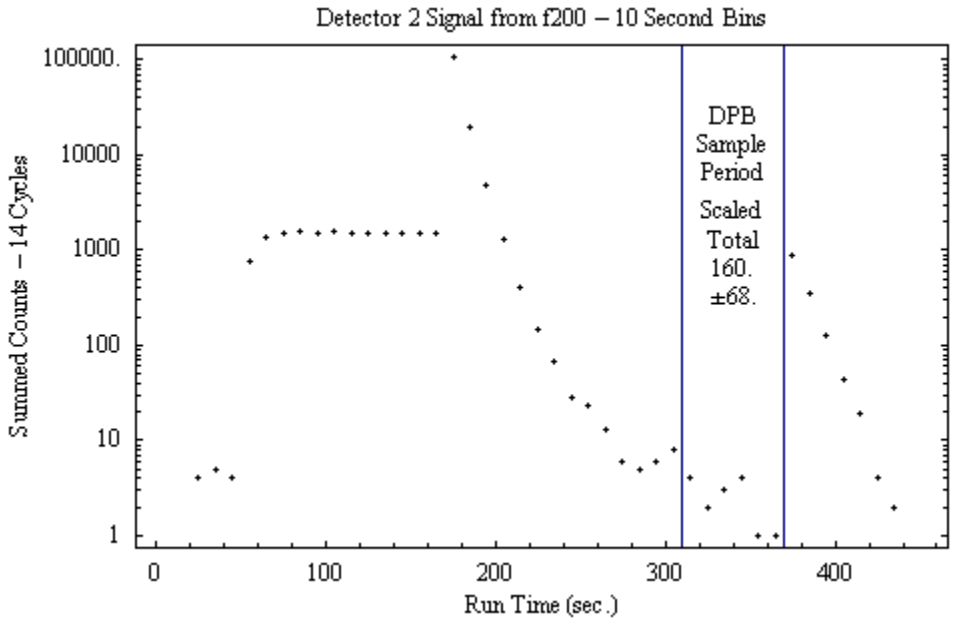

Figure 6-36 Detector 2 signal from f200 – 10–second bins: This plot shows the Detector 2 signal from the f200 run (this run has an AFP loaded trap). The data has been scaled to be comparable to that in Figure 6-35. The 160 scaled total number has had the depolarized UCN subtracted from it, and should be compared to the 105 background number in Figure 6-35.

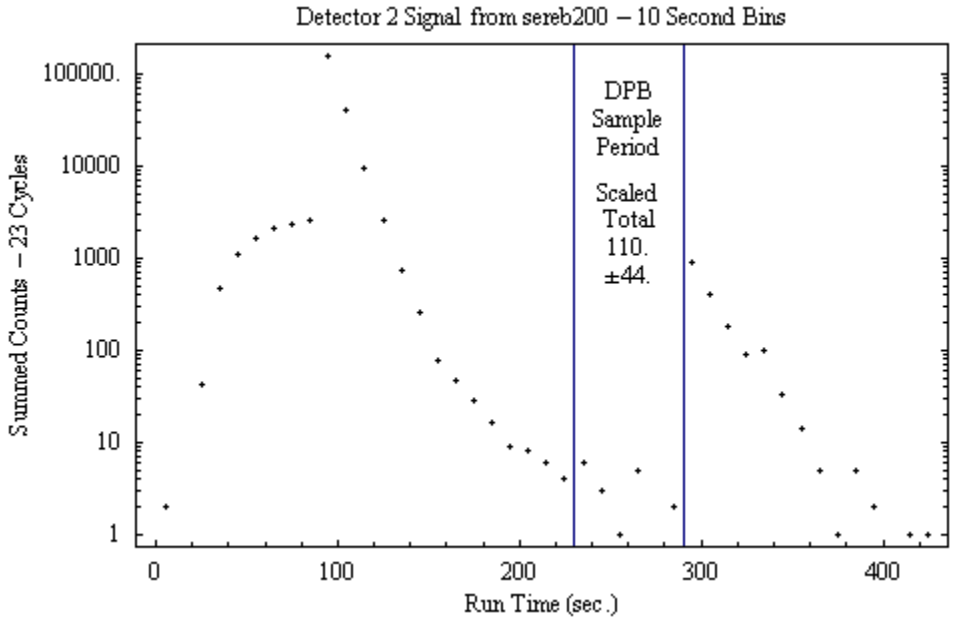

Figure 6-37 Detector 2 signal from sereb200 – 10–second bins: This plot shows the Detector 2 signal from the sereb200 run which has an AFP loaded trap. The data has been scaled to be comparable to that in Figure 6-35. The 110 scaled total number has had the depolarized UCN subtracted from it and should be compared to the 105 background number in Figure 6-35.

To justify the background subtraction, the background in the region of the AFP unload peak can studied in runs sereb200 and f200 where the signal in Detector 2 is due to depolarized UCN, free UCN and background. The depolarization signal can be estimated, and removed, using the rate in Table 6-12; and this has been done in Figures 6-36 and 6-37. The values are scaled to be comparable to the 105 background UCN events subtracted from the 247 cycle peak; both values are above this but the errors are very large since the values were scaled up from 14 and 23 cycles. Even with the large errors, these backgrounds, support the background subtraction method used to get the DPB rate of 6.4×10^{-7}.

6.3.2.2 Depolarization Rate via Method 2

The depolarization rate can be measured very accurately by monitoring a known population of trapped UCN for any that depolarize. This can be accomplished by filling the trap using the AFP and waiting until all the free spin–state UCN escape. The number of trapped UCN is then determined by dumping the trap into Detector 2 using the AFP.

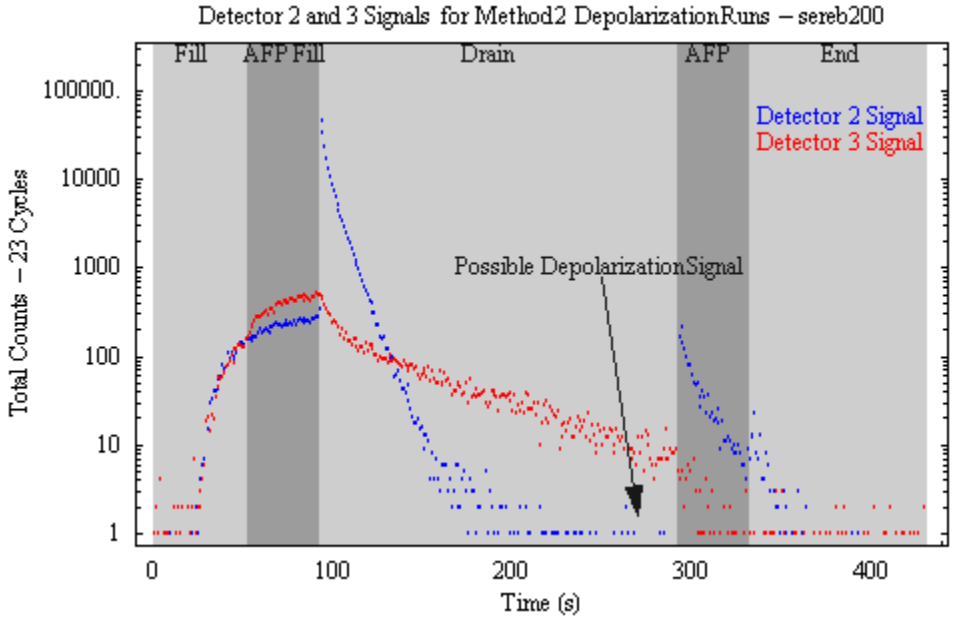

Figure 6-38 Detector 2 and 3 signals for method 2 depolarization runs – sereb200: This plot shows the Detector 2 and 3 signals for the sereb200 run. Any Detector 2 signal in the region before the AFP unload that is above background is evidence of depolarizing UCN. The depolarized UCN come from the trapped population that is later unloaded by the AFP. Then, by knowing the BPS rate the DPB rate can be found.

Data from the serebXXX series of runs is used for this method; the 200 second hold [Figure 6-38] is used to look for depolarization since it has the most runs and the longest drain time, while the whole series of hold times is used to establish the number of UCN in the trap. Looking at Figure 6-38 the red Detector 3 signal shows there are UCN in the trap before the unload peak at 292 seconds, while the lack of much signal from Detector 2 shows any depolarized UCN and background. The background, 0.15±0.05 Hz., is extracted from the final 60 seconds of the run.

The number of UCN in the trap that the depolarization signal comes from can be found using Detector 3 and the calibration from Section 6.3.1.5, or, from fitting the unload peaks of the serebXXX series. The fit of the peaks introduces less uncertainty into the calculation so it will be used. The two exponential fit to the seven unload peaks found in Section 6.3.1.3 fits the data the best and it will be used to predict the number of trapped UCN as a function of time, UCNT[t]. The number of depolarized UCN detected by Detector 2 is calculated by multiplying the number of UCN in the trap times the average number of bounces that a UCN makes in the trap and the depolarization per bounce. This number should be equal the signal in Detector 2 minus the background rate. By summing the signal for a period before the unload, a reasonable DPB number can be found. The following equations express this:

$$\sum_{t=ts}^{to} Det2[t] - BackDet2 = \sum_{t=ts}^{to} DPB \times BPS \times UCNT[t]$$

$$DPB = \frac{\sum_{t=ts}^{to} Det2[t] - BackDet2}{\sum_{t=ts}^{to} BPS \times UCNT[t]}, \; where$$

$$UCNT[t'] = (A\, e^{t'/tau1} + B\, e^{t'/tau2}), or \qquad .$$

$$UCNT[t] = \sum_{t=to}^{te} (Det3[t] - BackDet3) \times Calibration[t], or$$

$$UCNT[t'] = e^{t'/tau} \sum_{t=to}^{te} (Det2[t] - BackDet2)\; e^{(t-to)/tau}$$

The value of the depolarization per bounce should stay the same with time (if it is velocity independent), so summing for various time periods before the unload peak should give the same DPB value. Since the equation for the DPB does not include the

free UCN left in the trap this may not be true. By looking at the sixty seconds preceding the 200 second unload peak, a DPB of 6.2×10^{-7} is found. To find the uncertainly in the measurement, the DPB is calculated 10000 times using different values of BPS, tau1, tau2, and BackDet2 that are chosen from normal distributions around the mean value of each. For the sixty second sampling period the uncertainty is 5.5×10^{-7}. Figure 6-39 and Table 6-12 show values for various sampling times, each uncertainly is extracted from 10000 trails.

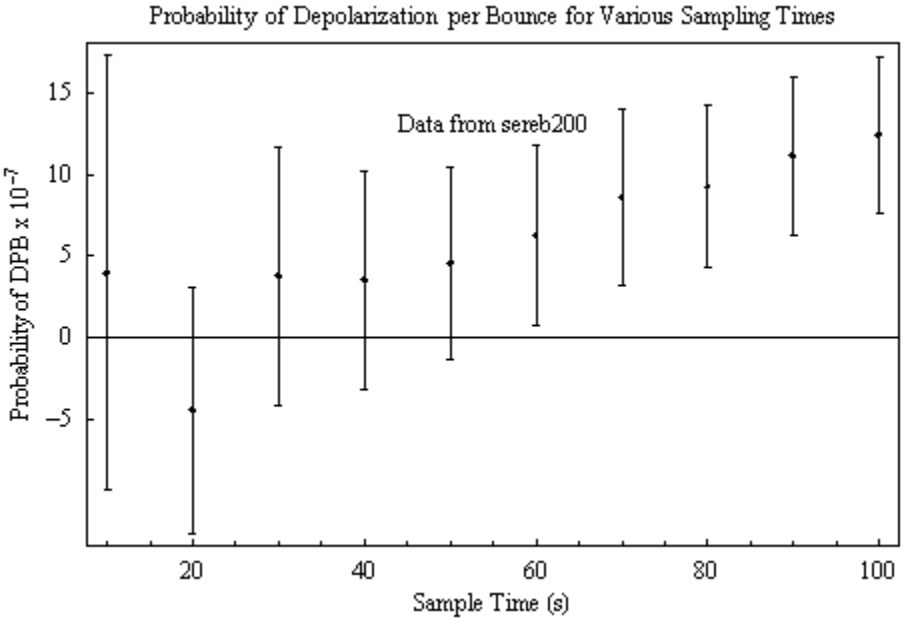

Figure 6-39 Probability of depolarization per bounce for various sampling times: This plot shows the calculated DPB found by the MCEM for various periods before the AFP unload of the sereb200 run. The increase of the DPB rate with increased sampling time shows that free UCN are still in the trap.

As longer periods of time are sampled looking for the DPB rate the rate increases; this starts noticeably at 60 seconds in Figure 6-39. One explanation is the presence of free UCN that are still exiting the system. The errors are large, but it looks like the DPB rate is around 5×10^{-7}. This is lower than the number obtained with the first method, but the background may not have been fully removed in the first method.

Sample Time	DPB	DPB Error
10	$4.\times10^{-7}$	1.3×10^{-6}
20	-4.4×10^{-7}	7.6×10^{-7}
30	3.8×10^{-7}	7.9×10^{-7}
40	3.5×10^{-7}	6.7×10^{-7}
50	4.6×10^{-7}	5.9×10^{-7}
60	6.2×10^{-7}	5.5×10^{-7}
70	8.6×10^{-7}	5.4×10^{-7}
80	9.3×10^{-7}	4.9×10^{-7}
90	1.1×10^{-6}	4.8×10^{-7}
100	1.2×10^{-6}	4.8×10^{-7}

Table 6-13 Method 2 depolarization per bounce: This table has the same data that was plotted in Figure 6-39. It shows an increase in the DPB measurement made by method two as more pre unload data is used. This indicated the presence of free UCN still in the trap.

6.3.3 Results

The UCNA depolarization experiment showed that the UCN depolarization rate was an order of magnitude below that achieved in previous experiments. Although the uncertainties are high, the rate appears to be below 10^{-6} per bounce; this is well below the level of anomalous loss. So although depolarization may contribute to anomalous loss, it is not the main factor for carbon.

The loss rate in the trap due to wall interactions was below $5x10^{-5}$ per bounce, and this includes losses due to the joints and any chips where the coating was removed [Section 6.3.1.2]. At a bounce rate of 45 BPS this would be equivalent to less than 1/1000 of an inch total gap in the two joints. This loss rate is also well below the $18x10^{-5}$ quoted for graphite foil in the first Serebrov depolarization experiment [Table 6-1] – the quality of this coating is unknown. It is also an order of magnitude higher than the theoretical loss per bounce rate (calculated using Ref . 22, Equation 2-70 and Table 2.1 - $\sim6x10^{-6}$).

6.4 Possible Improvements to the Experiment

If the experiment were performed again, there are several changes that could be made to its running and design. The uncertainties of several of the parameters could have been

improved with more data. And the timing of the runs could be changed to better extract the needed data. Also, by changing the design of the foil, aperture and pumping, the experiment could have been improved.

The uncertainty in the trap lifetime found by Detector 3 monitoring a trapped population of UCN could be reduced with more data. The 19 and 23 cycle runs with a 200 second holding time did not have enough data to constrain the fit. The data would also be improved by better transport from the trap to Detector 3. This could be done by improving the 90-degree elbow above the vertical guide.

The background is comparable to the signal in the DPB measurements, so lowering it or its uncertainty would be good. Simply taking more data would lower the uncertainty in the background. Also, taking runs with no UCN in the system that are timed the same as the normal runs would be helpful in understanding the backgrounds. Of course, lowering the noise in the detectors would be a lot of help too.

The first method of finding the depolarization would benefit by using several hold times and a lifetime experiment with the same timing. The basic idea is to make runs with holding times of 60, 80, 100, 120, 140, 160, 180 and 200 seconds, and have a similar set of runs with the trap loaded by the AFP. The DPB rate calculated for each time period should be the same if everything is correctly subtracted from the unload peak; this should happen at the longer times. The corresponding set of AFP load/unload runs would then give a very accurate trap lifetime needed to calculate the DPB.

The second method of depolarization calculation has a lower signal–to–noise ratio as reflected by the comparable uncertainties in 23 versus 247 cycles of data. The uncertainly in the second method would have been lowered considerably with more data to get a better fit on the background.

The removal of the aluminum foil left the system with a poor vacuum and possible contamination from the switcher and spectrometer. To fix this, the foil could be moved

to a position between the spectrometer and switcher; if this were combined with eliminating the pumping stack by pumping instead through the switcher, a much cleaner system would result. Of course, the switcher would have to be cleaned, as would the guides to Detector 2. The final result of these changes would be better vacuum conditions and faster drain time; but the foil would still lower the density of UCN in the trap. This could be helped by lowering the guide after it exits the spectrometer to increase the kinetic energy of the UCN that hit the foil; this seems reasonable since the velocity spectrum is fairly cool.

Another hardware change that would help, is an aperture that could be opened so the trap could be drained into Detector 3. The aperture could be replaced by a gap between the end of the guide and a movable endplate. Then, at minimal clearance, the gap would allow the trap density to be monitored – and when pulled back, the UCN could fall into Detector 3. This would allow a DPB measurement using only Detector 3, which could lower the uncertainty.

In general, all the measurements would have been improved with more data. In the second depolarization method, doubling the number of runs would have greatly improved the result. Also, moving the foil and eliminating the pumping port would lead to much better vacuum and faster drain times; this would improve the results and make the surfaces cleaner leading to a better understanding of UCN depolarization.

6.5 Quartz Guide Transmission Studies – ILL May/June 2002

The October 2001 depolarization test at the ILL showed the UCNA guides to have a low depolarization rate and a low loss per wall collision, but the transmission properties of the guides were not extractable from the data. A second run at the ILL was requested to study this and to further study the depolarization. The run was held during May and June of 2002. The transmission studies were a success, but the depolarization runs were marred with problems and no new results were obtained.

The experimental setup was a modified version of the one described in this chapter – some of the modifications suggested in the pervious section were implemented. For the transmission experiment the PNPI magnet was not present and the guides to be tested were added after the LANL switcher.

The basic transmission experiment has two steps: first, a detector is placed at the end of the short guide exiting the switcher and the number of UCN reaching this is logged; second, the test guide is attached to the switcher and the detector to the end of this, and again, the UCN reaching the detector are counted and logged. The transmission per meter (if the test guide is a meter long) is the ratio of these two numbers. The guides with the best coatings had transmissions of ~95%.

The specularity of the guide was approximated with the following formula: $S^{N_B} = .95$, where S is the specularity and N_B is the average number of bounces a UCN undergoes during transmission. If the population of UCN is assumed to have a random direction, the average forward directed UCN will have a 45 degree angle to the guide axis. This results in 100/6.5~15 bounces per meter, if the guide has a diameter of 6.5 cm. The specularity for 15 bounces per meter would be 99.7%, using this method and 99.5% for 10 bounces per meter. This can be compared to specularity value used in our Monte Carlo simulations, 97%, which was fit to the Serebrov type ^{58}Ni guides used during UCN source prototype development at LANL. This will give less that 80% transmission per meter. This comparison is not correct since a non-specular collision in the Monte Carlo results in a diffuse scattering, which has some probability of making it to the end of the guide. However, our result can be directly compared to the best result published by another group using Serebrov type guide – 85% transmission per meter.[170]

6.6 Current Status of UCNA Guide System

Due the great success of the PLD DLC coated quartz guides they have been used in the entire UCNA experiment, from the source to the decay region. The high specularity and low loss per bounce make them better than ^{58}Ni coated guides for the 12–meter guide system, even though ^{58}Ni guides have a higher critical velocity (~8 m/s instead of ~7.25

m/s). Of course, the decay region is also coated with PLD DLC, since this is what it was developed for. To date, guides for the entire system have been made at Virginia Tech by the UCN group, but the installation is not yet complete.

7 Future Coating Development

The standard coating for ucn guides is ^{58}Ni, which has a very high critical velocity, but also comes with a few problems specific to ucn. The neutron absorption cross section (4.6 barns) is high and the surface tends to absorb hydrogen and water. The PLD DLC guide coatings developed at Virginia Tech do not have any of these problems.

The coating system at Virginia Tech is ideally suited to combine the properties of these two coatings. The coating chamber is equipped with both PLD and e-beam deposition systems which can operate simultaneously without breaking vacuum. The e-beam is currently used to deposit ^{58}Ni and the PLD system is setup for DLC. The chamber is also equipped to provide a deuterium atmosphere to stabilize/terminate the fresh coatings with deuterium rather than, ucn upscattering, hydrogen (the upscattering is reduced by a factor of ~10).

The idea is to cap a ^{58}Ni film with a thin layer of DLC. DLC is very ucn friendly due to low neutron absorption (.0035 barns), very low surface hydrogen (less than a monolayer) and virtually zero hydrogen in the coating [Figure 7-1]. DLC is also hydrophobic. The DLC will reflect neutrons below it's critical velocity (7-7.5 m/s) and higher velocity neutrons will pass through and be reflected by the thicker ^{58}Ni coating. Since the DLC is thin (10 to 50 nm) the absorption will be low and the result will be a more reflective low loss coating.

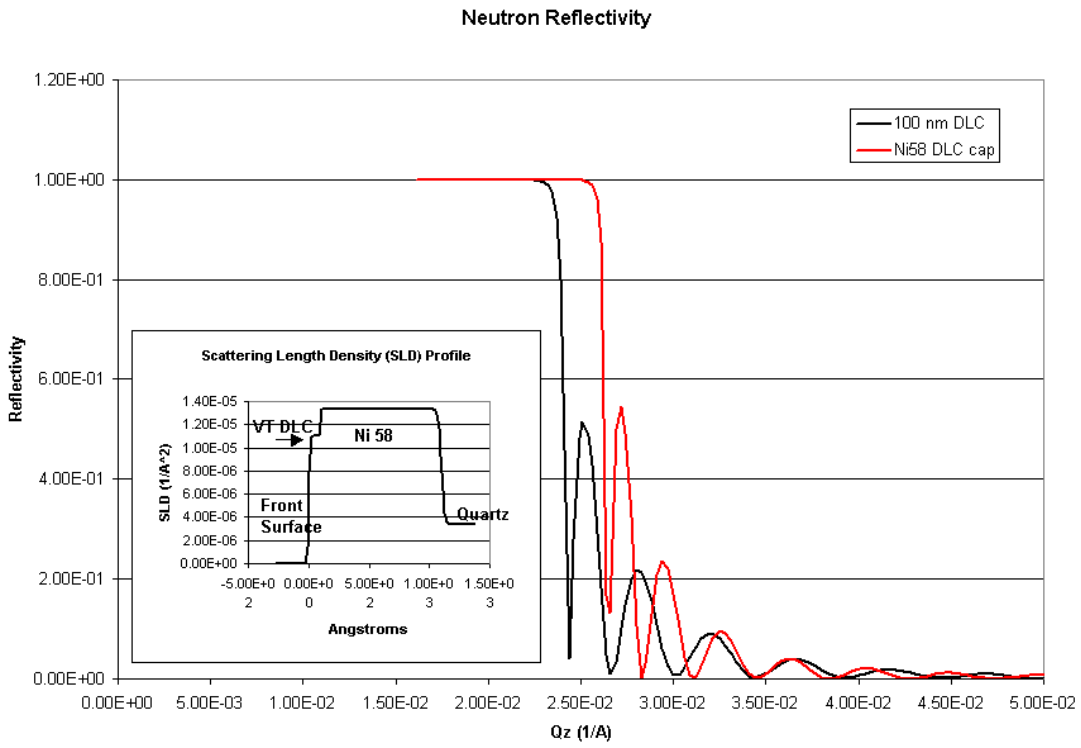

Figure 7-1 Neutron Reflectivity of PLD DLC and DLC capped ^{58}Ni: This plot shows the reflectivity increase by using DLC capped ^{58}Ni over DLC alone. The inset shows the scattering length density profile used to calculate the reflectance of the capped layer.

The capped hybrid coating will deliver more ucn to an experiment and keep them in it longer. This is due to two major factors: lower loss per bounce and higher critical velocity than ^{58}Ni alone. The loss per bounce for transmitting ucn will decrease by a factor of 10 or more. Also, higher critical velocity coatings give great gains in ucn flux, since the flux increases with the cube of the velocity in the ucn energy range (the UCN velocity distribution if Maxwellian).

The ultimate gains with this type of hybrid coating will only be know after testing and optimizing of the DLC layer thickness and density. Testing will be done on the test beam of the new ucn source under construction at LANL.

8 Summary

8.1 Introduction

Experiments with polarized ultracold neutrons (UCN) offer a new way to measure the decay correlations of neutron beta decay; these correlations can be used to test the completeness of the Standard Model and predict physics beyond it. Ultracold neutrons are very low energy neutrons that can be trapped inside of material and magnetic bottles. The decay correlations in combination with the neutron and muon lifetimes are used to experimentally determine the first element (V_{ud}) of the Cabibbo-Kobayashi-Maskawa (CKM) quark mixing matrix. The CKM matrix is a unitary transform between the mass and weak eigenstates of the d, s and b quarks; if the matrix is not unitary this would imply that the Standard Model is not complete. Currently the first row of the CKM matrix is over 2 sigma from unitarity and V_{ud} is the largest component of the row[1, 2].

Precision measurements of V_{ud} are obtained from two different types of experiments: the decay correlation between the electron and the polarized neutron (A–correlation, "A", A_0 – the subscript zero implies that the value has been corrected for known effects like recoil) in neutron beta decay and the super-allowed $0^+ \rightarrow 0^+$ nuclear beta decays. The super-allowed $0^+ \rightarrow 0^+$ decays currently give the most accurate values of V_{ud}, but theoretical errors dominate the uncertainly.[1, 2, 3] Neutron beta decay has less theoretical uncertainty but the experimental errors are great and the various experiments do not agree with each other. The goal of the UCNA experiment is to lower the error in V_{ud} obtained from neutron beta decay so that it is comparable to that from super-allowed $0^+ \rightarrow 0^+$ decays.

The UCNA experiment will be the first measurement of the A–correlation of polarized neutron beta decay using UCN; the previous precision measurements were made with cold neutron beams at reactors. The UCNA experiment will be a complete departure from previous cold neutron experiments with different, and lower backgrounds and

corrections to be applied in the extraction of the A–correlation. The two main advantages of the UCNA experiment are 100% polarization of the neutrons and a pulsed beam induced prompt background. The neutron source is a pulsed spallation target, rather than a reactor, so the backgrounds are time dependent and very different than previous reactor based cold neutron beam experiments. The 100% polarization is achieved by passing the UCN through a seven Tesla magnetic field; one spin-state is blocked by the interaction of the neutron's magnetic moment with the field, while the other is accelerated through it. In order to have high polarization in the experiment the UCN must maintain polarization until they decay or leave the decay region.

The UCN travel a couple of meters and bounce off the guide walls many times between the polarizer and the decay region; each of these wall interactions can potentially depolarize the UCN. This thesis details the development and testing of special diamond-like carbon (DLC) coated guides for transporting polarized UCN in the UCNA experiment. The result of this work sets a new standard in neutron guides for both polarized and unpolarized UCN.

8.2 The Search for a New Ultracold Neutron Guide Coating

Several technologies had to be developed to make the UCNA experiment successful: a brighter UCN source, guides for polarized UCN transport, a high efficiency UCN spin-flipper, and low energy beta detectors with low backscatter. We (VT) decided to take the lead in developing the guides for polarized UCN transport and with this came the responsibility for the rest of the guide system.

The coatings proposed for the UCNA experiment were ^{58}Ni for unpolarized UCN guides and Beryllium or diamond-like carbon (DLC) for the polarized UCN guides. The ^{58}Ni guides were to be made by the PNPI group lead by Anatoli Serebrov, this type of guide has been the standard for our UCN source development. While the PNPI group looked into beryllium for the polarized guides Albert Young of NCSU looked into the possibility of making guides with a DLC coating.

Our first involvement with the coating development was testing samples of diamond-like carbon for surface roughness using an Atomic Force Microscope (AFM) at VT. We sent several test samples to be coated with DLC to SURMET, the coating company that had provided DLC coating for the EDM experiment.[43, 44] While researching the process they used to make these DLC films several other dense carbon coating techniques were found. Some of these other films appeared to be better than the DLC used in the EDM experiment.

To pick the best process for making DLC coated UCN guides both the process and the resulting coating must be considered. The process needs to be able to coat the inside of long tubes – not a common requirement. The coating needs to be good for polarized UCN transport. Whether or not a coating is good can be estimated by looking at its material properties.

Two modern coating techniques produce dense, hydrogen–free, diamond-like carbon coatings. But only the pulsed laser deposition (PLD) of pyrolytic graphite seemed applicable to coating the inside of ultracold neutron guides.

8.3 Diamond-like Carbon from Pulsed Laser Deposition of Pyrolytic Graphite

Pulsed laser deposited diamond-like carbon is made by ablating a graphite target inside a vacuum chamber with a high–power pulsed laser and depositing the ablated carbon onto a substrate. The interaction between the laser beam and the target is highly dependent on the laser wavelength, power, and pulse width. UV lasers with short pulse widths give the best quality films due to the material properties of graphite.

The Virginia Tech deposition system uses an excimer laser operating at 248 nm with pulse energies over a Joule and a vacuum system capable of holding low to high vacuum in the deposition chamber. The laser beam is focused onto the target with a convex lens through a fused silica window. The substrates are held parallel to the target inside the vacuum chamber. The vacuum chamber can be held at high vacuum or a low–pressure

background gas can be maintained; each of these conditions produces a different type of DLC.

8.4 Diamond-like Carbon Coating Surface Characterization

After the initial setup of the PLD system, exploring of the parameter space of laser energy and beam focus started. The literature also pointed to other parameters to explore including adding some nitrogen gas to attempt making carbon nitride, which could be better than diamond for neutron transport. The primary goal was to see if we could make smooth, dense diamond-like carbon. The smoothness was tested with an atomic force microscope, while the density was initially estimated indirectly by the measuring the optical properties of the coating. As a final test the coating would need to be tested for its ability to reflect neutrons using neutron reflectometry

The studies of PLD DLC show that it has the properties to be a good UCN guide coating. The roughness is on the order of the substrate that is used and this is better than other types of UCN coatings. The critical velocity is above 7 meters per second, this is better than beryllium although well below ^{58}Ni. There is also very little hydrogen in the bulk of the film and less than a monolayer on the surface, this should lower the depolarization rate. In general, the results indicate that PLD DLC should be tested as a UCN guide coating.

8.5 Pulsed Laser Deposition Ultracold Neutron Guides

Since PLD DLC makes a coating with high critical velocity and surface roughness near that of the substrate, all that is needed to make a great UCN guide is a smooth substrate. Quartz tubing is extremely smooth on the inside and very low in impurities that could add to the depolarization rate. The combination of quartz tubing and PLD DLC coating should make a great UCN guide that has a low depolarization rate.

To manufacture meter long section of UCN guide a tube coating system was built at VT. And a process for cleaning the quartz surface was also developed. A complete set of

guides, for a UCNA depolarization experiment, were made using the techniques developed.

8.6 Ultracold Neutron Depolarization in Pulsed Laser Deposition Diamond-Like Carbon Coated Quartz Guides

The UCN depolarization in the UCNA experiment should be low enough that it does not need to be considered to obtain the desired precision in the A–correlation measurement. That is, the depolarization rate must be low enough that UCN traveling through the polarized sections of the experiment remain 99.91% polarized.[30] To determine the depolarization rate of UCN during transport through pulsed laser deposition (PLD) diamond-like carbon (DLC) coated quartz guides an experiment using UCN is necessary.

Prior to the UCNA depolarization experiment two experiments had already been done at the Institut Laue-Langevin (ILL) to determine the depolarization rates of UCN on several different surfaces; the results of these experiments looked promising but were insufficient to predict the success of our guides. Beryllium seemed to have a depolarization rate below 10^{-5} per bounce, this is in the range needed. Although carbon was tested, it was graphitic and not PLD DLC like we intended to use in the UCNA experiment. The previous experiments showed that the depolarization rate may be low enough, but a new experiment was needed to test the UCNA guide concept.

The only user facility for UCN research in the world is the ILL in Grenoble, France, so an experiment was designed to utilize this facility and find the depolarization rate for our guides. The experiment to test the Virginia Tech PLD DLC coated quartz guides was designed and built during 2002 with the data collection occurring during October 2002 at the ILL.

The UCNA depolarization experiment showed that the UCN depolarization rate was an order of magnitude below that achieved in previous experiments. Although the uncertainties are high, the rate appears to be below 10^{-6} per bounce; this is well below the level of anomalous loss. So although depolarization may contribute to anomalous loss, it is not the main factor for carbon.

The loss rate in the trap due to wall interactions was below 5×10^{-5} per bounce, and this includes losses due to the joints and any chips where the coating was removed [Section 6.3.1.2]. At a bounce rate of 45 BPS this would be equivalent to less than 1/1000 of an inch total gap in the two joints. This loss rate is also well below the 18×10^{-5} quoted for graphite foil in the first Serebrov depolarization experiment [Table 6-1] – the quality of this coating is unknown. It is also an order of magnitude higher than the theoretical loss per bounce rate (calculated using Ref . 22, Equation 2-70 and Table 2.1 - $\sim 6 \times 10^{-6}$).

The transmission of the guides was also tested during the depolarization experiment and found to be as high as 95% per meter. This is better than published values for standard UCN guides. It also compares well the specularity predicted from the guide's measured roughness.

8.7 Impact of Diamond-Like Carbon Coated Quartz Guides on the UCNA Experiment

Due the great success of the PLD DLC coated quartz guides they have been used in the entire UCNA experiment, from the source to the decay region. The high specularity and low loss per bounce make them better than ^{58}Ni coated guides for the 12–meter guide system from the source to the experiment, even though ^{58}Ni guides have a higher critical velocity (~8 m/s instead of ~7.25 m/s). The measured depolarization rate below 10^{-6} per bounce is more than sufficient for the transport from the polarizer to the decay region and the five–second lifetime in the decay region. In conclusion, the Virginia Tech polarized UCN guide project was a great success.

9 Bibliography

1. H. Abele, E. Barberio, D. Dubbers, F. Glück, J. C. Hardy, W. J. Marciano, A. Serebrov, and N. Severijns, "Quark Mixing, CKM Unitarity" xxx.lanl.gov, arXiv:hep-ph/0312150v1, 11, Dec. 2003
2. A. Czarnecki, W. J. Marciano, and A. Sirlin, "Precision Measurements and CKM Unitarity", xxx.lanl.gov, arXiv:hep-ph/0406324 v1, 29 June 2004
3. S. Eidelman et al. (Particle Data Group), Physics Letters, Vol. B592, No. 1, 2004
4. J. D. Jackson, S.B. Treiman, and H. W. Wyld, Jr., "Possible Tests of Time Reversal Invariance in Beta Decay", Physical Review, Vol. 106, No. 3, May 1, 1957, pp 517-21
5. T. D. Lee and C. N. Yang, "Question of Parity Conservation in Weak Interactions", Physical Review, Vol. 104, No. 1, October 1, 1956, pp 254-8
6. R. Sherr and R. H. Miller, "Electron capture in the decay of Na^{22}", Physical Review, Vol. 93, No. 5, March 1, 1954, pp 1076-81
7. J. B. Gerhart, "Fierz interference of the Fermi interactions in beta decay", Physical Review, Vol. 109, No. 3, February 1, 1958, pp 897-900
8. M.T. Burgy, V. E. Krohn, T. B. Novey, G. R. Ringo, V. L. Telegdi, "Measurement of Asymmetries in the Decay of Polarized Neutrons" Phys. Rev. Vol. 110, 1958, pp 1214
9. M. A. Clark, J. M. Robson, and R. Nathans, "Investigation of time-reversal invariance in the beta decay of the neutron", Physical Review Letters, Vol. 1, No. 3, August 1, 1958, pp 100-1
10. H. Abele, "The Standard Model and Neutron ß-Decay" NIM A, Vol. 440, 2000, pp 499-510
11. S. Gardner and C. Zhang, "Sharpening Low-Energy, Standard Model Tests vi Correlation Coefficients in Neutron Beta Decay", xxx.lanl.gov, arXiv:hep-ph/0012098 v3, 30 April 2001

12. I. S. Towner and J. C. Hardy, “Currents and their Couplings in the Weak Sector of the Standard Model”, “Symmetries and Fundemental Interactions in Nuclei”, Wick C. Haxton and Ernest M. Henley, World Scientific, 1996, pp 183
13. Timo van Ritbergen and Robin G. Stuart, “On the precise determination of the Fermi coupling constant from the muon lifetime”, Nucear Physics B, Vol. 564, 2000, pp 343-90
14. P. T. Debevec, “Precision measurements of fundamental muon properties”, Physica A, Vol. 326, 2003, pp 11-14
15. C. R. Brome et al., “Magnetic trapping of ultracold neutrons”, Physical review C, Vol. 63. No. 5, May 2001, pp 055502/1-15
16. F. J. Hartmann et al., “A magnetic trap for neutron-lifetime measurements”, Workshop on quark mixing and CKM unitarity, Heidelberg, September 2002: http://pi1.physi.uniheidelberg.de/physi/ckm/proceeding.php
17. Conversations with D. Bowman and C. L. Morris of Los Alamos National Lab about a proposed LANL lifetime measurement.
18. P. Bopp et al., “Beta –decay asymmetry of the neutron and g_A/g_V”, Physical Review Letters, Vol. 56, No. 9, mArch 3, 1986, pp 919-22
19. P. Liaud et al., “The measurement of the beta asymmetry in the decay of polarized neutrons”, Nuclear Physics A, Vol. 612, 1997, 53-81
20. H. Abele et al., “A measurement of the beta asymmetry A in the decay of free neutrons”, Physics Letters B, Vol. 407, 1997, pp 212-8
21. J. Reich et al., “A Measurement of the beat asymmetry in neutron decay with PERKEO II”, NIM A, Vol. 440, No. 3, 2000, pp 535-8
22. Golub, R., Richardson, D. and Lamoreaux, S.K., “Ultra-Cold Neutrons”, Adam Hilger, 1991
23. Ignatovich, V. K., “The Physics of Ultracold Neutrons”, Clarendon Press – Oxford, 1990
24. S. J. Seestrom, T. J. Bowles, R. Hill, G. L. Greene, and C. L. Morris, “Development of an ultra cold neutron source at MLNSC”, SPIE, Vol. 2867, 1997, pp 521-4

25. R. E. Hill et al., “Performance of the prototype LANL solid deuterium ultra-cold neutron source”, NIM A, Vol. 440, No. 3, February 11, 2000, pp 674-81
26. C. L. Morris et al., “Measurements of ultracold-neutron lifetimes in solid deuterium”, Physical Review Letters, Vol. 89, No. 27, December 30, 2002, pp “272501-1”-“ 272501-4”
27. A. Saunders et al., “Demonstration of a solid deuterium source of ultra-cold neutrons”, Physics Letters B, Vol. 593, July 22, 2004, pp 55-60
28. Monte Carlo simulations provided by Roger Hill
29. A. Petoukhov, T. Soldner, V. Nesvizhevsky, M. Kreuz, M. Dehn, and M. Brehm. “Toward a perfectly polarized neutron beam”, Workshop on quark mixing and CKM unitarity, Heidelberg, September 2002: http://pi1.physi.uniheidelberg.de/physi/ckm/proceeding.php
30. T. Bowles and A. R. Young et al, “TECHNICAL REVIEW REPORT FOR AN ACCURATE MEASUREMENT OF THE NEUTRON SPIN – ELECTRON ANGULAR CORRELATION IN POLARIZED NEUTRON BETA DECAY WITH ULTRA-COLD NEUTRONS” 2000
31. P. Langacker and S. U. Sankar, “Bounds on the Mass of W_R and the W_L-W_R mixing angle ζ in General $SU(2)_L$ x $SU(2)_R$ x SU(1) Models”, Physical Review D, Vol. 40, No. 5, September 1, 1989, pp 1596-85
32. M. J. Ramsey-Musolf, “Nuclear ß-Decay, Atomic Parity Violation, and New Physics”, Physical Review D, Vol. 62, August 11, 2000, Article # 056009
33. A. Kurylov and M. J. Ramsey-Musolf, “Charged Current Universality in the Minimal Supersymmetric standard Model”, Physical Review Letters, Vol. 88, No. 7, 18 February, 2002, Article # 071804
34. J. Erler and M. J. Ramsey-Musolf, “Low Energy Test of the Weak Interaction”, xxx.lanl.gov, arXiv:hep-ph/040429 v1, 30 April 2004
35. B. G. Yerozolimsky, “Free Neutron Decay: a Review of the Contemporary Situation”, NIM A, Vol. 440, 2000, pp 491-8
36. V. Gudkov, “New Generation of Neutron Decay Experiments and Radiative Corrections” Nuclear Theory Seminar at LANL October 2, 2003

37. V. Gudkov, "New Generation of Neutron Decay Experiments", xxx.lanl.gov, arXiv:nucl-th/0404001 v1, 1 April 2004
38. V. Bernard, S. Gardner, U-G. Meißner, C. Zhang, "Radiative Neutron β-Decay in Effective Field Theory", xxx.lanl.gov, arXiv:hep-ph/0403241 v1, 28 April 2004
39. Rodger L. Gamblin and Thomas R. Carver, "Polarization and relaxation processes in ^{3}He gas", Physical Review, Vol. 138, No. 4A, May 17, 1965, pp A 946-60
40. W. A. Lanford and R. Golub, "Hydrogen surface contamination and the storage of ultracold neutrons", Physical Review Letters, Vol. 39, No. 24, December 12, 1977, pp 1509-12
41. A. Serebrov et al., "Depolarization of UCN stored in material traps" NIM A, Vol. 440, 2000, pp 717-21
42. A. Serebrov et al., "Depolarization of ultracold neutrons during their storage in material bottles", Phys. Lett. A, Vol. 313,No. 5-6, pp 373-9
43. SURMET - http://www.surmet.com/contact.html 33 B Street Burlington, MA 01803 Contact: Richard A Cooke, Rickcooke@surmet.com 781-272-3969
44. M.G.D. van der Grinten et al., "Characterization and development of Diamond-like Coatings for Storing Neutrons", Nucl. Inst. and Meth. A, Vol. 423, 1999, pp. 421-427
45. A. I. Egorov et al., "Production, storage, and polarization of ultracold neutrons", Sov. J. Nucl. Phys., Vol. 19, No. 2, August 1974, pp 147-52
46. Y. Y. Kosvintsev et al., "Extraction of ultracold neutrons from t he high flux reactor SM-2", NIM, Vol. 143, 1977, pp 133-7
47. Leslie L. Foldy, "The multiple scattering of waves", Physical Review, Vol. 67, No. 3 and 4, February 1, 1945, pp 107-19
48. E. Fermi and L. Marshall, "Interference phenomena of slow neutrons", Physcial Review, Vol. 71, No. 10, May 15, 1945, pp 666-
49. Grundy, M. J. et al., "Characterization of plasma-deposited amorphous hydrogenated carbon films by neutron reflectivity", Thin Solid Films, Vol. 172, 1989, pp 269-82
50. http://www.ncnr.nist.gov/resources/n-lengths
51. CRC Handbook of Chemistry and Physics: http://www.hbpcnetbase.com

52. John C. Angus and Cliff C. Hayman, “Low-pressure, metastable growth of diamond and “diamondlike” phases”, Science, New Series, Vol. 241, Issue 4868, Aug. 19, 1988, pp 913-21
53. M. Nakayama, Y. Matsuba, J. Shimamura, Y. Yamamoto, H. Chihara, H. Kato, K. Maruyama, K. Kamata, “Physical properties of diamondlike carbon films deposited in mixed atmospheres of C_2H_4-Ar, C_2H_4-H_2, and C_2H_4-N_2”, J. Vac. Sci. Technol. A, Vol. 14, No. 4, Jul/Aug 1996, pp 2418-26
54. J. Robertson, “Diamond-like amorphous carbon”, Material science and engineering: R: Reports”, May 24, 2002, Vol. 37, No. 4-6
55. M. P. Siegal, D. R. Tallant, L. J. Martinez-Miranda, J. C. Barbour, R. L. Simpson, D. L. Overmyer, ”Nanostructural characterization of amorphous diamondlike carbon films”, Phys. Rev. B, Vol. 61, No. 15, april 15, 2000, pp 10451-62
56. N. Savvides, “Ion-assisted deposition and metastable structures”, Thin solid films, Vol. 163, 1988, pp 13-32
57. Sol Aisenberg and Ronald Chabot, “Ion-beam deposition of thin films of diamondlike carbon”, Journal of applied physics, Vol. 42, No. 7, June 1971, pp 2953-8
58. E. G. Spencer, P. H. Schmidt, D. C. Joy, F. J. Sansalone, “Ion-beam-deposited polycrystalline diamondlike films”, Applied physics letters, Vol. 29, No. 2, July 15, 1976, pp 118-20
59. N. Savvides, “Four-fold to three-fold transition in diamond-like amorphous carbon films: A study of optical and electrical properties”, Journal of applied physics, Vol. 58, No. 1, July 1, 1985, pp 518-21
60. N. Savvides and B. Window, “Diamondlike amorphous carbon films prepared by magnetron sputtering of graphite”, J. Vac. Sci. Technol. A, Vol. 3, No. 6, Nov/Dec 1985, pp2386-90
61. N. Savvides, “Optical constants and associated functions of metastable diamondlike amorphous carbon films in the energy range .5-7.3 eV”, J. Appl. Phys., Vol. 59, No. 12, June 15, 1986, pp 4133-45
62. Howard M. Smith and A. F. Turner, “Vacuum deposition thins films using a ruby laser”, Applied Optics, Vol. 4, No. 1, January 1965, pp 147-8

63. P. D. Zavitsanos, “Mass spectrometric analysis of carbon species generated by laser evaporation”, Carbon, Vol. 6, 1968, pp 731-7
64. Hugo Weichel, C. D. David, Jr., P. V. Avizonis, “Effects of radiation pressure on a laser-produced plasma”, Applied Physics Letters, Vol. 13, No. 11, Dec. 1,1968, pp 376-9
65. C. D. David, Jr. and H. Weichel, “Temperature of a laser-heated carbon plasma”, Journal of Applied Physics, Vol. 40, No. 9, Aug. 1969, pp 3674-9
66. Susumu Fujimori and Kazutoshi Nagai, “The effect of ion bombardment of carbon films prepared by laser evaporation”, Japanese journal of applied physics, Vol. 20, No. 3, March 1981, pp L194-6
67. C. L. Marquardt, R. T. Williams, D. J. Nagel, “Deposition of amorphous carbon films from laser produced plasmas”, Mat. Res. Soc. Symp. Proc., Vol. 38, 1985, pp 325-35
68. Tetsuya Sato, Shigeo Furuno, Satoshi Iguchi, “Deposition of diamond-like carbon films by pulsed-laser evaporation”, Japanese journal of applied physics, Vol. 26, No. 9, 1987, pp L1487-8
69. T. Sato, S. Furuno, S. Iguchi, M. Hanabusa, “Diamond-like carbon films prepared by pulsed-laser evaporation”, Appl. Phys. A, Vol. A45, No. 4, pp 355-60
70. S. S. Wagal, E. M. Juengerman, C. B. Collins, “Diamond-like carbon films prepared by with a laser ion source”, Appl. Phys. Lett., Vol. 53, No. 3, July 1988, pp 187-8
71. T. A. Friedmann, M. P. Siegal, D. R. Tallant, R. L. Simpson, F. Dominuez, “Residual stress and Raman spectra of laser deposited highly tetrahedral-coordinated amorphous carbon films”, Mat. Res. Soc. Symp. Proc., Vol. 349, 1994, pp 501-6
72. Fulin Xiong and R. P. H. Chang, “Hard amorphous carbon films deposited be ArF pulsed laser ablation of graphite at room temperature”, Mat. Res. Soc. Symp. Proc., Vol. 270, 1992, pp 451-6
73. E. Findeisen, R. Feidenhans’l, M. E. Vigild, M. Nielsen, K. N. Clausen, M. Foss, “Distribution function, density and hydrogen concentration of amorphous

diamond-like, carbon films obtained by x-ray and neutron scattering", Mat. Res. Soc. Symp. Proc., Vol. 349, pp 495-500

74. E. Findeisen, R. Feidenhans'l, M. E. Vigild, K. N. Clausen, J. Bindslev Hansen, M. D. Bentzon, J. P. Goff, "Hydrogen concentration and mass density of diamond-like carbon films obtained by x-ray and neutron reflectivity", J. Appl. Phys. Vol. 76, No. 8, October 15, 1994, pp 4636-42
75. Y. Huai, J. N. Broughton, E. Gat, M. Chaker, C. F. M. Borges, Y. Beaudoin, H. Pepin, M. Moisan, "Pulsed-laser deposition and characterization of amorphous diamondlike carbon films", Mat. Res. Soc. Symp. Proc., Vol. 349, 1994, pp 471-6
76. T. A. Freidmann, private communication
77. V. S. Veerasamy, G. A. J. Amaratunga, W. I. Milne, P. Hewitt, P. J. Fallon, D. R. McKenzie, C. A. Davis, "Optical and electronic properties of amorphous diamond", Diamond and related materials, Vol. 2, 1993, pp 782-7
78. M. C. Polo, J. L. Andujar, A. Hart, J. Robertson, W. I. Milne, "Preparation of tetrahedral amorphous carbon films by filtered cathodic vacuum arc deposition", Diamond and related materials, Vol. 9, 2000, pp 663-7
79. V. E. Strel'nitskii, V. G. Padalka, S. I. Vakula, "Properties of diamond-like carbon films produced by the condensation of a plasma stream with an RF potential", Sov. Phys. Tech. Phys., Vol. 23, No. 2, Febuary 1978, pp 222-4
80. S. I. Vakula, V. G. Padalka, V. E. Strel'nitskii, A. J. Usoskin, "Optical properties of diamond-like carbon films", Sov. Tech. Phys. Lett., Vol. 5, No.11, Nov. 79, pp 573-4
81. N. N. Matyushenko, V. E. Strel'nitskii, V. A. Gusev, "A dense new version of crystalline carbon C_8", JETP Lett., Vol. 30, No. 4, August 20, 1979, pp 199-202
82. A. S. Bakai, V. E. Strel'nitskii, "Structure of carbon films formed by the deposition of fast ions", Sov. Phys. Tech. Phys, Vol. 26, No. 11, November 1981, pp 1425-6
83. QQC Inc. - http://www.thriller.com/ 12825 Ford Rd. Dearborn, MI 48126, Ph#: 313-581-0043
84. Chrisey, D.B. and Hubler, G.K., "Pulsed laser deposition of thin films", John Wiley and sons, Inc., 1994

85. K. J. Koivusaari, J. Levoska, and S. Leppavuori, “Pulsed-laser deposition of diamond-like carbon: Relations between laser fluence, velocity of carbon ions and bonding in the films”, Journal of Applied Physics, Volume. 85, No. 5, March 1, 1999, pp 2915-20
86. R. F. Wood, K. R. Chen, J. N. Leboeuf, A. A. Puretzky, and D. B. Goehegan, “Dynamics of plume propagation and splitting during pulsed-laser ablation”, Physical Review Letters, Vol. 79, No. 8, August 25, 1997, pp 1571-4
87. D. L. Greenaway, G. Harbeke, F. Bassani, and E. Tosatti, “Anisotropy of the optical constants and the band structure of graphite”, Physical Review, Vol. 178, No. 3, February 15, 1969, pp 1340-8
88. J. G. Carter, R. H. Huebner, R. N. Hamm, and R. D. Birkhoff, “Optical properties of graphite in the region 1100 to 3000 Angstrom”, Physical Review, Vol. 137, No. 2A, January 18, 1965, pp A639-41
89. J. R. Reitz, F. J. Milford, R. W. Christy, “Foundations of electromagnetic theory”, Addison-Wesley Publishing Company, 4th ed., C 1993
90. V. I. Merkulov, D. H. Lowndes, G. E. Jellison, A. A. Puretzky, D. B. Goehegan, “Structure and optical properties of amorphous diamond films prepared by ArF laser ablation as a function of carbon ion kinetic energy”, Applied Physics Letters, Vol. 73, No. 18, November 2, 1998, pp 2591-3
91. A. A. Puretzky, D. B. Goehegan, G.E. Jellison, and M. M. McGibbon, “Comparative diagnostics of ArF- and KrF-laser generated carbon plumes used for amorphous diamond-like carbon film deposition”, Applied Surface Science, 96-98, 1996, pp 859-65
92. D. H. Lowndes, V. I. Merkulov, A. A. Puretzky, D. B. Goehegan, G. E. Jellison, C. M. Rouleau, and T. Thundat, “Amorphous diamond films deposited by pulsed-laser ablation: the optimum carbon ion kinetic energy and effects of laser wavelength”, Mat. Res. Soc. Symp. Proc., Vol. 526, 1998, pp 325-30
93. J. J. Ewing, and C. A. Brown, “Laser action on the $^2\Sigma^+_{1/2}$ ->$^2\Sigma^+_{1/2}$ bands of KrF and XeCl”, Applied Physics Letters, Vol. 27, No. 6, Sept. 15, 1975, pp 350-2

94. M. Rokni, J. H. Jacob, and J. A. Mangano, "Dominate formation and quenching processes in E-beam pumped ArF^* and KrF^* lasers", Physical Review A, Vol. 16, No. 6, December 1977, pp 2216-24
95. C. W. Werner and E. V. George, "Principles of laser plasmas: Chpt. 10, Excimer lasers", John Wiley and Sons, 1976, pp 421-456
96. G. Popovici, T. Sung, M. A. Prelas, S. Khasawinah, and R. G. Wilson, "Diffusion of impurities under bias in CVD diamond films", Diamond, SiC and Nitride Wide Bandgap Semiconductors. Symposium Mater. Res. Soc. 1994, pp 601-6
97. Marvin L. Cohen, "Calculations of bulk moduli of diamond and zinc-blende solids", Physical Review B, Vol. 32, No. 12, December 15, 1985, pp 7988-91
98. A. L. Liu, M. L. Cohen, "Prediction of new low compressibility solids", Science, Vol. 245, No. 4920, pp 841-2
99. D. M. Teter, "Computational alchemy: the search for new superhard materials", MRS Bulletin, Vol. 23, No. 1, January, 1998, pp 22-7
100. David Michael Teter, "Computational alchemy: the rational design of new superhard materials", Virginia Tech Disertation, 1998
101. J. Hu, P. Yang, and C. M. Lieber, "Nitrogen-driven sp^3 to sp^2 transformation in carbon nitride materials", Physical Review B, Rapid Communications, Vol. 57, No,. 6, February 1, 1998, pp R3185-8
102. I. Alexandrou, I. Zergioti, M. J. F. Healy, G. A. J. Amaratunga, C. J. Kiely, H. Davock, A. Papworth, and C. Fotakis, "Enhancements of the properties of pulsed laser-deposited carbon nitride by the synchronization of laser and N_2 gas jet pulses", Surface and Coating Technology, Vol. 110, 1998, pp 147-52
103. R. F. Bunshah et al., "Deposition technologies for films and coatings, development and applications", Noyes Publications, 1982
104. R. Henck, C. Fuchs, E. Fogarassy, J. Hommet, and F. LE Normand, "Vacuum ultraviolet and visible optical emission spectra from laser ablation of graphite at 193 nm: application to carbon nitride thin films deposition", Mat. Res. Soc. Symp. Proc., Vol. 526, 1998, pp 337-42
105. Y. Yamagata, A. Sharma, J. Narayan, R. M. Mayo, J. W. Newman, and K. Ebihara, "Optical emission study of ablation plasma plume in the preparation of

diamond-like carbon films by KrF excimer laser", Journal of Applied Physics, Vol. 86, No. 8, October 15, 1999, pp 4154-9

106. Q. R. Hou, J. Gao, "Influence of a magnetic field on deposition of diamond-like carbon films", Applied Physics A, Vol. 67, 1998, pp 417-20

107. D. L. Pappas, K. L. Saenger, J. J. Cuomo and R. W. Dreyfus, "Charcterization of laser vaporization plasmas generated for the deposition of diamond-like carbon", Journal of Applied Physics, Vol. 72, No. 9, November 1, 1992, pp 3966-70

108. T. A. Friedmann, J. P. Sullivan, J. A. Knapp, D. R. Tallant, D. M. Follstaedt, D. L. Medlin, and P. B. Mirkarimi, "Thick stress-free amorphous-tetrahedral carbon films with hardness near that of diamond", Applied Physics Letters, Vol. 71, No. 26, December 29, 1997, pp 3820-2

109. Chr. Weissmantel, C. Schürer, F. Fröhlich, P. Grau, and H. Lehmann, "Mechanical properties of hard carbon films", Thin Solid Films, Vol. 61, 1979, pp L5-L7

110. D. Nir, Stress relief forms of diamond-like carbon thin films under internal compressive stress", Thin Solid Films, Vol. 112, No. 1, pp 41-9

111. Q. H. Fan, A. Fernandes, E. Pereeira, and J. Grácio, "Evaluation of adhesion of diamond coating by thermal quench method", Journal of Applied Physics, Vol. 83, No. 10, May 15, 1998, pp 5588-90

112. W. Pompe, H. -J. Scheibe, A. Ricnter, H. –D. Bauer, k. Bewilogua, C. Weissmantel, "On the influence of residual stresses and density fluctuation on the crystallization of amorphous carbon films", Thin Solid Films, Vol. 144, 1986, pp 77-92

113. A. C. Ferrari, B. Kleinsorge, N. A. Morrison, A. Hart, V. Stolojan, and J. Robertson, "Stress reduction and bond stability during thermal annealing of tetrahedral amorphous carbon", Journal of Appied Phisics, Vol. 85, No. 10, may 15, 1999, pp 7191-7

114. Private communication: John Hauer, GM Associates

115. Private communication: Kevin McBreen, Heraeus-Amersil Quartz

116. http://www.rathmfg.com/TRUE10.htm

117. A. Steyerl, “Effect of surface roughness on the total reflection and transmission pf slow neutrons (guide tubes)”, Zeitschrift fur Physik A, Vol. 254, No. 2, 1972, pp 169-88

118. M. Brown, R. Golub, J. M. Pendlebury, “Monte carlo calculation of ultra cold neutron flow through long tubes with a realistic angular distribution of reflected neutrons”, Vacuum. Vol. 25, No. 2, Sept. 30, 1974, pp 61-4

119. M. A. Havstad, M. Schildback, and W. McLean II, “The optical constants and spectral specular reflectivity of highly oriented pyrolytic graphite (HOPG)”, Radiative Heat Transfer: Theory and Application, HTD-Vol. 244, ASME 1993, pp 85-95

120. E. A. Taft and H. R. Philipp, “Optical properties of graphite”, Physical Review, Vol. 138, No. 1A, April 5, 1965, pp A197-202

121. http://www.jawoollam.com/vase.html

122. J. A. Woollam, VASE user manual

123. C. F. Klingshirn, “Semiconductor Optics”, Springer, 1997

124. http://www.jawoollam.com/wvase32.html

125. G. E. Jellison, Jr. and F. A. Modine, “Parameterization of the optical functions of amorphous materials in the interband region”, Applied Physics Letters, Vol. 69, No. 3, July 15, 1996, pp 371-3, Erratum: Applied Physics Letters, Vol. 69, No. 14, September 30, 1996, p 2137

126. P. R. Athey, F. K. Urban III, M. F. Tabet and W. A. McGahan, “Optical properties of cobalt oxide films deposited by spray pyrolysis”, Journal of Vacuum Technology A, Vol. 14, No. 3, May/June, 1996, pp 685-93

127. W. E. Baitinger, P. W. French and E. L. Swarts, “Characterization of tin in the bottom surface of float glass by ellipsometry and XPS”, Journal of Non-Crystalline Solids, Vol. 38-39, 1980, pp 749-754

128. L. Colombin, A. Jelli, J. Riga, J. J. Pireaux and J. Verbist, “Penetration depth of tin in float glass”, Journal of Non-Crystalline Solids, Vol. 24, 1977 pp 253-8

129. M. Feldmann and R. Weißmann, “Initial stages of float glass corrosion”, Journal of Non-Crystalline Solids, Vol. 218, 1997, pp 205-9

130. B. Dugnoille and O. Virlet, "Optical profile of surface layers on a float glass determined by ellipsometry", Applied Optics, Vol. 33, No. 25, September 1, 1994, pp 5853-8

131. P. R. Athey, M. F. Tabet and F. K. Urban III, "Determining the optical properties of a mixed-metal oxide film", $Co_{3-x-y}Cr_xFe_yO_4$, with spectroscopic ellipsometry and atomic force microscopy", Journal of Vacuum Technology A, Vol. 15, No. 3, May/June 1997

132. http://lansce.lanl.gov/lujan/instruments/spear/spear.htm

133. L. G. Parratt, "Surface Studies of solids by total reflection of x-rays", Physical Review, Vol. 95, No. 2, July 15,1954, pp359-69

134. Berlin Neutron Scattering Center at Hahn-Meitner-Institut

135. T. P. Russell, "X-ray and neutron reflectivity for the investigation of polymers", Vol. 5, No. 4-5, December, 1990, pp 171-271

136. Marek Tuleta, "The influence of plasma processing on the surface composition of float glass", Vacuum, Vol. 54, 1999, pp 41-5

137. F. Caccavale, R. Coppola, A. Menelle, M. Montecchi, P. Polato, G. Principi, "Characterization of SnO_x films on architectural glass by neutron reflectometry, SIMS, CEMS, and spectrophotometry", Journal of Non-Crystalline Solids, Vol. 218, 1997, 292-5

138. R. M. Richardson, R. M. Dalgliesh, T. Brennan, M. R. Lovell, A. C. Barnes, "A neutron reflection study of the effect of water on the surface of float glass", Journal of Non-Crystalline Solids, Vol. 292, 2001, pp 93-107

139. Yasou Hayashi, Ryoji Akiyama and Marahiro Kudo, "Surface characterization of float glass related to changes in the optical properties after reheating", Surface and Interface Analysis, Vol. 31, 2001, pp 87-92

140. P. Keil, D. Lützenkirchen-Hecht, and R. Frahm, "Grazing Incidence X-ray and Diffuse Scattering Measurements of Float Glass Surfaces"

141. Olaf Anderson and Klaus Bange, "Characterization of glass surfaces by x-ray reflectivity", Glastech. Ber. Glass Sci. Technol., Vol. 70, No. 10, 1997, pp 316-21

142. M. P. Siegal, J. C. Barour, P. N. Provencio, D. R. Tallant, and T. A. Friedmann, "Amorphous-tetrahedral diamondlike carbon layered structures resulting from film growth energetics", Applied Physics Letters, Vol. 73, No. 6, August10, 1998, pp 759-61

143. R. Kalish, Y. Lifshitz, K. Nugent, and S. Prawer, "Thermal stability and relaxation in diamond-like-carbon. A Raman study of films with different sp^3 fractions (ta-C to a-C)", Applied Physics Letters, Vol. 74, No. 20, May17, 1999, pp 2936-8

144. S. M. Leeds, T. J. Davis, P. W. May, C. D. O. Pickard, M. N. R. Ashfold, "Use of different wavelengths for the analysis of CVD diamond by laser Raman spectroscopy" , Diamond and Related Materials, Vol. 7, 1998, pp 233-7

145. A. C. Ferrari and J. Robertson, "Interpretation of Raman spectra of disordered and amorphous carbon", Physical Review B, Vol. 61, No. 20, May 15, 2000, pp 14095-14107

146. http://physics.nist.gov/PhysRefData/XrayMassCoef/tab3.html

147. http://physics.nist.gov/PhysRefData/XrayMassCoef/chap2.html

148. http://www.webmineral.com/X-Ray.shtml

149. R. Sappok and H. P. Boehm, "CHEMIE DER OBERFLÄCHE DES DIAMANTEN-I. BENETZUNGSWARMEN, ELEKTRONENSPINRESONANZ UND INFRAROTSPEKTREN DER OBERFLÄCHEN- HYDRIDE,-HALOGENIDE UND-OXIDE", Carbon, Vol. 6, No 3 June 1968

150. http://genesis.jpl.nansa.org

151. Private communications with Donald R Burnett, Genesis Project P.I.

152. V. K. Leko and L. A. Komarova, "Effect of surface impurities on the crystallization kinetics of quartz glasses", Izvestiya Akademii Nauk Sssr, Neorganicheskie Materialy, Vol. 10, No. 10, October, 1974, pp 1872-4, Translation: Inorganic Materials, Vol. 10, No. 7-12, pp 1605-7

153. V. K. Leko and L. A. Komarova, "Investigation of the impurity distribution in the surface layers of fused silica tubes (for light source sheaths)", Optiko-Mekhanicheskaya Promyshlennost, Vol. 41, June, 1974, pp 33-5, Translation: Sov. J. Opt. Technol, Vol. 41, No. 6, June, 1974, pp 326-7

154. J. Yoshiyama, F. Y. Genin, A. Salleo, I. M. Thomas, M. R. Kozowski, L. M. Sheehan, I. D. Hutcheon, D. W. Camp, "Effects of polishing, etching, cleaving, and water leaching on the UV damage of fused silica", SPIE-Int. Soc. Opt. Eng. Proceedings of Spie – the International Society for Optical Engineering, Vol. 3244, 1998, pp 331-40

155. Da-Tung Liang and Dennis W. Readey, "Dissolution kinetics of crystalline and amorphous silica in hydrofluoric-hydrochloric acid mixtures", J. Am. Ceram. Soc, Vol. 70, No. 8, 1987, pp 570-7

156. HTTP://UCN.web.psi.ch/proposals/depol/depol_final_update.html

157. A. Steyerl et al., "A new source of cold and ultracold neutrons", Physics Letters A, Vol. 116, No. 7, June 30, 1986, pp 347-52

158. A. Steyerl, "A "neutron turbine" as an efficient source of ultracold neutrons", NIM, Vol. 125, 1975, pp 461-9

159. http://www.ill.fr/YellowBook/PF2

160. Data from the PNPI group lead by A. Serebrov

161. Chen Yu's dissertation or article

162. C. E. Hayes, W. A. Edelstein, J. F. Schenck, O. M. Mueller and M. Eash, "An efficient, highly homogeneous radio-frequency coil for whole-body NMR imaging at 1.5 Tesla", Journal of Magnetic Resonance, Vol. 63, 1985, pp 622-8

163. http://www.pnpi.spb.ru

164. http://UCN.web.psi.ch

165. Albert Young, private communication

166. Discussions with Chris Morris, Los Alamos National Lab

167. John F. O'Hanlon, "A user's guide to vacuum technology", John Wiley and Sons, Inc., Copyright 1980

168. Philip R. Bevington and D. Keith Robinson, "Data reduction and error analysis for the physical sciences", McGraw-Hill, Second Edition, pp 141-7

169. R. A. Arndt and M. H. MacGregor, "Nucleon-nucleon phase shift analysis by Chi-squared minimization", Methods in Computational Physics, Vol. 6, 1966, pp 253-95

170. C. A. Baker, et al., “Development of solid-state silicon devices as ultra cold neutron detectors”, NIM A, Vol. 487, 2002, pp 511-20